

DAMAGE DETECTION TECHNIQUES FOR CONCRETE APPLICATIONS

FINAL PROJECT REPORT

by

Lev Khazanovich
Katelyn Freeseaman
Lucio Salles
Aziz Asadollahi
University of Minnesota

Sponsorship
(List CHPP and matching external sponsors, e.g. DOT)

for

Center for Highway Pavement Preservation
(CHPP)



In cooperation with US Department of Transportation-Research and Innovative Technology Administration (RITA)

August 2016

Disclaimer

The contents of this report reflect the views of the authors, who are responsible for the facts and the accuracy of the information presented herein. This document is disseminated under the sponsorship of the U.S. Department of Transportation's University Transportation Centers Program, in the interest of information exchange. The Center for Highway Pavement Preservation (CHPP), the U.S. Government and matching sponsor assume no liability for the contents or use thereof.

Technical Report Documentation Page			
1. Report No. CHPP Report-UMN#1-2016	2. Government Accession No.	3. Recipient's Catalog No.	
4. Title and Subtitle Damage Detection Techniques for Concrete Applications		5. Report Date	
		6. Performing Organization Code	
7. Author(s) Lev Khazanovich, Katelyn Freeseaman, Lucio Salles, Aziz Asadollahi		8. Performing Organization Report No.	
9. Performing Organization Name and Address CHPP Center for Highway Pavement Preservation, Tier 1 University Transportation Center Michigan State University, 2857 Jolly Road, Okemos, MI 48864		10. Work Unit No. (TRAIS)	
		11. Contract or Grant No.	
12. Sponsoring Organization Name and Address United States of America Department of Transportation Research and Innovative Technology Administration		13. Type of Report and Period Covered	
		14. Sponsoring Agency Code	
15. Supplementary Notes Report uploaded at http://www.chpp.egr.msu.edu/			
16. Abstract <p>New technological advances in nondestructive testing technology have created the opportunity to better utilize ultrasonic waves to aid in damage detection applications for concrete. This research utilizes an ultrasonic array device for nondestructive damage detection purposes. The ultrasonic shear velocity array system used for this research is particularly advantageous because it can obtain measurements on virtually any concrete specimen, from columns and beams to concrete pavements, and provides a wealth of data from a single measurement. Novel signal interpretation methods were developed for several important concrete applications.</p> <p>Detection of load-induced damage in a full-scale reinforced concrete column, as well as standard life-cycle damage in concrete pavements caused by freeze thaw or alkali-silica reaction degradation were considered. In addition, cracking in continuously reinforced concrete pavements was considered. These investigations culminated in the development of successful and efficient quantitative damage detection methods.</p>			
17. Key Words		18. Distribution Statement No restrictions.	
19. Security Classification (of this report) Unclassified.	20. Security Classification (of this page) Unclassified.	21. No. of Pages	22. Price NA

Table of Contents

CHAPTER 1 - INTRODUCTION.....	10
CHAPTER 2 - LITERATURE REVIEW.....	11
2.1 Nondestructive Testing Methods.....	11
2.2 Non-Destructive Testing Methods	11
2.2.1 Electromagnetic Methods	11
2.2.2 Elastic Wave-Based Methods	15
2.2.3 Deflection-Based Methods.....	18
2.3 Current Applications of NDE Methods.....	19
2.3.1 Cracking.....	19
2.3.2 Delamination and Spalling.....	21
2.3.3 Voids and Pumping.....	24
2.3.4 Reinforcement Misplacement	26
2.3.5 Reinforcement Corrosion.....	29
2.3.6 Layer Boundary Evaluation	31
2.3.7 Thickness Evaluation	34
2.3.8 Structural Assessment.....	36
2.4 Summary of NDE Methods	38
2.5 Ultrasonic Linear Array.....	39
2.5.1 Shear Velocity Determination.....	40
2.5.2 Reconstruction Formulation.....	42
2.6 Wave Propagation Simulation.....	43
2.7 Improvements to Current Technology	44
2.8 Damage Detection Methods	45
2.8.1 Quantitative Indicator Development.....	45
CHAPTER 3 - EARTHQUAKE DAMAGE	50
3.1 Introduction	50
3.2 Experimental Investigation.....	52
3.2.1 Instrumentation and Loading.....	53
3.2.2 Nondestructive Testing	55
3.3 Analytical investigation.....	57
3.3.1 Qualitative Analysis.....	58
3.3.2 Quantitative Analysis.....	62
3.4 Experimental Results and Discussion	64
3.5 Conclusions	66
CHAPTER 4 - FREEZE THAW DAMAGE.....	67
4.1 Previous Methods	67

4.1.1 Ultrasonic Shear Velocity Array Device	68
4.2 Experimental Investigation.....	68
4.3 Ultrasound Evaluation Techniques	71
4.3.1 Panoramic Reconstructions.....	71
4.3.2 Quantitative Analysis.....	75
4.4 Results	78
4.5 Conclusions	81
CHAPTER 5 - Alkali-Silica Reaction Damage	83
5.1 Previous Research in ASR Detection.....	83
5.2 Materials and Methods	83
5.2.1 Experimental Procedure.....	84
5.3 Panoramic Reconstructions	86
5.4 Quantitative Analysis	89
5.5 Results	91
5.6 Conclusions	92
CHAPTER 6 - CONTINUOUSLY REINFORCED CONCRETE PAVEMENT CRACKING...94	
6.1 Testing procedure.....	94
6.2 Visible Crack Results	94
6.3 Non-Visible Crack Results.....	101
6.4 Conclusions	112
CHAPTER 7 - SIMULATION	113
7.1 Governing Equations.....	113
7.2 Finite Integration Technique	114
7.3 Developed Program.....	118
7.4 Parallelization with OpenMP and GPU.....	123
CHAPTER 8 - SUMMARY	128
REFERENCES	129
Appendix A - EFIT Program User Manual.....	148
A.1 Preparing input files for EFIT	148

List of Figures

Figure 1. A schematic representation of electromagnetic NDE imaging system (adapted from Deng et al., 2011).....	11
Figure 2. Example infrared thermography and laboratory measurements (Halabe, 2007).....	12
Figure 3. Pachometer: a magnetic pulse-induction device and its application on concrete pavement (adapted from Hoegh, 2013)	13
Figure 4. MIT Scan-2: a magnetic pulse-induction device and its application on concrete pavement (adapted from Yu et al., 2005)	13
Figure 5. Ground-coupled GPR system and example output at a transverse joint (adapted from Hoegh, 2013).....	14
Figure 6. Air coupled GPR mounted on a van for highway speed measurements (Maser, 2000).	14
Figure 7. Impact echo setup with a steel ball mounted on a steel spring rod (Carino, 2001).....	16
Figure 8. An example SASW-based equipment: Portable seismic pavement analyzer (PSPA) (adapted from Celaya et al., 2007).....	17
Figure 9. UPV test – (a) direct sensor configuration; (b) indirect sensor configuration (adapted from Al-Qadi et al., 2010).....	18
Figure 10. UK1401 ultrasonic pulse velocity device (Khazanovich et al., 2005)	18
Figure 11. A sample GPR output for a test area with confirmed delamination (adapted from Liu et al., 2008)	22
Figure 12. Typical combined GPR/infrared condition map (adapted from Maser, 2009).....	23
Figure 13. Visualization of the deck of the bridge on interstate I-287 over route 1 in Woodbridge, New Jersey (adapted from Gucunski et al., 2011)	24
Figure 14. Comparison of thermograms (top) and phase images (bottom) of voids at different depths. The heating time was 30 min, the recording time of the thermograms is related to the switch off time (0 s) of the heating source (adapted from Maierhofer et al., 2006).....	26
Figure 15. Scanning a joint using magnetic pulse-induction method; a) MIT Scan-2, b) analysis of the data for misaligned dowel bars (Adapted from Yu et al., 2005).	27
Figure 16. Time delay estimation stages: a) original data; b) difference image; c) thresholded image; d) detected time delays and survey distances (adapted from Al-Qadi et al., 2005b).....	28
Figure 17. Locating reinforcement at different depths with ground-coupled GPR antenna (adapted from Loulizi, 2001)	28
Figure 18. GPR data of the top layer rebar at different times: a) 6 month after casting, b) one month of corrosion experiment, c) three months of corrosion experiment (adapted from Andrt et al., 2011)	30
Figure 19. Sample ultrasonic based NDE method used for corrosion detection (adapted from Yoon et al., 2000).....	31
Figure 20. Impact echo technique and the associated normalized spectra analysis: a) good (Test Point D2), (b) poor (Test Point B1) conditions in terms of debonding (adapted from Celaya et al., 2007)	32
Figure 21. Left: test specimen with CFRP laminates, which have no contact at the shaded areas (nominal glue thickness is written on the right side). Right: thermogram directly recorded after a heating time of 15 s (adapted from Maierhofer et al., 2006).	33
Figure 22. IR testing contour plot for the bridge ramp overlay (Davis, 2003)	34
Figure 23. A sample raw GPR data on CRC pavement (adapted from Al-Qadi et al, 2005c)	35

Figure 24. Average thickness measured by IE method versus curing age (adapted from Gibson, 2005)	36
Figure 25. a) Schematic representation of a typical testing configuration to measure reflection at the interface of buffer material and cementitious material; b) Typical reflected signals at different instance of time; c) frequency (amplitude) domain representation of the reflected signals (adapted from Popovics et al., 2014).	37
Figure 26. Comparison of normalized S-wave reflection (blue points) and strength gain (magenta points) in slabs with different concrete compositions using a steel buffer. The 7-day strengths of Mix 1, Mix 2 and Mix 3 determined from cores were 26, 37 and 55MPa, respectively (adapted from Subramaniam et al., 2002)	38
Figure 27. MIRA ultrasonic linear array device (Hoegh 2013).	39
Figure 28. MIRA transducer interactions emitted from transducer 1 (left) and for all transducer pairs (right).	40
Figure 29. Example impulse time history (left), and corresponding cross section schematic (right) (Hoegh 2013).	40
Figure 30. Example array data for calculation of shear wave velocity.	41
Figure 31. Ultrasonic array measured shear wave velocities for concrete beams vs. slabs at various concrete ages (K. Hoegh, personal communication).	42
Figure 32. Sample normalized signals for clean concrete (left) and damaged concrete (right) highlighting key differences.	45
Figure 33. Example raw signals for two clean cases (top) and two damaged cases (bottom).	46
Figure 34. Sample Hilbert transform envelope.	47
Figure 35. Typical Hilbert transform envelopes for sound and damaged specimens.	48
Figure 36. 95% confidence interval for sound concrete.	49
Figure 37. Column specimen assembly and detailing.	53
Figure 38. Assembly of the specimen under the loading crosshead at the MAST Lab (Nojavan et al. 2015).	54
Figure 39. Near-collapse loading protocol in terms of column drift ratios (MIRA scans were conducted at the points shown after returning from the labelled peak drift locations).	54
Figure 40. (left) Lateral load vs. drift ratio response and (right) enlarged cycles of interest (MIRA scans were conducted at the points shown after returning from the labelled peak drift locations).	55
Figure 41. MIRA ultrasonic linear array device	56
Figure 42. Column condition for 2nd set of MIRA measurements (after 0.5% drift ratio was attained).	57
Figure 43. Column condition for 3rd set of MIRA measurements (after 1% drift ratio was attained).	57
Figure 44. MIRA Reconstructions for 1st round (left) and 2nd round (middle), and 3rd round (right) for a location with relatively low level of damage with loading.	58
Figure 45. MIRA Reconstructions for 1st round (left) and 2nd round (middle), and 3rd round (right) for a location with relatively high level of damage with loading.	59
Figure 46. Schematic outlining the merging of 6 individual SAFT scans to create one panoramic reconstruction.	60
Figure 47. (a) Panoramic reconstructions for 1st measurement showing location of reinforcement and back wall presence, and (b) corresponding design schematic.	61

Figure 48. Panoramic reconstructions for 1st measurement (left), 2nd measurement (middle), and 3rd measurement (right) for a location on the bottom of the column.	62
Figure 49. Experimental reconstruction from round 1 of testing (left), and fabricated reconstruction containing noise (right).	63
Figure 50. Effect of changes in α on the Pearson's correlation coefficient value.	64
Figure 51. Reconstruction for α of 0.01 (top left), 0.05 (top right), 0.1 (bottom left), and 0.25 (bottom right).	64
Figure 52. MIRA gradient results after 0.5% drift ratio.	65
Figure 53. MIRA gradient results after 1% drift ratio.	65
Figure 54. Visual condition surveys of slabs A, B, C and D.	69
Figure 55. Photograph of condition of slab D.	70
Figure 56. Experimental investigation setup (left), and schematic of measurement locations (right).	71
Figure 57. Panoramic reconstruction compilation schematic.	72
Figure 58. Reconstruction in the middle of slab A indicating sound concrete condition.	72
Figure 59. Reconstruction on the west side of slab B, indicating partially damaged concrete. ...	73
Figure 60. Reconstructions in the middle of slab C indicating partially damaged concrete condition.	74
Figure 61. Reconstruction in the middle of slab D indicating damaged concrete condition.	75
Figure 62. Reconstruction from the west side of slab D indicating damaged concrete condition.	75
Figure 63. Average HTI values for five cases.	76
Figure 64. HTI color maps for: slab A, clean slab; slab B, partially damaged; slab C, partially damaged; and slab D, damaged.	77
Figure 65. Comparison of panoramic reconstructions (left) and HTI index (right) analyses for slab B.	79
Figure 66. Comparison of panoramic reconstructions (left) and HTI index (right) analyses of slab C.	80
Figure 67. Ultrasonic device positioned on slab 2 (a) and readings location schematic (b).	85
Figure 68. SAFT-Pan Reconstruction of specimen Slab 0, panoramic 3	87
Figure 69. SAFT-Pan Reconstruction of specimen Slab 0, panoramic 5	87
Figure 70. SAFT-Pan Reconstructions of specimen slab 3, (a) panoramic 4 and (b) panoramic 6	87
Figure 71. SAFT-Pan Reconstruction of slab 2, panoramic 5	88
Figure 72. SAFT-Pan Reconstruction of slab 1, panoramic 1	88
Figure 73. SAFT-Pan Reconstruction of specimen slab 2, panoramic 1	89
Figure 74. HTI versus shear wave velocity	90
Figure 75. HTI color map for specimens slab 0-3.	91
Figure 76. Visible cracking in south portion of slab 2 (top) and north portion of slab 1 (bottom).	92
Figure 77. February, 2015 crack map	94
Figure 78. Signals for (a) sound concrete and (b) crack F3.4 (Right).	96
Figure 79. Examples of typical SAFT-Pan reconstructions at transversal cracks	96
Figure 80. SAFT-B Scan of sound concrete	97
Figure 81. Locations of backwall signals in a MIRA grid simulation (a) and identification of the 45 signals (b).	98
Figure 82. Normalized HTI for every signal in crack F2.5-R (first scan)	99

Figure 83. Simulation of crack F2.5-R scans based on HTI.....	99
Figure 84. Signal loss due to high HTI in two partial cracks	100
Figure 85. SAFT-Pan reconstruction of the panel between cracks F4.9 and F4.12 in Section 4.	102
Figure 86. SAFT-Pan reconstruction of the panel between Section 1 and crack F2.2 in Section 2.	102
Figure 87. HTI trough Section 1	104
Figure 88. HTI trough Section 2	105
Figure 89. HTI trough Section 3	106
Figure 90. HTI trough Section	107
Figure 91. Distresses in the transaction between interlock pavement and the short CRCP	108
Figure 92. Signal loss due to high HTI in non-visible cracks.....	109
Figure 93. Crack map with non-visible cracks	110
Figure 94. The cell for EFIT, in which velocity components are placed along the edges of the cell while the diagonal elements of the stress tensor are placed on the corners and the of-diagonal elements on the faces	114
Figure 95. Wavefield Snapshots for an elastic medium with delamination.	119
Figure 96. Instantaneous and full wave images for an elastic medium with delamination.	119
Figure 97. Wavefield Snapshots for a medium with vertical surface cracks.....	120
Figure 98. Instantaneous and full wave images for an elastic medium with two vertical cracks.	121
Figure 99. Wavefield Snapshots for a reinforced concrete.	122
Figure 100. Instantaneous and full wave images for an elastic medium with three rebars.	122
Figure 101. Effects of different GPU memory management techniques.....	126
Figure 102. Comparison between PSI and GNU compilers on OpenMP runs.	126
Figure 103. Effect of OpenMP parallelization and compiler optimization on the GNU compiler.	127

List of Tables

Table 1. Wave type information (adapted from Graff, 1991; Carino, 2001; Hoegh, 2013).....	15
Table 2. Preliminary HTI values for sound concrete	48
Table 3. Statistical results for concrete slab data	76
Table 4. Mix design for concrete slabs	84
Table 5. Summary of results for all panoramics.	85
Table 6. Expansion and HTI values for all four slabs.....	92
Table 7. Crack ultrasonic evaluation	95
Table 8. Locations and reaching signals in a MIRA grid simulation	98
Table 9. Crack depth	100
Table 10. Non-visible cracks	108
Table 11: Runtime for serial and parallel simulations	125

List of Abbreviations

CHPP: Center of Highway Pavement Preservation

MDOT: Michigan Department of Transportation

CHAPTER 1 - INTRODUCTION

The nondestructive evaluation of concrete involves unique complications due to the heterogeneous nature of the material itself. The presence of reinforcement and aggregates impose additional challenges when attempting to detect damage. Moreover, the demand for in-situ evaluation of concrete structures with associated access limitations (i.e. one-sided access to pavements), provide further impediments. While previous methods have been employed for these reasons in the past, an in-situ and objective method for nondestructively detecting subsurface damage has yet to be successfully developed and implemented.

To address this shortcoming in the nondestructive testing realm, the research presented here utilized a linear array of dry point contact transducers which emit shear waves. This technology, called MIRA, was chosen due to its high measurement repeatability, immunity to moisture conditions, and avoidance of computation-intensive nonlinearity and mode conversion efforts. This device in particular is useful in that the shear wave propagation and subsequent data analyses techniques allow for a deeper understanding of the condition of concrete specimens due to the multitude of data it provides.

The research presented here focused upon the nondestructive detection of damage in a variety of concrete applications. The cases considered include:

- Reinforced concrete column subjected to simulated earthquake loading
- Varying levels of freeze thaw damage present in concrete pavements
- Varying levels of alkali-silica reaction damage present in concrete pavements
- Visible and non-visible crack presence in continuously reinforced concrete pavements

The utilization of panoramic reconstructions, as well as the development of a quantitative indicator of the presence of damage were utilized to assess the condition of these concrete specimens. Detection of damage at early stages of initiation is critical, especially for concrete pavement applications. Early detection of damage caused by both environmental and load related factors allows for rehabilitation efforts to be determined and implemented prior to excessive failure of the infrastructure. This served as the motivation behind the pavement applications, and the successes of these experimental investigations are discussed further in this report.

CHAPTER 2 - LITERATURE REVIEW

An extensive literature review was performed regarding pavement preservation methods, as well as nondestructive technologies and their applications. The content from this search is included here.

2.1 NONDESTRUCTIVE TESTING METHODS

An extensive literature review was performed regarding pavement preservation methods, as well as nondestructive technologies and their applications. The content from this search is included here.

2.2 NON-DESTRUCTIVE TESTING METHODS

A variety of NDE methods are available for pavement assessment. Based on the nature of physical principals used in each of these NDE methods, they are classified under electromagnetic, elastic wave-based, and deflection-based methods. In this section, some of the most applicable NDE methods, especially those used for rigid (concrete) pavement evaluation, are introduced.

2.2.1 Electromagnetic Methods

Electromagnetic (EM) methods include techniques and devices that employ electromagnetic energy to induce an excitement in the test medium and analyze the response of the material. They depend on technologies such as electrical impedance, electromagnetic wave, magnetic resonance, and infrared thermography (Al-Qadi et al., 2010). EM methods are widely used in a variety of scientific fields. Physically inaccessible anomalies or defects can be detected in both conducting and dielectric materials by generating two-dimensional (2D) or three-dimensional (3D) image data based on the electromagnetic principles. Figure 1 schematically represents a generic EM NDE imaging system (Deng et al., 2011).

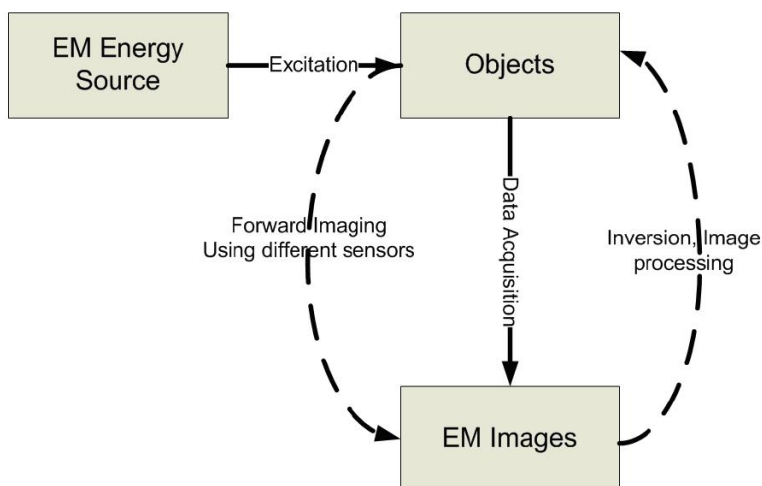


Figure 1. A schematic representation of electromagnetic NDE imaging system (adapted from Deng et al., 2011)

Depending on different energy types, and/or frequency levels, various EM sensors/transducers can be used for a broad range of applications, one of which is concrete pavements. The most

important EM NDE methods applicable for concrete pavements are infrared thermography, magnetic-pulse induction, and ground penetration radars. A short description of these methods is presented here.

Infrared Thermography

In infrared thermography, the infrared energy emitted from an object is detected via sensors and converted into temperature data. The collected temperature data is used to map the temperature contour of the object. The inhomogeneties would manifest themselves as local hot or cold regions. Based on the thermal anomalies in the obtained thermal color-map, the inconsistencies such as defects or distressed regions existing on the surface of a pavement can be detected (Maser et al., 1990; Al-Qadi et al., 2010; Hoegh, 2013). Example thermography equipment and laboratory measurements are shown in **Error! Reference source not found..** When conducting infrared tests in the field, it is possible to mount the infrared camera using tripods or poles attached to a vehicle, so that large areas can be covered in a short time (Halabe et al., 2007).



Figure 2. Example infrared thermography and laboratory measurements (Halabe, 2007).

Magnetic Pulse-Induction

Magnetic pulse-induction relates to the detection of conducting metal target objects situated in environments which, through their own magnetic and electrical properties, interact with the fields transmitted by metal detectors (Candy, 1996). In concrete pavements, the embedded metal objects can be detected by analyzing the eddy current distribution induced by the applied magnetic field and the interference caused by self-induction of the metal object. Position, size, shape, and orientation of metal inclusion in concrete pavements can be accurately identified with magnetic pulse-induction (Hoegh, 2013). However, this method cannot be utilized for detecting non-metal defects and surface anomalies (Rao et al., 2009). **Error! Reference source not found.** and Figure 4 provide examples of devices that operate with magnetic pulse-induction method.



Figure 3. Pachometer: a magnetic pulse-induction device and its application on concrete pavement (adapted from Hoegh, 2013)



Figure 4. MIT Scan-2: a magnetic pulse-induction device and its application on concrete pavement (adapted from Yu et al., 2005)

Ground Penetrating Radar

Ground Penetrating Radar (GPR) refers to a geophysical method that emits short electromagnetic pulses into the test object, and records the reflected signals. GPR is typically composed of an antenna, a data acquisition system, a distance measuring instrument (DMI), a survey vehicle or cart, and an optional GPS (Hoegh et al., 2015; Hoegh, 2013; Cao et al., 2011; Al-Qadi et al., 2010).

Depending on the apparatus setup, GPR systems are classified as either air-coupled or ground-coupled systems. **Error! Reference source not found.** shows a MnDOT owned and operated 2.6 GHz ground-coupled antenna as well as an example output of GPR where parabolic reflections can be observed due to the presence of dowels embedded in a transverse joint (Cao et al., 2011; Hoegh, 2013). The ground-coupled antenna is in direct contact with the pavement surface, which allows the EM radiation to penetrate deeper in comparison to

those emitted by an air-coupled GPR system with the same frequency. One of the drawbacks, however, is the limitation imposed by the full contact antenna that lowers the speed of the GPR survey to usually less than 8 km/h (5 mph). Also, due to the full contact, an overlap occurs between the GPR emitted signals and reflected ones at the surface. Special signal processing is required to analyze the results (Al-Qadi et al., 2010).

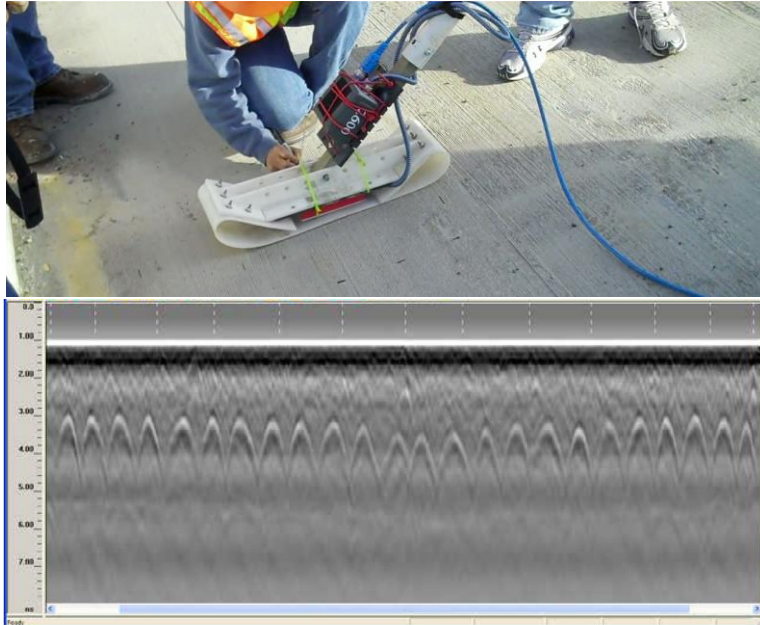


Figure 5. Ground-coupled GPR system and example output at a transverse joint (adapted from Hoegh, 2013).

One sample air-coupled GPR system is shown in **Error! Reference source not found.** Previous studies have demonstrated that the data can be collected at a significantly higher speed (highway speed) (Al-Qadi et al., 2010), however, higher speed impacts the accuracy of the data collection. For instance, detecting non-uniform cracks would be difficult (Griffiths et al., 1999). While the separation of antenna and the pavement surface provides a clearer surface reflection and facilitates the signal processing, it reduces the penetration depth of the emitted EM radiation. Also, the undesirable effects of antenna movement at high speed are inevitable. Considering all these pros and cons, air-coupled GPR system is more preferable for pavement evaluation purposes (Al-Qadi et al., 2010).



Figure 6. Air coupled GPR mounted on a van for highway speed measurements (Maser, 2000).

Ground penetrating radar (GPR) technology has been used to assess pavement performance and structure for the past 30 years in a variety of ways (Al-Qadi 2005a). Different methods are available to analyze the reflected signal and identify the anomalies, metal inclusions, and their depth and location in the pavement (Cao et al., 2007 & 2011; Cao, 2011; Abdallah et al., 2009; Clemena, 1991; Economou et al., 2012; Loulizi, 2001; Maierhofer, 2003; Plati et al., 2012; Scott et al., 2000). Results show that GPR works well for some situations but not as well for others. This type of performance is in part related to the dependency of signal processing to unknown dielectric properties of the composing materials in the test medium (Al-Qadi, 2005a; Evans et al., 2007). GPR signals are also highly affected by environmental conditions such as moisture (Scott et al., 2003; Griffiths et al., 1999). The best performance is expected where the dielectric contrast is greatest between the anomaly of interest and the test medium composition. Depending on the type of material lying between the anomaly and the pavement surface, GPR can be used to locate both metal and non-metal objects up to depth of 15 m (50 ft) (Cao, 2007).

2.2.2 Elastic Wave-Based Methods

Elastic wave-based methods involve the application of a force causing a disturbance in the elastic or viscoelastic materials, which results in propagation of elastic waves in the test medium (Soize, 2001; Al-Qadi et al., 2010; Hoegh, 2013). Two types of stress waves are available depending on their propagation medium: 1) body wave, and 2) surface wave. When a material is subjected to a short duration external impact, its behavior can be described based upon the distortion and subsequent movement of its consisting particles. Accordingly, the body wave is classified into two categories (Al-Qadi et al., 2010). P-waves, also known as longitudinal, primary or compression wave, refer to those body waves that cause the particles to move parallel to the direction of wave propagation. S-waves, also known as transverse or shear wave, on the other hand, refer to body waves that induce particle motions perpendicular to the propagation direction. The R-wave, also known as Rayleigh wave, is a combination of P- and S-waves where particles move in a retrograde elliptical direction (Krstulovic-Opara et al., 1996; Zhu et al., 2004; Hoegh, 2013). Table 1 provides a summary and additional information for the various wave types (Graff, 1991; Hoegh, 2013; Nazarian et al., 1999).

Table 1. Wave type information (adapted from Graff, 1991; Carino, 2001; Hoegh, 2013)

Propagation Medium	Wave Type	Particle Motion	Relative Wave Speed, $\mu = 0.2$	Energy Content % (Graff 1991)
Body wave	P-wave (compression)	Parallel to propagation direction	0.61	7
	S-wave (shear)	Perpendicular to propagation direction	1.00	26
Surface wave	R-wave (Rayleigh)	Retrograde elliptical	1.09	67

The relative wave speed and energy content of the various wave types are presented in Table 1. P-wave has the lowest amount of energy content. It can propagate in different mediums including solid, liquid, and gas. This ability allows for air-coupled evaluation of the concrete pavement (Hoegh, 2013; Bhardwaj et al., 2000; Green, 2004; Luukkala et al., 1973); however,

the low energy content prevents deep penetration of elastic waves in the medium. S-wave is another body wave that requires a solid medium to propagate because of its higher energy content (Achenbach, 1973; Graff, 1991). For the same reason, the emitted S-waves are able to penetrate deeper in concrete pavement (Hoegh, 2013). The highest amount of energy content belongs to R-waves. This type of wave can only travel on the surface at a depth approximately equal to its wavelength (Achenbach, 1973; Graff, 1991).

The velocity of wave in the medium is correlated to the stiffness of the material. This property makes the reflection of elastic waves highly sensitive to anomalies such as cracks, voids, delaminations or any location in the test medium that shows sudden a change of density and velocity (Kellezi, 2000; Sadri et al., 2009; Sansalone et al., 1987). Also, depending on the type of material interface that caused the reflection, the phase of the reflected wave is different that allows for identifying the type of anomaly (Achenbach, 1973; Keefe et al., 1992; Colton et al., 1998). Therefore, elastic waves can be useful in detecting subsurface properties in concrete pavement such as flaws, inclusions, and layer boundaries (Barbone et al., 2004; Al-Qadi et al., 2010; Hoegh, 2013). Different types of elastic wave-based methods are described in the following section.

Conventional Impact Echo

Conventional impact echo (IE) is a NDE testing technique that generates elastic waves such as P-, S-, and R-waves using a mechanical impact or an ultrasound pulse (Schubert et al., 2001; Al-Qadi et al., 2010; Hoegh, 2013). Figure 7 provides an example conventional impact echo device. In this case, a mechanical impact is made using a round metal bar, and the reflected waves are recorded and interpreted usually based on spectral analysis (Scott et al., 2003; Carino, 2001; Sansalone, 1997).



Figure 7. Impact echo setup with a steel ball mounted on a steel spring rod (Carino, 2001).

In spite of the ability of IE to capture planar layer interface properties such as a concrete/air interface caused by a delamination, the time-consuming test procedure makes this test less favorable especially for complex geometries (Carino, 2001; Schubert et al., 2003 & 2008). Air-coupled impact echo testing technique have been developed to reduce the testing time consumption and allow for more productive measurements (Borwick, 1990; Buckley et al., 1999; Popovics et al., 2012; Zhu et al., 2002 & 2007).

Spectral Analysis of Surface Waves

Spectral analysis of surface waves (SASW) test technique involves generation, dispersion, and measurement of surface waves. As shown in Figure 8, two receivers are located on the ground surface and a transient impact containing a range of frequencies is transmitted to the pavement by means of a simple hammer (Celaya et al., 2007; Nazarian et al., 1985). Previous studies have shown that the Rayleigh waves (R-wave) provide more accurate information compared to S- and P-waves, as they carry about two-thirds of the seismic energy (Nazarian et al. 1999). The most challenging step in SASW testing is the inversion process which is an analytical solution for developing the elastic wave velocity profile (Nazarian et al., 1985). Time-domain and frequency-domain methods can be carried out to analyze the recorded wave data. The frequency-domain analysis, however, is reported to work exceptionally well for SASW testing technique (Nazarian et al. 1999; Al-Qadi et al., 2010). This method has been used for applications such as estimating concrete pavement stiffness and other properties (Krstolovic-Opara et al., 1996; Cho, 2003; Gucunski et al., 2000; Park et al., 1999; Stokoe et al., 1994).

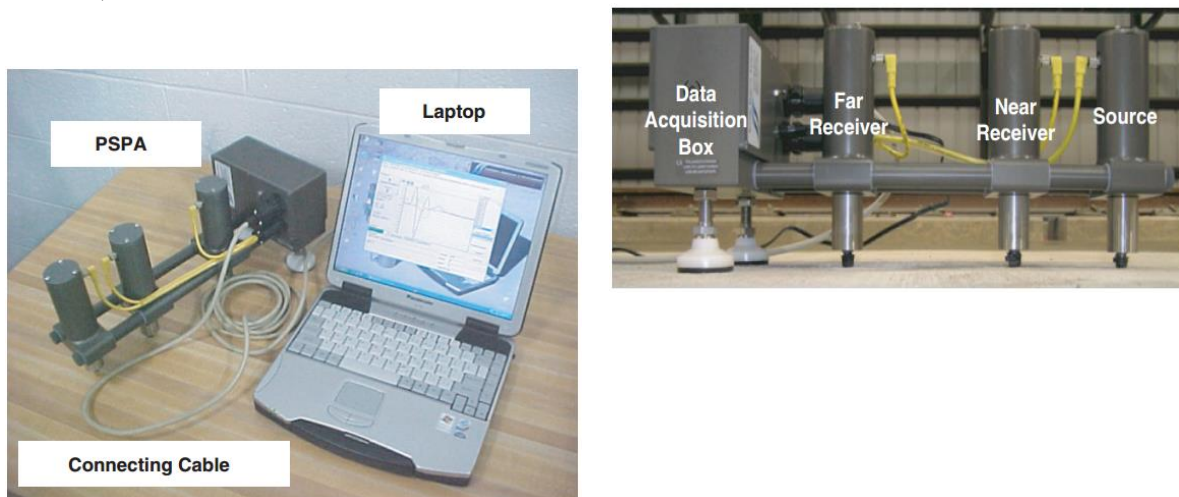


Figure 8. An example SASW-based equipment: Portable seismic pavement analyzer (PSPA) (adapted from Celaya et al., 2007)

Ultrasonic Pulse Velocity

Ultrasonic pulse velocity (UPV) involves the emission and receiving of an elastic wave impulse by ultrasonic transducers located on the test medium. The wave velocity is measured using the distance between transducers and wave travel time. UPV test setup consists of a transmitter, receiver, and a timer to record the wave travel time. As depicted in Figure 9, the transmitter and receiver can be located in different configurations. Only the indirect sensor configuration (Figure 9-b) is applicable for NDE testing for pavements, as only the top surface is accessible (Khazanovich et al. 2005; Hoegh, 2013).

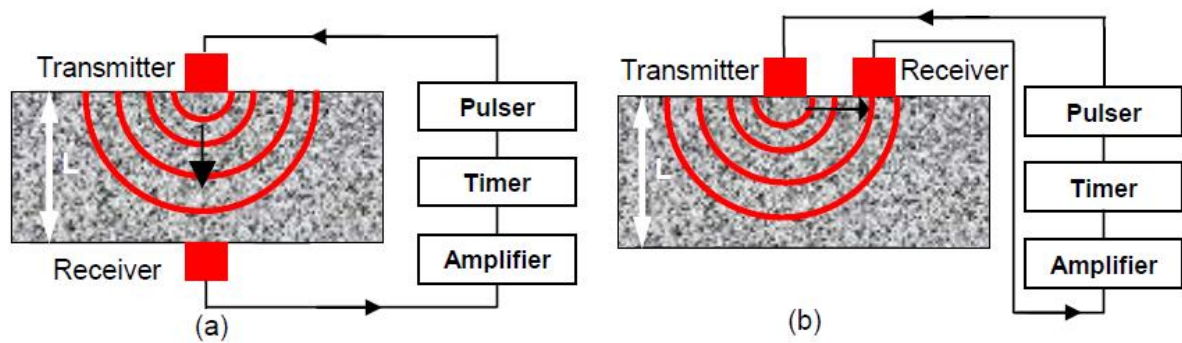


Figure 9. UPV test – (a) direct sensor configuration; (b) indirect sensor configuration (adapted from Al-Qadi et al., 2010)

The conventional UPV test device requires the application of a liquid coupling material such as grease or cellulose paste at the interface between the sensors and the test surface. A relatively modern technique, however, uses dry point contact (DPC) transducers to enhance the time consuming characteristic of conventional test method. The lower frequency elastic waves (30 kHz to 150 kHz) and higher power impact provided by DPC transducers eliminate the need for liquid coupling materials, and also allow for evaluation of the pavement structures at greater depths (Nesvijski, 1997; Liang et al., 2009; Moheimani, 2003; Vladisauskas et al., 2010 & 2011; Dutoit, 2005). Figure 10 shows an ultrasonic pulse velocity (UPV) device that was one of the first applications of DPC transducers for pavement applications (Khazanovich et al., 2005; Hoegh, 2013).



Figure 10. UK1401 ultrasonic pulse velocity device (Khazanovich et al., 2005)

2.2.3 Deflection-Based Methods

Deflection-Based methods refers to those techniques and devices that evaluate the pavement properties (mainly structural properties) based on the measured deflections at the pavement surface induced by an external loading. Depending on the loading mechanism and application, different types of deflection-based methods are available as briefly described here:

- Static load deflection equipment, such as Benkelman Beam, employs a static or quasi-static loading. The static nature of loading of such devices does not accurately represent the dynamic effects of moving wheels on the pavements, and does not provide deflection basins.

- Steady-state dynamic load deflection equipment, such as Dynaflect and Road Rater, utilizes a static preload and a dynamic (sinusoidal) vibration. These devices can produce deflection basins using geophones.
- Impulse load deflection equipment, such as Falling Weight Deflectometer (FWD) and Lower Weight Deflectometer (LWD), more realistically represents the effects of moving wheels on the pavement by applying sinusoidal loads to the pavement surface, similar in magnitude and duration to that of a single heavy moving wheel load. The deflection-time history provided by these equipment can be used to determine the structural properties of the pavement such as elastic moduli and bearing capacity of pavement layers (Al-Qadi et al., 2010; Khazanovich et al., 2015).
- Continuous load deflection equipment, such as Rolling Weight Deflectometer (RWD), is very similar to FWD but continuously collects the deflection of the pavement surface as opposed to the discrete data collection of FWD. This device is not as precise as FWD but can trace the sections with potential problems. More detailed evaluations can be performed only on identified areas using FWD.

Deflection-based methods have already been accepted by the pavement agencies, and are being used by engineers and practitioners to evaluate different properties of pavements (mainly structural) as part of typical condition surveying programs. In this study, the applications of deflection-based methods in pavement preservation are not taken into consideration.

2.3 CURRENT APPLICATIONS OF NDE METHODS

Based on the evaluations performed by the NDE methods mentioned above, information could be obtained with regards to different pavement distresses, their locations, properties, and pavement structural capacity. Such information can be fundamental for many applications such as quality assurance of the pavement construction or maintenance treatments, decision making in pavement management systems, and others. NDE techniques have a variety of applications in both flexible and rigid pavements; however, in line with the focus of this study, only the applications of NDE for rigid pavements were considered. Some of the current applications of NDE methods are presented here to illustrate their contribution to rigid pavement industry and their potential role in pavement management.

2.3.1 Cracking

Cracking is a common phenomenon in concrete pavements. Cracking might happen due to many reasons such as poor construction, multiple application of heavy wheel axle loading, as well as environmental actions including thermal expansion and contraction, shrinkage, and freeze-thaw cycles (Hoegh, 2013). For certain pavements, such as continuously reinforced concrete pavements, a nominal level of cracking is expected to occur but in many cases, the extent and severity exceed the desirable amount.

Early detection of cracking both for top-down and bottom-up cracking and also estimation of the extent of cracking is of utmost importance. If cracks are identified at an early enough stage, the repair and removal of the distressed area can prevent subsequent and more substantial damages (Forest et al., 2004). Bottom-up cracks initiate in subsurface areas which are not detectable with visual inspection. Knowledge of the extent and type of such

subsurface cracking can lead to selection of proper treatment and timing to mitigate and postpone the failure of the concrete pavement (Darter et al., 1993). Top-down cracks can be identified with visual inspection, however, the results of a study conducted by the Colorado department of transportation showed that a visual observation of the longitudinal cracks cannot serve as a reliable indicator to determine the extent of a crack (i.e. if the crack is partial or full depth) (Harmelink et al., 2003). Previous studies have shown that some of the NDE techniques are able to provide additional information on the cracking type, severity, and extent.

GPR is one of the most frequently studied NDE methods in this regard. Early studies did not suggest the use of GPR for identifying cracks in pavements and bridge decks. In these studies, the GPR profiles were collected at highway speed with only a few traces per meter. Therefore, the inadequate resolution did not allow for capturing the vertical cracks, except for large cracks or those located near the surface (Maser, 1991; Maser et al., 1992). Using a higher frequency antenna (1.0 GHz) with a very high sampling density (10-20 scans/m) enabled the GPR scanning device to identify the vertical cracks in flexible pavements as sharp hyperbolas on GPR profiles (Saarenketo et al., 1994; Loken, 2007). Another study was performed by Chen et al. (1994) on 15 concrete bridge deck specimens of dimensions 610 x 610 x 150 mm (24 x 24 x 6in.). To investigate the ability of GPR radars to identify cracks with different internal conditions, specimens were fabricated with air cracks, plain water-filled cracks, saline water-filled cracks, reinforcement, and no reinforcement. The difference in dielectric values of each crack type and reinforcement condition resulted in a different reflected GPR waveform. The comparison of the GPR scans showed that cracks can be easily detected with the radar system especially when they are filled with water. A similar study performed by Halabe et al. (1996) reported that cracks with 127 mm depth were difficult to detect because of the attenuation of the wave in the concrete.

GPR has also been used in the UK to identify the type and depth of cracks in flexible pavement. Because the reflection due to the presence of cracks is much smaller than the change in waveform caused by the layer interface, a certain configuration of antenna was used. The proper frequency was found to vary between 700 MHz to 2.5 GHz, with at least 100 scans/m. Crack depths in the range of 25 mm to 160 mm were measured with acceptable accuracy. The results of this study encouraged the UK highways agency to pilot further trials to monitor and assess the ability of this method (Forest et al., 2004). In line with the application of GPR in detecting vertical cracks in flexible pavements, Diamanti et al. (2010 & 2012) recommended a multi-frequency approach to GPR surveys of pavements including a high frequency for crack characterization and lower frequency for crack detection. Ultrasonic pulse velocity (UPV) has also been used for crack detection. The application of this method for estimating the degree of crack propagation through asphalt concrete layer thickness was studied (Khazanovich et al., 2005). The results of laboratory testing and field testing at the MnROAD test facility demonstrated a good potential of the technology. Also, the combination of ultrasonic linear array and GPR showed its ability to identify honeycombing in concrete structures (Clayton et al, 2013 & 2014).

Surface waves (Rayleigh waves) have been a subject of some research studies as they are more sensitive to surface irregularities and cracks (Hevin et al., 1998). In one of these efforts, Popovics et al. (2000) introduced a self-compensating measurement scheme by obtaining the response across a range of frequencies. The results of performing this wave test on notches, open cracks, and closed cracks confirmed the sensitivity and repeatability of this test, and showed potential for detection and sizing of surface-breaking cracks in concrete structures.

The proposed relationship appeared to be largely unaffected by the type of concrete and the nature of the discontinuity (Popovics et al., 2000).

In another study performed by Hevin et al. (1998), a model based on an indirect boundary element method was adapted to calculate the three-dimensional seismic response of two-dimensional structures. The variation of spectral ratios between the transmitted and incident waves was used to determine the crack depth for various crack geometries. This model was evaluated by performing the surface wave test on a concrete slab (4 x 4 x 0.6 m) with artificial cracks (5 mm opening and three different depth values: 4, 9 and 16 cm). The experimental and numerical results were in good agreement (within 15% error) (Hevin et al., 1998). Many researchers studied the application of impact-echo NDE technique in locating low density concrete (honeycombing) and cracking in concrete elements (Lin et al., 1992; Sansalone et al., 1997; Sansalone, 1997; Davis et al., 1997; Hertlein et al., 1998; Gucunski et al., 2000; Yuan et al., 2000). Also, different analysis algorithms have been proposed for diffracting the transmitted and received elastic waves (Wu et al., 1995; Liu et al., 1996; kuo et al., 1998). They showed that this method could successfully detect the flaws in concrete pavement and with more technological and analytical advancements, could be a promising tool for such purpose.

Also, as suggested by Maierhofer et al. (2006), infrared thermography can be applied for identifying the cracks in concrete structures especially for concrete covers of 10 cm and near surface regions.

2.3.2 Delamination and Spalling

Delamination of bridge deck concrete occurs when rebar corrodes after long-term exposure to chloride ions and moisture that penetrate into the concrete (Warhus et al., 1995). Similar mechanisms can occur in continuously reinforced concrete pavement, or uncut tie wires in dowel baskets (Clear, 1989; Hoegh, 2013). Delamination and spalling might initiate due to other reasons such as improper consolidation of concrete, alkali-silica reaction, and freeze/thaw damage (Rao et al., 2009; Loulizi, 2001). When concrete is decoupled from the reinforcement or dowels and ties, the structural strength reduces and horizontal plane cracks propagate which leads to spalling at the surface (Zollinger et al., 1994; Warhus et al., 1995). Spalling affects pavement characteristics such as smoothness and ride quality (Al-Qadi et al., 2010). The early detection and repair of delaminations would prevent the deterioration of the entire road or bridge, and replacement of reinforcement and slabs (Warhus et al., 1995). Depending on the type, extent, and severity of induced damage, usually partial or full depth repair are the appropriate treatments (ACPA, 2004).

Since GPR shows a great sensitivity to moisture, its ability to detect delamination/spalling is promising (Loulizi, 2001). In early studies on the application of GPR for detecting delaminations, the analysis was based on qualitative investigation of the graphical output of the GPR. Based on the encouraging results, they recommended GPR as a tool to quickly assess the general conditions of bridge decks with respect to delaminations (Clemena, 1983; Joyce, 1985).

In another study, the effect of delamination (with and without water) and chloride content on the dielectric properties of concrete over a frequency range of 1 GHz to 10 GHz was examined. The fabricated slabs with artificial delaminations filled with water and caused high changes in the dielectric constants. Also, due to the presence of delaminations, even for the

smallest delamination in the study (6.4 mm thick), a shift factor and a change in the waveform amplitude were reported (Al-Qadi et al., 1996). Based on GPR surveying conducted on 32 bridge decks in the New England region, a good correlation was observed between GPR profiles and directly measured values (4.4% error) (Maser, 1996b).

Other studies were conducted to improve the analysis technique for GPR scanning with regards to delaminations (Warhus et al., 1994 & 1995; Azevedo et al., 1996; Davidson et al., 1996; Hutson et al., 2000; Belli et al 2008; Catapano et al., 2012; Benedetto et al., 2012). Rhazi et al. (2003) tried to evaluate the real ability of GPR in detecting delaminations in concrete bridge decks. In contrast to many successful theoretical and laboratory studies, they found that GPR analysis was still ambiguous in some cases. They attributed this observation to the low dimensions of delaminations, the proximity of the delamination to the reinforcement, and the insufficient scanning resolution.

The application of GPR for detecting shallow delaminations in continuously reinforced concrete pavement (CRCP) was studied by Liu et al. (2008). Figure 11 illustrates a sample GPR output. The delamination occurred at the obvious disturbance of the signals. However, in some conditions, it is difficult to visually review the GPR graphic output and detect the possibility of the occurrence of delamination. Several reasons are involved. First, concrete has dielectric properties similar to those of granular base, and second, the early-age delamination occurs at shallow depths. Therefore, a three-step analysis was employed by Liu et al. (2008) to improve the quality of GPR data interpretation including (a) a preliminary evaluation, (b) a site-calibration algorithm, and (c) a threshold amplitude difference. Field measurements, coring tests and numerical analysis showed that shallow early-age delamination in CRCP could be easily detected by the application of GPR technique if proper analysis procedure was employed.

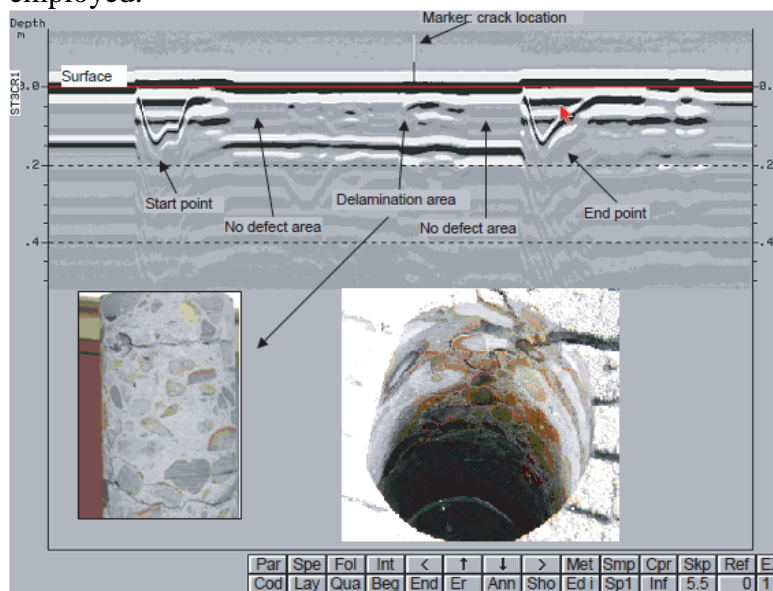


Figure 11. A sample GPR output for a test area with confirmed delamination (adapted from Liu et al., 2008)

In addition to GPR radar, infrared thermography has been used to locate concrete delaminations in bridge decks and roads. In 1988, ASTM published a standard test method for detecting delaminations in bridge decks using this technique (ASTM, 2013). Maierhofer et al. (2006) fabricated pre-stressed beams with some non-grouted areas. Then, the test specimens were tested with three different heat sources: a) heat generated through the cement hydration

process, b) the external infrared radiators with a total electrical connected load of 5200 W, and c) internally heating the wires inside the ducts. The results showed that for case b, only some of the flaws from the side with small concrete covering were detectable while clear images were obtained from the other two cases.

Some benefits as well as limitations were reported at different conditions, crack type, and the depth of the defect (Carino, 1993; Halabe et al., 2007; Marchetti et al., 2008). For instance, it was reported that infrared thermography is capable of detecting air-filled delaminations for bridge decks with and without wearing surface, while water-filled delaminations could not be clearly detected in decks with wearing surface (Halabe et al., 2007).

In a few studies it was found that a better evaluation of the delaminated area can be obtained by combining the results of both GPR radar and infrared thermography. GPR radar is fast and more susceptible to moisture and chloride associated with deterioration but cannot directly detect delaminations. In contrast, infrared thermography is a relatively slower test which directly detects delaminations but loses its detectability when moisture or thick overlays are present. In one of these studies, the combination of the radar and infrared measurements were capable of predicting total area of deteriorated deck to within 5% of total deck area (Maser et al., 1990). The same combined NDE testing was employed to survey 87 bridge decks in Wisconsin. The collected data was analyzed and some cores were sampled to evaluate the accuracy of this approach. Out of a total of 214 defective cores, 83% of them were correctly identified by this approach. Figure 12 provides an example GPR/infrared condition map. It can be seen that two types of defects, delamination due to reinforcement corrosion and debonding of the overlay, are detected with this approach (Maser, 2008 & 2009).

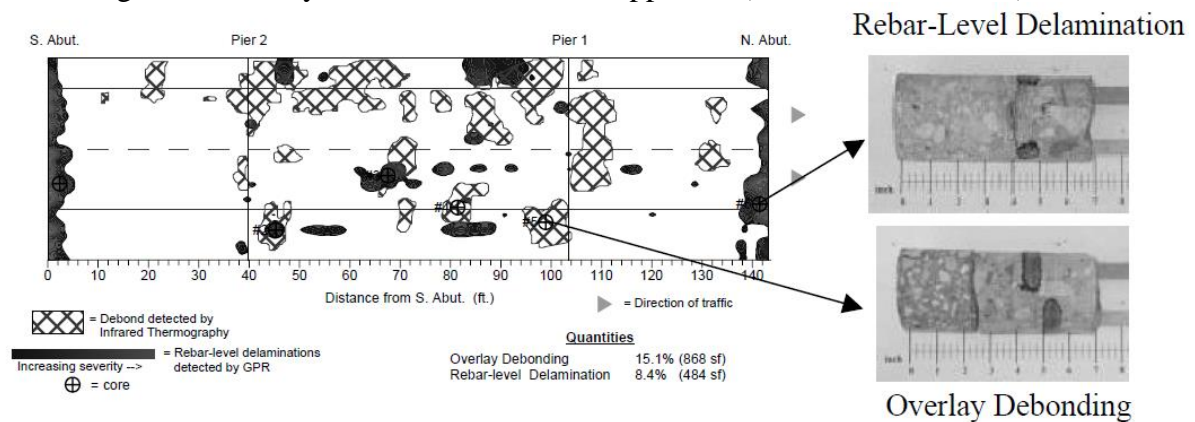


Figure 12. Typical combined GPR/infrared condition map (adapted from Maser, 2009)

Impact-echo (IE) is another NDE technique used for detection of delaminated areas. In one of the early studies conducted by Sansalone et al. (1989), the IE method was evaluated using embedded delaminations at known locations in reinforced concrete slabs. At the second stage, the slabs were overlaid with a layer of asphalt concrete and tested again. It was found that IE could successfully locate the delaminations in the slabs before and after the overlay was present. Application, analysis, and improvement of IE have been the topic of more studies (Sansalone, 1993; Sansalone et al., 1997; Cheng et al., 1993; Gucunski et al., 2000 & 2006 & 2008; Schubert et al., 2001 & 2008).

In another effort done by Gucunski et al. (2011), a new approach based on three dimensional data visualization was proposed. The associated interpretation provided an overall assessment of the condition of the deck. It also allowed for identification of deteriorated zones of the

deck. Therefore, an advantage of the IE method is that it allows for detection of delamination zones at various stages of deterioration: from initial to progressed and developed (Gucunski et al., 2006 & 2011). In Figure 13, which is a sample of 3-D IE image of bridge deck located in New Jersey, three distinctive layers can be observed. Green, yellow, and red each represent the good, fair to poor, and serious condition, respectively.

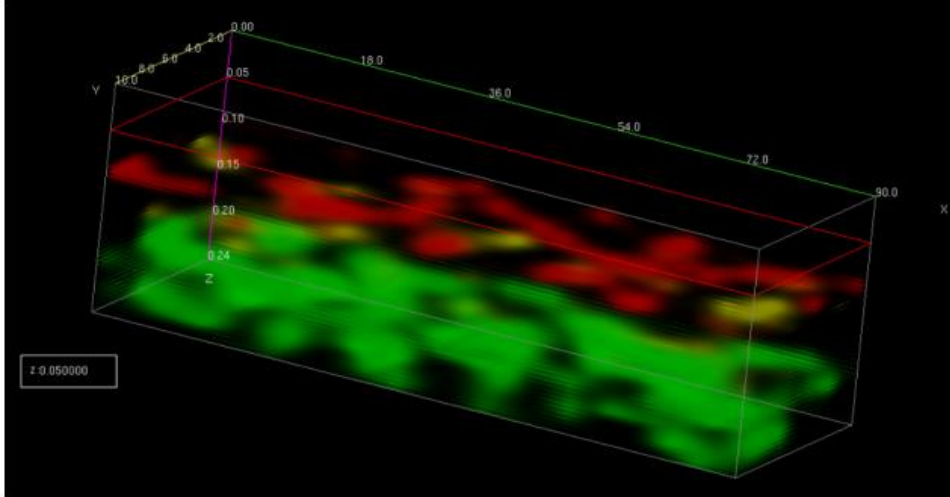


Figure 13. Visualization of the deck of the bridge on interstate I-287 over route 1 in Woodbridge, New Jersey (adapted from Gucunski et al., 2011)

2.3.3 Voids and Pumping

Void Pumping is defined as movement of water and fines under the leading slab due to the suction caused by the rebounding of the trailing slab after the passage of traffic. The repetition of this phenomenon could lead to loss of support for the rigid slab at the location of the joints, and in turn, increase in deflections and stresses. This distress is mainly prevalent in jointed concrete pavements. Early detection of pumping can prevent the advancement of deterioration of the subsurface support and the resulting pavement structural damages (Loulizi, 2001). Presence of voids under the joints is a sign of initiation of loss of support, which can be detected by some of the NDE methods. In addition, mapping of air voids are of interest because of slab curling, consolidation, subsidence, and erosion of the base material (Al-Qadi et al., 2010; Pederson et al., 1986).

GPR shows a great sensitivity to voids and moisture (Loulizi, 2001); therefore, its ability in detecting air voids in the underlying layers have been tested by different studies. In theory, air voids and water-filled voids are both detectable using GPR because the dielectric constants of both air (1.0) and water (81) are substantially different than most pavement materials (3-10) (Loken, 2007; Cao et al., 2007).

Early studies showed the possibility of using GPR as a nondestructive tool for mapping the voids located under concrete pavements (Moore et al., 1980; Steinway et al., 1981; Koerner et al., 1982; Clemena et al., 1986; Bomar et al., 1988; Smith et al., 1993; Saarenketo et al., 1994b; Scullion et al., 1994 & 1995). For instance, Clemena et al. (1986) reported that the coring of some slabs and subsequent use of a devised water test revealed that the radar was very effective in detecting voids deeper than 4 mm (1/8 in) but considerably less effective in spotting shallow voids. Comparison with the laboratory measurement showed insufficient accuracy (68%), which indicated that the device needed to be improved. As tested by Clemena et al. (1986), GPR can be utilized to provide an estimation of the volume of grout needed for performing slab stabilization on rigid pavements. However, the accuracy of this

estimation was 51%. Overall, they concluded that information obtained from GPR survey accompanied by direct measurements can be used to develop a cost-effective and efficient slab stabilization operation by proper placement of grout holes (Clemena et al., 1986). Another study reported that the voids with 50 to 400 mm (2 to 16 in) were identified by a GPR testing device and verified. However, it was recommended to perform drilling and coring in order to determine the extent and depth of the voids (Chen et al., 2008).

In contrast, some researchers have reported some issues with the ability of GPR in void detection (Sheftick et al., 1997; Morey, 1998, Al-Qadi et al., 1996). Due to the differences in dielectric constants, void detection is more suitable when voids are filled with water, and the reflection pattern looks completely different when the voids are dry, semi-dry, or saturated. Also, it is almost impossible when they are located under the concrete pavement reinforcement because of the significantly more pronounced effect of the steel on the wave reflection (Loken, 2007; Cao et al., 2007; Al-Qadi et al., 2010; Jiang et al., 2010).

The impulse response (IR) test method, which uses the same principles as in impact-echo testing, was used by Pederson et al. (1986) to identify the voids under the concrete slab for the purpose of slab stabilization. In this study, the objective was to propose a method that can quantify the materials needed for slab stabilization. The authors expressed that a general solution was not found but the results of IR testing could be a basis for the method of void mapping.

Most of the existing NDE methods (i.e. GPR, ultrasonic, and impact-echo) are mainly suited for the detection and characterization of anomalies in concrete and masonry structures at depths between 5 and 100 cm. Infrared thermography, on the other hand, is a useful method for quantitative investigations of the near surface region (0 to 10 cm) of various structures (Maierhofer et al., 2002 & 2004). In one of the studies related to the application of infrared technology in concrete structures, Maierhofer et al. (2005) proposed a computer program for numerical simulation of the heating up and cooling down processes developed based on finite difference concept. This method was tested to investigate its ability to detect voids. Concrete specimens and slabs were fabricated with different reinforcement configurations and concrete type, and artificial voids were embedded. External heating was performed to impose the thermal difference during the warming and cooling process. The results showed that this method is very well suited for the detection of voids and honeycombing in concrete, up to concrete covers of 10 cm. It was pointed out that with increasing rebar density, the temperature contrast of the underneath voids decreases slightly. Also, the effects of increased density and increased thermal conductivity superimpose each other. Figure 14 depicts the produced images using the infrared technique on the fabricated specimens (Maierhofer et al., 2006).

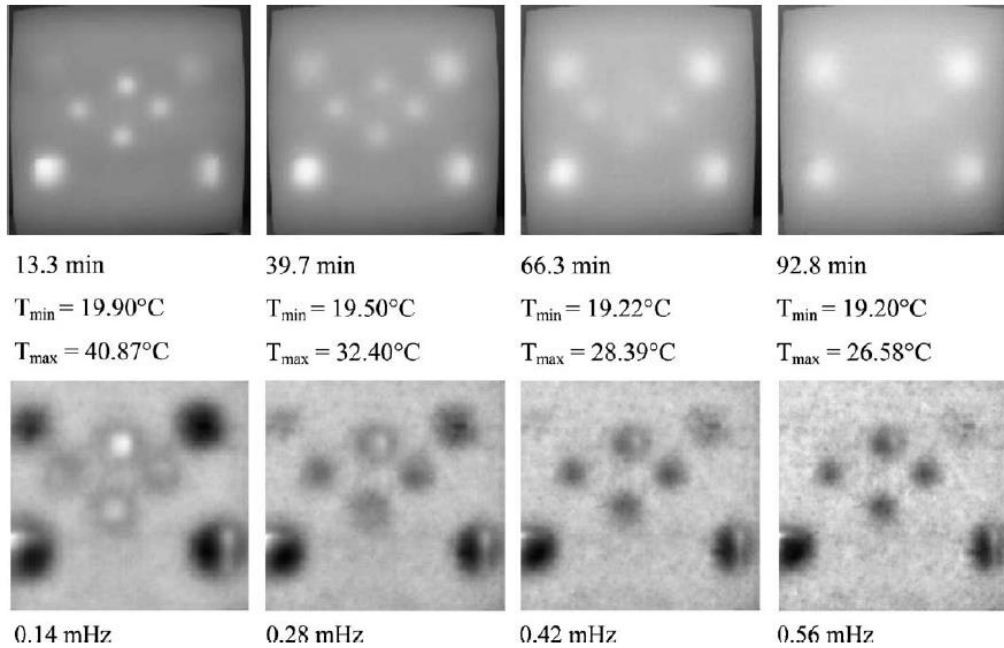


Figure 14. Comparison of thermograms (top) and phase images (bottom) of voids at different depths. The heating time was 30 min, the recording time of the thermograms is related to the switch off time (0 s) of the heating source (adapted from Maierhofer et al., 2006)

2.3.4 Reinforcement Misplacement

Different types of reinforcement are available depending on the type of concrete pavement. Reinforcement in concrete pavements is placed at specific locations to assure their proper functioning. Dowels in jointed concrete pavements (JCP) can prevent faulting caused by high volumes of heavy truck traffic if proper size and placement are assured (Yu et al., 2005). Dowel and tie bars are recommended to be placed at the mid-depth, parallel to the surface with equal embedment on both sides of jointed plain concrete pavement (JPCP) transverse joints to provide load transfer (Hoegh et al., 2008). If the dowels are placed much deeper than the mid-depth of the slab, the concrete below the dowels might crush. On the other hand, inadequate concrete cover due to dowel misplacement close to the surface leads to spalling and corrosion of the dowels. Also, the dowels function more efficiently if their center is placed at the center of the joint. Horizontally misaligned dowels can also cause spalling or cracking of the concrete, and in severe cases, they can lead to looseness of the dowel bars and drastically reduced efficiency (Yu et al., 2005 & 2007; Saxena et al., 2012; Leong, 2006; Leong et al., 2006). Knowledge of the proper placement of reinforcement in continuously reinforced concrete pavement (CRCP) is important as well to address any potential constructability issues (Hoegh, 2013).

Magnetic pulse-induction can be a reliable tool for locating the depth and alignment of metal inclusions. High accuracy is achievable if the dimensions or metal properties are known (Hoegh et al., 2008; Hossain et al., 2006; Yu et al., 2005). In one of the related studies, extensive laboratory and field testing were performed to evaluate the performance of MIT Scan-2, a device that works based on the concept of magnetic pulse-induction (Yu et al., 2005). The authors claimed that MIT Scan-2 could be a useful tool for rapidly monitoring dowel placement. The laboratory tests confirmed that the device could capture the misalignments and misplacements with reasonable accuracy. As Yu et al. (2005) reported, the advantages of magnetic pulse-induction over other available techniques are the insensitivity of this method to weather conditions (dry vs. wet), and the possibility of performing the

evaluations on fresh concrete. As the downside of using this method, the interference in the wave radiation due to presence of other metals in the test medium can be mentioned. Figure 15 provides a sample testing device and analysis profile based on magnetic pulse-induction method.

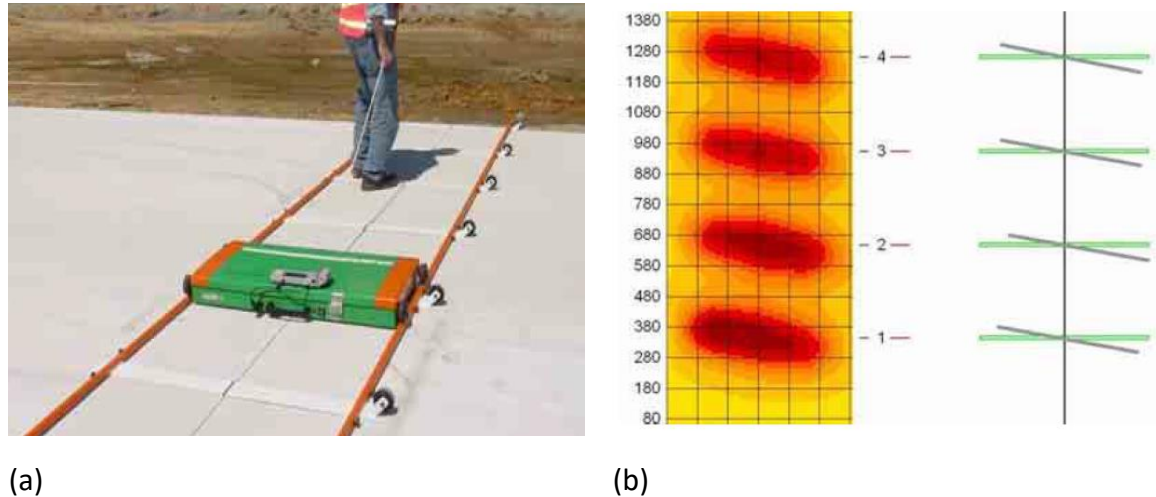


Figure 15. Scanning a joint using magnetic pulse-induction method; a) MIT Scan-2, b) analysis of the data for misaligned dowel bars (Adapted from Yu et al., 2005).

GPR is another NDE method which has been widely used for locating the metal inclusions in concrete structures and pavement. Compared to water and air, metal provides the largest contrast in dielectric properties, and therefore, GPR has already proven to be feasible to locate dowels (Warhus et al., 1994 & 1995; Loulizi, 2001; Al-Qadi et al. 2005b & 2010; Catapano et al., 2012).

Halabe et al. (1993) used an inversion technique to estimate the rebar depth and other parameters on the basis of the measured reflected signal and an empirical reflection model. Bungey et al. (1994) examined GPR's ability to detect round steel reinforcing bars ranging in diameter between 6 mm and 32 mm, and cover depth of up to 280 mm. 250 different configurations were tested by simulating the concrete specimen using an emulsion of oil and water with dielectric and conductivity properties equal to concrete. They reported that as long as the spacing of the steel bars is larger than 200 mm, they are detectable by GPR. Al-Qadi et al. (2005b) proposed image-processing techniques to automatically detect the rebar parabolic signature in GPR data collected with a high frequency ground-coupled GPR antenna. The evaluation of these techniques were performed on a CRCP section with known properties. The results showed an average error of 2.6% on the estimated rebar cover depth. Figure 16 provides the results of a sample analysis of the GPR survey (Al-Qadi et al., 2005b).

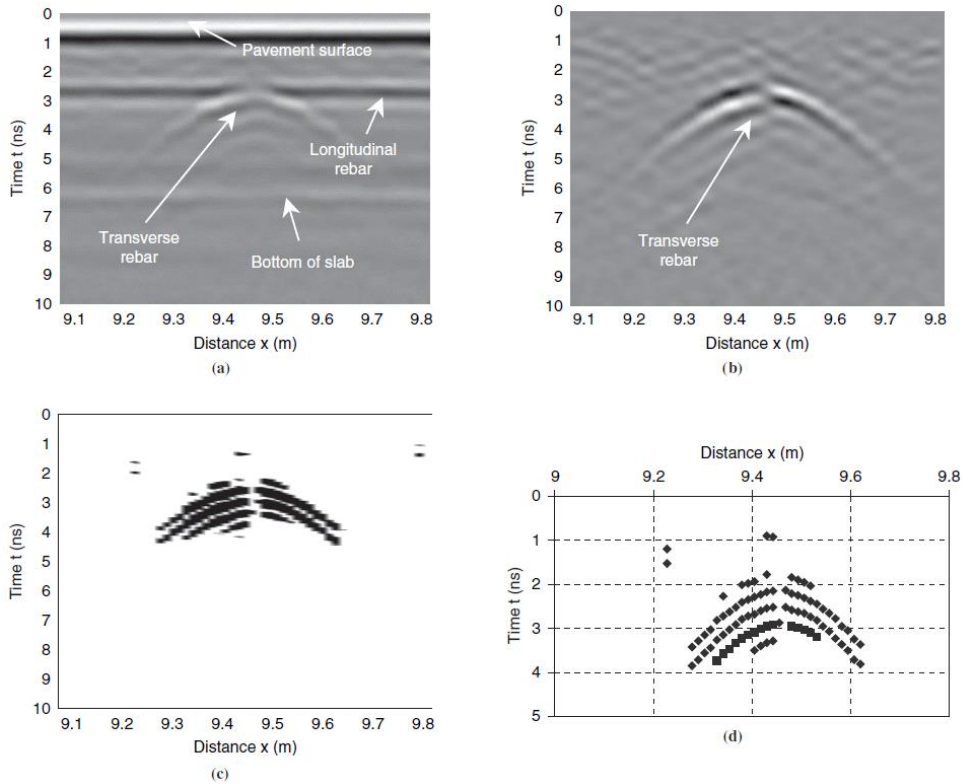


Figure 16. Time delay estimation stages: a) original data; b) difference image; c) thresholded image; d) detected time delays and survey distances (adapted from Al-Qadi et al., 2005b).

Figure 17 shows the result of a GPR survey using a ground-coupled antenna (900 MHz) over a bridge deck. It can clearly be seen that the rebar is located at a depth of 80 to 150 mm, and improper installation during construction was diagnosed by the aid of this NDE technique (Loulizi, 2001).

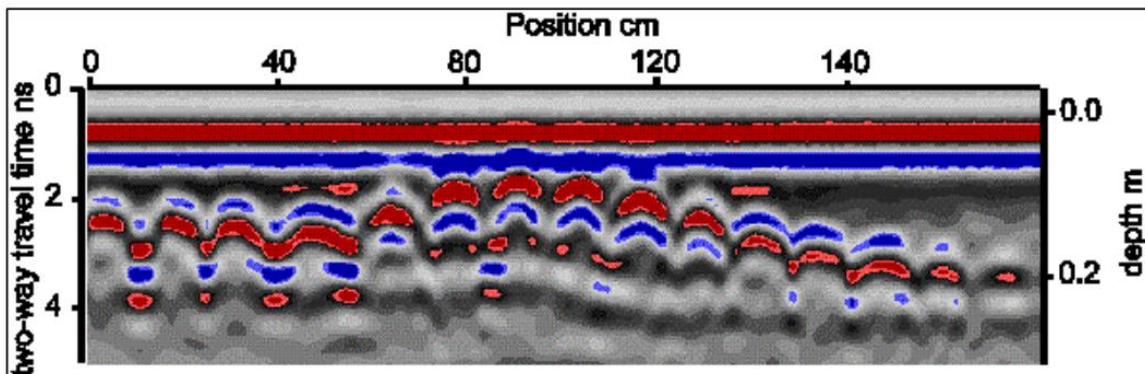


Figure 17. Locating reinforcement at different depths with ground-coupled GPR antenna (adapted from Loulizi, 2001)

A study performed by Clayton et al. (2013 & 2014) confirmed the ability of an ultrasonic linear array device to detect reinforcement, along with the processing and analysis conducted by University of Minnesota. The use of this NDE technology showed promise as it was able to detect all the embedded reinforcement and their sizes, even in a congested area. Also, the combination of ultrasonic linear array and GPR showed its ability in locating reinforcement in concrete structures (Clayton et al., 2013 & 2014).

Induction-thermography was the subject of study carried out by Hillemeier (1984). In this method, the steel embedded in the concrete was heated by the induced electromagnetic waves, while the concrete itself remained unheated. In accordance with the law of electromagnetic induction, a sufficiently powerful alternating magnetic field, directed onto a concrete surface, generates a current in the bars below the surface. The authors claimed that this method is able to accurately locate the reinforcement in concrete elements at a millimeter scale.

2.3.5 Reinforcement Corrosion

Corrosion of reinforcement is one of the common problems in concrete structures and pavements which affects the structural integrity of the element. Reinforcement in concrete elements can resist corrosion if the alkaline environment around them remains intact. Carbonization of concrete and/or long-term exposure to chloride ions and moisture that penetrates into the concrete can break the passivating film formed on the steel due to the high pH environment. Corrosion products generated during this process impose radial and hoop stress within the surrounding concrete which eventually causes fracturing and cracking of the distressed region (Warhus et al., 1995; Andrt et al., 2011). If this remains undetected, corrosion induced cracks in concrete pavements can result in delamination of the cover concrete. The delaminated concrete can then spall off when subjected to traffic and a freeze/thaw environment. Concrete disintegration is caused by freeze/thaw damage to the cement matrix. This type of damage is caused by poor quality concrete conditions at the top surface and lack of air entrainment (Maser et al., 1990; Warhus et al., 1995).

One NDE method that has not been introduced in “Non-Destructive Testing Methods,” because of its limited use in concrete pavement industry, is the half-cell potential method. Corrosion of reinforcement produces a corrosion cell caused by differences in electrical potential. This difference can be detected by placing a half-cell, e.g. a copper sulphate half-cell, on the surface of the concrete and measuring the potential differences between the half-cell and steel reinforcement. Measurements of resistivity of concrete can provide an indication of the presence, and possibly the amount, of moisture in a concrete structure; therefore, the extent and rate of corrosion of reinforcement could indirectly be evaluated (Haardt, 2003). Haardt (2003) investigated different electrode configurations and found that several of those were sufficiently capable of detecting the corrosion rate in concrete elements. Carino (1999) mentioned that the Half-cell method provides an assessment of the likelihood that there is active corrosion in the structure. However, this method, by itself, does not provide information on the corrosion rate. One of the controlling factors for corrosion rate is the concrete resistivity, and measurement of concrete resistivity can be a useful complement to the half-cell potential survey.

GPR is also capable of identifying the corrosion in steel inclusions (Clemena et al., 1992). A study was done by Andrt et al. (2011) to investigate the capability of NDE methods in identifying the amount of corrosion in reinforced concrete structures, bridge deck in particular. The results of this study showed that the GPR signals may distinctly indicate the corrosion in the form of blurring of rebar image features. As shown in Figure 18, the advancement of corrosion blurred the obtained image (Andrt et al., 2011).

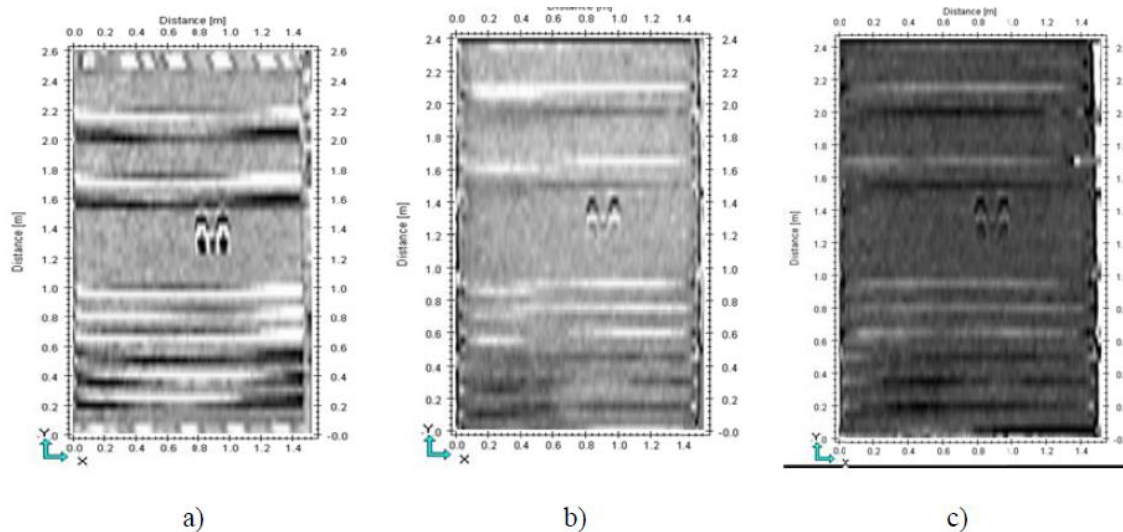


Figure 18. GPR data of the top layer rebar at different times: a) 6 month after casting, b) one month of corrosion experiment, c) three months of corrosion experiment (adapted from Andrt et al., 2011)

The use of magnetic based NDE techniques was investigated by Ghorbanpoor et al. (1996). This technique functions based on the variation in the magnetic fields due to loss of steel. Based on the experimental tests performed on specimens reinforced with bars and prestressing cables, the authors claimed that the amplitude of signals could be related to the extent of the corrosion. The results were in good agreement with the finite element analysis. This technique offered promise for field assessment of the corrosion advancement in steel reinforcement because a loss of cross sectional area of approximately 3% could be detected by this method. In a recent study, Fernandes et al. (2013) performed a field survey on a bridge that was scheduled for demolition. The purpose of these tests was to demonstrate the ability of the magnetic methods to detect hidden corrosion in box-beams in the field and tackle the logistic problem of inspecting box-beams from the bottom. The comparison of the survey with inspections on the dissected bottom of the box-beams showed that the magnetic methods used in this study can be employed to predict hidden corrosion in prestressing strands of box-beams. This observation suggests that the same method might be applicable for concrete pavements as well.

Impact-echo is another NDE method that has been a subject of studies related to the evaluation of the corrosion rate of steel inclusions in concrete structures (Cheng et al., 1993; Liang et al., 2001). For instance, Liang et al. (2001) examined this technique combined with three electrochemical methods to detect the rebar corrosion in concrete including open-circuit potential (OCP), direct current (DC) polarization, and alternating current (AC) impedance. The experimental study confirmed that impact-echo is certainly able to detect the development of microcracks in the concrete blocks. Among the tested techniques, DC polarization and AC impedance methods correctly predicted the corrosion rate and corrosion thickness of the specimens.

Yeih et al. (1998) evaluated the amplitude attenuation method, which is an ultrasonic NDE method, in terms of its ability to detect the corrosion damage in reinforced concrete elements. Analyzing the data obtained from the experimental investigation of reinforced concrete blocks resulted in obtaining relationships between the average ultrasonic testing amplitude attenuation and the electrochemical parameters. However, the authors mentioned that this

method requires additional investigation to become a mature ultrasonic NDE method for corrosion damage evaluation.

Acoustic emission (AE) monitoring is another non-invasive and passive NDE technique in which ultrasonic elastic waves are generated due to rapid release of energy from a localized source within a material (Sagar et al., 2012). AE monitoring was conducted in reinforced concrete beams subjected to corrosion of reinforcing steel (Yoon et al., 2000; Uddin et al., 2004). In one of these studies carried out by Yoon et al. (2000), it was observed that the degree of corrosion of reinforcing steel greatly influenced the rate of AE hits and the behavior of AE generation. Figure 19 provides the plot of cumulative hits with time under cyclic load. The AE counts decreases with the increase in the degree of corrosion (Yoon et al., 2000; Sagar et al., 2012).

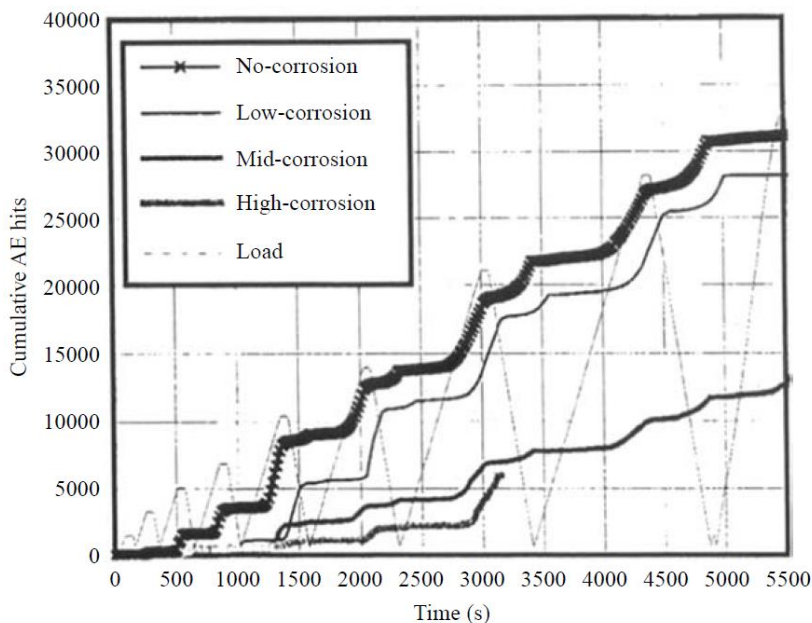


Figure 19. Sample ultrasonic based NDE method used for corrosion detection (adapted from Yoon et al., 2000)

It is also worth mentioning that Bjegovic et al. (2001) summarized the NDE methods applicable for monitoring the corrosion of steel reinforcement in concrete structures.

2.3.6 Layer Boundary Evaluation

In concrete pavements rehabilitated using partial depth repair, or newly constructed two-lift concrete pavement, or slabs placed on the bridge decks, the bond condition at the layer boundary is critical to assure the proper performance of the pavement system (Tompkins et al., 2009). If undetected, the horizontal cracks and initial debonding will progress into spalling, which is very expensive to repair (Celaya et al., 2007). Similarly, the bond condition of two lift concrete construction can lead to a loss in structural capacity if the layers are designed to perform with fully bonded interface (Hoegh, 2013).

A combination of impact-echo (IE) and ultrasonic surface wave techniques was used to locate debonding in concrete slabs at several locations by Celaya et al. (2007). A time-frequency analysis was proposed as a complementary tool to assess the condition of the slab when the IE record is more complex or noisy. As shown in Figure 20, in a case of an intact slab, a large portion of input energy is reflected back from the bottom of the slab, or concrete-base

interface. In the case of a debonded slab, a portion of the energy will be reflected from the concrete-air interface created by the debonding. The authors reported that this method was effective in locating and characterizing the intact and fully debonded slabs but was not sufficiently conclusive when the slab is in marginal condition (Celaya et al., 2007).

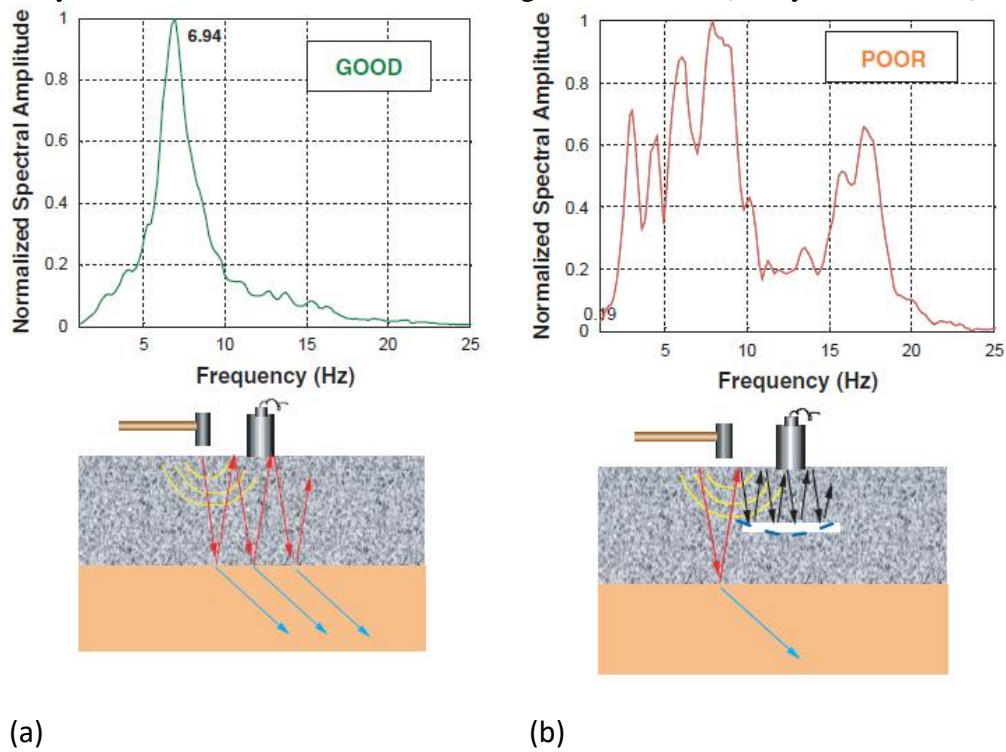


Figure 20. Impact echo technique and the associated normalized spectra analysis: a) good (Test Point D2), (b) poor (Test Point B1) conditions in terms of debonding (adapted from Celaya et al., 2007)

In another study on the application of an impact-echo testing device, the bonding between the asphalt and concrete overlays to concrete substrates was evaluated (Davis et al., 1996). Also, this method has shown promise in detection of discontinuities in concrete pavement such as delaminations, voids, cracks, and debonding within concrete members with different deterioration conditions (Cheng et al., 1993; Sansalone et al., 1997; Gucunski et al., 2000; Yuan et al., 2000).

Maierhofer et al., (2006) investigated the ability of infrared thermography in identifying the bonding between the carbon fiber reinforced plastic (CFRP) laminates and concrete. As Figure 21 illustrates, this method was able to distinguish the artificial unbonded laminates. Also, On-site investigations on a pre-stressed concrete bridge were carried out for the detection of delaminations inside or debonding below the top asphalt layer. The bridge deck consisted of a 5 cm concrete slab, 1 cm mastic for sealing, and 5 cm asphalt layer, and the test was performed using the sun as the heating source. Based on the acquired data, the authors suggested that this method can be useful for evaluating the bonds and detecting delamination in multi-layered systems (Maierhofer et al., 2006).

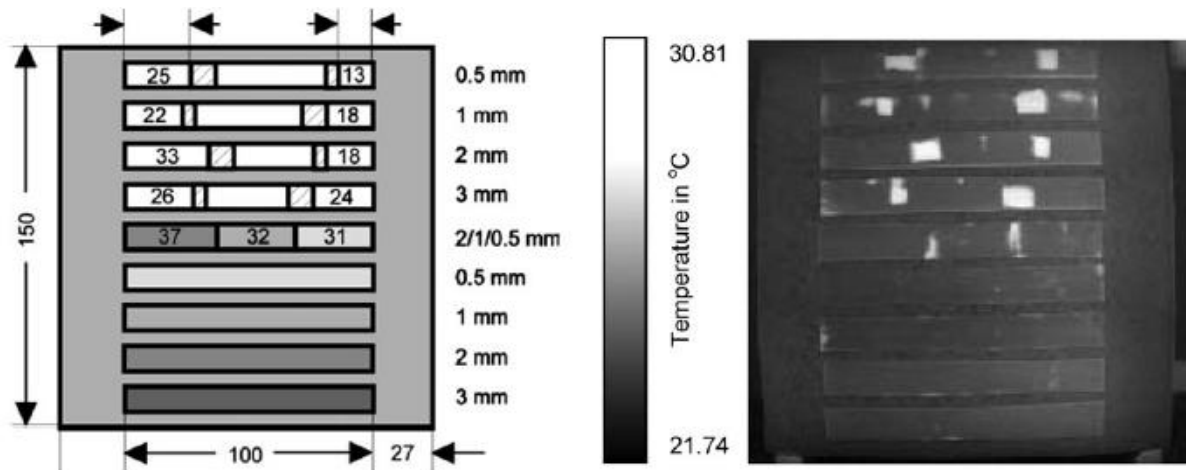


Figure 21. Left: test specimen with CFRP laminates, which have no contact at the shaded areas (nominal glue thickness is written on the right side). Right: thermogram directly recorded after a heating time of 15 s (adapted from Maierhofer et al., 2006).

Halabe et al. (2007) also carried out a study on the ability of infrared thermography to detect debonding in pavements by conducting an experiment on a fiber reinforced polymer (FRP) bridge deck. They concluded that this technique could effectively detect both air-filled and water-filled debondings between the wearing surface layer and the underlying deck. It was mentioned that this method works best on a hot sunny day, but when this desirable condition is not available, an external heating (or cooling) source could be employed. The presence of loose dirt and gravel and oil spills were other challenging issues in implementation of automated infrared image analysis (Halabe et al., 2007).

In a comprehensive field testing of 87 bridge decks in Wisconsin, Maser (2009) looked at the applicability of a NDE survey consisting of a combination of GPR testing and infrared thermography (mentioned in “Delamination and Spalling”). The results of this study confirmed that this approach can detect two types of defects including delamination due to reinforcement corrosion, and debonding of the overlay (Maser, 2009).

The impulse response (IR) test method, a case of impact-echo testing, was used on a 75 mm thick silica fume unreinforced concrete overlay located in Illinois, which suffered early deterioration six months after construction. At certain locations on the slab, debonding of the overlay was becoming apparent. The IR testing, which was completed in 3 hours, determined the exact extent of debonding over the whole 300 m long deck. Figure 22 shows the result of the IR testing analysis for the desired overlay (Davis, 2003).

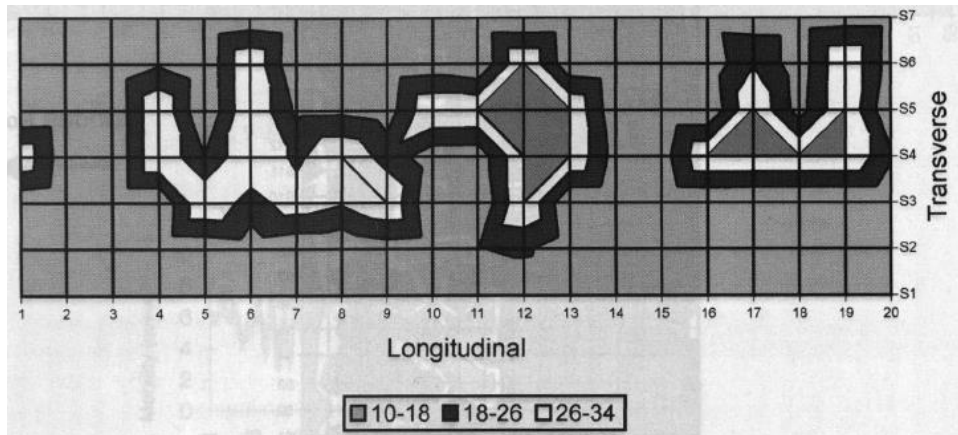


Figure 22. IR testing contour plot for the bridge ramp overlay (Davis, 2003)

2.3.7 Thickness Evaluation

Designing overlays, assessment of the contractor job in newly built pavements, and backcalculation of structural properties of existing pavements to estimate their remaining service life are some of the applications that require pavement thickness as an input information (Khazanovich et al., 2015; Loulizi, 2001). In spite of its importance, Often this information is unknown or records are inaccurate, inaccessible, or out of date (Maser et al., 1992). To underline the importance of having accurate knowledge of the pavement thickness, Maser et al. (1992) showed that the variation of the asphalt layer thickness by 20% can lead to errors of up to 95% in base moduli back-calculated from falling weight deflectometer (FWD) data. Several pavement design procedures, including the guides for the American Association of State Highway and Transportation Officials (AASHTO), Portland Cement Association (PCA), and Illinois DOT Mechanistic Design, emphasize the importance of this parameter showing that thickness deficiency can lead to premature pavement failure (AASHTO, 1993; Packard, 1984; Hoegh, 2013). Currently, many agencies use destructive methods such as coring that allow for only a limited sampling of the in-situ pavement thickness (Grove, 2012). Core sampling is destructive, time-consuming, labor-intensive, and intrusive to traffic, while only providing limited information (Maser et al., 1992). As an alternative, NDE methods can be used to get more detailed information about the pavement thickness (Schubert et al., 2004; Edwards et al., 2011; Grove et al., 2012; Hoegh, 2013).

Layer thickness measurement is by far the most common and successful application of GPR for pavements applications (Al-Qadi et al., 2010, Cao et al., 2007). The pavement thickness can be obtained based on the variation in the propagation velocity within each layer and the measurements of time difference for the reflected electromagnetic pulse (Maser, 1996a; Cao et al., 2007; Loulizi, 2001; Hoegh, 2013). Experience has shown that GPR may be more effective on flexible pavements compared to rigid pavement because of the strong dielectric contrast between layers. The interface between the concrete and the base is often indistinct (Cardimona et al., 2003), especially when the radar waves are attenuated due to the presence of moisture or high-content clay subgrade (Cao et al., 2007). In spite of these limitations, GPR has been used frequently to measure the thickness of the concrete slab (Maser et al., 1994 & 2006; Seusy et al. 1992; Lenngren et al., 2000; Saarenketo et al., 2000; Davis et al., 2005; Al-Qadi et al., 2005a & 2005b & 2005c; Willett et al., 2006; Harris et al., 2006; Loken, 2007; Belli et al., 2008; Cao et al., 2011).

For instance, Maser et al. (1994) reported that the average absolute deviation between GPR calculated thickness and core data was 13.5 mm. They attributed the difference to inadequate

contrast between the concrete and the base material, and the inability of the waves to penetrate through the whole concrete slab. Loken (2007) claimed that the accuracy of GPR thickness calculations was 7.5% for asphalt and concrete pavements, and within 12% for unbound base layers.

Al-Qadi et al. (2005c) performed GPR survey on 17 pavement sites with pavements of different types (flexible, rigid, and composite), different structures, and different ages. Flexible pavements were found to have a relatively high thickness error (4.4%) compared with the continuously reinforced concrete pavements (3.0%) and with the jointed plain concrete pavements (2.3%). The results also showed that the GPR thickness error increased as the pavement's age increased (4.4% error for pavements 0 to 5 years old versus 5.8% error for pavements older than 20 years with surfaces older than 10 years). Figure 23 presents a sample raw GPR data and the distinctive changes with the change in the layer properties (Al-Qadi et al, 2005c).

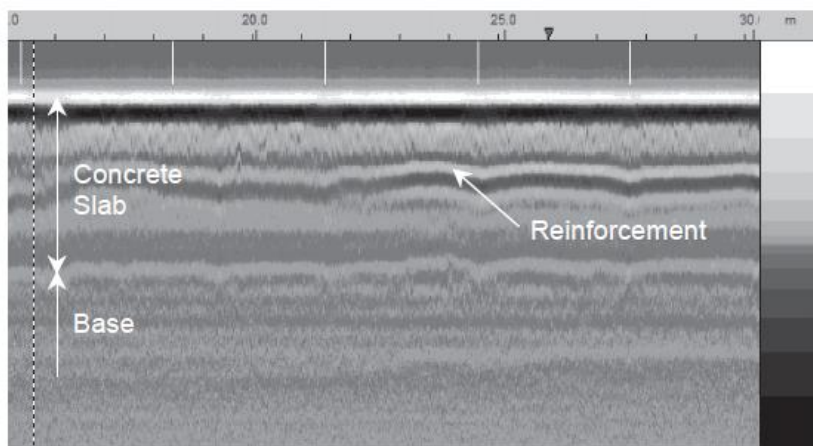


Figure 23. A sample raw GPR data on CRC pavement (adapted from Al-Qadi et al, 2005c)

Impact-echo is also used for measuring the concrete pavement thickness (Schubert et al., 2004; Gibson, 2005). Gibson (2005) proposed two approaches to analyze the data obtained from IE testing, one based on frequency-domain and the second based on time-domain analysis. To validate the proposed methods, a series of experimental tests were carried out on three full-scale (3 m x 4 m plan) concrete slabs with design thickness of 20, 25, and 30 cm at different curing ages. The maximum experimental errors of 3% in terms of average thickness along a 2 m centerline on each of the three slabs were obtained (Figure 24). The author recommended the use of a limited number of cores for calibration purposes (Gibson, 2005).

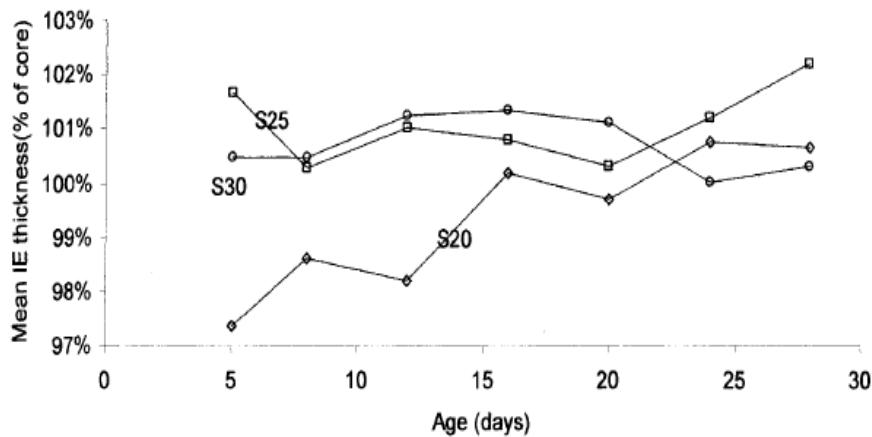


Figure 24. Average thickness measured by IE method versus curing age (adapted from Gibson, 2005)

2.3.8 Structural Assessment

NDE evaluations are able to assess the structural integrity of the pavement, and to characterize the material properties of the test object. They can be used as part of the pavement condition survey program along with other conventional methods such as deflection-based NDE techniques, visual distress survey, roughness and friction survey, shoulder survey, and drainage evaluation.

In addition to all of the previously mentioned applications of GPR, this NDE technique can be used to detect rutting mechanism especially in severe conditions where the magnitude of rutting deformation is greater than 10% of the overall thickness of the layer. However, this method is relatively time-consuming to implement due to difficulties in data collection and analysis, as well as the need for a reference location to compare the results to (Cao et al., 2007).

The ultrasonic wave reflection (UWR) method, also known as ultrasonic shear wave reflection (USWR), is normally applied to cementitious materials, such as concrete, mortar or cement paste, at early ages (within the first day after mixing cement and water). This method is preferred over other early age test methods for different aspects, including the ability of continuous data collection, one-sided access for measurements, and direct connection to mechanical and microstructural properties of the test medium. However, one disadvantage of this method is its limitation in evaluating the structural properties of the materials at some distance away from the interface between the buffer and test object (Popovics et al., 2014). Figure 25 depicts a schematic representation of the UWR testing device and its outputs.

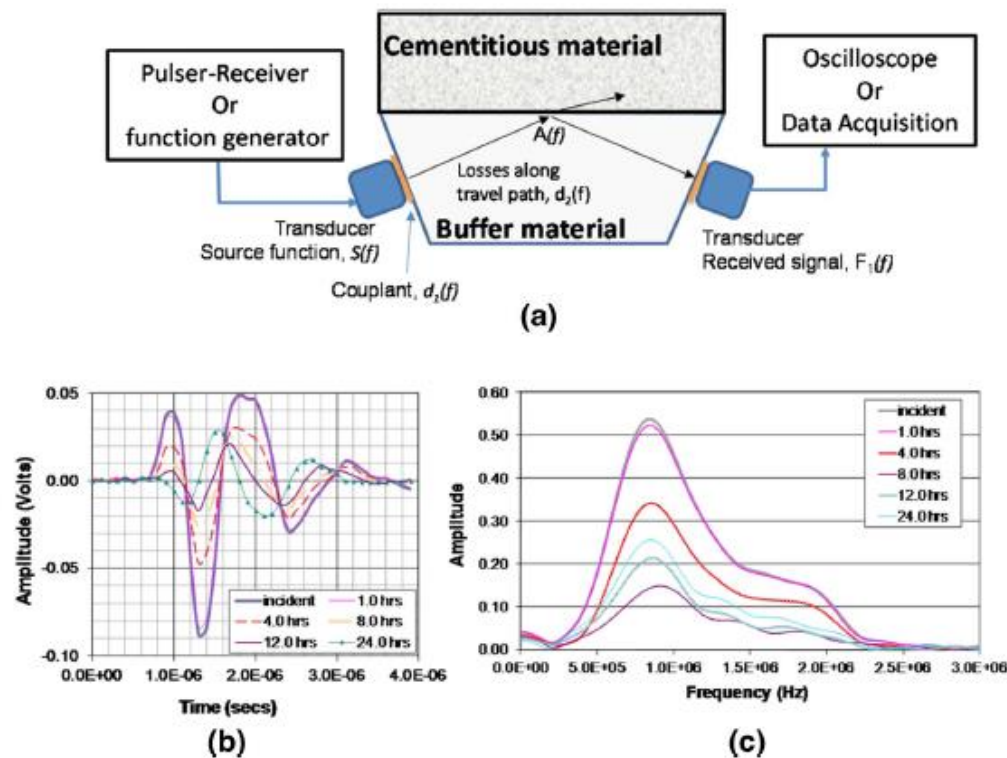


Figure 25. a) Schematic representation of a typical testing configuration to measure reflection at the interface of buffer material and cementitious material; b) Typical reflected signals at different instance of time; c) frequency (amplitude) domain representation of the reflected signals (adapted from Popovics et al., 2014).

Because this method is very sensitive to phase changes, it has been successfully used for monitoring stiffening and setting behavior of cementitious materials (Rapoport et al., 2000; Öztürk et al., 2006; Chung et al., 2012). This method has been used for monitoring material strength development for in-situ assessment by placing a steel plate as the buffer material inside the concrete slab at the time of casting. The experimental results have confirmed the acceptable relation between the reflected ultrasonic wave and the material strength. Figure 26 presents a sample data that shows a good agreement between the normalized S-wave reflection and the material strength (Subramaniam et al., 2002; Popovics et al., 2014).

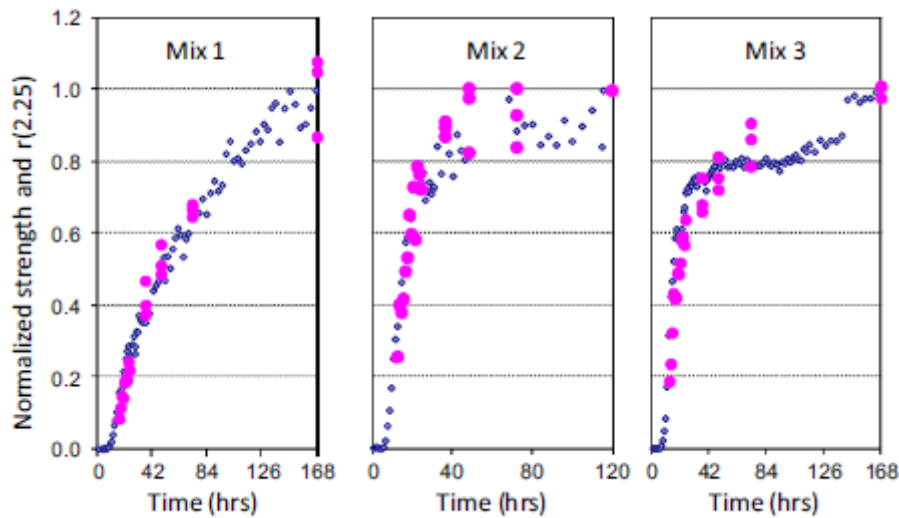


Figure 26. Comparison of normalized S-wave reflection (blue points) and strength gain (magenta points) in slabs with different concrete compositions using a steel buffer. The 7-day strengths of Mix 1, Mix 2 and Mix 3 determined from cores were 26, 37 and 55MPa, respectively (adapted from Subramaniam et al., 2002)

Evaluation of the compressive strength of high strength concrete using spectral analysis of surface waves (SASW) and impact-echo was the focus of a study conducted by Cho (2003). In this effort, three high-strength concrete slabs of 600, 850 and 1100 kg/cm² compressive strengths were prepared together with cylinders from the same batches. Then, relations between the wave velocity and the compressive strengths tested at different curing ages were found both for SASW and impact-echo NDE techniques. The author concluded that this method could be applied in the integrity analysis of high strength concrete structures with a finite thickness (Cho, 2003).

A similar study was performed by Lee et al. (2003) to evaluate the early strength of normal and high strength concrete using the wave velocity obtained from impact-echo testing method. The tests were carried out on concrete specimens with water to cement ratios between 0.58 and 0.27, and at curing ages between 12 h and 28 days. The results demonstrated that the velocity-strength relationship of normal-strength concrete is noticeably different from that of high strength concrete. Also, this relationship is influenced by curing ages for normal-strength concrete. Based on the obtained information, equations were proposed to evaluate the strength of the concrete using the wave velocity measured by impact-echo testing (Lee et al., 2003).

2.4 SUMMARY OF NDE METHODS

The above discussion of nondestructive evaluation methods highlights the strengths of each individual method. Regardless of the technique chosen for evaluation, the incorporation of NDE in pavement management strategies allows for early detection of anomalies which can result in longer service life, enhanced safety and potential cost savings. Due to fundamental differences of the methods discussed, the most suitable applications for each device rely heavily on the proper understanding of the strengths and limitations of each technique. The following sections will discuss the applications of NDE techniques with respect to a variety of loading and damage scenarios.

2.5 ULTRASONIC LINEAR ARRAY

While conventional nondestructive testing methods provide useful information as described in section 2.1, ultrasonic array technology provides an opportunity to mitigate issues with limited transducer pairs and associated signal variability via the use of sending and receiving transducer pairs at set spacings. Spatial diversity is achieved through an array of elements within a single transducer.

To allow for field testing of heterogeneous materials such as PCC, dry point contact (DPC) transducers are used, which eliminates the need for a manual mechanical impact and time-intensive surface coupling. The use of DPC transducers also introduces multiple impulse angles that can increase reliability of measurements, allowing for reduced transducer spacing and greater precision (Bishko et al. 2008). One version of DPC ultrasonic array technology, MIRA, is shown in Figure 27 and consists of a linear array of transducers.

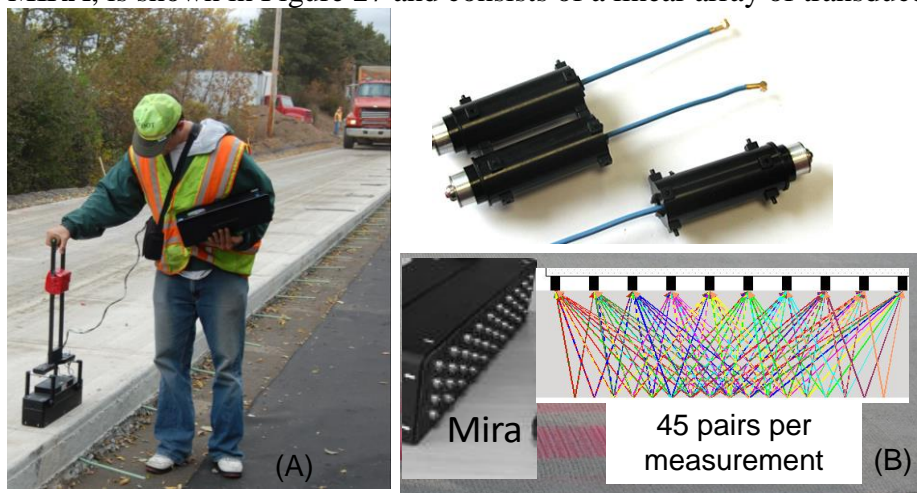
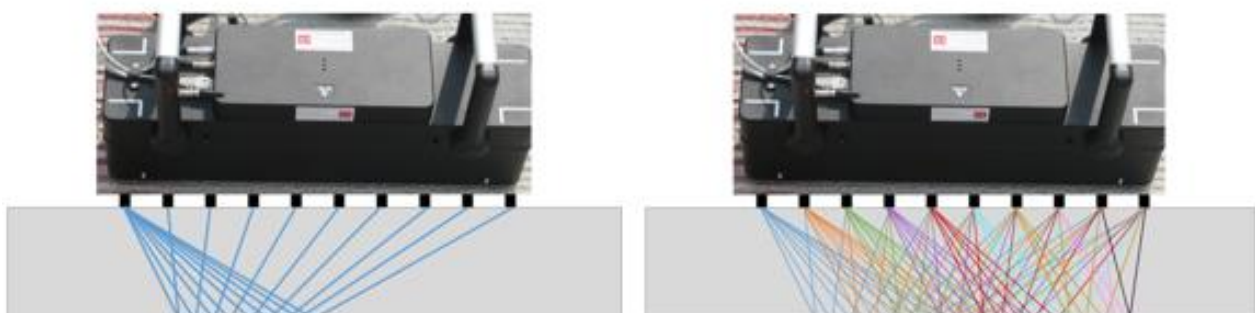


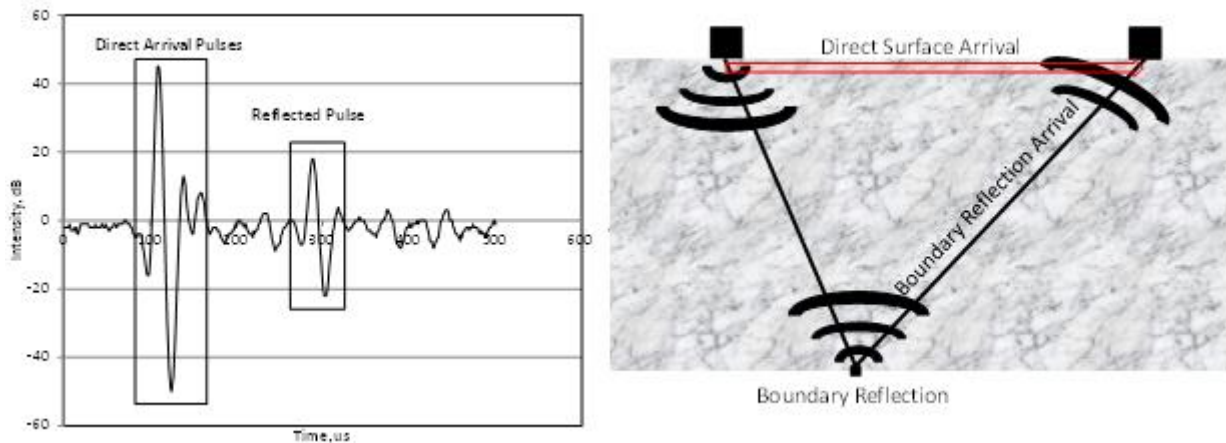
Figure 27. MIRA ultrasonic linear array device (Hoegh 2013).

MIRA is an ultrasonic shear wave device that utilizes a linear array of 40 dry point contact transducers for diagnostics. This array is arranged into groups of 4 transducers, acting essentially as one unit, which results in out-of-plane shear waves acting in a linear fashion. The emitted waves travel into the specimen, allowing for cross-sectional analysis. Because shear waves, and not compression waves, are utilized, the results are independent of moisture conditions. Each set of four transducers interacts with the remaining nine sets of transducers, resulting in 45 unique transducer pairs (i.e., 1 to 2, 1 to 3, 1 to 4, ..., 8 to 9, 8 to 10, 9 to 10) as shown in Figure 28. The spacing between adjacent transducer channels is 40 mm (1.6 in.). As such, each acquired measurement results in nine impulse histories at 40 mm (1.6 in.) spacing, eight at 80 mm (3.1 in.) spacing, seven at 120 mm (4.7 in.) spacing, six at 160 mm (6.3 in.)



spacing, five at 200 mm (7.9 in.) spacing, four at 240 mm (9.4 in.) spacing, three at 280 mm (11.0 in.) spacing, two at 320 mm (12.6 in.) spacing and one at 360 mm (14.2 in.) spacing. The utilization of this array setup allows for increased redundancy and measurement confidence. The incorporation of multiple impact angles is ideal for the analysis of heterogeneous materials, which is essential for concrete applications (Hoegh 2013).

Figure 28. MIRA transducer interactions emitted from transducer 1 (left) and for all transducer pairs (right).



The 45 unique impulse time histories provide valuable information about the specimen. The impulse time histories contain reflectivity information, caused by any change in acoustic impedance that the wave encounters. Changes could be caused by air voids, damage, inclusions, or layer interfaces. An example impulse time history is shown in Figure 29 (left), along with a schematic which would result in this type of time history (right). The direct arrival pulse is the result of a portion of the wave traveling the shortest/fastest distance, in this case along the surface of the specimen, and being received by another transducer. The reflected pulse is the result of the wave propagating through the specimen and encountering a change in acoustic impedance, in this case the bottom surface of the specimen, and reflecting back to the surface. An impulse time history is created by each of the 45 transducer pairs, resulting in a large amount of information and data per scan.

Figure 29. Example impulse time history (left), and corresponding cross section schematic (right) (Hoegh 2013).

MIRA can be used for various nondestructive subsurface diagnostic applications including poor consolidation and non-uniformity (Hoegh et al., 2012a), de-bonding between layers (Hoegh et al., 2012c), horizontal delamination (Hoegh et al. 2012b; Hoegh et al., 2013), and joint deterioration and spalling or poor consolidation around dowels (Hoegh et al. 2012c; Hoegh et al., 2013).

2.5.1 Shear Velocity Determination

In addition to providing ultrasonic reflection information, the direct arrival of the multiple channels can provide velocity information as well. The impulse time histories (such as that shown in Figure 29, left) can be utilized to determine important properties of the specimen, such as calculating the shear wave velocity. Because the transducer spacing is known, as well

as the time of the direct arrival pulse, the shear wave velocity can be calculated using the redundant information provided by the 45 pairs. This velocity can be calculated as follows:

$$v_s = \frac{x_{i,j}}{t_{i,j}} \quad (3)$$

Where v_s is the calculated shear wave velocity, i and j are the transducers 1 through 10, $x_{i,j}$ is the distance between transducer i and j , and $t_{i,j}$ is the time of the direct arrival pulse for the time history related to transducer i and j . While Equation 3 is quite simplistic, multiple transducer pairs are needed to calculate velocity accurately due to the time delay incorporated into the system. By plotting the $x_{i,j}$ and $t_{i,j}$ values for all transducer pairs, a best fit linear trendline will reveal the actual shear wave velocity, removing the time delay from all points because the delay is a constant for all transducers. An example plot, with corresponding trendline can be seen in Figure 30. As can be seen, the data points are highly linear, which allows for the accurate determination of shear wave velocity (in this case, 2.3007 mm/us or 2301 m/s) when the direct arrival is evident. This calculation is possible due to the repeatability of equally-spaced transducer pairs and the redundancy of data provided by the linear array system (Hoegh 2013). It should be noted that this calculation is only valid when the concrete is in sound condition, or without shallow damage which would inhibit the direct arrival.

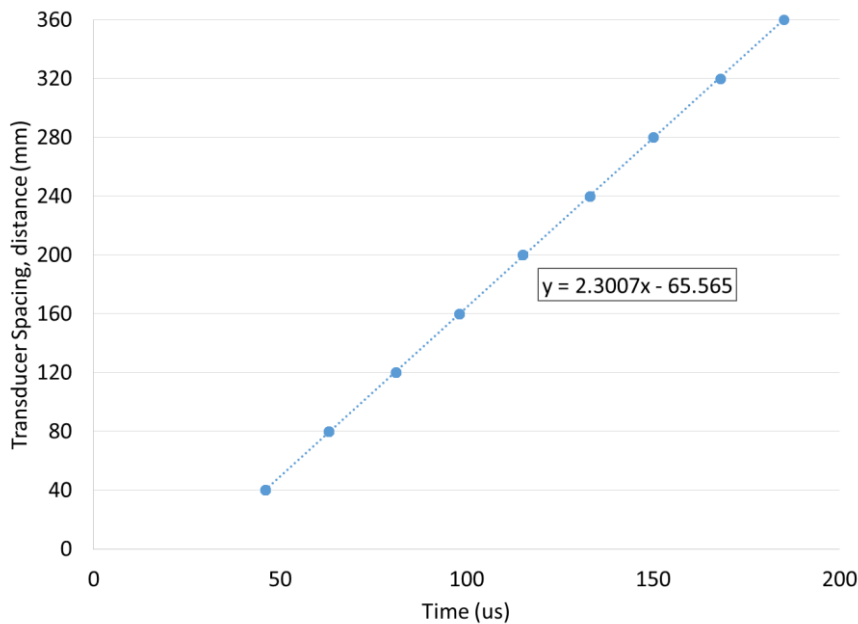


Figure 30. Example array data for calculation of shear wave velocity.

Previous research has shown that this calculated shear velocity is independent of specimen type, given the same concrete mix. Figure 31 shows the results of beam and slab measured velocities at various concrete ages. It can be observed that there is a very good agreement between the beam and slab velocities of the same mix, as shown by the linear and nearly 1:1 relationship. The monotonic relationship is positively correlated with concrete age, allowing for an extremely accurate, while practical, estimate of concrete properties.

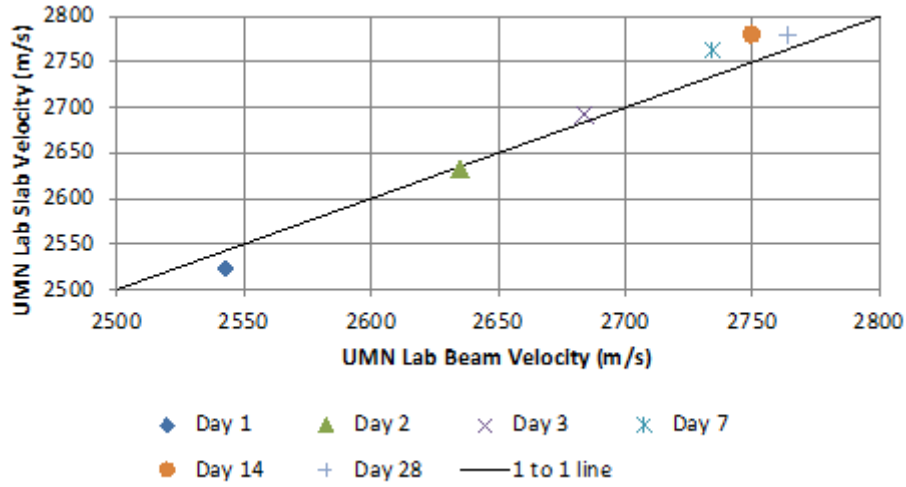


Figure 31. Ultrasonic array measured shear wave velocities for concrete beams vs. slabs at various concrete ages (K. Hoegh, personal communication).

2.5.2 Reconstruction Formulation

This shear velocity information described in section 2.2.1 can be further implemented to allow for the formulation of visual reconstructions. For visual analysis of cross section characteristics, the unique impulse time histories provided by MIRA can be used to create reconstructive images of the cross section of interest. The method used to create these images is called Synthetic Aperture Focusing Technique (SAFT). The following equations are utilized in order to create SAFT B-scans, a typical reconstruction:

$$\hat{\theta}_{i,k} = \sum_{e=1}^{T-1} \sum_{r=e+1}^T A(x_r, x_e, x_i, z_k) \Psi_{e,r}(x_i, z_k) \quad (4)$$

where,

$$\Psi_{e,r}(x_i, z_k) = s \left(x_r, x_e, \frac{1}{c} \left(\sqrt{z_k^2 + (x_i - x_e)^2} + \sqrt{z_k^2 + (x_i - x_r)^2} \right) \right) \quad (5)$$

where $\hat{\theta}_{i,k}$ is the image reflectivity assigned to each position within the ROI, T is the number of transducer locations, e and r are the indexes for the emitting and receiving transducers, and i and k are the indexes for the horizontal and vertical positions of the ROI, such that the ROI is represented by a $W \times D$ set of points contained in W columns and D rows, s is the magnitude of the response at the evaluated time of flight for the given transducers, x_e and x_r , and A is the apodization coefficient (Hoegh and Khazanovich 2015). This apodization factor accounts for the various incident angles and other traits of the signal (Balmer 1992).

It is then useful to implement Hilbert transform in order to calculate the instantaneous attributes of the series, computed via equations (6) through (11):

$$HT(z) = \frac{1}{\pi} \int_{-\infty}^{\infty} \frac{f(s)}{t-s} ds \quad (6)$$

where $HT(t)$ is the Hilbert transform of a given function, $f(x)$. The complex signal, $Z(z)$ is then given by:

$$Z(z) = f(z) + j HT(z) \quad (7)$$

This complex signal can then be calculated at each coordinate of the reconstruction to calculate the instantaneous amplitude:

$$\hat{\theta}^{IA}(x, z) = \sqrt{(\hat{\theta}(x, z))^2 + \left(\frac{1}{\pi} \int_{-\infty}^{\infty} \frac{\hat{\theta}(x, s)}{z-s} ds \right)^2} \quad (8)$$

where $\widehat{\delta}^{IA}(x, z)$ is the relative reflectivity that defines the new instantaneous amplitude-based SAFT reconstruction. A typical apodization factor utilized for the creation of these reconstructions is as follows:

$$A(x'_r, x'_e, x_i, z_k) = \alpha_e(x'_e, x_i, z_k) * \alpha_r(x'_r, x_i, z_k) \quad (9)$$

Where:

$$\alpha_e(x'_e, x_i, z_k) = \frac{z_k}{\sqrt{(x_i - x'_e)^2 + z_k^2}} \quad (10)$$

$$\alpha_r(x'_r, x_i, z_k) = \frac{z_k}{\sqrt{(x_i - x'_r)^2 + z_k^2}} \quad (11)$$

These equations account for the fact that a transducer can act as both the emitting transducer and as the receiving transducer (Hoegh and Khazanovich 2015). Standard software to create SAFT B-scans is included with MIRA; however, a signature analysis developed at the University of Minnesota (Hoegh 2013) was instead used for greater freedom in the apodization factor, and for the corresponding increased understanding of the reconstruction components.

However, SAFT B-scan reconstructions have their limitations. The edges of each scan reconstruction spans only 400 mm, making comprehensive cross section analysis difficult. To incorporate greater confidence and redundancy via capitalizing on the overlapping nature of the eleven measurements, panoramic reconstructions can improve the results via the compiling of individual SAFT reconstructions (Hoegh 2013). Equation (12) is used to combine the individual reconstructions to create the panoramic reconstructions which have a larger region of interest:

$$\widehat{\mathcal{O}}_{PAN}^m(x, z) = \begin{cases} \widehat{\mathcal{O}}_{PAN}^{m-1}(x, z), & \text{if } x < D \\ \max\left(\widehat{\mathcal{O}}_{PAN}^{m-1}(x, z), \widehat{\mathcal{O}}_I^m(x, z)\right), & \text{if } D < x < x_{PAN}^{m-1} \\ \widehat{\mathcal{O}}_I^m(x, z), & \text{if } x > x_I^m \end{cases} \quad (12)$$

where each SAFT scan, $\widehat{\mathcal{O}}_I^m$, where m is the index of the current SAFT scan and I denotes that it is an individual scan, is combined to form the new region of interest, ROI_{PAN}^m . This region has a vertical dimension of z and a horizontal dimension of x_{PAN}^m , and D is the distance from the global origin (Hoegh 2013, Hoegh and Khazanovich 2015, Freese et al. 2016).

These panoramic reconstructions can be powerful tools for locating dowels, determining slab thickness, and other applications (Hoegh 2013). However, these reconstructions rely upon the presence of sound concrete and difficulties can arise when significant reinforcement is present.

2.6 WAVE PROPAGATION SIMULATION

Simulations also serve as a valuable tool for improvements in the interpretation of results from nondestructive testing. Simulation programs allow for reverse engineering methods to be applied via comparative analyses. The finite-difference method (FDM) is the dominant method for modeling wave propagation, specifically for structural modeling (Mozco et al. 2010). FDM can be applied to isotropic or anisotropic materials, and is relatively accurate and computationally efficient. Advanced schemes have been developed that allow for a heterogeneous formulation of equations which was not previously possible (Mozco et al. 2010, Levander 1988, Olsen et al. 1995, Graves 1988, Pitarka 1999, Moczo et al. 2002).

The finite element method (FEM) is an alternative method that allows for free surface boundary conditions to be handled easily (Bathe 1996). FEM is very flexible and capable of solving any 3D problem; however, it requires a huge amount of memory and sizable computational time. As such, FEM is less computationally efficient when compared to FDM.

The finite integration technique (FIT) can be used for simulation purposes and was first proposed by Weiland in 1977 to study electromagnetic waves (Weiland 1977). This method is essentially a generalization of the finite difference time domain method (FDTD), and it has tight links to the finite element method (FEM). FDTD is faster than FEM but is not applicable to arbitrary geometry, unlike FIT. Additionally, FEM mass matrices are not diagonal, unlike the ones arising in FIT, when used in the frequency domain.

Fellinger (1991) adapted Weiland's ideas to the governing equations of ultrasonic waves in solids, and developed a numerical procedure called the Elastodynamic Finite Integration Technique (EFIT), which is used for this research. In EFIT, partial differential equations are replaced by integral equations. The integrals are then approximated on finite volumes or cells. Assuming linear interpolation of the integrand, a mean value is approximated by the value of the integrand in the center of the cells or its edges.

EFIT is an efficient numerical approach to study wave propagation in homogeneous, strongly heterogeneous, isotropic, and anisotropic linear and nonlinear elastic media (Peiffer et. al 1997). Thus EFIT is an ideal method to study ultrasonic waves in concrete. This method also allows for flexibility in handling various boundary conditions. Simplicity is another advantage of the EFIT; it can be implemented easily and efficiently on various computer platforms. In the Cartesian coordinate system, velocity-stress finite-difference formulation with a staggered grid (Virieux 1984 and 1986), which is widely used to study earthquake motions, results in exactly the same equations as EFIT. For these reasons, EFIT was utilized for this simulation program.

Since MIRA is sending horizontal shear waves, EFIT is used to obtain the discretized equations of motion for this case. The following equation shows how velocity is related to shear stresses in this method:

$$v_y^{n+1}(i, j) = v_y^n(i, j) + \frac{\Delta t}{\rho} \left(\frac{\tau_{xy}^{n+\frac{1}{2}}(i, j) - \tau_{xy}^{n+\frac{1}{2}}(i, j-1)}{\Delta x} + \frac{\tau_{zy}^{n+\frac{1}{2}}(i, j) - \tau_{zy}^{n+\frac{1}{2}}(i-1, j)}{\Delta z} \right) \quad (13)$$

and shear stresses are determined using the following two equations:

$$v_y^{n+1}(i, j) = v_y^n(i, j) + \frac{\Delta t}{\rho} \left(\frac{\tau_{xy}^{n+\frac{1}{2}}(i, j) - \tau_{xy}^{n+\frac{1}{2}}(i, j-1)}{\Delta x} + \frac{\tau_{zy}^{n+\frac{1}{2}}(i, j) - \tau_{zy}^{n+\frac{1}{2}}(i-1, j)}{\Delta z} \right) \quad (14)$$

$$\tau_{zy}^{n+3/2}(i, j) = \tau_{zy}^{n+1/2}(i, j) + \frac{\mu \Delta t}{\Delta z} (v_y^{n+1}(i+1, j) - v_y^{n+1}(i, j)) \quad (15)$$

Where $v^k(i, j)$ and $\tau^k(i, j)$ stand for velocity and stress at time $t = k\Delta t$ and at a point with coordinates $x = i\Delta x$ and $z = j\Delta z$. These equations serve as the basis for the implementation of EFIT. Further execution and discussion of these EFIT methods and equations will be discussed in Chapter 6.

2.7 IMPROVEMENTS TO CURRENT TECHNOLOGY

The technologies and analysis techniques outlined in the previous sections show promise for applications regarding damage detection in concrete. Recent technological advancements have improved efficiency and allowed for in-situ applications in the last several years via the improvements created by SAFT reconstructions. However, these methods have their limitations when applied to damaged concrete sections and remain highly subjective. Moreover, when concrete is extensively damaged, many of the principles incorporated into these methods are no longer applicable. It is these shortcomings that are addressed via the research presented in the following chapters.

2.8 DAMAGE DETECTION METHODS

Two methods were employed for the detection of environmental damage. Those methods include a visual reconstruction analysis, as well as the development of a quantitative indicator of the concrete condition. The method utilized for the visual reconstructions has been discussed previously in both the literature review, and within the reinforced concrete column discussion found in Chapter 3. However, the basis of the visual analysis used for the environmental damage cases is comparative in nature for diagnosing each individual reconstruction image based upon typical reconstruction characteristics. The methods used for the quantitative indicator analysis are presented here.

2.8.1 Quantitative Indicator Development

A visual investigation of raw signal data from both sound and damaged concrete slabs resulted in several key differences between the two slab conditions to be identified. To illustrate the differences between sound and damaged concrete with respect to the raw signal, two representative normalized signals are shown below in Figure 32. On the left is an example of a signal from a slab in good condition, while the signal on the right shows a signal which was obtained from a slab with damage present. The two key differences between these signals are the shape of the direct arrival impulse (highlighted earlier in the time history), and the increased oscillation which occurs after the direct arrival (highlighted later in the time history). The precise change in direct arrival signal shape is not consistent in all damaged slabs, however the shape is consistently different from the sound condition. In some cases, the signal appears to show a phase change (as shown in this example), which is exhibited by the inversion in signal shape. The increased oscillation occurs after the direct arrival, but this oscillation is not present in the sound concrete condition. These two qualitative differences in signal shape served as the basis for the development of a numerical indicator to diagnose the condition of concrete in a nondestructive manner.

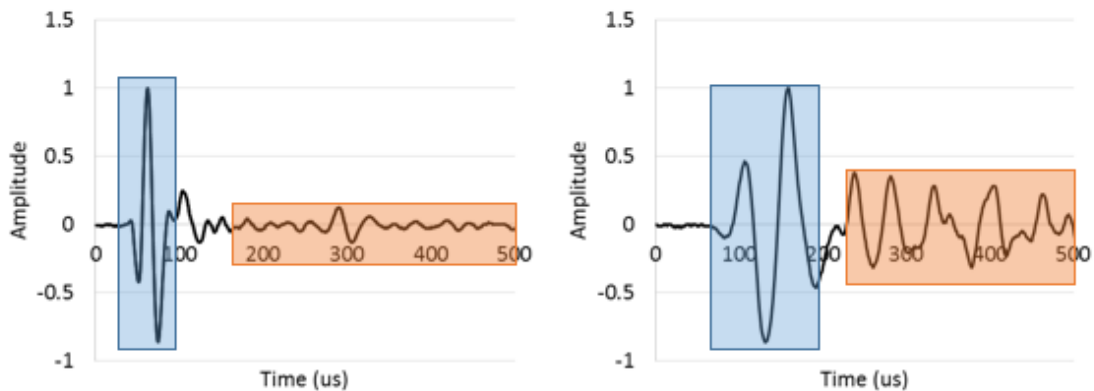


Figure 32. Sample normalized signals for clean concrete (left) and damaged concrete (right) highlighting key differences.

While the above signals have been normalized, it is worth discussing the trends in magnitude of the raw signals. A thorough visual inspection of an extensive data set of both clean and damaged signals revealed that the magnitude of the signal is not an indicator of the condition of the concrete. The magnitude or amplitude is instead dependent upon the contact conditions and pressure applied when using the device. To show the variability in magnitude within each condition level, consider the two graphs shown below in Figure 33. The first graph shows two signals from scans on sound concrete. The first signal has a maximum

magnitude of 183, while the second example signal has a magnitude peak of 270. These signals were obtained from the same slab, seconds apart from each other, yet have considerably different magnitudes. The same observations can be made from the two signals obtained from a damaged concrete slab, as shown in the second graph. One signal has a magnitude of 173, while the other peaks at 268. Again, these signals were both obtained from the same slab, in the same time period. While the magnitudes vary greatly, the condition of the concrete remains the same. As such, magnitude is not an indicator of the condition of concrete and has thus been removed from this analysis, as detailed in the development of the quantitative indicator.

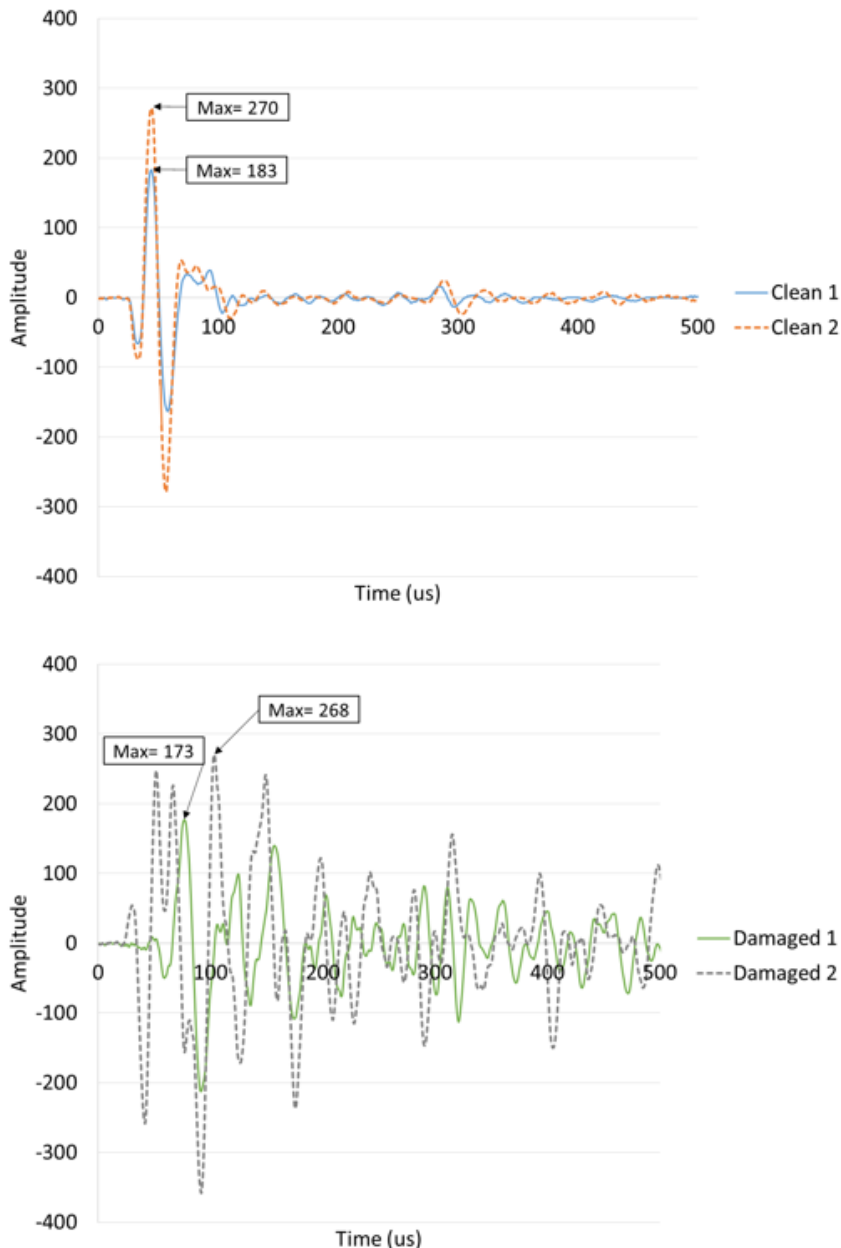


Figure 33. Example raw signals for two clean cases (top) and two damaged cases (bottom).

The numerical indicator which was developed is based upon the instantaneous amplitude envelope that is created using Hilbert transform. Hilbert transform is a common technique in signal data analysis, especially when interested instantaneous attributes of the

signal. The Hilbert transform, $HT(t)$ of a certain function, $f(x)$, as calculated by Matlab is commonly defined as:

$$HT(t) = \sqrt{(f(t))^2 + \left(\frac{1}{\pi} \int_{-\infty}^{\infty} \frac{f(\tau)}{t-\tau} dx\right)^2} \quad (21)$$

To illustrate the output of this transformation, consider the example shown below. Shown via dashed line is the raw signal data, and the solid line is the resulting Hilbert transform envelope.

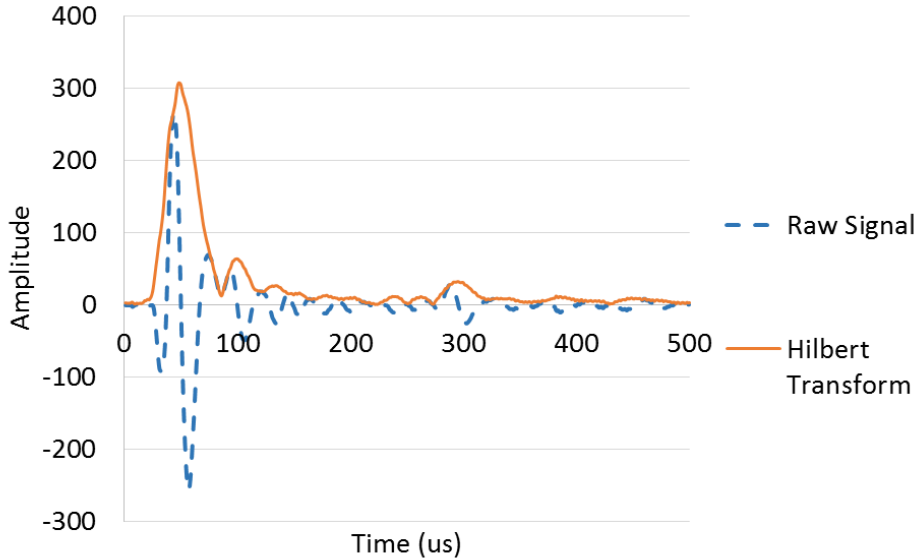


Figure 34. Sample Hilbert transform envelope.

This Hilbert transform envelope served as the basis for the creation of a numerical indicator which captured the increased oscillations which were present in the damaged signal case. As such, the indicator must be greatly affected by the presence of these oscillations. The following indicator, referred to as the Hilbert Transform Indicator (HTI), was created:

$$HTI = \int_0^{500} \frac{HT(t)}{\max(HT(t))} dt \quad (22)$$

This equation considers a time frame of 500 microseconds, chosen in order to both capture the direct arrival impulse, as well as the subsequent oscillations which occur in the damaged case. The Hilbert transform envelope is normalized in order to remove any effect of magnitude on the results.

To illustrate the ability of the HTI in capturing the condition of the concrete, consider two example Hilbert transform envelopes which are graphed below. Shown in a solid line is the clean case, and in dotted line is the damaged case envelope. The HTI for the clean signal was 55, while the HTI for the damaged was 137. One can see the drastic changes in the Hilbert transform envelope for the damaged case, which result from the increased oscillations present. The HTI value captures this difference numerically, as exhibited by a value of over twice that of the clean case. The extensive data set which was analyzed allowed for the creation of typical numerical categories for the HTI values in order to classify the condition of the specimen. Typical HTI values for concrete in sound condition are below 90, usually in the 70s. HTI values for extensively damaged concrete are typically above 120. Those HTI values which fall in-between these categories are beginning to show signs of damage but do not show signs of heavy degradation. The discussion and analysis of HTI values for damaged slabs will be further discussed for each damage application in sections 5.2.3.2 and 5.3.4.

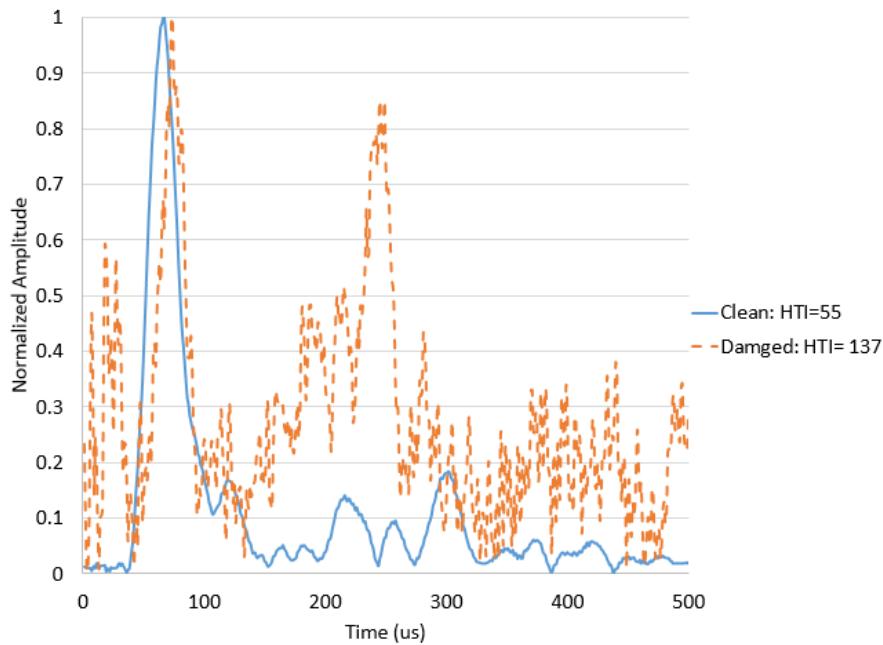


Figure 35. Typical Hilbert transform envelopes for sound and damaged specimens.

To show the repeatability of HTI values, a large data set compiled from past research efforts performed on sound concrete was analyzed, as mentioned above. 45 scans were analyzed, resulting in the calculation of over 2,000 HTI values. Statistical values for this data set are shown below in Table 2. It is also important to note that there are trends in HTI value within each scan. The HTI value increases in magnitude as transducer spacing increases, as would be expected due to greater noise associated with greater distances in wave travel. As such, it is useful to average the HTI values obtained from all 45 transducer pairs to result in one comprehensive indicator value which incorporates redundancy and results in increased measurement confidence. It is this averaged value that is shown in the table.

Table 2. Preliminary HTI values for sound concrete

Number of averaged HTI values	45
Average HTI Value	72.5
Standard Deviation	6.47

A confidence interval based upon the analysis of undamaged concrete signals can also be created, and is shown below in Figure 36. As can be seen, the HTI values increase significantly with transducer spacing, in a repeatable fashion. The 95% confidence interval is reasonable due to the low standard deviations seen. Again, these values are averaged in order to incorporate redundancy while also lessening the complexity of analysis required. This is justified due to the repeatability observed in this sample analysis.

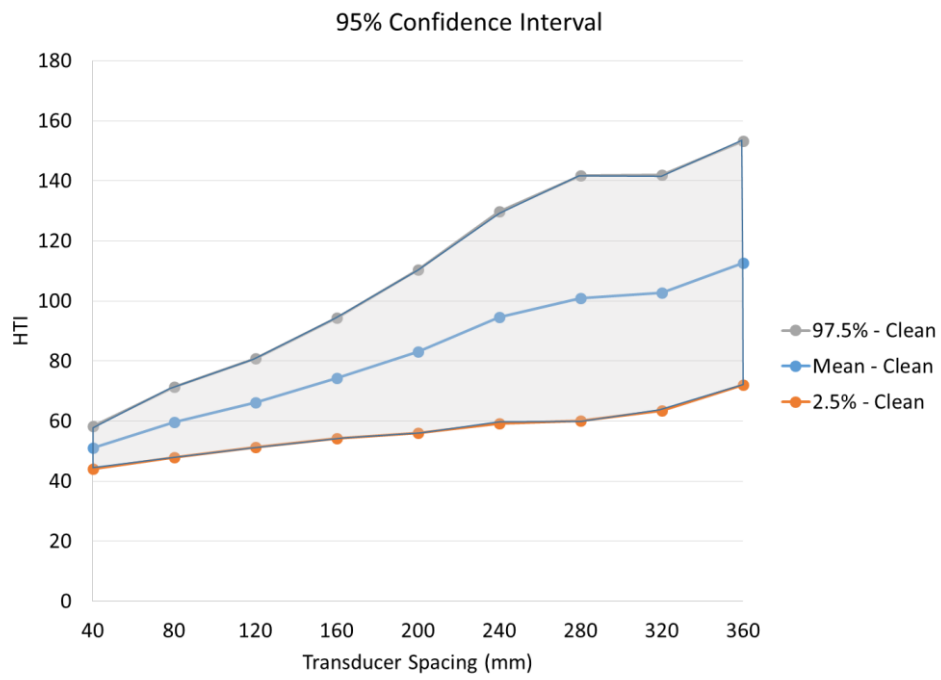


Figure 36. 95% confidence interval for sound concrete.

CHAPTER 3 - EARTHQUAKE DAMAGE

[This chapter is adapted from the following publication: Freeseaman, K., Khazanovich, L., Hoegh, K., Nojavan, A., Schultz, A. E., Chao, S. (2016). Nondestructive monitoring of subsurface damage progression in concrete columns damaged by earthquake loading. *Engineering Structures*, Volume 114, 1 May 2016, 148-157.]

The assessment of the structural integrity of infrastructure after extreme events is an important application of nondestructive technology. Advancements in elastic wave-based methods in recent years have allowed for productive and accurate quantitative analysis which was previously lacking. In this study, ultrasonic array measurements coupled with a modified signature analysis method were implemented for damage detection purposes. Full-scale testing of a reinforced concrete column subjected to simulated earthquake loading was tested using ultrasound nondestructive testing at various stages of loading. A signature analysis technique was adapted to create improved reconstructions and was coupled with a quantitative analysis incorporating Pearson's correlation coefficient. The results demonstrated the ability to detect internal damages and defects prior to appearance on the surface using one-sided access, showing promise for health monitoring applications.

3.1 INTRODUCTION

The scale of damage caused by earthquakes has been well documented and portrayed in the media in recent history. While earthquakes can cause severe damage to buildings, there are also cases where there may be no visible damage but the structure has been weakened as a result of the earthquake. Identifying both visible and nonvisible signs of earthquake damage is extremely important in the aftermath of a quake in order to categorize the condition and serviceability of remaining infrastructure. This scenario creates the need for nondestructive evaluation in order to assess the safety and remaining structural capacity. Specifically, reinforced concrete (RC) systems create added complexity due to their heterogeneous nature.

Extensive research has been done in the past regarding the response of RC structures to earthquake loading (e.g. Park and Ang 1985, Takeda et al. 1970, Bracci et al. 1997, and Ghee et al. 1989), which shows that damage in concrete structures may occur even under small drifts. Effective repair methods for damaged RC structural members have been developed, as verified by recent RC bridge columns tested using ground motion similar to that of the 1994 Northridge earthquake (Vosooghi and Saiidi 2013). However, for proper implementation of repair techniques, it is critical for damage to first be accurately identified, preferably by a nondestructive method.

Often, structural evaluation can only be conducted using nondestructive techniques that require access to only one side of the structure. Donnelly (2012) outlined the accuracy of many nondestructive techniques via the analysis of bridge decks, of which infrared thermography (IT) and impact echo (IE) proved to be the most successful. IT is able to identify less than half of the delaminations present and is highly affected by the depth of the delamination. IE is a common nondestructive testing method that involves generation of compression, shear, and Rayleigh waves using a mechanical impact at the surface. The waves reflected from internal changes in acoustic impedance or external boundaries are recorded on the surface, where the impact was generated to give information about the structure using signal interpretation techniques normally based on spectral analysis. IE has been shown to be effective in detecting layer interfaces for applications such as thickness determination and inclusion detection. However, testing with this method can be time-intensive and only allows

for one signal pair to be sent and received per scan. This lack of signal redundancy associated with a single impact signal causes difficulties when complex geometries are present due to the requirements of the spectral analysis method (Carino 2001). In addition, IE is able to detect top and bottom delaminations, but is not able to detect all cases of damage and in some instances results in false positives. When applied to concrete slabs, IE also proves to be sensitive to the overall dimension and thickness of the slab (Azari et al. 2014).

Shear wave based ultrasound methods have also been tested for crack detection in uniform concrete elements (Godinho et al. 2013). This research also identified the effect of rebar, aggregates, or damaged concrete as a complicating factor that needs to be addressed. Shubert and Kohler also found that the presence of aggregate and air voids creates scattering and attenuation of ultrasound signals (Schubert and Koehler 2001). Additionally, one-sided nondestructive ultrasound techniques have had difficulty in detecting damage behind dense reinforcement in concrete structures (Choi and Popovics 2015).

These methods are able to detect some cases of damage, but the limitations of their applicability highlight the need for a more quantitative nondestructive testing method, especially for thick reinforced concrete elements with one-sided access. To this end, evaluation techniques and hardware such as air coupled impact echo have multiple measurement pairs and allow for more productive measurement acquisition (Popovics et al. 2012). Highly productive and repeatable measurements are needed to ensure measurement accuracy. To attain this reliability, dry point contact transducers have also been utilized. Dry point contact transducers allow for diagnostics up to 36 in. (914 mm) deep. This device uses low frequency (~50 kHz) stress waves to assess various types of structural systems, including reinforced concrete members (Choi and Popovics 2015).

While this high productivity allows for more reliable measurements, the analysis methods involved often require qualitative interpretation. To provide quantitative interpretation, Impact Echo Signature Analysis (IESA) has been proposed. IESA compares one-dimensional (1D) impact-echo signals with a reference signal in either the time or frequency domain. For time domain analysis, Pearson's correlation equation has been used for comparison of 1D impact-echo signals and is shown in Equation 16 (Schubert and Koehler 2008):

$$C_{XY}^j = \frac{Cov[X, Y^j]}{\sqrt{Var[X]Var[Y^j]}} = \frac{\sum_{i=1}^N (x_i - x_{mean})(y_i^j - y_{mean}^j)}{\sum_{i=1}^N (x_i - x_{mean})^2 \sum_{i=1}^N (y_i^j - y_{mean}^j)^2} \quad (16)$$

Where j is the j-th signal, i is the i-th value within a signal, X and Y_j are the intensity amplitude vectors of the reference and j-th IE scans, respectively; Cov and Var stand for the covariance and variance; x_i is the i-th intensity value within the reference signal and y_i is the i-th intensity value within the current signal, respectively; x_{mean} and y_{mean}^j are the mean intensity of the reference signal and current signal, respectively; N is the number of intensity values in each signal being compared; and C_{XY}^j is Pearson's correlation coefficient, which measures the strength of the linear dependence between IE intensity measurements X and Y_j. Thus, no correlation would result in a C_{XY}^j value of 0, while a linear relationship between signals would have a C_{XY}^j value of 1.0. This quantification of similarity via referencing a signal representative of a "damage-free" position allows for qualitative analysis. The implementation of array technology further improves the nondestructive testing previously outlined by incorporating redundancy and measurement accuracy (Schubert et al. 2003).

The IESA method was generalized for two-dimensional reconstructions to allow for use with ultrasonic linear array technology. The resulting two-dimensional ultrasound

tomography signature analysis (2D-UTSA) method has been applied for identification of plain concrete degradation under the surface (Hoegh et al. 2012).

This paper presents a modification of the 2D-UTSA method in order to monitor damage progression of a heavily reinforced concrete member and applied for evaluation of full-scale reinforced concrete moment frame columns that were tested by extreme earthquake loading protocols. These tests are part of a research project sponsored by George E. Brown, Jr. Network for Earthquake Engineering Simulation (NEES) of the National Science Foundation (NSF). Details of this experimental investigation have been reported by Nojavan et al. (2015).

Preliminary findings on the nondestructive evaluation of a reinforced concrete column are presented. In collaboration with the University of Texas at Arlington, columns were tested at the University of Minnesota's Multi-Axial Subassemblage Testing (MAST) Laboratory under simulated earthquake loading. This provided an opportunity to gain insight on the internal behavior of the system before external damage was present through nondestructive evaluation.

3.2 EXPERIMENTAL INVESTIGATION

Full-scale reinforced concrete (RC) columns were constructed and tested under distinct earthquake loading protocols. These specimens were cast at the University of Texas at Arlington and tested at the Multi-Axial Sub-assemblage Testing (MAST) lab at the University of Minnesota. The columns are representative of a portion of a column bent in double-curvature at the ground floor of a 20-story modern high-rise moment frame building. The specimens had a clear height of 106 in. (2693 mm) between the footing (bottom) and the loading (top) blocks, and were designed in accordance with Chapter 21 of ACI 318-11 (ACI 2011). A Perimeter-Frame (PF) column was utilized for the nondestructive ultrasonic array testing described in this paper and had (16) #9 longitudinal bars with a cross-sectional dimension of 36x28 in. (914x711 mm). The column represents a ground level column of a 20-story perimeter moment frame used in modern RC buildings with interior post-tensioned flat slab system. Longitudinal bars were tied with #5 hoops and ties placed at 5 in. (127 mm) spacing. Figure 37 shows the reinforcement details and the dimensions of the columns.

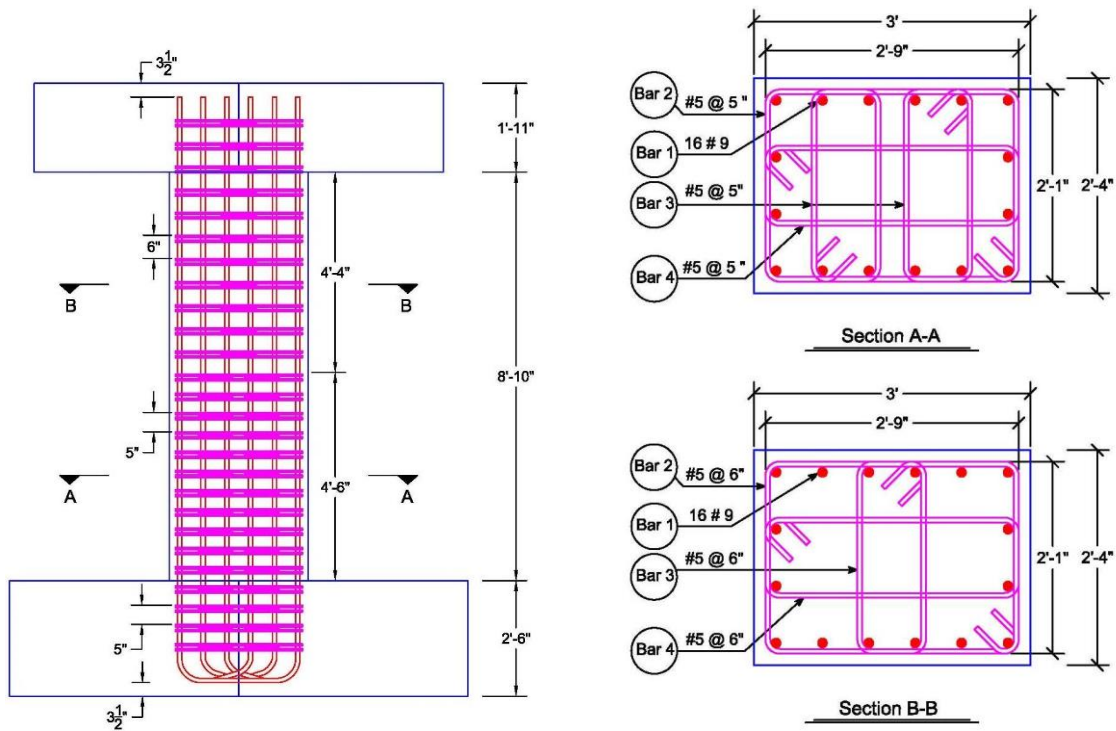


Figure 37. Column specimen assembly and detailing.

3.2.1 Instrumentation and Loading

The specimens were instrumented to measure deflection, rotation, and strains. Linear variable differential transformers (LVDTs) were installed vertically on opposite faces of the specimen in order to measure curvature along the height of the column. Horizontal LVDTs were also used to measure horizontal deflections. String potentiometers were installed to measure transverse displacement and shear deformations. In addition, strain gages were used to measure longitudinal and transverse steel and concrete core strains at locations along the columns. The specimen was placed on top of a three-piece spacer block and connected to the MAST strong floor and the loading crosshead (Figure 38). The columns were then loaded to simulate earthquake activity via a drift history representative of multiple cycles of reversed motion with increasing amplitude. Figure 39 shows the near-collapse loading protocol in terms of the column drift ratios, while Figure 40 shows the lateral load vs. drift ratio hysteresis loops where drift ratio is defined as the lateral displacement at the inflection point of the column (96 in. (2438mm) above the column base) divided by the distance from the column base to the inflection point (96 in., 2438 mm). Testing was truncated once the strength of the column was reduced to 20% of its maximum capacity, as determined by the reduction in peak lateral load resisted by the system in a given cycle. Further details regarding experimental program can be found elsewhere (Nojava et al. 2015, Nojavan et al. 2014).

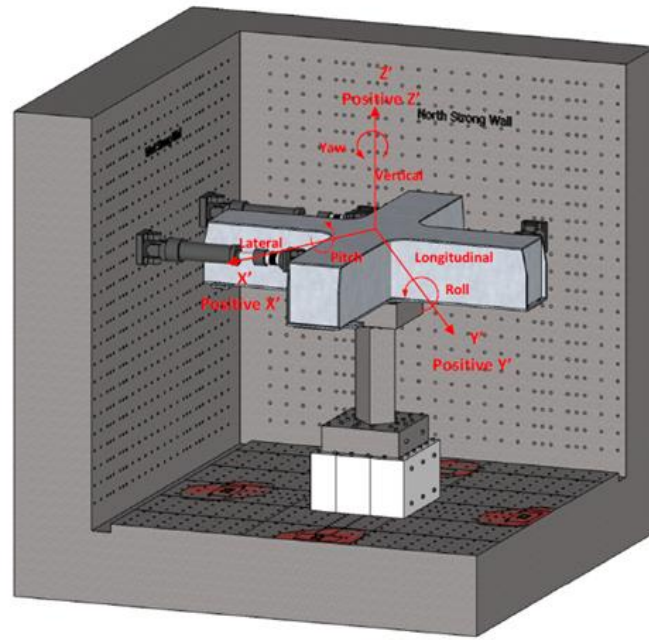


Figure 38. Assembly of the specimen under the loading crosshead at the MAST Lab (Nojavan et al. 2015).

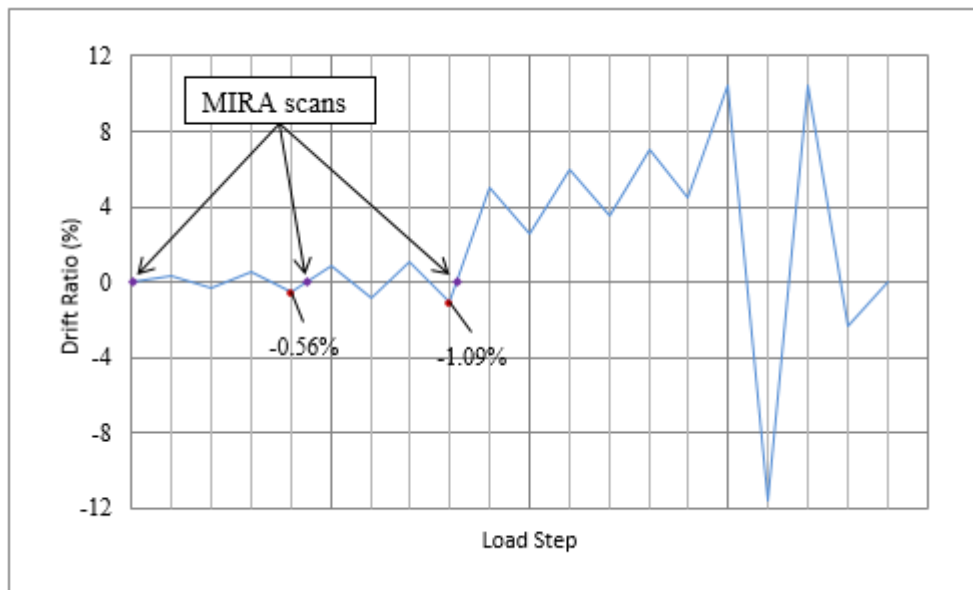


Figure 39. Near-collapse loading protocol in terms of column drift ratios (MIRA scans were conducted at the points shown after returning from the labelled peak drift locations).

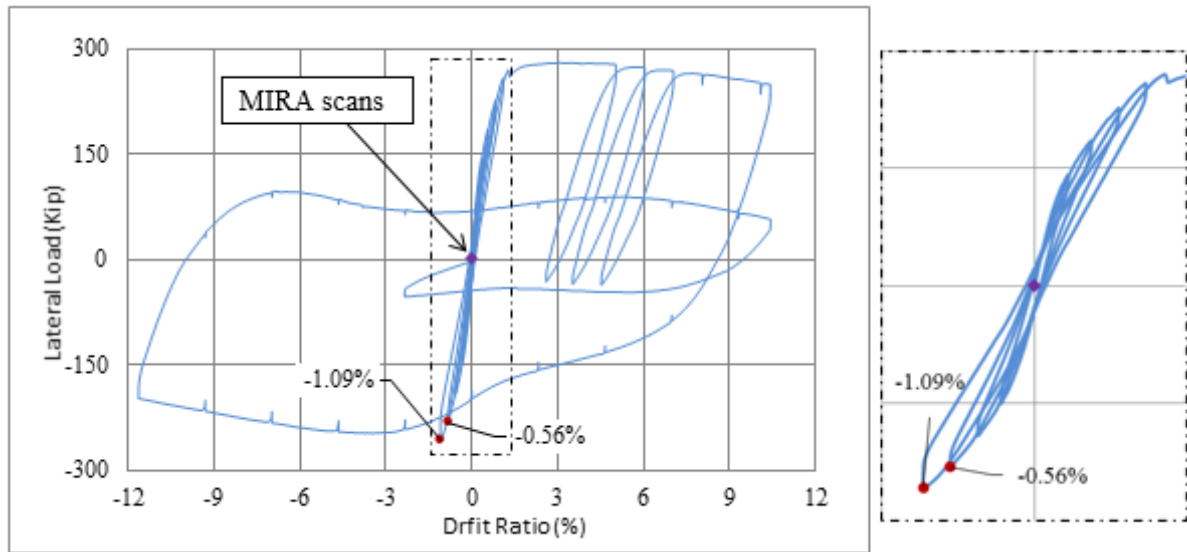


Figure 40. (left) Lateral load vs. drift ratio response and (right) enlarged cycles of interest (MIRA scans were conducted at the points shown after returning from the labelled peak drift locations).

3.2.2 Nondestructive Testing

While the specimen was being tested for earthquake loading, scans were obtained incrementally using the ultrasonic tomography device MIRA (Shevaldykin et al. 2002). MIRA incorporates 10 channels, with each channel composed of four transmitting and receiving transducers, as seen in Figure 41. This linear array allows for 45 time-of-flight measurements in less than three seconds. The change in acoustic impedance causes reflection of the waves traveling from one medium to another (i.e. from concrete to rebar or concrete to air). The recorded wave reflections at the surface from the transducers are processed using the Synthetic Aperture Focusing Technique (SAFT, discussed later) to yield a visual representation of the cross section that was measured. The results can then be analyzed to help gain insight into the inner structure (Hoegh et al. 2012, Hoegh et al. 2013, Hoegh and Khazanovich 2012). For example, pavement applications have shown the device to be capable of detecting inclusions and internal flaws (Hoegh et al. 2012, Hoegh et al. 2013, Hoegh and Khazanovich 2012, Hoegh et al. 2011).

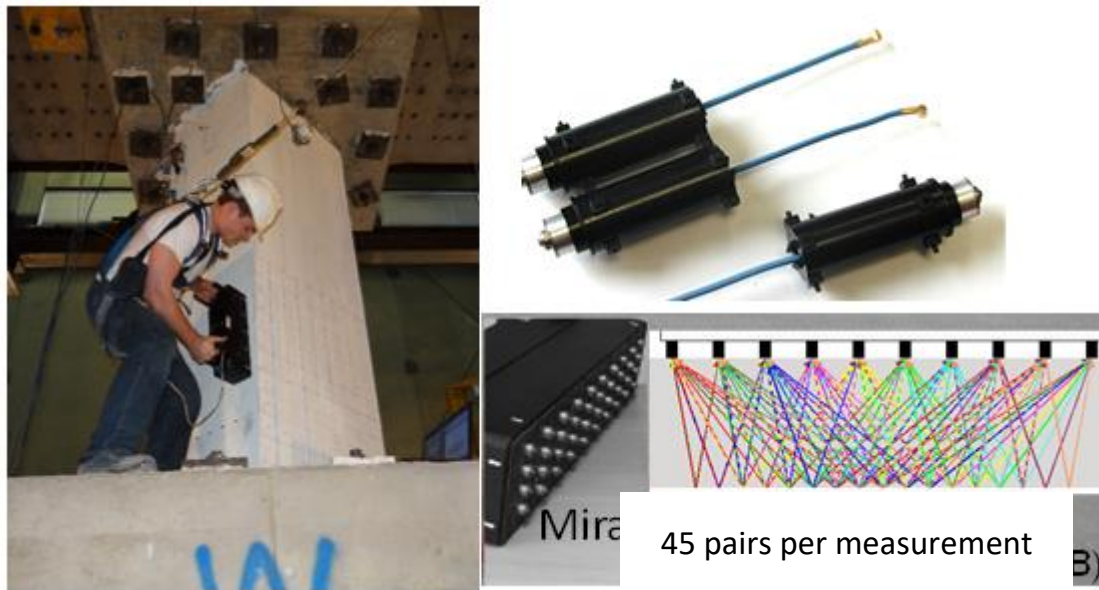


Figure 41. MIRA ultrasonic linear array device

In this study, ultrasonic array measurements were taken at three discrete times during testing in which the column was brought back to its neutral position (zero drift) for safety reasons. Measurements were taken prior to any loading, once zero drift was attained after loading resulting in 0.5% drift level, and after achieving 1% drift level. These drift levels were selected based upon the observed damage progression of previous rounds of testing. The loading corresponding to these locations was detailed in Figure 39 and Figure 40, with dots designating when testing took place and the point of maximum drift achieved prior to measurement acquisition. A total of 60 ultrasound readings were taken, organized in sets of 6 progressing from left to right with approximately 4 in. (102 mm) between sequential readings. This spacing resulted in 12 in. (305 mm) of overlap from scan to scan due to the 16 in. (406 mm) width of the testing device. Figure 42 shows the state of the column when the 2nd set of measurements was taken, while Figure 43 shows the condition of the column when the 3rd set of measurements was taken. As can be seen in the first set of images, there were no external signs of damage when the 2nd set of measurements was taken, but the 3rd set of measurements were taken when external damage was present.

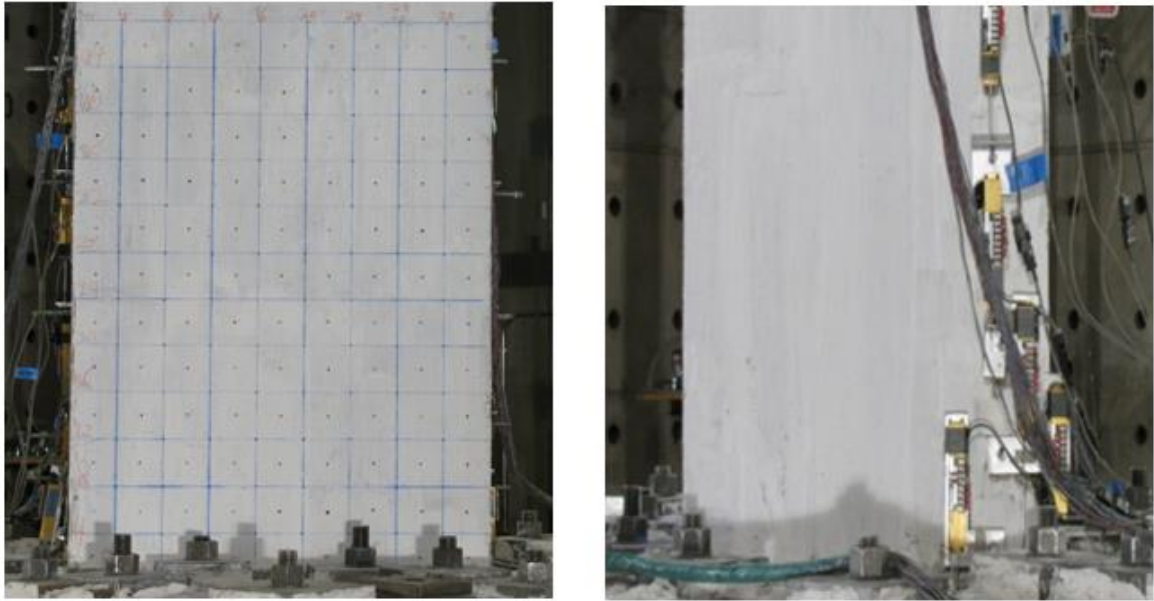


Figure 42. Column condition for 2nd set of MIRA measurements (after 0.5% drift ratio was attained).



Figure 43. Column condition for 3rd set of MIRA measurements (after 1% drift ratio was attained).

3.3 ANALYTICAL INVESTIGATION

A signature quantitative analysis method was utilized to collect data at different damage levels. SAFT is an ultrasonic imaging technique that allows for back-propagating of a set of impulse time-histories to achieve reconstructions with improved resolution. In addition, this technique allows for improvements in signal to noise by reducing the backscattering effects of the concrete material through the natural deconvolution characteristics of the algorithm (Langenberg et al. 2012). The following equation allows for the formulation of reconstructed images at a point via integration.

$$\hat{\delta}(x, z) = \int_{x'_{min}}^{x'_{max}} \alpha(x', x, z) s \left(x', \frac{z}{c} \sqrt{z^2 + (x - x')^2} \right) dx' \quad (17)$$

where $\alpha(x', x, z)$ is the apodization factor that is typically a function of the distance traveled, divergence of the wave propagation, and incident angle of reflecting interface at each reflection point location with respect to the emitted/received signal (Lingvall et al. 2003), x'_{min} and x'_{max} are the interval in which the signals are measured, c is the sound velocity, x and z are the horizontal and vertical positions in the region of interest (ROI), x' is the transducer location, and s is the received impulse.

3.3.1 Qualitative Analysis

SAFT reconstructions at pre-loading, after 0.5% drift ratio, and after 1% drift ratio are shown in Figure 44 and Figure 45. Figure 44 shows an example of readings that indicate little change in relative reflectivity, while Figure 45 shows an example location that exhibits a large change in relative reflectivity. Lighter (white) areas correspond to areas of high reflectivity, indicating the presence of changes in acoustic impedance. For example, presence of reinforcement, flaws, or layer boundaries cause an increase in reflectivity. In this case, the lighter regions were roughly 2 in. (51 mm) deep and are representative of the #5 transverse bars. These figures show only the first 12 in. (305 mm) due to the limited accuracy at large depths of individual scans. In order to address this and other limitations, as well as utilize the overlapping scans that were captured during data collection, panoramic images were of interest.

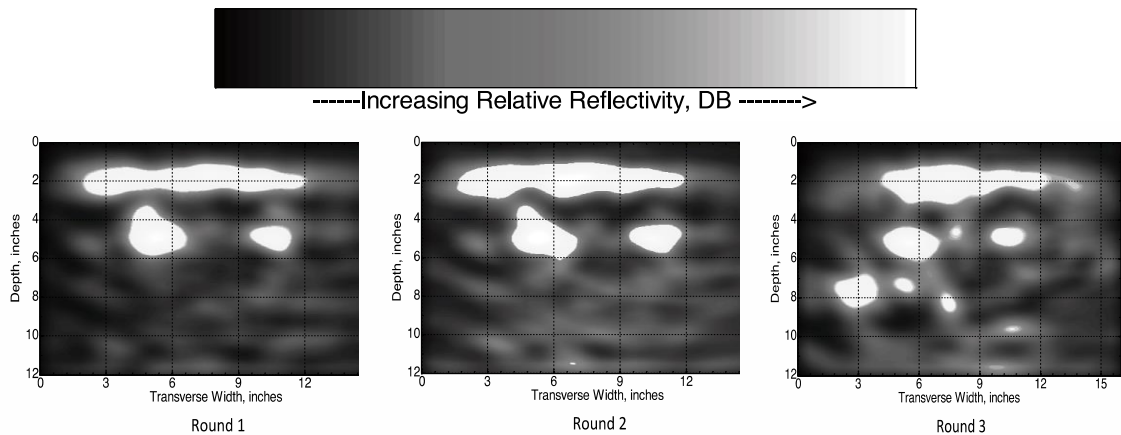


Figure 44. MIRA Reconstructions for 1st round (left) and 2nd round (middle), and 3rd round (right) for a location with relatively low level of damage with loading.

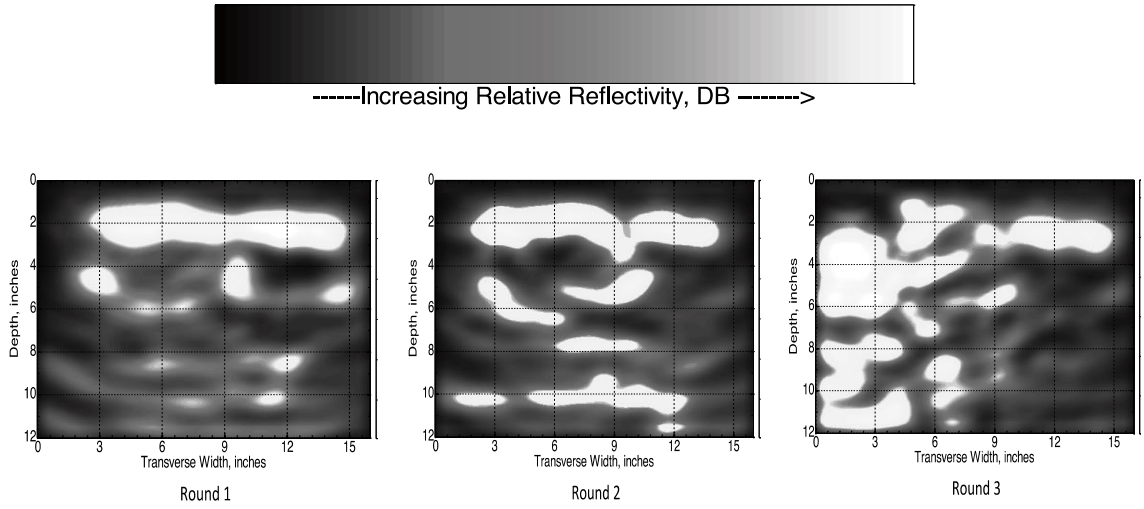


Figure 45. MIRA Reconstructions for 1st round (left) and 2nd round (middle), and 3rd round (right) for a location with relatively high level of damage with loading.

Because there is limited coverage at the edges of individual scans due to the presence of fewer overlapping transducers, panoramic reconstructions allow for a more accurate and redundant form of analysis. This also mitigates the limited aperture effect, allowing for quantitative comparisons of relative reflectivity within a wider region of SAFT panoramic reconstructions (Hoegh and Khazanovich 2015). Because the region of interest (the entire cross-section of the column) is larger than the individual SAFT reconstructions, multiple sets of reconstructions can be combined to add redundancy and create a large panoramic cross-section with high resolution. To achieve this, individual scans are combined in a string formation in which each SAFT scan overlaps with the next to create an encompassing region of interest, or ROI_{PAN} . For those regions in which the SAFT scans overlap one another, the larger value is selected for the panoramic image.

To formulate these panoramic images, each SAFT scan, $\widehat{\mathcal{O}}_I^m$, where m is the index of the current SAFT scan and I denotes that it is an individual scan, is combined in the following manner to form the new ROI_{PAN} . The ROI_{PAN}^m has the same vertical dimension, z , as all of the individual SAFT scans, while the horizontal dimension spans from 0 to x_{PAN}^m . Each individual scan has a horizontal dimension of x_I^m . In this case, ROI_{PAN} has a width of 36 in. (914 mm) and a depth of 30 in. (762 mm), while individual SAFT scans had a width of only 16 in. (406 mm). SAFT scans are merged, with each individual SAFT scan starting a distance D from the global origin (0, 0). The SAFT scans, $\widehat{\mathcal{O}}_{x,z}^m$, are combined according to the following expression for all values of x and z :

$$\widehat{\mathcal{O}}_{PAN}^m(x, z) = \begin{cases} \widehat{\mathcal{O}}_{PAN}^{m-1}(x, z), & \text{if } x < D \\ \max\left(\widehat{\mathcal{O}}_{PAN}^{m-1}(x, z), \widehat{\mathcal{O}}_I^m(x, z)\right), & \text{if } D < x < x_{PAN}^{m-1} \\ \widehat{\mathcal{O}}_I^m(x, z), & \text{if } x > x_I^m \end{cases} \quad (18)$$

For each panoramic reconstruction in this study, six individual SAFT scans were merged, as shown in the schematic in Figure 46. The first SAFT scan covers surface areas A-D, the second scan covers areas B-E, and so on with the sixth SAFT scan covering the areas F-I.

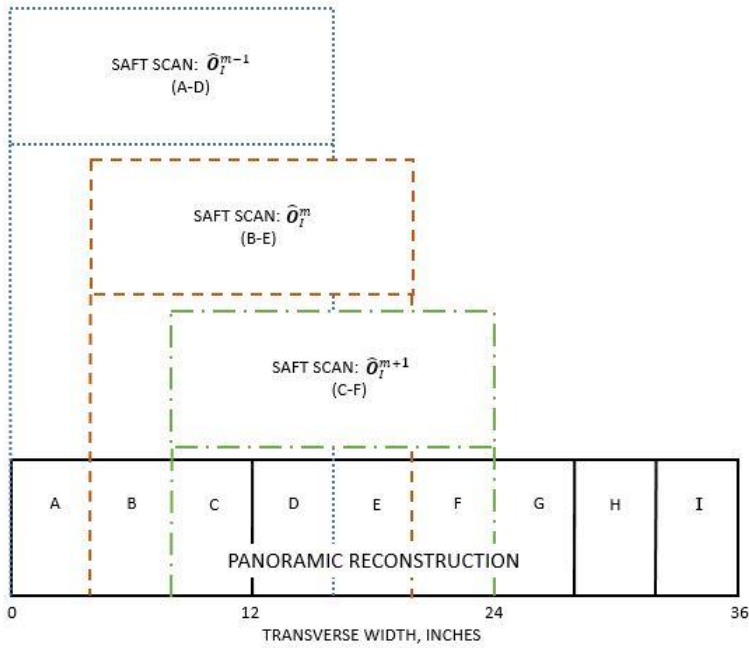


Figure 46. Schematic outlining the merging of 6 individual SAFT scans to create one panoramic reconstruction.

Figure 47 gives an illustrative example cross-section comparing the ultrasound panoramic reconstruction to the designed features along the width of the column at a height of 9 in. (229 mm) from the base. Figure 47(a) shows the example panoramic created using Equation 18 at that location. Figure 47(b) shows the corresponding designed cross-section. It can be observed that increases in reflectivity occur at the shallower reinforcement locations, as well as the depth of the column along the evaluated cross-section. Even though there is significant attenuation of the wavefront at 28 in. of depth, the change in acoustic impedance at the layer boundary from concrete to air is significant enough to show up in the reconstruction. This is only true if there is not significant enough damage to cause additional scattering of the wavefront. Figure 47 shows the location of the #9 reinforcing bars, as well as the presence of

the backwall.

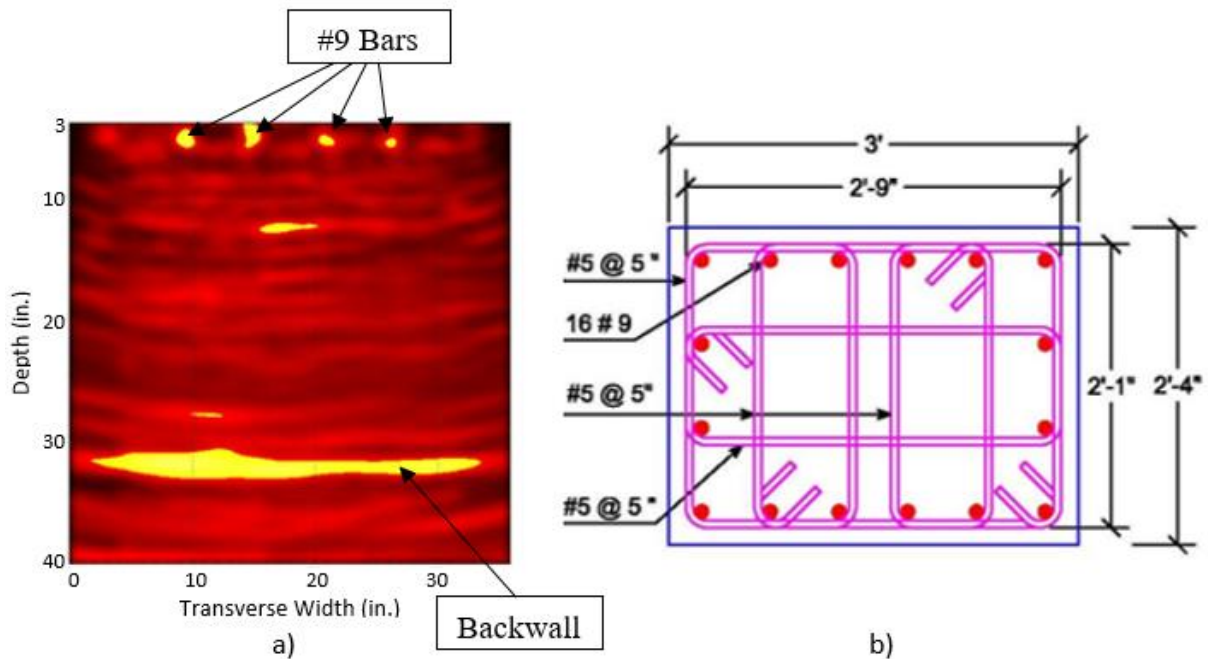


Figure 47. (a) Panoramic reconstructions for 1st measurement showing location of reinforcement and back wall presence, and (b) corresponding design schematic.

A series of panoramic reconstructions can be seen in Figure 48. This figure shows the scans for all three rounds of testing at a location near the base of the column, highlighting the damage progression and subsequent shadowing of the backwall captured by the scans. It can be observed from Figure 47(a) that the backwall reflection is strong for the evaluated width of the reconstruction indicating no significant damage. Scattering, referring to any deviation in wave propagation from that which is expected for a homogenous body, can be used as an indicator of the damage level. The backwall on the left side of the reconstruction is not present after the 2nd round of loading, indicating increased scattering of the wavefront toward the left. The backwall is not present after the 3rd round of testing, indicating significant scattering of the wavefront. The increase in scattering (shadowing of the wavefront) indicates the presence of increased damage at a shallower depth (Schickert et al. 2003). However, since this analysis is qualitative in nature, signature analysis is presented in the following section to quantify the damage caused by loading.

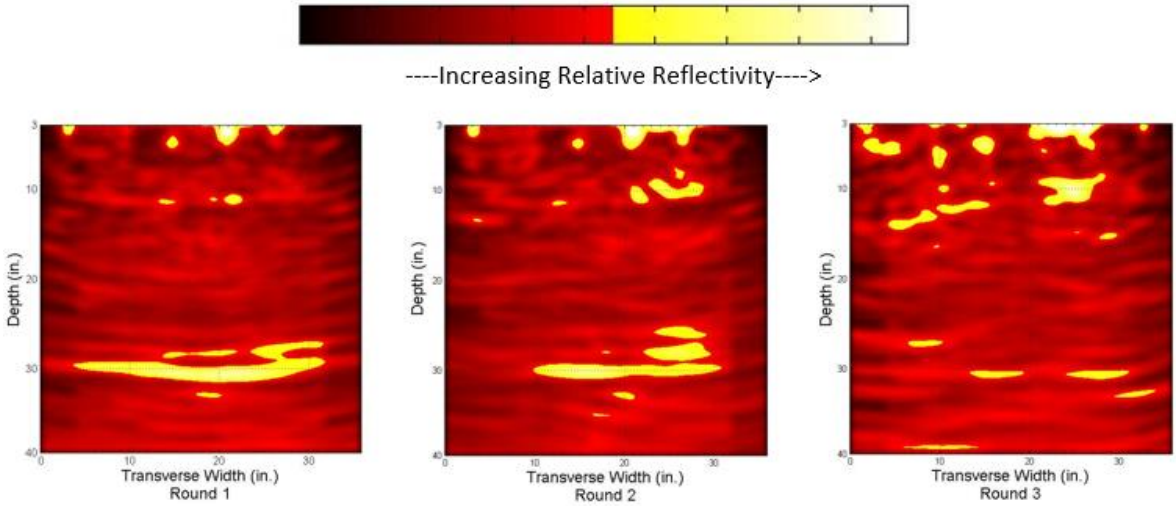


Figure 48. Panoramic reconstructions for 1st measurement (left), 2nd measurement (middle), and 3rd measurement (right) for a location on the bottom of the column.

3.3.2 Quantitative Analysis

While this change in reflectivity can be qualitatively observed via panoramic images, and indicates increased damage of the concrete around the reinforcement as shown in Figure 10, these types of interpretations require significant engineering judgment and time. Because of this, an ultrasonic tomography signature analysis (2D-UTSA) method has been adapted to quantify the level of damage by comparing each scan to the corresponding undamaged condition. It has been shown in previous studies that Pearson's correlation is a good indicator of linear dependence, and thus damage, in comparing IE and ultrasound measurements (Schubert and Koehler 2008, Hoegh and Khazanovich 2012). Pearson's correlation coefficient is adapted for comparison of reconstructed intensity matrices from testing conducted before and after loading as follows using the SAFT variables shown below in Equation 19:

$$C^{IA,m} = \frac{Cov[\widehat{\mathcal{O}}^{IA,ref}, [\widehat{\mathcal{O}}]^{IA,m}]}{\sqrt{Var[\widehat{\mathcal{O}}^{IA,ref}]Var[\widehat{\mathcal{O}}]^{IA,m}}} = \frac{\sum_{i=1}^W \sum_{k=1}^D (\widehat{\mathcal{O}}_{i,k}^{IA,ref} - \widehat{\mathcal{O}}_{mean}^{IA,ref})(\widehat{\mathcal{O}}_{i,k}^{IA,m} - \widehat{\mathcal{O}}_{mean}^{IA,m})}{\sum_{i=1}^W \sum_{k=1}^D (\widehat{\mathcal{O}}_{i,k}^{IA,ref} - \widehat{\mathcal{O}}_{mean}^{IA,ref})^2 \sum_{i=1}^W \sum_{k=1}^D (\widehat{\mathcal{O}}_{i,k}^{IA,m} - \widehat{\mathcal{O}}_{mean}^{IA,m})^2} \quad (19)$$

where $[\widehat{\mathcal{O}}]^{IA,ref}$ and $[\widehat{\mathcal{O}}]^{IA,m}$ are the matrices of reflection intensity for the reference SAFT scan for the preloading condition and SAFT scan taken after loading and damage occurred, respectively; $\widehat{\mathcal{O}}_{i,k}^{IA,ref}$ and $\widehat{\mathcal{O}}_{i,k}^{IA,m}$ are the single intensity values of the reference signal and damaged reconstruction, respectively, with depth increasing with k and the horizontal location of the scan increasing with i ; $\widehat{\mathcal{O}}_{mean}^{IA,ref}$ and $\widehat{\mathcal{O}}_{mean}^{IA,m}$ are the mean intensities of the reference scan and damaged scan, respectively; W and D are the number of width and depth intensity values in the depth and device aperture direction, respectively; and $C^{IA,m}$ is Pearson's correlation coefficient, which measures the strength of the linear dependence between $[\widehat{\mathcal{O}}]^{IA,ref}$ and $[\widehat{\mathcal{O}}]^{IA,m}$.

In this study, the unloaded scan condition was used as the reference scan (i.e. the left image in Figure 47). This quantitative analysis method makes the technique more feasible for routine implementation due to the reduced interpretation time. Thus, flawed concrete locations can be identified due to the similar scan locations of the reference and damaged scan conditions. On the extremes, a $C^{IA,m}$ value of 0 would indicate no correlation and a

$C^{IA,m}$ value of 1.0 would indicate that the two SAFT scans are related linearly. Therefore, a higher $C^{IA,m}$ would indicate that the SAFT scan was taken on sound concrete, and a significant decrease in the correlation coefficient would indicate non-uniform SAFT scans, or damaged concrete, especially if observed in a group of adjacent scans. This type of analysis will be referred to as the 2D-UTSA method. Lower UTSA values indicate an increase in damage as compared to the original condition.

To demonstrate the ability of UTSA values to characterize damage, consider an example analysis using a reconstruction from round 1 experimental data serving as a clean condition, and a scan containing random noise, as shown below in Figure 49.

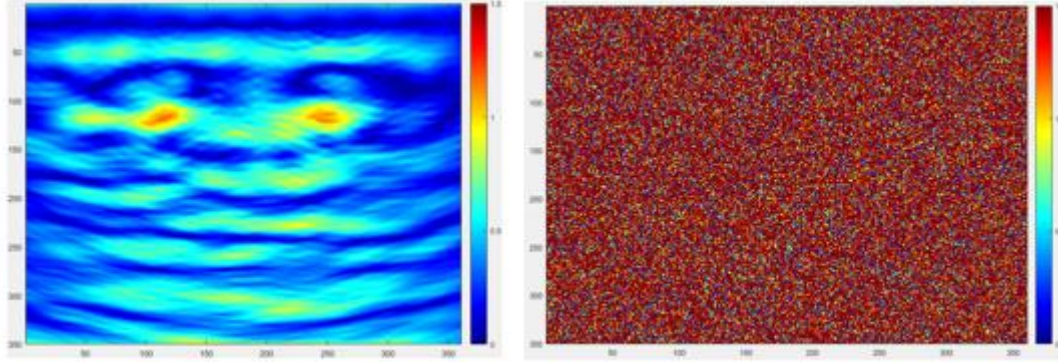


Figure 49. Experimental reconstruction from round 1 of testing (left), and fabricated reconstruction containing noise (right).

Multiple artificial reconstructions can be generated as detailed in Equation 20:

$$[\hat{\mathcal{O}}]_i = [\hat{\mathcal{O}}]^{IA,ref} + \alpha_i [\hat{\mathcal{O}}]^{IA,noise} \quad (20)$$

where $[\hat{\mathcal{O}}]_i$ is the new matrix, $[\hat{\mathcal{O}}]^{IA,ref}$ is the reference matrix of reflection intensity for the clean case, as shown in Figure 13 (left), $[\hat{\mathcal{O}}]^{IA,noise}$ is the matrix of reflection intensity containing random noise, as shown in Figure 13 (right), α is the coefficient of noise intensity for all i cases considered for analysis. If the coefficient α is small, the reconstruction should be similar to the original reference reconstruction, while an increase in α leads to an increase in noise that is often associated with damage.

A sample analysis was performed in which α values of 0.01, 0.05, 0.1, and 0.25 were used to create artificial reconstructions. Each of these artificial matrices were compared with the reference case (Figure 49, left) and Pearson's correlation coefficients were computed using Equation 19. The effect of these α values on the resulting Pearson's correlation coefficient is shown in Figure 50. It can be observed that for very small α values, the Pearson's correlation coefficient approaches one, while increasing α leads to very low correlation.

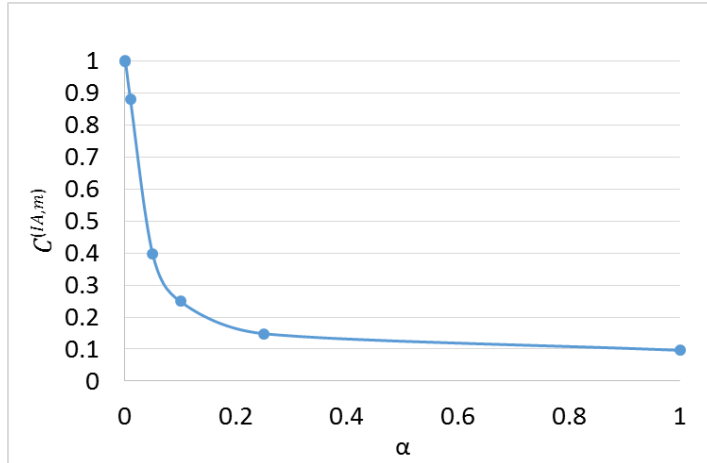


Figure 50. Effect of changes in α on the Pearson's correlation coefficient value.

This analysis can be confirmed by visual comparison of the corresponding reconstructions shown in Figure 51. As can be seen, reconstructions with high Pearson's correlation coefficient values appeared similar to the reference case, whereas reconstructions with low values show significant deviation from the base case. This same principal holds for the analysis of subsequent rounds of experimental data, and the results of this analysis are shown in the following section.

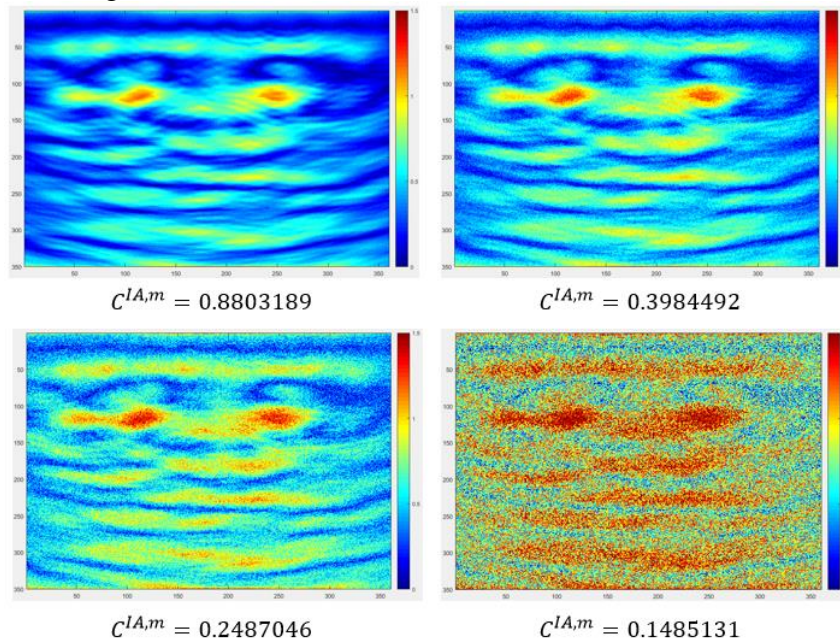


Figure 51. Reconstruction for α of 0.01 (top left), 0.05 (top right), 0.1 (bottom left), and 0.25 (bottom right).

3.4 EXPERIMENTAL RESULTS AND DISCUSSION

The analysis presented in this study is based on analysis of shear horizontal waves (SH waves) where a portion travels along the surface and a portion reflects from within the medium. Since the 50 kHz shear waves correspond to a wavelength of approximately 2 inches (51 mm), the reconstructions of the first two inches below the surface need to account for both wave paths. Below this point, the surface path of the signal can be ignored. Because

damage detection below the surface is of interest in this study, the surface path is not included in this analysis

Figure 52 and Figure 53 show a representation of the 2D-UTSA results comparing the original panoramic scans to those after 0.5% and 1% drift ratios, respectively. For each tested location, the $C^{IA,m}$ value was plotted on a scale with 0 indicated by dark shading and 1 indicated by white, with intermediate values shown in lighter shading. In this case, darker locations (lower $C^{IA,m}$ values) indicate an increase in subsurface damage from the original condition, while light locations (higher $C^{IA,m}$ values) indicate little change from the original condition. As can be seen from these figures, ultrasonic array testing can identify levels of degradation before there are external signs of failure. When analyzing these two figures, a general trend of higher damage intensity (dark coloring) can be seen in the left and lower left portion of the images. This area corresponds to the portion of the column that exhibited external damage first, as seen in Figure 43.

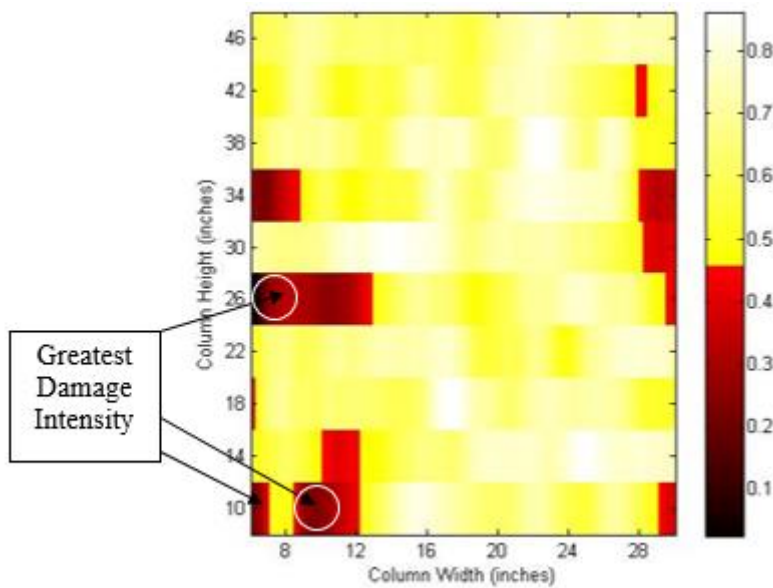


Figure 52. MIRA gradient results after 0.5% drift ratio.

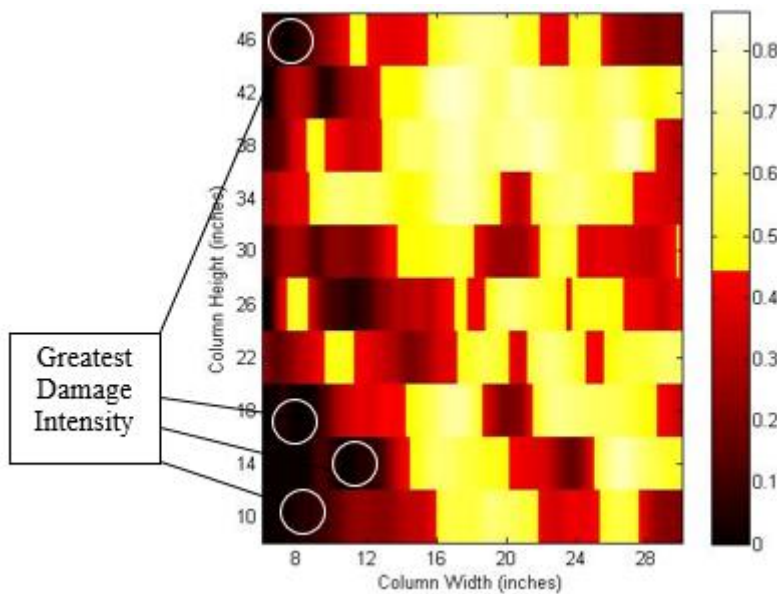


Figure 53. MIRA gradient results after 1% drift ratio.

3.5 CONCLUSIONS

Advancements in elastic wave methods have allowed for productive and accurate quantitative analysis which was previously lacking. In this study, ultrasonic array measurements coupled with a modified signature analysis method were implemented. The full-scale testing of a heavily reinforced concrete column subjected to simulated earthquake loading demonstrated the ability to detect internal damages and defects prior to appearance on the surface using one-sided access. This meets an important infrastructure health monitoring goal of identifying damage development beneath the surface nondestructively before visual failure occurs. Shadowing analysis of the ultrasonic imaging reconstructions indicated damage below the surface caused by scattering of the ultrasonic wavefronts. The shadowing and other indicators of damage were quantified through the use of correlation coefficient signature analysis. The results of signature analysis showed increased subsurface damage in the areas that failed first after further loading. This demonstrates the ability of ultrasonic array testing and signature analysis to aid in detecting not only damage below the surface, but also to indicate which area of the column will show signs of failure first. It should be noted that the current analysis presented in this chapter requires measurements of the undamaged state of the specimen to evaluate the relative damage progression. As such, the techniques can be employed in actual cases if monitoring of structural health begins before damage has occurred. Further work will be done in the future by the authors, in fusion with alternative nondestructive testing methods, to increase the applicability of the current findings for implementation on structures which have not been analyzed in an undamaged state.

The applicability of ultrasonic methods presented in this paper is promising in the field of health monitoring due to its nondestructive nature and its ability to detect issues that are not visible on the surface at the time of testing. This type of subsurface characterization provides a practical input for improved assessment of the safety and remaining service life of structures since the methods presented in this paper require only one-sided access for data collection and provide quantitative early detection of subsurface conditions.

CHAPTER 4 - FREEZE THAW DAMAGE

[This section is partially adapted from a submission to ASCE Journal of Infrastructure Systems, which is currently under review]

Freeze thaw damage in concrete structures is a serious issue for infrastructure in cold regions. Accurate detection of this type of damage at early stages allows for the selection of optimum strategies for preservation and rehabilitation activities. This section explores the feasibility of utilizing ultrasonic shear wave technology for quantification of damage in concrete slabs, which could be successfully applied for the detection of freeze thaw damage. Four slabs with varying levels of freeze thaw damage were tested and two analysis techniques were developed to characterize the damage present. These methods involve the formulation of reconstructions to analyze the subsurface condition, as well as the creation of a numerical index based upon recorded signal characteristics. The results of both analyses showed agreement both with each other and with the visual survey assessments. However, the methods were able to detect damage in portions of the slab where no visual cracks were observed. These techniques showed promise for an accurate nondestructive quantification of the extent of freeze thaw damage, or similar damage manifestations, in concrete structures.

4.1 PREVIOUS METHODS

Freeze thaw damage in concrete structures continues to be a serious issue for infrastructure in regions which experience temperature swings below freezing (Korhonen 2002), creating the most persistent problems associated with deterioration to concrete infrastructure in cold weather climates (Tanesi and Meininger 2006). As such, significant research effort has been devoted to this type of damage (Yang 2004, Farnam et al. 2014, Li et al. 2012, Hazaree et al. 2011, Eiras et al. 2015). Freeze thaw damage is caused by expansive pressures resulting from the freezing of excess water present in the concrete microstructure. As a result, microcracking ensues and eventually creates spalling and distress to the concrete system (Yang et al. 2006).

Resistance of concrete mix to freeze thaw damage can be measured via standardized tests (ASTM C666). This testing involves a beam specimen undergoing multiple rounds of freezing and thawing cycles, combined with periodic measurement of the fundamental transverse frequency and calculation of the Relative Dynamic Modulus of Elasticity, which is used to assess the relative damage condition (i.e. lower Relative Dynamic Modulus of Elasticity values occur after a number of freeze thaw cycles have occurred and indicates the presence of damage). While this procedure is beneficial for comparing freeze thaw resistance of concrete mixes via small laboratory specimens (Wang et al. 2008), this is an infeasible option when considering in-situ conditions and damage detection applications. Additionally, the testing involved in this method does not allow for the location or extent of damage to be determined, and is not effective when considering microcracking which is associated with the early stage of freeze thaw damage.

Accurately detecting damage at its initial stages, and before excessive deterioration occurs, is a goal which has yet to be achieved by nondestructive testing techniques. Many nondestructive testing technologies have been employed for general cracking detection purposes, though freeze thaw damage is of particular interest to this paper. Wave-based nondestructive evaluation techniques have been employed in the past for the detection of microcracking in cement paste. For instance, using diffuse ultrasound, quantitative measures of dissipation and diffusion coefficients can be found based upon the frequency and microstructure of cement-based materials (Becker et al. 2003). While the results showed

promise for gaining insight as to the propagation of ultrasonic waves in cement-based materials, limitations were present due to sensitivity to diffusivity parameter selections.

Seismic tomography has also been utilized to detect cracking. This method differentiates zones based upon variation in the velocity of compression or P-waves. The seismic tomography analysis was successful in locating a major visible tensile crack in the structure. While this technology showed promise for the detection of damage below the surface, the device employed was only successful in detecting major cracks and thus not ideal for microcrack detection (Rivard et al. 2010).

Nonlinear acoustics, however, were seen to detect and track the formation of microcracks at a promising sensitivity level (Boukari et al. 2015). The ultrasonic approach enabled the type of damage to be determined based upon granular swelling assessment in order to designate ASR damage. While the results showed promise, there are limitations to the approaches used including limited applicability for certain ranges of ASR development and difficulty in detecting the reaction at its early stages. Additionally, the nonlinear parameter is extremely sensitive to microcracking. While this is a valuable asset for damage detection, the nonlinear parameter is not only sensitive to the number of cracks but also the features of the crack and the level of heterogeneity of the sample. This highlights the need for a method which has high measurement efficiency, accuracy, and decreased subjectivity for concrete damage detection applications.

4.1.1 Ultrasonic Shear Velocity Array Device

In this study, shear waves were utilized for nondestructive evaluation in order to address the limitations discussed above. The utilization of shear waves allows for an analysis which is independent of moisture conditions. The ultrasonic shear velocity array device used for this research employs dry point contact (DPC) transducers capable of deep diagnostics (Shevaldykin et al. 2002), as described in depth previously.

The array setup accommodates multiple transducer pairs which allow for heightened measurement confidence, as well as incorporating redundancy (Hoegh and Khazanovich 2012, Hoegh and Khazanovich 2012a, Hoegh et al. 2012b, Hoegh et al. 2011). The measurements acquired by this device were used to develop methods for detecting freeze thaw damage in concrete slabs.

4.2 EXPERIMENTAL INVESTIGATION

The Electric Power Research Institute (EPRI) commissioned the fabrication of four slabs with various levels of freeze thaw damage, with each slab measuring 48 by 36 inches (122 by 91 cm) and 8 inches deep (20 cm). The mix was prepared with a 0.5 w/c ratio with no air entrainment. After fabrication, the four samples were moist cured for 14 days. The control sample was removed from the curing room and maintained at ambient temperature and relative humidity in the laboratory. The remaining samples were placed in an environmental chamber and subjected to cycles of freezing and thawing. The cycles consisted of temperatures in the chamber fluctuating between -20 degrees C and 12 degrees C at a relative humidity of approximately 98%. The duration of each cycle was approximately 45 hrs. A summary of the slabs which were tested is provided here, with corresponding visual survey results shown in Figure 54:

- Slab A: Control slab: no freeze thaw cycles induced, no visible cracking
- Slab B: Partially damaged condition: 72 freeze thaw cycles
- Slab C: Partially damaged condition: 80 freeze thaw cycles
- Slab D: Damaged condition: 114 freeze thaw cycles

Crack widths ranged from hairline cracks to 0.3 mm in width. Figure 55 shows a photo of the condition of slab D, further showing the damage present, as highlighted by chalking.

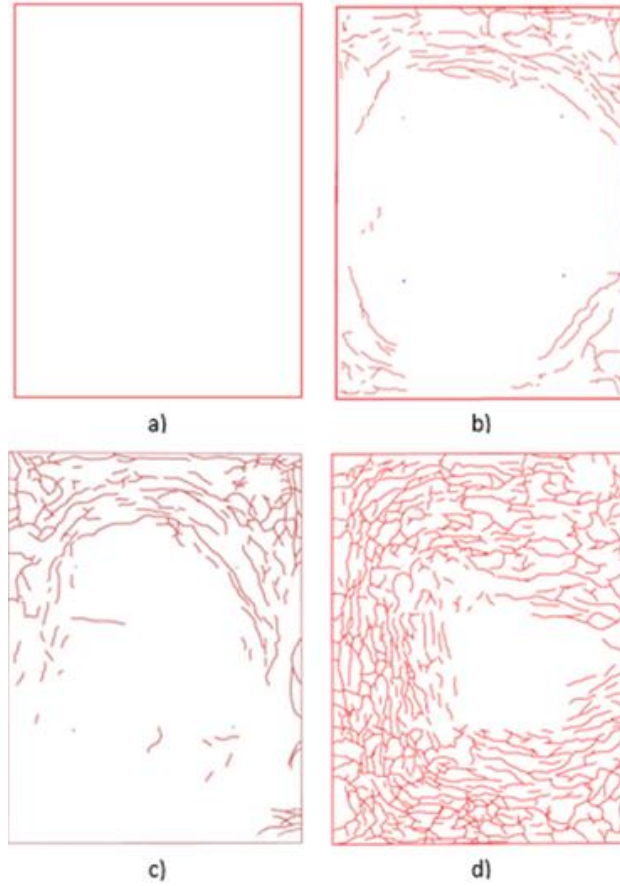


Figure 54. Visual condition surveys of slabs A, B, C and D.

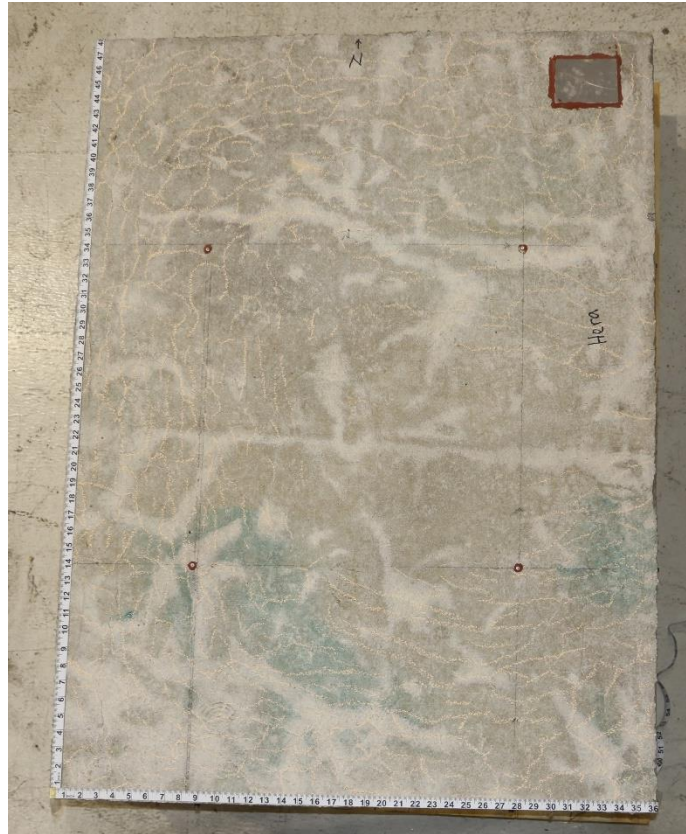


Figure 55. Photograph of condition of slab D.

These four slabs were tested using the ultrasound linear array device MIRA, as shown in Figure 56 (left). This device yields 45 individual time histories per individual scan. A total of 66 scans were obtained for each slab, using a frequency of 50 kHz. Because of the multiple transducer pairs, an expansive data set containing over 10,000 impulse time histories was obtained from this analysis. The 36-cm wide scans were taken in sets of 11 positions with a 5 cm step size (allowing for 35 cm of overlap from the previous scan), moving from north to south of each slab. This set of 11 scans was then taken in 6 different locations with a 12.5 cm step size moving east to west, as shown in Figure 56 (right). As a result, the entire surface of the slab was analyzed and redundancy was incorporated via the overlapping nature of the measurement acquisition process.

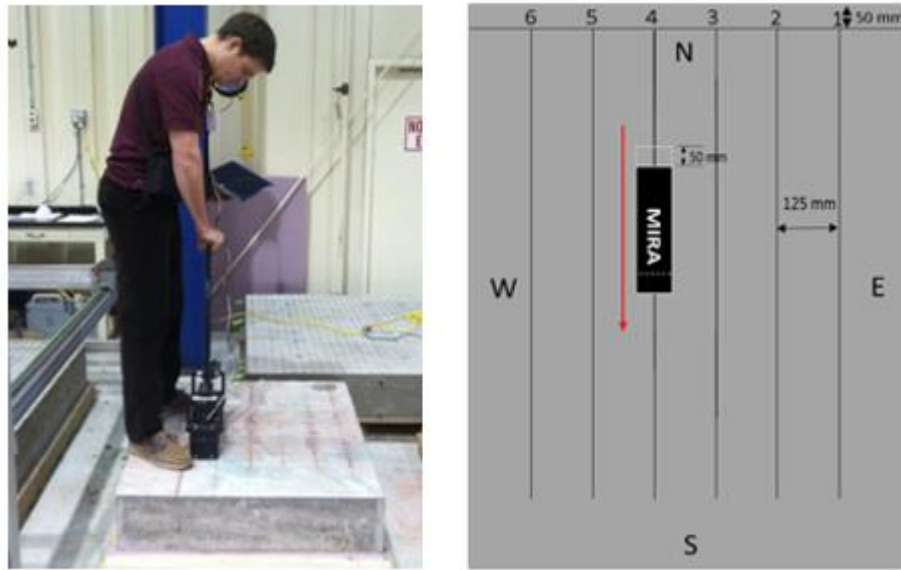


Figure 56. Experimental investigation setup (left), and schematic of measurement locations (right).

4.3 ULTRASOUND EVALUATION TECHNIQUES

The ultrasound signals collected via the experimental investigation were analyzed to determine the condition of the concrete slabs. When the surface of the slab is excited by one of the transducers, the wave propagates through the specimen and a portion of the wave will reflect back when they encounter changes in properties, such as inclusions or layer boundaries. Each individual scan which is obtained results in the acquisition of 45 unique raw signals. The ultrasound signals collected via the experimental investigation were analyzed using two methods: one which focused upon the portion of the signal caused by the wave traveling along the surface, and another which utilized the subsurface reflection portion of the signal. These methods are described in the following sections, and the respective results are compared both with each other and with the visual survey results.

4.3.1 Panoramic Reconstructions

The experimental investigation yielded 6 rows of 11 overlapping MIRA scans per slab. The measurements from each row of scans were used to create panoramic reconstructions, as detailed previously in section 3.2.2.1. Reconstructions provide focused images which show the presence of damage or inclusions, or in undamaged cases, the presence of only the backwall. Combining these individual SAFT reconstructions into one comprehensive panoramic reconstruction allows for analysis of the entire cross section and reduce signal to noise effects caused by the heterogeneous nature of concrete (Langenberg et al. 2012). For each panoramic reconstruction in this study, eleven individual SAFT scans were merged in this manner, as shown in Figure 57, yielding 6 panoramic reconstructions for each slab.

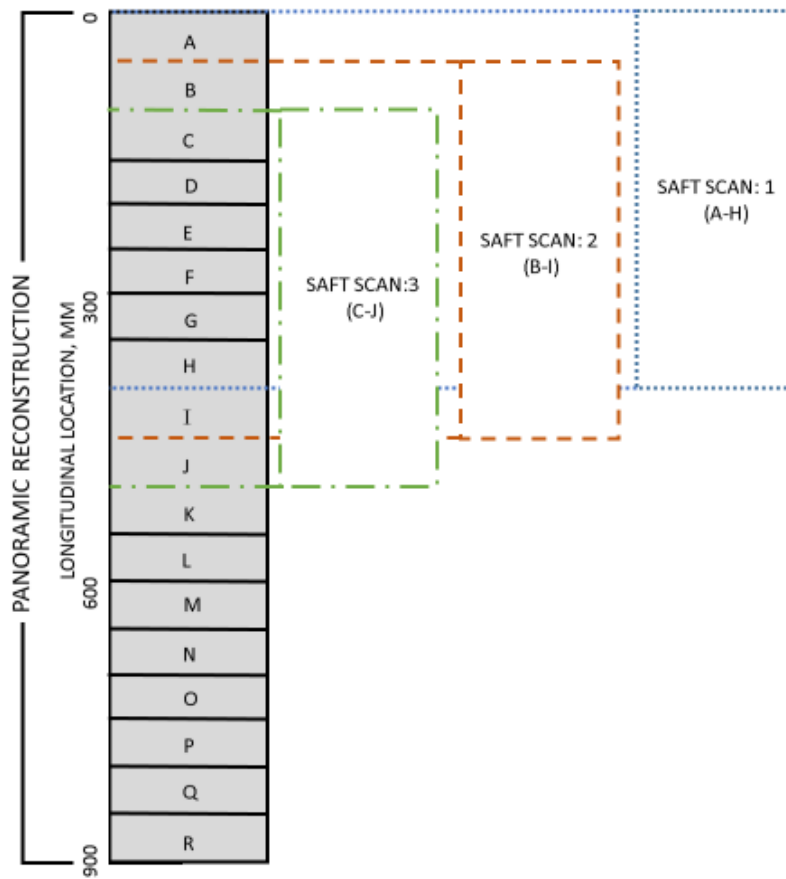


Figure 57. Panoramic reconstruction compilation schematic.

Visual analysis of the panoramics showed differences in the slab condition, most prominently through the presence of the backwall reflection (or the reflection caused by the bottom surface of the slab). This backwall presence is expected due to the sound condition of the concrete and lack of relative reflection prior to this depth. A typical scan on sound concrete (Slab A) is shown below in Figure 58. The backwall presence (at a depth of ~200 mm) is consistently strong, indicating strong relative reflection at the thickness interface as compared to its shallower features when evaluating the SAFT panoramic reconstructions. In other words, there is no damage present.

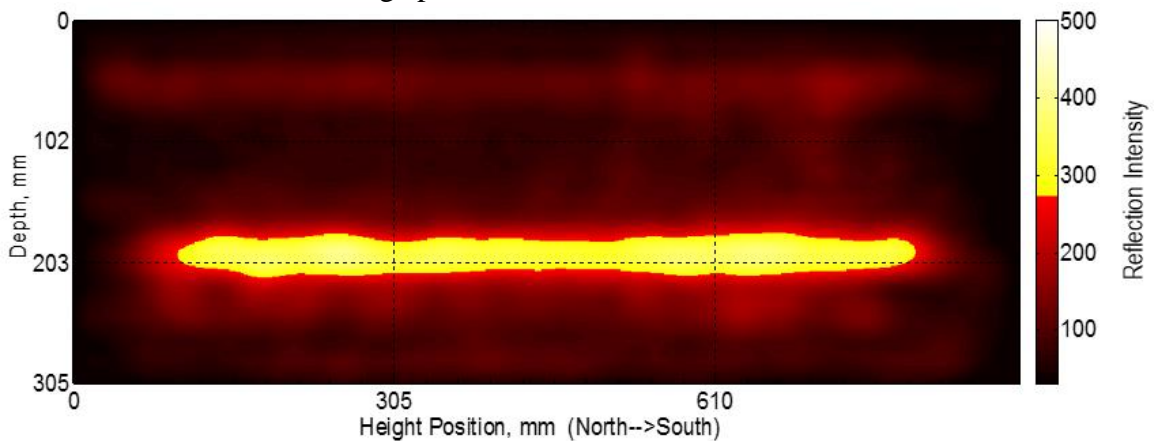


Figure 58. Reconstruction in the middle of slab A indicating sound concrete condition.

With conditions such as those shown in Figure 58 serving as the clean or reference case, categories could be created based upon deviations from this case. The following three categories were observed: 1) sound: reconstructions showing a strong and continuous relative reflectivity at the backwall; 2) partial damage: reconstructions exhibiting a strong backwall reflection at selected locations along with features indicating the presence of damage such as a discontinuity in the backwall reflection; 3) damaged: reconstructions showing no presence of a backwall reflection. Since this initial categorization is very general, it allows for reconstructions that are visually different to fit in the same category. To show the variation of reconstructions within a category and give a background in the indications used to categorize the sections, two examples of the partially damaged and fully damaged conditions are given below along with a description.

Figure 59 and Figure 60 show example reconstructions indicating a slightly damaged concrete condition. Figure 59 was taken on the West side of slab B (5th SAFT-Pan). It shows a mostly sound concrete condition with a continuous and uniform backwall reflection in the middle and right side of the reconstruction. However, the lack of a backwall reflection on the leftmost (North) portion and a shift deeper in the backwall reflection on the left indicates the presence of damage. In this case, attenuation from damage could have shadowed the backwall in the former observation and increased the travel path in the latter. Figure 60 was taken in the middle of slab B (3rd and 4th SAFT-Pans). While both scans showed a shift in the backwall reflection deeper in the center, the scan taken at the 3rd SAFT-Pan (top) also shows direct reflections at a shallower depth, both indicating damaged concrete. However, these scans were still categorized as only slightly damaged, since portions on the left and right showed a strong backwall reflection.

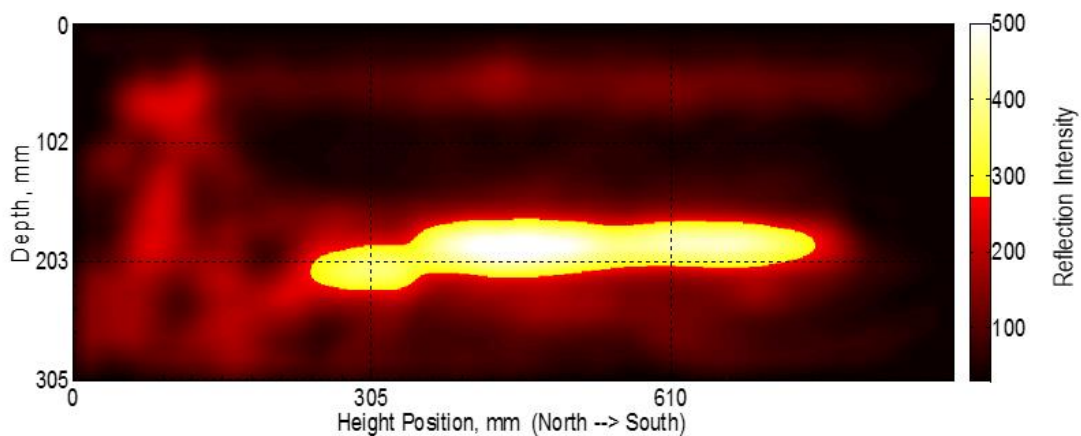


Figure 59. Reconstruction on the west side of slab B, indicating partially damaged concrete.

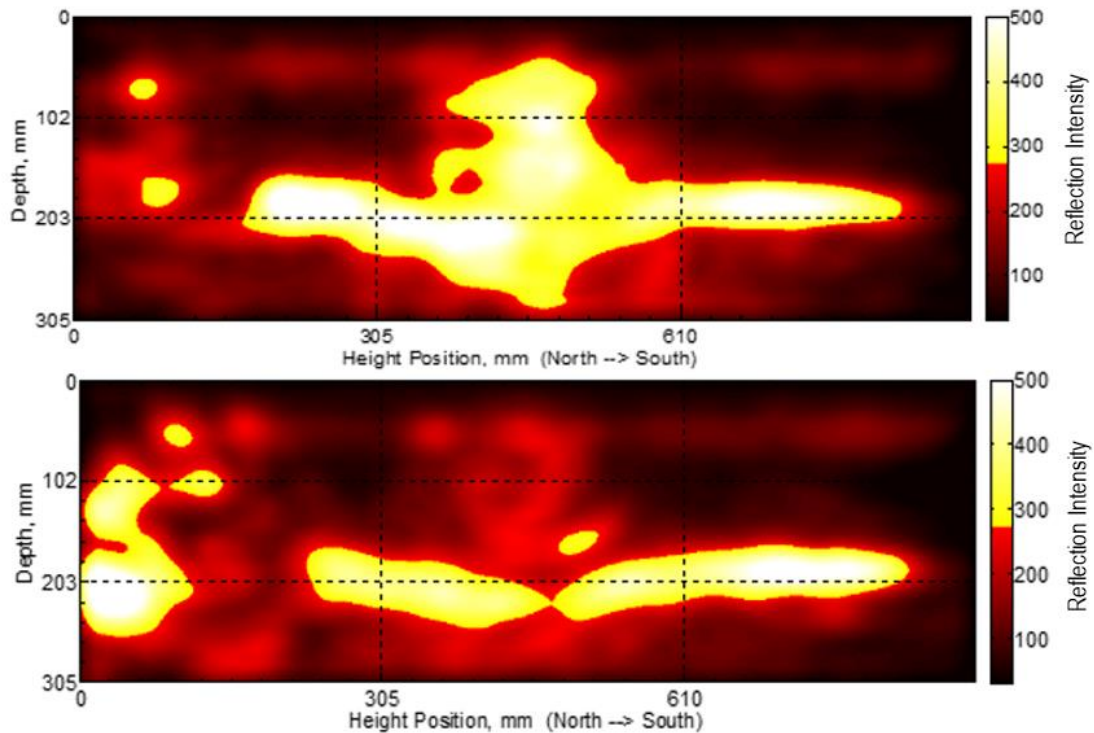


Figure 60. Reconstructions in the middle of slab C indicating partially damaged concrete condition.

Figure 61 and Figure 62 show example reconstructions indicating a damaged concrete condition. Figure 61 shows a scan taken in the middle of slab D (3rd SAFT-Pan). It shows a high reflectivity throughout the reconstruction and absence of a backwall reflection indicating the presence of damage. Figure 62 shows a scan taken on the west side of slab D (5th SAFT-Pan). Both scans showed a lack of a backwall reflection, either due to prohibitive noise at shallow depths or attenuation of the signal prior to arrival at the concrete depth interface, indicating damaged concrete. It is also worth noting that if regions of the upper layer of the concrete are severely damaged, then zones exhibiting significantly lower stiffness are present. This may cause multiple secondary reflections which can appear on the SAFT reconstruction as irregular damage zones, not necessarily corresponding to the boundaries of the damaged area. This illustrates that SAFT techniques which are intuitive for planar defects and inclusions parallel to the surface (Hoegh and Khazanovich 2015) may lead to misinterpretation if applied to specimens with irregular damage present near the surface.

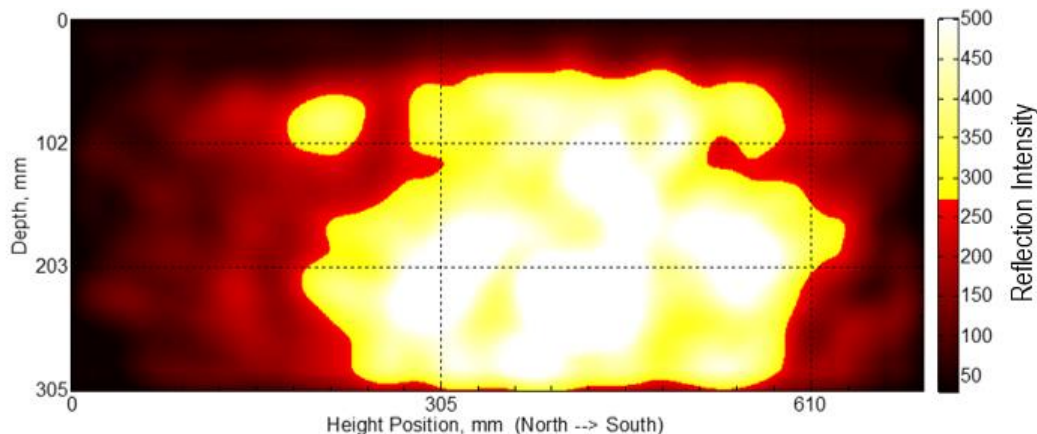


Figure 61. Reconstruction in the middle of slab D indicating damaged concrete condition.

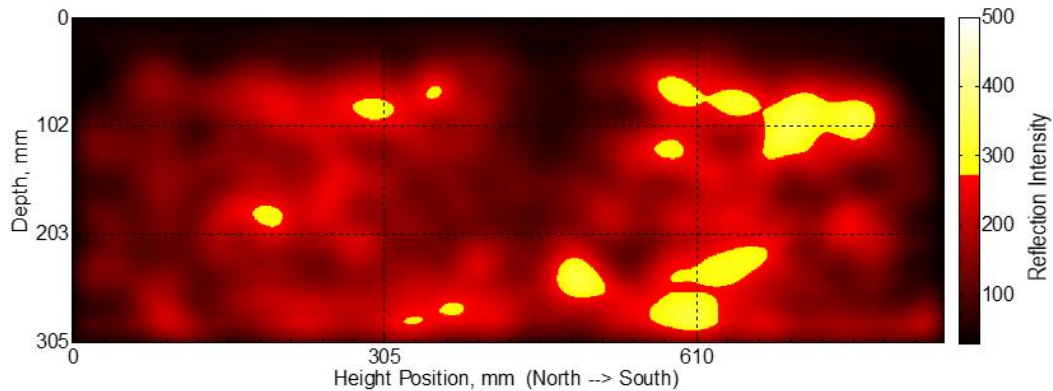


Figure 62. Reconstruction from the west side of slab D indicating damaged concrete condition.

4.3.2 Quantitative Analysis

While the panoramic reconstructions provide valuable qualitative information regarding the condition of the concrete, a quantitative analysis is desirable due to the objectiveness and efficiency of the results. The qualitative analysis requires subjective decisions, such as threshold selection and visual inspection, but the quantitative method suggested here is completely objective and utilized identical analytic variables for all scans.

The same impulse time histories which were implemented in the reconstruction analysis were utilized for the subsequent numerical analysis. As previously described, the linear array system which was used for testing creates an output of 45 unique impulse time histories. This raw data was used in order to perform a signal analysis, as detailed previously in section 5.1.1.

In order to incorporate redundancy and provide increased measurement confidence, the HTI values which are provided here are the result of averaging all 45 values to provide one more accurate designation per scan. These averaged HTI values are shown below in Figure 63 for all cases, with the clean data resulting from previous research efforts, as outlined previously. The median and quartile bars allow for the variability in values to be seen. The results from the clean and slab A data are very similar, showing that slab A is in sound condition, as was thought.

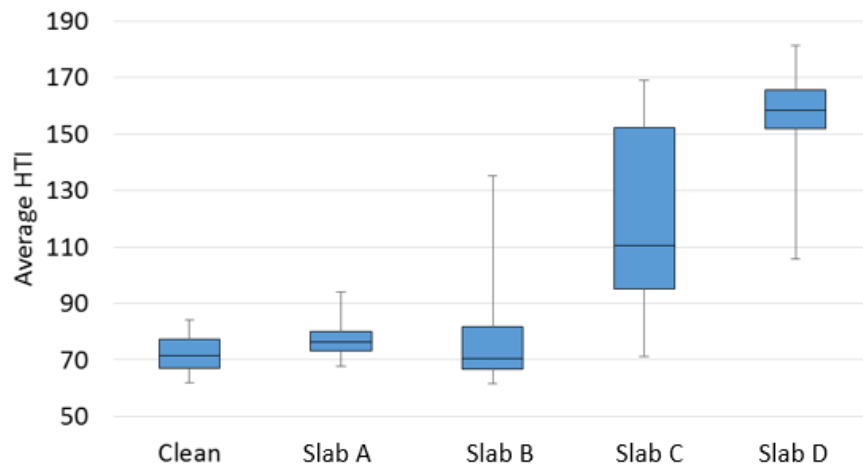


Figure 63. Average HTI values for five cases.

It is also worth discussing the variability in HTI values for the partially damaged and damaged slabs. This variability in indicator value stems from the variation in concrete condition throughout the slab. This is expected, as not all areas of the slab would be expected to be damaged to the same extent. Some regions still exhibit concrete in sound condition, as highlighted by the presence of low HTI values for slabs B and C. This is indicative of the partially damaged designations, as not all HTI values indicated damaged concrete. While variability is still present in slab D, the values all exceed 100 and thus all areas exhibit some signs of degradation, unlike the partially damaged slabs. The variability seen in all the cases shows the ability of the HTI values in properly diagnosing the progression of degradation present, regardless of extent of damage.

To further illustrate the statistical differences between the sample sets, a t-test and F-test were performed to compare the various cases. A summary of these results can be seen in Table 3. The results are as would be expected regarding the F-test conclusion, such that the partially damaged and damaged slabs had unequal variances with respect to the control slab. The t-test results for the comparison of slab A to slabs C and D resulted in the rejection of the null hypothesis, meaning their means are unequal. The same conclusion was drawn from the Clean vs. slab A comparison, which is somewhat surprising. The cause of this result is the larger mean associated with slab A. Possibly the most surprising result is the P value for the slab A vs. slab B comparison. This high P value results in accepting the null hypothesis, indicating that the two data sets are statistically similar. This result stems from the fact that the means of the two samples are extremely similar (77.16 and 77.76 for slab A and B, respectively). However, the variation present in the values for slab B is not sufficiently accounted for in this result.

Table 3. Statistical results for concrete slab data

Cases Compared	t-test results: P value	F-test results	F-test Conclusion
Clean vs. Slab A	0.00013	F= 1.45, $F_{crit}= 1.56$	Variances are not unequal
Slab A vs. Slab B	0.7798	F= 9.50, $F_{crit}= 1.51$	Variances are unequal
Slab A vs. Slab C	1.0157×10^{-16}	F= 32.48, $F_{crit}= 1.51$	Variances are unequal
Slab A vs. Slab D	4.925×10^{-55}	F= 9.50, $F_{crit}= 1.51$	Variances are unequal

The variations present in the HTI values prove to be valuable when considering the scan locations. The HTI values for all scan locations from the freeze thaw slabs are shown in

Figure 64. The color maps shown utilize a gradient in which white is indicative of the lowest HTI value seen (in this case, 62) and darker shades are indicative of the highest HTI value seen (in this case, 182). In other words, white or very light sections are representative of concrete in sound condition, while darker shades would indicate damaged concrete. In general, an HTI value less than 90 is indicative of concrete which is in good condition. This threshold was determined based upon an extensive analysis of undamaged data from prior projects and is independent of mix design or other variables. As can be seen, the HTI values seem to capture the presence of damage accurately. Slab A, the undamaged slab, is the lightest in color and contains HTI values of 94 or less. Slab D, the most damaged slab, is the darkest in color with a minimum HTI value of 106 and a maximum value of 182. Slabs B and C have conditions ranging from sound to damaged, as would be expected, with slab C in a more damaged state than slab B.

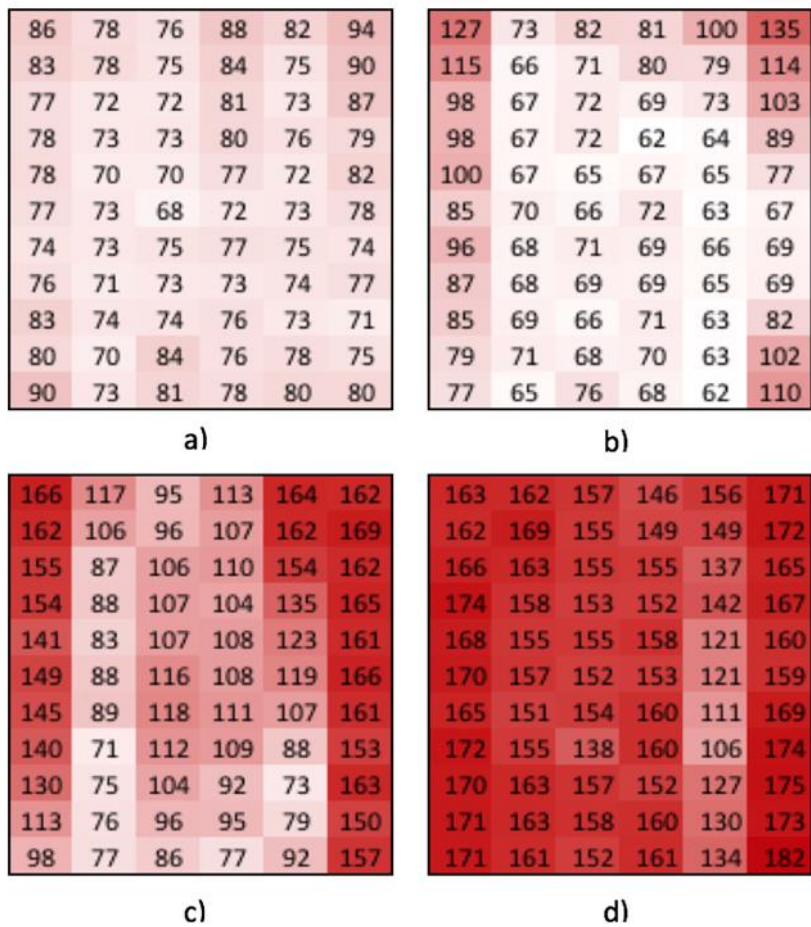


Figure 64. HTI color maps for: slab A, clean slab; slab B, partially damaged; slab C, partially damaged; and slab D, damaged.

While the progression of damage level in the slab data set is apparent, there are other trends that can be seen. In general, the greatest HTI values are those which are in the corners or edges of the slab. This can be explained via two rationales. The first of which involves the effects of edges on the ultrasound measurements. Because of the presence of edges and the proximity to walls, there can be additional distortion of the signal due to bouncing off of the boundaries. This can create slightly increased HTI values, though not significant. The greater justification for these increased values is the behavior of freeze-thaw damage. Water is most quickly absorbed via joints and edges due to their increased surface area and water

penetration capabilities. As a result, freeze-thaw damage generally initiates at the edges or at pavement joints and moves inward, thus confirming the trend of greater HTI values present along the perimeter.

4.4 RESULTS

Both methods described above produced categorized damage results for the slabs in a nondestructive manner. To compare the results of both analyses, the panoramic reconstructions are presented in conjunction with the HTI values which resulted from the numerical analysis. The results for this comparison are shown for slab B in Figure 65 and slab C in Figure 66. These figures show the six panoramic reconstructions on the left, with the HTI values for the same slab location shown both numerically and graphically on the right. The horizontal axis of the panoramic reconstructions, “Height Position”, corresponds to the actual location along the surface of the slab from north to south. The horizontal axis of the HTI graphs corresponds to the scan number from 1 to 11. These axes are essentially the same, as the scans were taken in numerical order from north to south, aligning with the height position. Again, HTI values with dark shades indicate damaged concrete, while lighter shades indicate sound concrete.

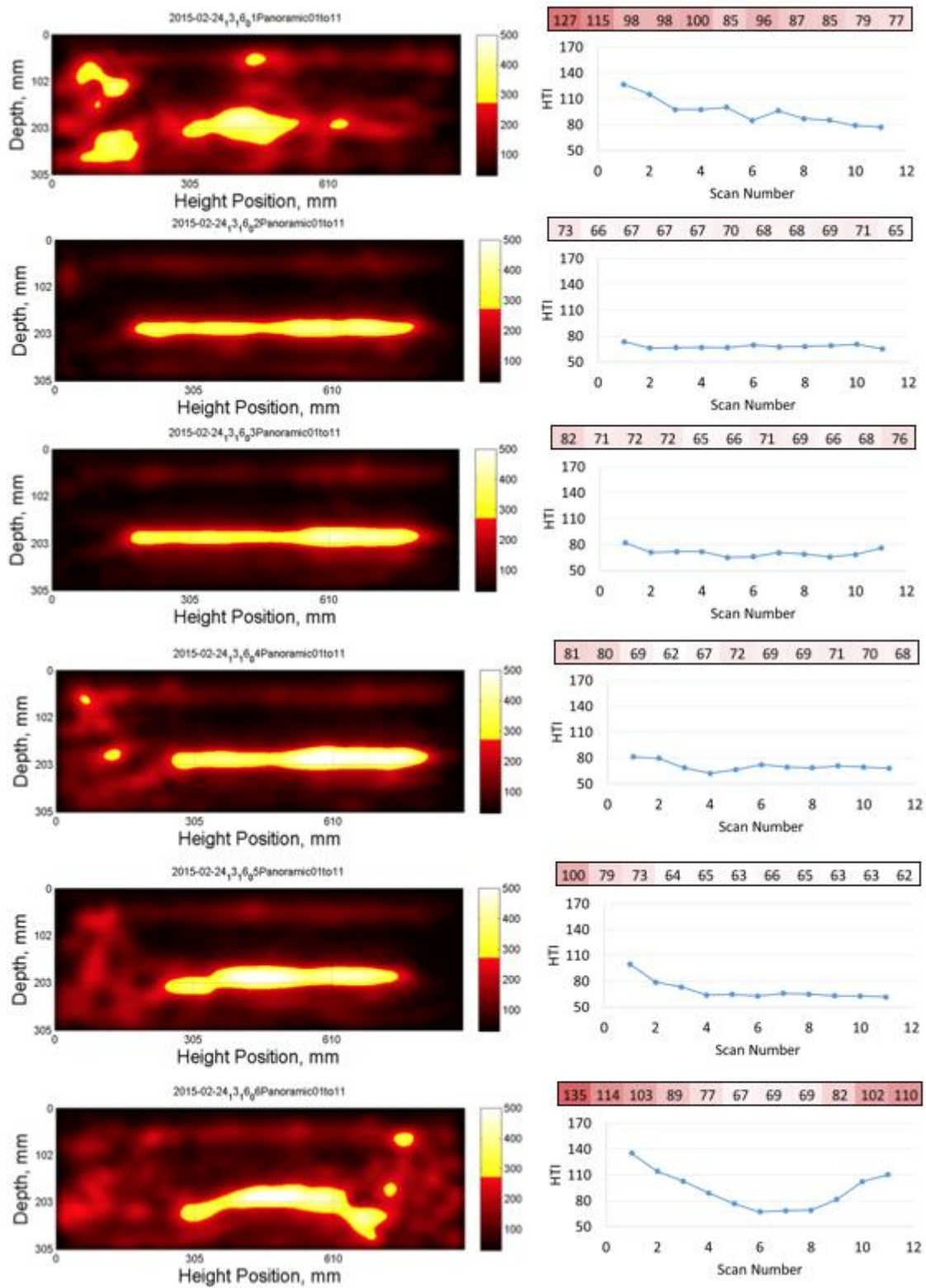


Figure 65. Comparison of panoramic reconstructions (left) and HTI index (right) analyses for slab B.

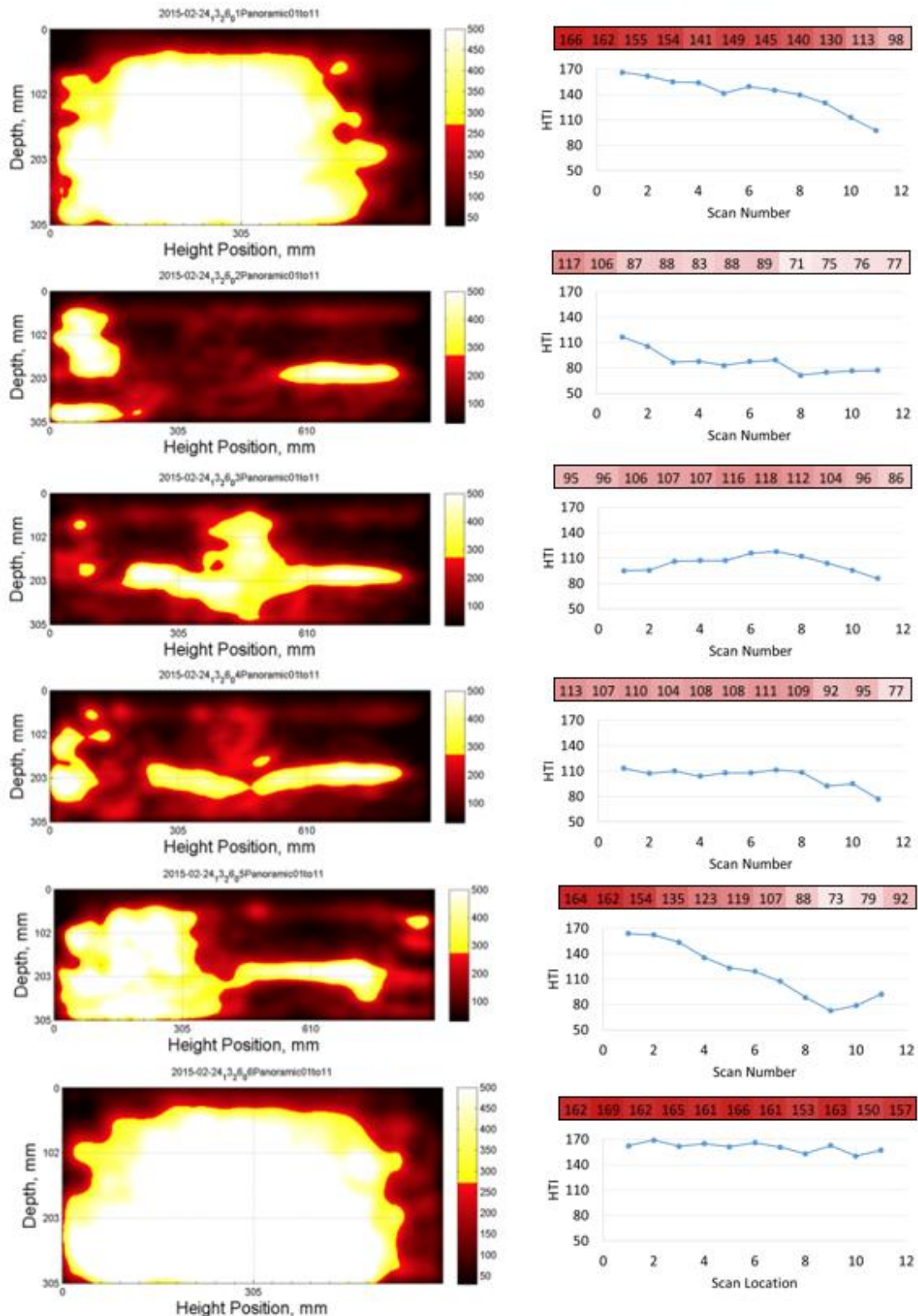


Figure 66. Comparison of panoramic reconstructions (left) and HTI index (right) analyses of slab C.

As can be seen from these figures, the HTI values show the same damage trends that can be deduced via the backwall presence in the reconstructions. For example, the bottom (sixth) panoramic reconstruction in Figure 65 shows that the backwall was not as apparent on the north and south regions, but was present in the center of the slab. The HTI results for the

same scans show higher HTI values (over 100) for these same outer regions, while HTI values indicated sound concrete in the center (values in the 60s and 70s). As such, both methods showed that concrete was in sound condition in the center of the slab, but damage was present in the north and south regions. Conversely, the second and third panoramic and HTI results shown in Figure 65 indicate sound concrete throughout the entirety of that portion of the slab, as indicated by a strong backwall presence and consistently low HTI values. To summarize the condition of slab B, the 2nd and 3rd panoramics and HTI values showed sound concrete, while the remaining four sections showed signs of partially damaged concrete.

The same similarities can be seen in the results for slab C. The most damaged panoramics shown in Figure 66 are the first and sixth reconstructions. These scans also resulted in high HTI values, as indicated by the dark shading of the HTI color maps shown. Additionally, the fifth panoramic showed considerable damage on the left (north) side of the slab, with concrete in good condition on the right (south). These same trends are seen in the HTI color map and graph. The results for both slab D and slab A also showed very good agreement. These cases are not shown here for simplicity, as the scans were either all damaged or all sound. Instead, the intricacies of the intermediate partially damaged slabs were shown to highlight the robustness of the analyses presented.

As a result of the visual interpretation of all 24 panoramic reconstructions (6 panoramics per slab, each consisting of 11 individual scans), the condition of the slabs could be qualitatively determined via the diagnosis procedure discussed previously. All six panoramics for slab A had strong backwall presence and were deemed sound. Slab B had two reconstructions showing sound concrete and 4 reconstructions showing partially damaged conditions. Slab C had 2 reconstructions indicating partially damaged concrete and four reconstructions indicating damaged concrete. Finally, all six panoramic reconstructions of slab D were considered damaged, with no backwall presence. Additionally, more detailed conditions within each slab can be observed via trends in damaged locations. For example, the north side of the slabs generally showed greater damage levels than the south side. These same trends and damage categorizations were seen in the quantitative analysis results as well. The HTI values captured the same damage presence, without requiring visual interpretation.

The results of the qualitative and quantitative analyses can then be compared to the actual crack patterns demonstrated by the sample test slabs to confirm the results. The survey results shown in Figure 54 confirm the results of both analyses. When comparing Figure 64 and Figure 54, the same damage trends can be seen in the slabs, which were further confirmed via the qualitative analysis. Additionally, the trends of increased damage on the northern portion of the slabs was confirmed via the visual surveys. Moreover, the survey of slab D (d) shows that no visible damage was present in the center portion of the slab, while the quantitative analysis indicates that the concrete in this area is not sound with HTI values of over 100 for the entire slab. This shows promise for detecting damage prior to its appearance at the surface.

4.5 CONCLUSIONS

The methods presented in this section were implemented in order to categorize the damage level within concrete slabs with varying levels of freeze thaw damage. While the two methods employed vary in their analysis type, they both utilize the same signal data obtained by an ultrasonic shear wave linear array device. Both methods were successful in determining the presence of damage in a noninvasive and efficient manner. The qualitative analysis of the panoramic reconstructions highlighted specific slab areas in which damage was causing shadowing of the backwall, while the quantitative analysis utilized the effect of damage on signal shape in order to numerically indicate the condition of the concrete. Both methods are

advantageous from a confidence standpoint as well. The panoramic reconstructions utilize overlapping scans, adding redundant measurements to increase measurement assurance. The quantitative indicator, HTI, is based upon the numerical analysis of all 45 impulse time histories from each scan. As a result, the sample set is large and produces confidence in the indicator. Moreover, the HTI method can be implemented on in-situ pavements for determining real-time concrete condition, without requiring previous measurements for comparative purposes. As a result, the applications of this technique are vast. The results of this study show promise for the implementation of methods which can characterize the condition of concrete in an efficient and nondestructive manner. Further work is necessary in order to determine the depth of the damage, a limitation which is present in both methods, and can be accomplished in conjunction with simulation efforts.

CHAPTER 5 - Alkali-Silica Reaction Damage

[This section is partially adapted from a submission to Cement and Concrete Research] Alkali-silica reaction (ASR) causes degradation similar to that of freeze thaw damage but is the result of a different physical mechanism. ASR refers to the chemical reaction which occurs in concrete, caused by the interaction of alkalis present in Portland cement and silica found in aggregates. The result of this process is the formation of a gel, referred to as ASR gel, which creates expansive pressures and microcracks within the material. This cracking results in extensive degradation to the concrete system, a phenomenon which plagues aging infrastructure. Though much research has focused upon the mechanisms of ASR, this type of degradation remains problematic and preventative methods have yet to be successfully determined. Because of this, much research has focused upon the modeling and intensive understanding of ASR (e.g. Bazant 2000, Bazant 2000a, Berra 2010, Giaccio 2008, Multon 2009), including a focus upon the conscious selection of aggregates to mitigate ASR (Berra 1999, Chen 2010, Multon 2010). A review of the current techniques for modeling of ASR was performed by Pan et al. in 2012 and the authors concluded that the models are based upon empirical concepts, while more complex approaches fall short due to shortcomings in the modeling and understanding of microcracks.

5.1 PREVIOUS RESEARCH IN ASR DETECTION

Due to the extent of degradation associated with ASR, this type of damage has been the focus of nondestructive evaluation efforts in recent history. Diffuse ultrasound has been employed Deroo et al. (2010) to quantify microcracking in concrete. This research focused specifically on the diffusivity and dissipation parameters, noting that diffusivity decreased with increased damage, while dissipation saw little change. Increased scattering caused by microcracks was the cause of the decrease in diffusivity which occurred.

Methods incorporating the nonlinear evaluation of concrete have also been utilized in the past. One such method, Nonlinear Impact Resonance Acoustic Spectroscopy (NIRAS) was used to measure the nonlinearity in a specimen caused by microcracks (Lesnicki 2013). The results of this analysis showed that the method could identify microstructural damage, however the samples utilized were small in size and required laboratory implementation with a mechanical impact. Further nonlinear analysis has been performed using ultrasonic waves and an associated acoustic nonlinearity parameter to assess ASR damage (Qu 2015). An initial investigation of the wave speed and wave attenuation showed a lack of sensitivity to ASR damage, however the nonlinearity parameter had increased performance with respect to ASR damage levels. This method again used mortar bars in the laboratory, creating applicability issues including aggregates and in-situ concrete specimens.

The methods described above have obvious limitations with respect to ASR damage detection. While the above method showed some initial success and promise in detecting ASR gel, no work was done on in-situ or full-scale samples. Additionally, these methods were unable to successfully detect all damage levels. To address these limitations, an ultrasonic linear array device was utilized for this research.

5.2 MATERIALS AND METHODS

To test the applicability of the nondestructive evaluation of concrete slabs with ASR damage using an ultrasonic linear array device, an experimental investigation was performed on

sample slabs and a subsequent data analysis was performed. The methods employed by these analyses are described in the following sections.

5.2.1 Experimental Procedure

The Electric Power Research Institute (EPRI) commissioned the fabrication of four slabs with various levels of alkali-silica reaction, with each slab surface measuring 48 by 36 inches (122 by 91 cm) by 8 inches (20 cm) thick. The following four slabs were tested:

- Slab 0: Unreactive aggregates; no damage (control specimen)
- Slab 1: Highly reactive aggregates: Partially damaged condition
- Slab 2: Highly reactive aggregates: Partially damaged condition
- Slab 3: Highly reactive aggregates: Low damage condition

The reactive aggregates which were used came from Wells, Maine (ASR-AC1), Bernalillo, New Mexico (ASR-AC2), and El Paso, Texas (ASR-FA). Additionally, a high equivalent alkali content Type I Portland cement was used for the ASR slabs. Sodium hydroxide was added to the mixtures in order to obtain an equivalent alkali content of 1.25%. The mix design used for the construction of the slabs is shown below in Table 4, with a w/cm ratio of 0.50 used for all mixes.

Table 4. Mix design for concrete slabs

Component	Control- Slab 0 kg/m ³ (lb/yd ³)	ASR- Slabs 1, 2 and 3 kg/m ³ (lb/yd ³)
Cement – Type I	-	420 (708)
Cement – Type II	420 (780)	-
Water	210 (354)	210 (354)
ASR-CA1*	-	429 (723)
ASR-CA2*	-	429 (723)
CA*	1095 (1845)	-
ASR-FA*	-	818 (1379)
FA*	639 (1077)	-

* Oven Dry

To induce ASR in the reactive slabs, temperature and relative humidity in the environmental chamber were maintained at 27°C (80.6°F) and 65%. Temperature within the chamber was increased to 32°C (89.6°F) on day 93 to speed up the ASR damage. Slabs were draped with wet burlap and wrapped in plastic once per week to maintain a supply of sufficient moisture. The non-reactive control slab remained in the concrete laboratory at a constant 23°C (73°F) and was draped in wet burlap once weekly.

The ultrasonic linear array device described previously was utilized to obtain scans on the slabs on day 103 (January 25th), as shown below in Figure 67. The entire surface of the slab was tested, using overlapping scans in the orientation and sequences shown in Figure 67 (b). The scans were taken along 6 rows from east to west, with 12.5 cm step sizes utilized. Within each row of scans, overlapping measurements were obtained with a step size of 5 cm moving north to south. As a result, 66 scans were obtained for each slab, allowing for the formulation of 6 panoramic reconstructions.

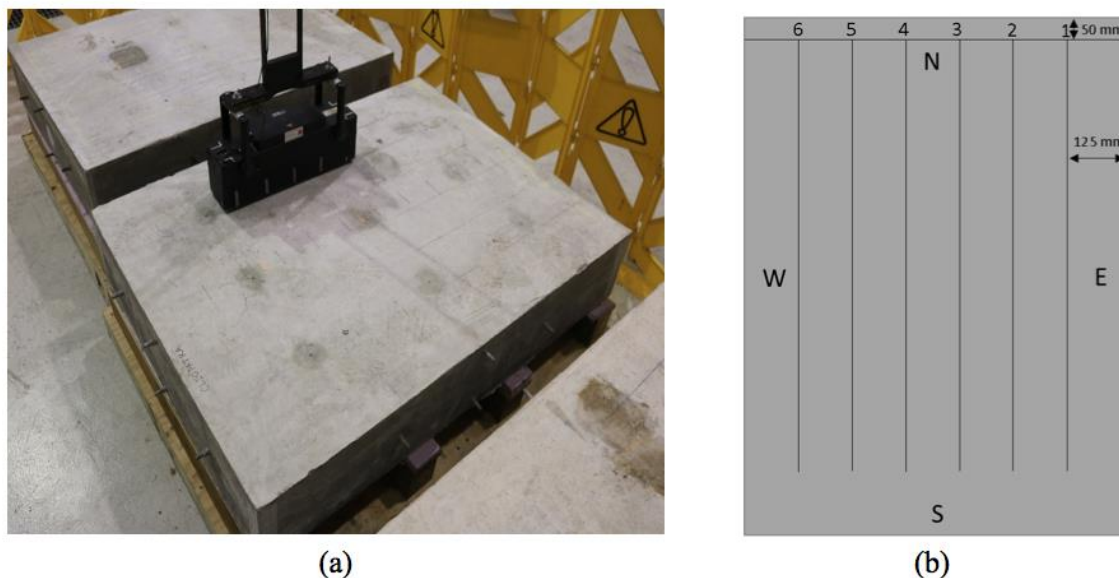


Figure 67. Ultrasonic device positioned on slab 2 (a) and readings location schematic (b).

This scan data was utilized for a similar analysis to that which was performed for the slabs with freeze thaw damage, however, an additional velocity analysis was performed. The results of these analyses are shown in Table 5. The HTI values given in this table are the result of averaging the 45 individual HTI values from all 11 scans within the panoramic locations. The same holds true for the velocity values given in this table. The column labeled “Concrete Condition” refers to the result of the visual panoramic reconstruction analysis, performed in the same fashion as that which was outlined in section 3.2.2.5. The results presented in this table again show that the trends in HTI values correspond well with the concrete condition designation resulting from the panoramic reconstructions. Further exploration of the HTI and velocity values is given in section 5.3.4.

Table 5. Summary of results for all panoramics.

Slab	Panoramic Location	HTI	Velocity (m/ms)	Concrete Condition
Slab 0	1	74.95	2.349	Sound
	2	68.26	2.407	Sound
	3	69.49	2.417	Sound
	4	66.95	2.412	Sound
	5	72.67	2.297	Sound
	6	71.42	2.451	Sound
Slab 1	1	108.03	2.096	Partial Damage
	2	97.01	2.148	Partial Damage
	3	105.97	2.130	Partial Damage
	4	108.31	2.102	Partial Damage

	5	105.31	2.129	Partial Damage
	6	109.50	2.100	Partial Damage
Slab 2	1	104.31	2.118	Partial Damage
	2	106.87	2.142	Partial Damage
	3	110.11	2.144	Partial Damage
	4	101.71	2.157	Partial Damage
	5	107.23	2.162	Partial Damage
	6	105.39	2.124	Partial Damage
Slab 3	1	90.98	2.128	Partial Damage
	2	83.91	2.122	Sound
	3	79.67	2.131	Sound
	4	81.08	2.133	Sound
	5	85.96	2.133	Sound
	6	88.82	2.146	Partial Damage

5.3 PANORAMIC RECONSTRUCTIONS

Since the initial categorization of concrete condition is very general, reconstructions that are slightly different can fit in the same category. A few examples with commentary will be shown in this section. It is also worth noting that as no reconstruction achieved the third categorization level (damaged), there are only examples of the first two categories. Figure 68 and Figure 69, shown below, are both taken from slab 0 and are representative of the sound concrete condition seen for all panoramics taken from this slab. Figure 68 is a reconstruction taken in the middle of slab 0 (3rd SAFT-Pan). While this scan shows a sound concrete condition with a continuous backwall reflection spanning the width of the reconstruction, slightly more attenuation of the backwall reflection was observed around the 300 mm marking. This may indicate the presence of a developing stress or poor concrete consolidation being reflected above the backwall. The same happens to panoramic 5 taken on slab 0 (Figure 69). Figure 69 is still representative of sound concrete, but a weaker reflection after the middle of the reconstruction (400 mm marking) is present. This indicates a more sound concrete in the north region of the specimen than in the south.

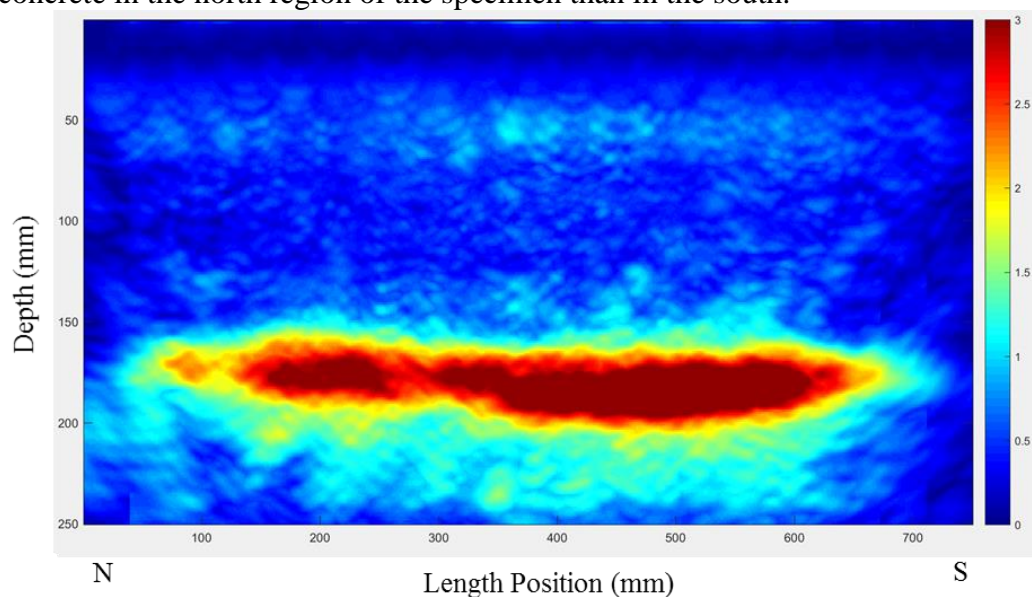


Figure 68. SAFT-Pan Reconstruction of specimen Slab 0, panoramic 3

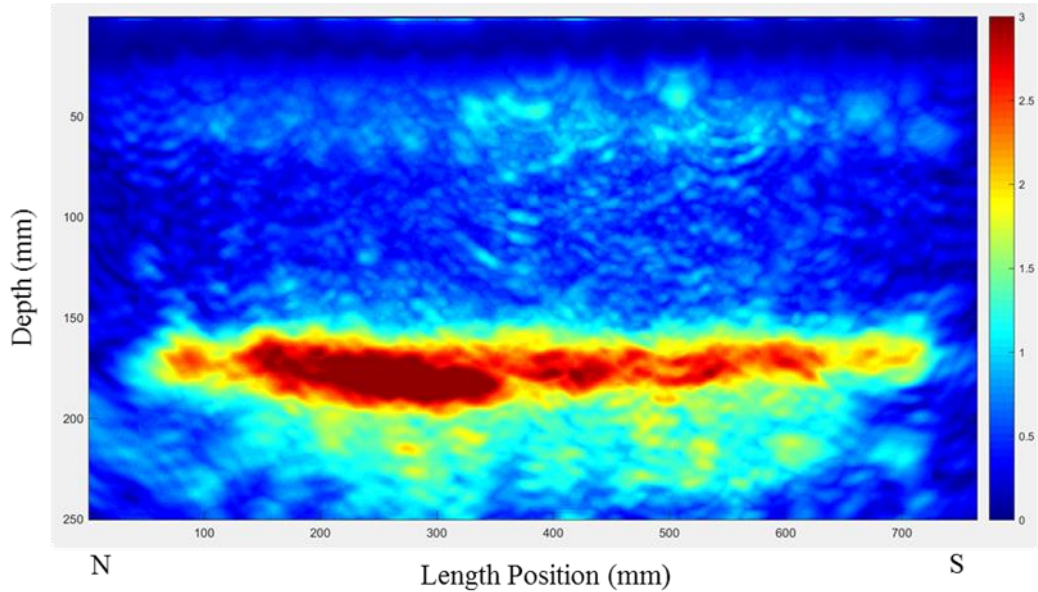


Figure 69. SAFT-Pan Reconstruction of specimen Slab 0, panoramic 5

Slab 3 presents both characterizations “sound” and “partial damage”. Reconstructions of these conditions are shown in Figure 70. Figure 70a displays the middle of slab 3 (4th SAFT-Pan) showing a clear sound concrete condition with a continuous and uniform backwall reflection throughout the width of the reconstruction. On the other hand, Figure 70b (6th SAFT-Pan) presents more attenuation at shallower depths, indicating the existence of partial damage.

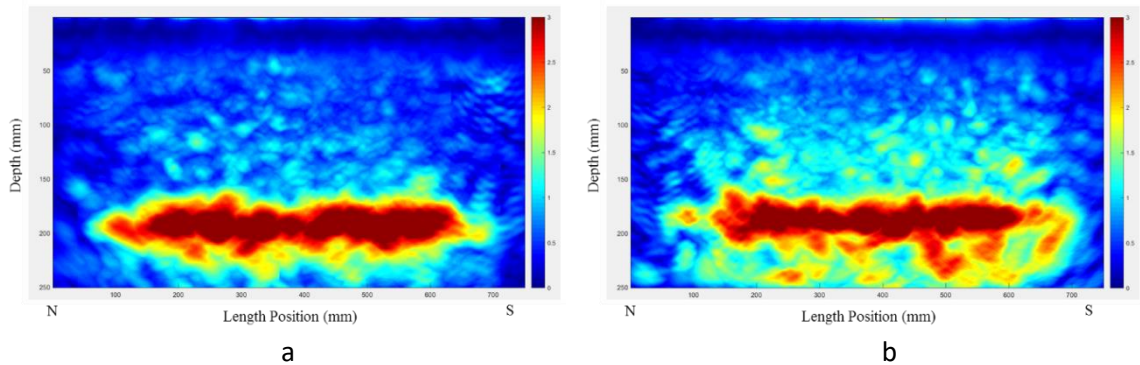


Figure 70. SAFT-Pan Reconstructions of specimen slab 3, (a) panoramic 4 and (b) panoramic 6

Figure 71, Figure 72, and Figure 73 show reconstructions which serve as examples that indicate a slightly damaged concrete condition (or partially damaged). Figure 71 was taken on the west side of slab 2 (5th SAFT-Pan). It shows a mostly sound concrete condition with a continuous and uniform backwall reflection in the middle of the reconstruction. However, the breaks in backwall continuity at the edges of the reconstructions, in conjunction with more attenuate reflections near the backwall, indicates the damage presence. Figure 72 shows a reconstruction for slab 1 (1st SAFT-Pan) with more strong reflections and a clear

break in the backwall at the end of the reconstruction (south area). In both cases, attenuation from damage could have shadowed the backwall in some parts of the reconstruction.

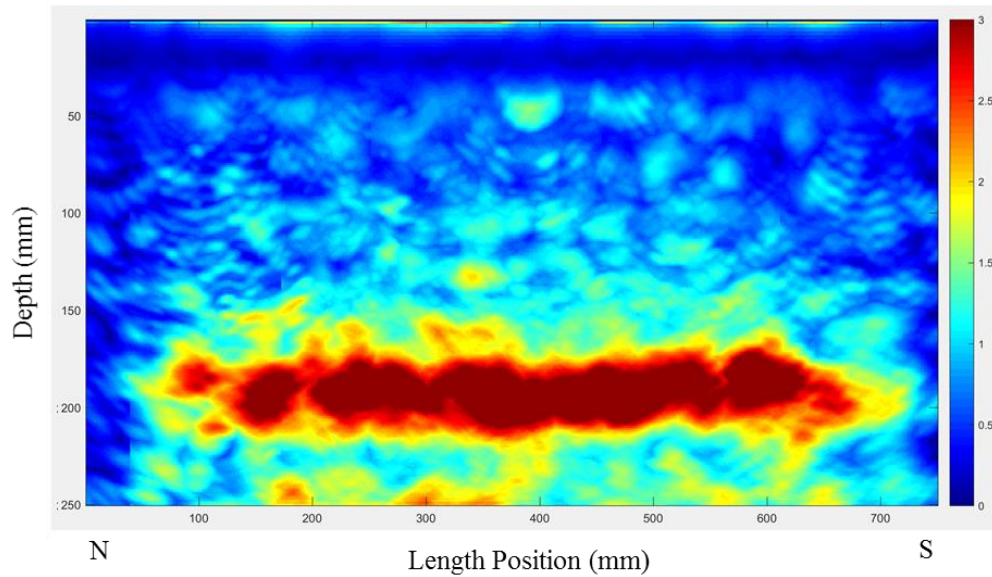


Figure 71. SAFT-Pan Reconstruction of slab 2, panoramic 5

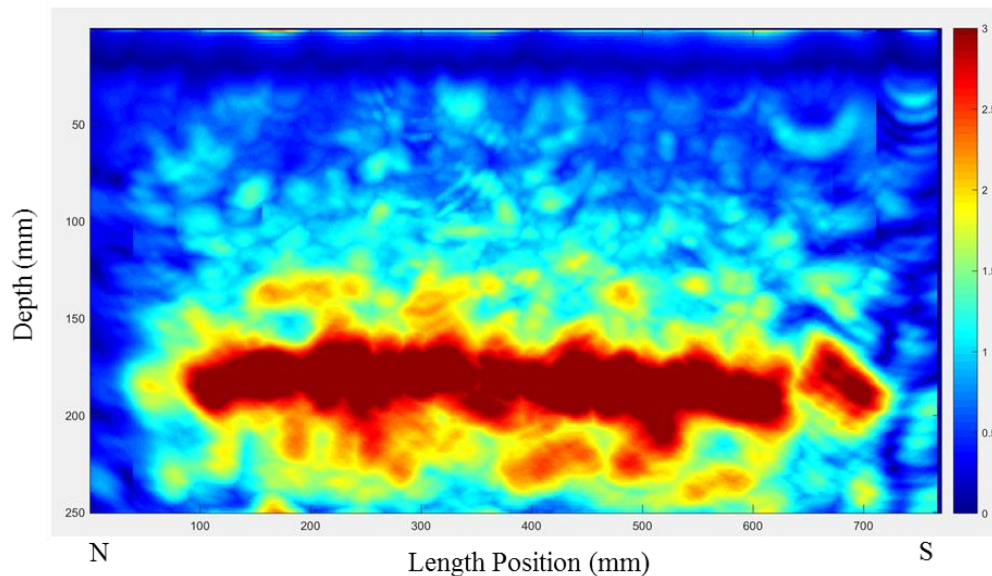


Figure 72. SAFT-Pan Reconstruction of slab 1, panoramic 1

Figure 73 was taken from the east side of slab 2 (1st SAFT-Pan). The reconstruction shows a possible distress in the middle of the specimen (dark reflection above the backwall). This reflection has a shadowing effect on the backwall right before and after the reflection position. Also, the north part of the specimen presents a weaker backwall than the south part, indicating a more damaged condition associated with the north region. It is again worth noting that these panoramic reconstructions show partial damage conditions, or the early onset of degradation, with no panoramic reconstructions showing characteristics associated with the presence of severe damage.

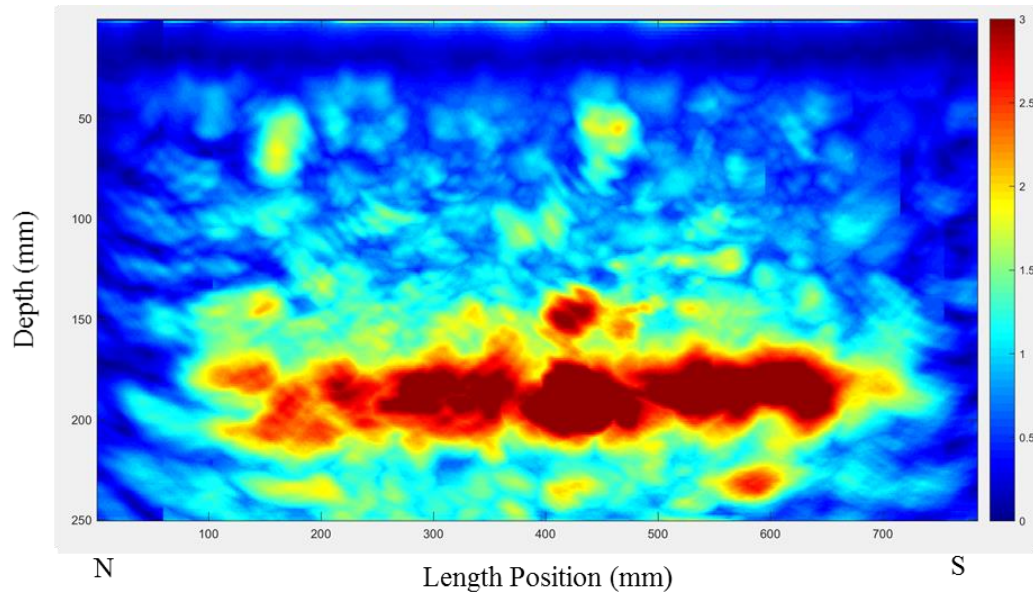


Figure 73. SAFT-Pan Reconstruction of specimen slab 2, panoramic 1

5.4 QUANTITATIVE ANALYSIS

The same quantitative analysis involving the HTI index was performed on the ASR slabs. Additionally, the shear wave velocity was calculated, as described in section 2.2.1, for each scan location. This data was previously presented in Table 5. To compare the results of the HTI and shear velocity analysis, Figure 74 was created to show the relation between the HTI and the shear wave velocity. As can be seen, the control specimen (slab 0) presents HTI values consistently below 80, while the shear wave velocity varies greatly. The most damaged specimens (slabs 1 and 2) show most scans with HTI values above 100 and low velocity. Slab 3 shows what can be interpreted as the first stages of damage. Only three scans presented HTI values above 100, with the remaining values averaging around 85. The specimen has reactive aggregate but still presents concrete in mostly sound conditions, as shown by the majority of low HTI values throughout the slab. These results confirm the lack of accuracy associated with shear wave velocity measurements in detecting damage that was seen for in the laboratory beam tests. The Hilbert Transform Indicator was much more successful in characterizing the concrete condition, and moreover was able to distinguish between varying levels of distress.

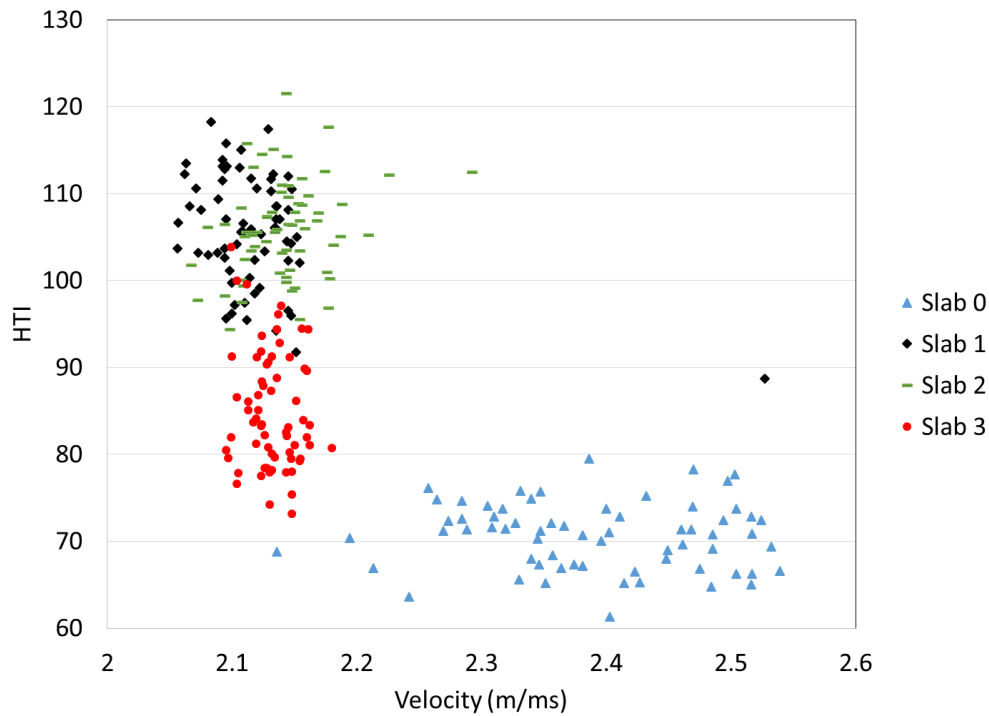


Figure 74. HTI versus shear wave velocity

The ability of the HTI values in distinguishing between areas of damaged concrete is exhibited by the color map results shown in Figure 75. Again, darker shading indicates a higher HTI value, or a more damaged area. The maps show that the control specimen, Slab 0, was in good condition, while slabs 1 and 2 exhibited higher levels of damage as indicated by the HTI values. It should be noted that extreme damage conditions were not present in any of the slabs, as would be indicated by very dark shading not seen here. In other words, even the darkest shade seen in Figure 75 is not indicative of severe damage, only signs of partially damaged concrete. Slab 3 has both damaged and sound concrete conditions, as also shown by the concrete condition diagnosis resulting from the visual analysis of the reconstructions, indicating the early stages of damage progression.

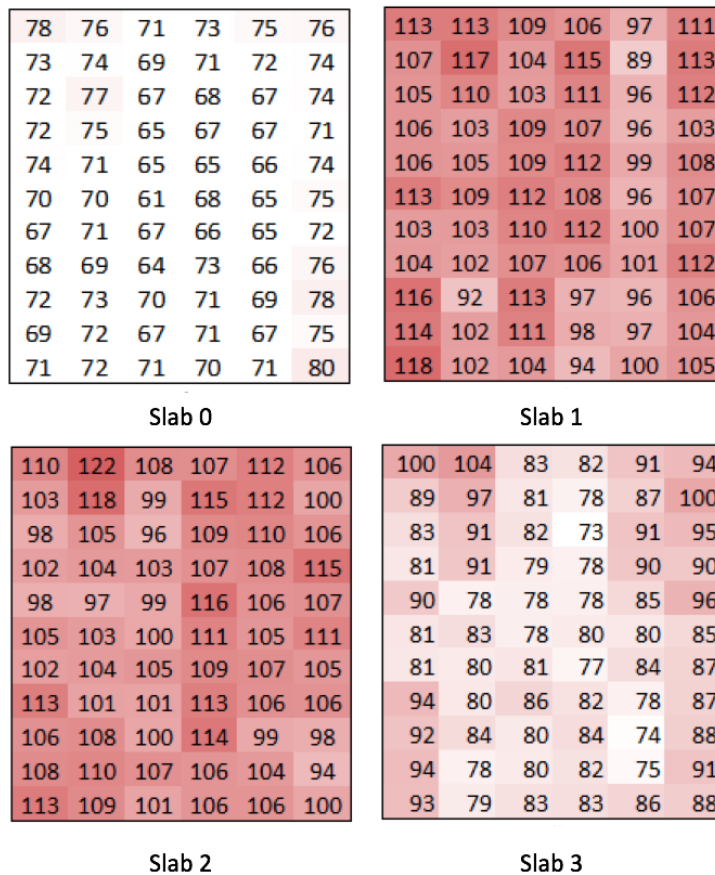


Figure 75. HTI color map for specimens slab 0-3.

5.5 RESULTS

To confirm the results shown by the HTI and reconstruction analyses, visual cracking patterns were obtained from EPRI. Examination of surface cracking in all specimens confirms the damage presence on slabs 1 and 2, as shown in Figure 76, with cracks highlighted for greater ease of identification. The rectangle on Figure 76 (top) shows an enlarged section of the specimen in order for cracks to be more easily visible. Slabs 0 and 3 did not have any visible surface cracks.

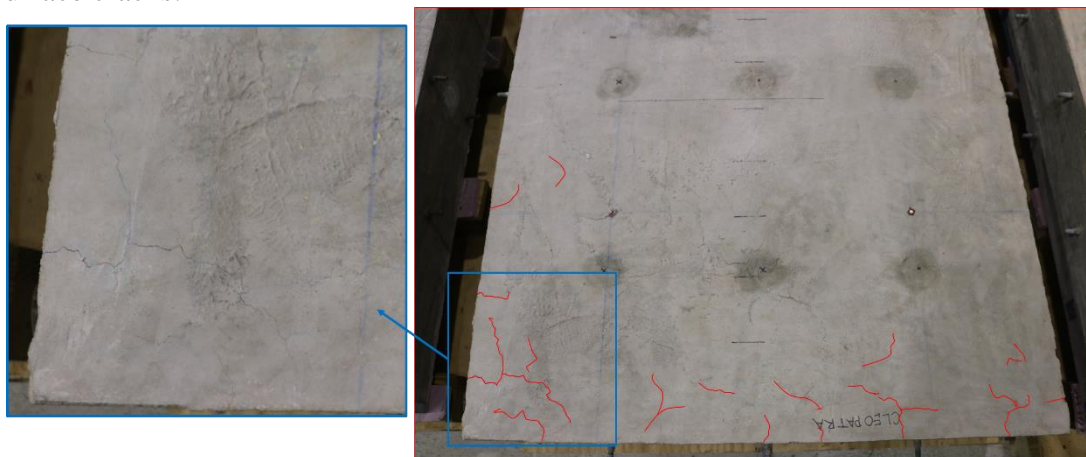




Figure 76. Visible cracking in south portion of slab 2 (top) and north portion of slab 1 (bottom).

Additional data regarding the condition of the slabs was gathered by EPRI via the utilization of DEMEC discs (Demountable Mechanical strain gauges) to obtain expansion data. The expansion values for each slab are shown in Table 3 for two different dates: firstly at 45 days, right before the specimens were shipped to EPRI (Klenke and Giaanni, 2015), and at 215 days of age, 20 days before the MIRA testing. Expansion for the latter data was obtained through personal communication with EPRI engineer Salvador Villalobos. Table 3 also brings the average HTI values for each slab. Again, these average HTI values are the result of the averaging of all 66 scan values, with each individual scan containing 45 individual HTI values as a result of the transducer pair interaction. As can be seen, there is good agreement between the expansion and HTI values. It is also worth noting that the standard deviation of the HTI values is quite low, further validating the accuracy of this method.

Table 6. Expansion and HTI values for all four slabs.

Slab	Expansion (45 days)	Expansion (215 days)	Average HTI	HTI (Std)
Slab 0	-0.012%	-0.0278%	70.6	2.70
Slab 1	0.087%	0.179%	105.7	4.13
Slab 2	0.046%	0.141%	105.9	2.61
Slab 3	0.057%	0.091%	85.1	4.00

5.6 CONCLUSIONS

The investigation of ASR damage in concrete slabs resulted in similar results to those seen for the freeze thaw analysis. The visual comparison of reconstruction images again provided concrete condition information via the presence, or lack thereof, of the backwall. However, none of the slabs were severely damaged, therefore those observations for a heavily damaged freeze thaw slab were not able to be confirmed via this investigation. The HTI results were promising and seemed to also adequately capture the presence of ASR damage. Moreover, the control slab (slab 0) added further to the sound data inventory and confirmed previous trends

in that regard, despite differing mix designs and concrete location. This further proves that the implementation of the HTI analysis is possible on a widespread basis due to its lack of dependence on these variables. The ASR slabs also involved an analysis of shear wave velocity with respect to damage detection capabilities. The variation in shear wave velocity that was seen was similar to those found in the laboratory beam trials. As such, this method does not accurately detect the presence of damage due to its observed inconsistencies.

CHAPTER 6 - CONTINUOUSLY REINFORCED CONCRETE PAVEMENT CRACKING

Locating cracking and distress in concrete pavements is a major focus for proper maintenance and rehabilitation decisions. However, most modern cracking evaluation methods can only successfully locate well-developed surface cracking, yielding no information regarding partial cracks which are still in development. This chapter addresses visible and non-visible crack identification in four experimental sections of a short continuously reinforced concrete pavement (CRCP) constructed in Brazil in a research cooperation between the University of Sao Paulo (USP) and the Sao Paulo Research Foundation (FAPESP). As the pavement presented an unusual cracking pattern (less visible cracks than traditional CRCP) as seen in Salles et al. (2014), there was a need to verify if most cracks were not yet fully developed in the slab. Ultrasonic testing and novel-techniques of signal interpretation and simulation were applied to investigate cracking in the four sections.

6.1 TESTING PROCEDURE

For visible cracks, measurements were taken using the same ultrasonic device discussed in previous chapters. The crack map can be seen in Figure 77. Measurements were taken on every visible crack in three positions as illustrate on crack F4.12 in Figure 77: right (40 mm from the longitudinal edge), center and left (40 mm from the longitudinal joint). Three readings per position were made, moving the device 45 mm from one reading to the other. One crack per section received a more in-depth evaluation with five readings on each position and with a transversal reading covering the whole crack (90 mm readings offset). Cracks F2.1, F2.5, F3.8 and F4.12 were selected for this procedure. Calibration was performed every time the device was moved to a new crack. Non-visible crack evaluation was performed in panels between two cracks or between a crack and the transversal edge. The device was placed longitudinally at the lane center and readings were taken every 90 mm. Calibration was performed for every panel.

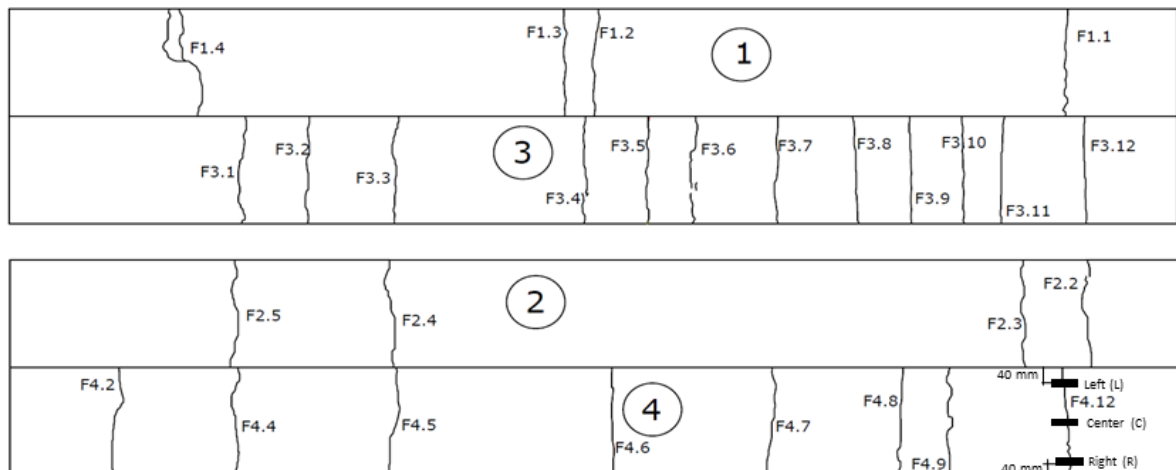


Figure 77. February, 2015 crack map

6.2 VISIBLE CRACK RESULTS

The HTI analysis described in previous chapters was applied to the data obtained from the CRCP sections. The value of the HTI (the average of all 45 signals) for crack locations showed

high values for most cracks, as seen in Table 7. The differences in signals from sound and damaged concrete cause this increase in HTI. Two signals can be seen in Figure 78, illustrating the difference in signal shape with respect to concrete condition. The signal shown on the right contains much greater oscillation than that of the sound signal shown on the left. This is in agreement with the trends from other damage types seen in the previous chapters.

Table 7. Crack ultrasonic evaluation

Section 1			Section 2			Section 3			Section 4		
Crack	HTI										
F1.1	R	99	F2.2	R	102	F3.1	R	98	F4.2	R	78
	C	81		C	72		C	103		C	66
	L	60		L	81		L	107		L	83
F1.2	R	106	F2.3	R	66	F3.2	R	107	F4.4	R	68
	C	106		C	73		C	104		C	100
	L	107		L	62		L	110		L	103
F1.3	R	116	F2.4	R	78	F3.3	R	97	F4.5	R	71
	C	95		C	73		C	81		C	92
	L	62		L	77		L	84		L	95
F1.4	R	126	F2.5	R	98	F3.4	R	100	F4.6	R	77
	C	117		C	81		C	104		C	80
	L	91		L	74		L	120		L	77
						F3.5	R	112	F4.7	R	62
					C		93	C		63	
					L		106	L		62	
						F3.6	R	105	F4.8	R	79
					C		110	C		70	
					L		112	L		83	
						F3.7	R	111	F4.9	R	88
					C		100	C		94	
					L		112	L		92	
						F3.8	R	115	F4.12	R	116
					C		105	C		95	
					L		118	L		101	
						F3.9	R	96			
					C		111				
					L		111				
						F3.10	R	99			
					C		98				
					L		111				
						F3.11	R	97			
					C		97				
					L		74				
						F3.12	R	86			
					C		86				
					L		108				

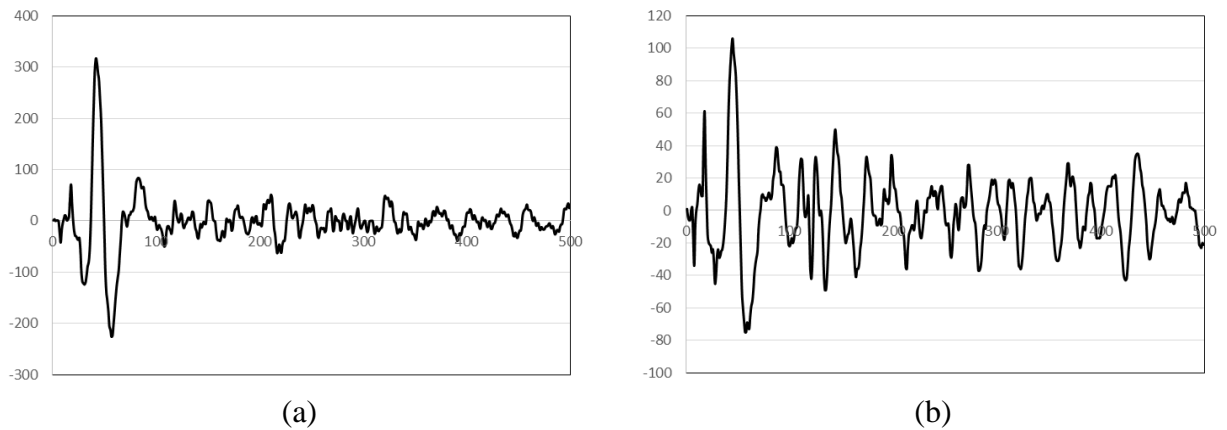


Figure 78. Signals for (a) sound concrete and (b) crack F3.4 (Right).

However, some cracks, such as F4.7 and F2.3, exhibited low HTI values. To further investigate this abnormality, reconstructions were created and visually analyzed. SAFT-Pan reconstructions of scans at crack locations resulted in two major kinds of features: a continuous slab backwall with a circular shaped inclusion located at 50 to 100 mm from the surface (Figure 79a and b), or a continuous backwall with another reflection around 150 mm followed by the same circular shaped inclusion described above (Figure 79c and d). To illustrate the features of a reconstruction taken at a sound location, Figure 80 can be used for visual comparison.

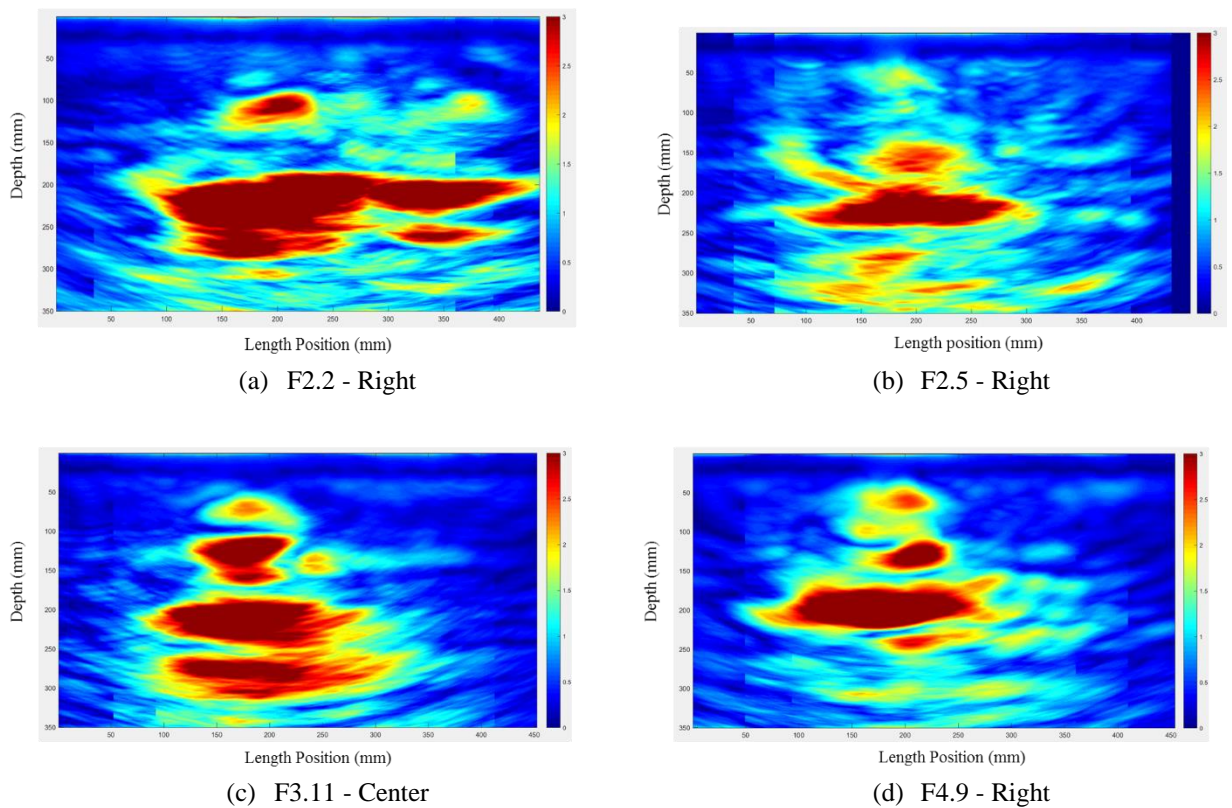


Figure 79. Examples of typical SAFT-Pan reconstructions at transversal cracks

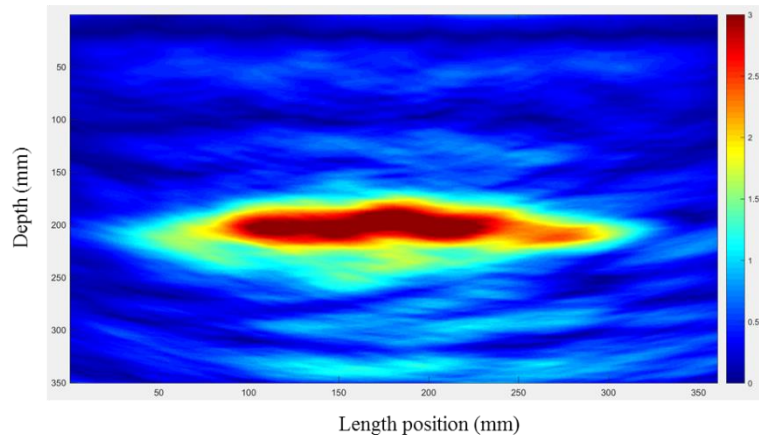
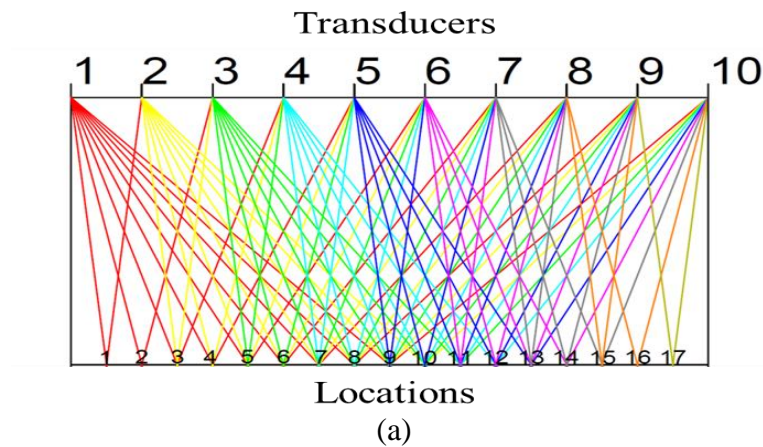


Figure 80. SAFT-B Scan of sound concrete

Some SAFT-Pan reconstructions, however, were not as conclusive as the ones featured in Figure 79. As such, an investigation of the individual HTI values was performed. As can be seen in Figure 81a, each pair of transducers reaches the simulated backwall at a particular position creating 17 backwall reflection locations. The interaction of the transducers creates a total of 45 signals (Figure 81b). Some locations present only one signal reflection (locations 1, 2, 16 and 17), while others have an abundance of signal reflections like location 9 (center of simulation) with 5 reflections. Table 8 presents the number of signal reflections for each of the 17 locations. As the consecutive sensor spacing is constant (40 mm), the locations of the signal reflections will be the same regardless of the analysis depth. By analyzing the 45 individual HTI values from each signal, it is possible to decipher the detailed condition of each signal. If a signal has a high corresponding HTI value, it could mean that there is a distress on the signal's path.



		Receiving Transducers								
		2	3	4	5	6	7	8	9	10
Emitting Transducers	1	1	2	3	4	5	6	7	8	9
	2		10	11	12	13	14	15	16	17
	3			18	19	20	21	22	23	24
	4				25	26	27	28	29	30
	5					31	32	33	34	35
	6						36	37	38	39
	7							40	41	42
	8								43	44
	9									45

(b)

Figure 81. Locations of backwall signals in a MIRA grid simulation (a) and identification of the 45 signals (b)

Table 8. Locations and reaching signals in a MIRA grid simulation

Location	Distance from sensor 1 (mm)	Signal (s)
1	20	1-2 (1)
2	40	1-3 (2)
3	60	1-4 (3) 2-3
4	80	1-5 (4) 2-4
5	100	1-6 (5) 2-5 3-4
6	120	1-7 (6) 2-6 3-5
7	140	1-8 (7) 2-7 3-6 4-5
8	160	1-9 (8) 2-8 3-7 4-6
9	180	1-10 (9) 2-9 3-8 4-7 5-6
10	200	2-10 3-9 4-8 5-7
11	220	3-10 4-9 5-8 6-7
12	240	4-10 5-9 6-8
13	260	5-10 6-9 7-8
14	280	6-10 7-9
15	300	7-10 8-9
16	320	8-10
17	340	9-10

Figure 82 displays the normalized HTI values (minimum 90) for every signal on crack F2.5 (Right). As can be seen, most signals emitting from sensors 1 and 2 (signals 1-17) have high HTI values, as well as all signals from sensor 3 (signals 18-24). Signal 30, emitted from sensor 4 and received by sensor 10, also exhibits a high HTI value.

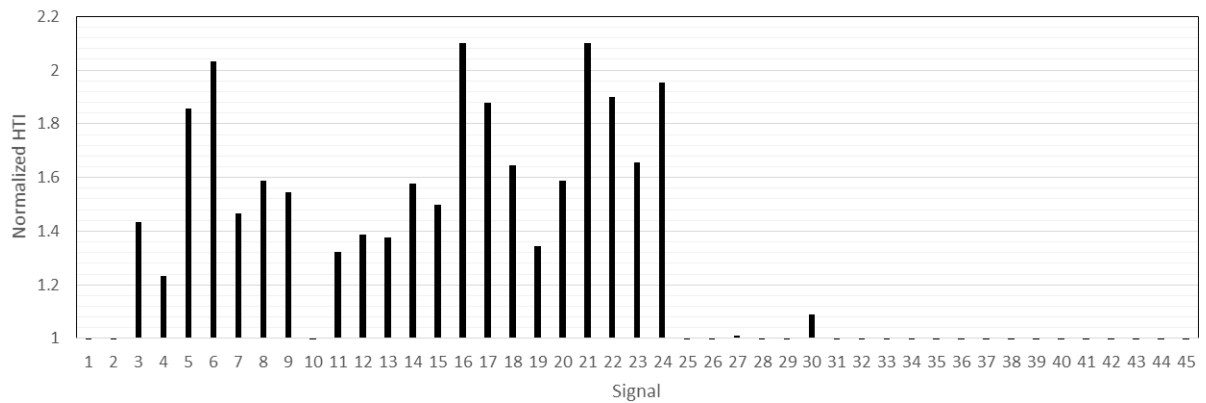


Figure 82. Normalized HTI for every signal in crack F2.5-R (first scan)

By looking at detailed HTI results, rather than solely the averaged value, the precise location of distresses can be determined. For example, crack F2.5 received five overlapping MIRA scans with a 45 mm step size between scans. The simulation of signal loss due to high HTI (higher than 90) can be determined for each scan, and is presented in Figure 83. This simulation of signal loss essentially ignores signal paths which correspond to high HTI values in order to simulate the location of cracks. As can be seen on the first scan, crack F2.5 is positioned in between sensors 3 and 4, and as the scan location moves along the crack, the crack location with respect to the sensors also changes accordingly. Moreover, the simulation of signal loss for the five scans proves that the crack is fully developed along the slab depth. It is also important to note that cracks are usually non-uniform and exhibit wandering shapes across the slab's depth. This helps to explain why this particular crack is positioned below sensor 3 and 4 and not below sensor 5 and 6 (MIRA's center).

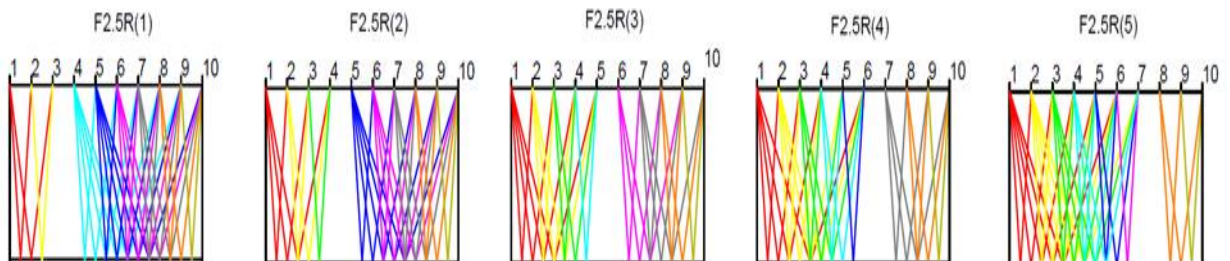


Figure 83. Simulation of crack F2.5-R scans based on HTI

Figure 84 shows two examples where the crack is not yet fully developed. The presence of low HTI signals (or uninhibited signal paths) in the area near the backwall imply one of two situations: a top-bottom partial crack, or a crack that originates from the reinforcement location (around the slab mid-depth). These partial cracks can be detected when looking at detailed signal data, and the resulting signal path patterns.

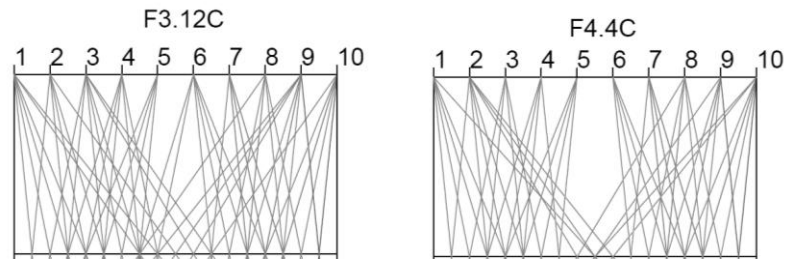


Figure 84. Signal loss due to high HTI in two partial cracks

The same simulation of signal loss was attempted on reinforced concrete sections to determine if signals reaching the inclusion (longitudinal bars) would result in high HTI. This analysis was performed to eliminate the possibility of steel bars causing increased HTI values, or to be incorrectly categorized as cracking. The results showed low HTI values (less than 90) for signals at the reinforcement, indicating that the HTI values are not affected by the presence of reinforcement.

The assessment of every visible crack as a partial (P) or full (F) depth crack is shown in Table 9. There is a clear trend in which cracks presenting HTI values higher than 93 are fully developed cracks, while cracks with HTI values between 66 and 92 are partially developed cracks. Cracks with HTI values below 65 presented inconclusive signal loss patterns. Further evaluation of these locations are necessary in order to determine the cause of the irregularity in HTI values.

Table 9. Crack depth

Section 1			Section 2			Section 3			Section 4		
Crack	HTI	Depth									
F1.1	R 99	F	F2.2	R 102	F	F3.1	R 98	F	F4.2	R 78	P
	C 81	F		C 72	P		C 103	F		C 66	P
	L 60	N/A		L 81	P		L 107	F		L 83	P
F1.2	R 106	F	F2.3	R 66	P	F3.2	R 107	F	F4.4	R 68	P
	C 106	F		C 73	P		C 104	F		C 100	F
	L 107	F		L 62	P		L 110	F		L 103	F
F1.3	R 116	F	F2.4	R 78	P	F3.3	R 97	F	F4.5	R 71	P
	C 95	F		C 73	P		C 81	P		C 92	P
	L 62	N/A		L 77	P		L 84	P		L 95	P
F1.4	R 126	F	F2.5	R 98	F	F3.4	R 100	F	F4.6	R 77	P
	C 117	F		C 81	F		C 104	F		C 80	P
	L 91	F		L 74	P		L 120	F		L 77	P
F3.5	R 112	F	F4.7	R 62	N/A	F3.6	R 105	F	F4.8	R 79	P
	C 93	F		C 63	N/A		C 110	F		C 70	P
	L 106	F		L 62	N/A		L 112	F		L 83	P
F3.7	R 111	F	F4.9	R 88	F	F3.7	R 111	F	F4.9	R 88	F
	C 100	F		C 94	F		C 100	F		C 94	F

N/A = inconclusive
P = Partial crack
F = Full crack

	L	112	F		L	92	P
F3.8	R	115	F	F4.12	R	116	F
	C	105	F		C	95	F
	L	118	F		L	101	F
F3.9	R	96	F				
	C	111	F				
	L	111	F				
F3.10	R	99	F				
	C	98	F				
	L	111	F				
F3.11	R	97	F				
	C	97	F				
	L	74	P				
F3.12	R	86	P				
	C	86	P				
	L	108	F				

6.3 NON-VISIBLE CRACK RESULTS

SAFT-Pan reconstructions were also created for every panel from the scan data. Figure 85 shows an example reconstruction of the panel between cracks F4.9 and F4.12 from Section 4. It should be noted that this testing and analysis was performed before cracks F4.10 and F4.11 were visible at the slab surface. The scans began at F4.9, with a 90 mm step size until the F4.12 position was reached. Two regions (circled in red) present similar inclusions as that of the transverse cracks discussed previously, and thus indicate the development of cracks not yet visible at the surface. A crack survey performed one month after the MIRA testing showed that both cracks are now visible on the surface. New cracks F1.5, F2.1 (shown in Figure 86), F4.1 and F4.3 were discovered in this same manner. The first non-visible crack in Figure 86 has not yet fully developed to the slab surface, and the second one shown is crack F2.1.

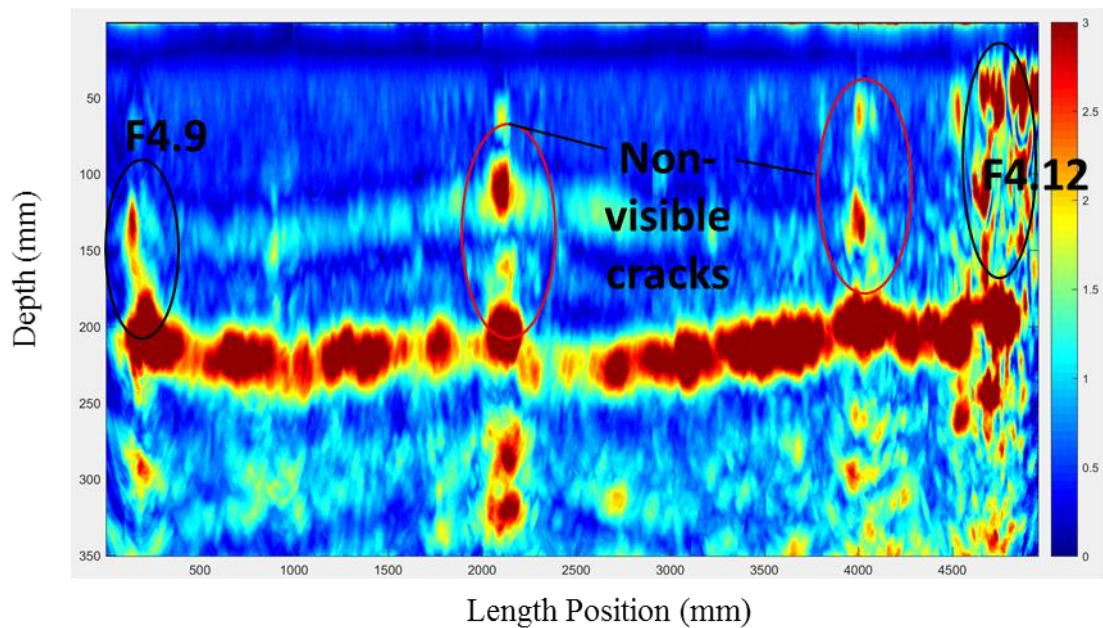


Figure 85. SAFT-Pan reconstruction of the panel between cracks F4.9 and F4.12 in Section 4.

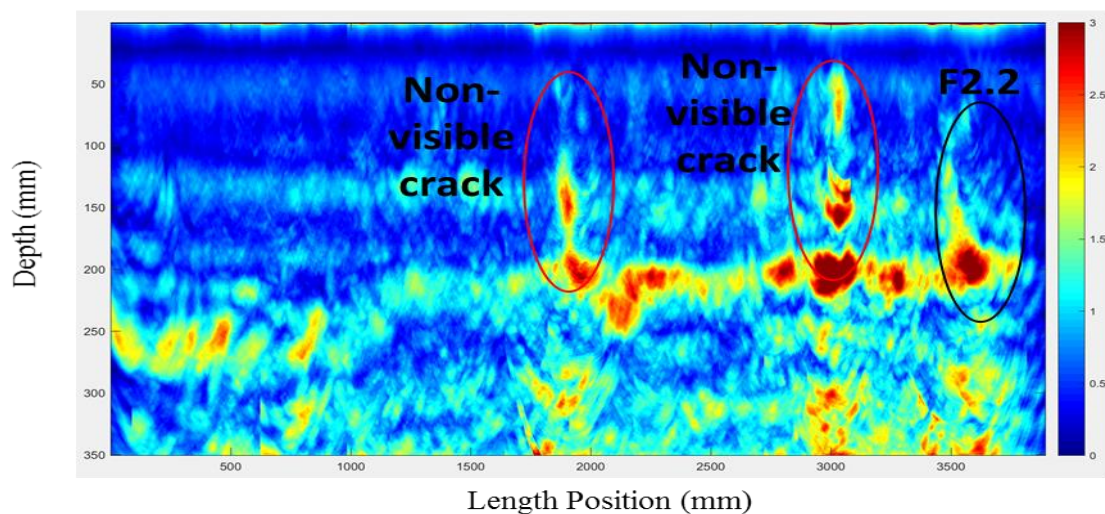


Figure 86. SAFT-Pan reconstruction of the panel between Section 1 and crack F2.2 in Section 2.

However, for some panels the identification of non-visible cracks was not as conclusive. Some mid-depth reflections can be misleading, most probably due to the presence of possible transverse bars or other delaminations. For a more comprehensive analysis of the panels, the HTI across the panel was also considered. Figure 87 to Figure 90 show the HTI variation trough the section's length along with the crack map for each section. Note that because of their short length, panels between cracks F1.2 and F1.3 (Section 1) and F3.10 and F3.11 (Section 3) were not selected for this evaluation. Also, section 1's edge and F1.1 panel was not considered for

further crack evaluation. As can be seen in Figure 87, the panel presents high HTI values throughout the entire panel length. This indication of damaged concrete was expected because there is poor consolidation in the interlock pavement near the short CRCP joint, causing a vertical gap between both pavements. This resulted in abnormal impact by heavy vehicles on section 1, which lead to joint faulting and corner cracks (Figure 91). As can be seen, there is a rise in HTI values at every visible crack, with the exception of crack F4.7. Again, a more in-depth analysis may be necessary to determine the cause of this abnormal result.

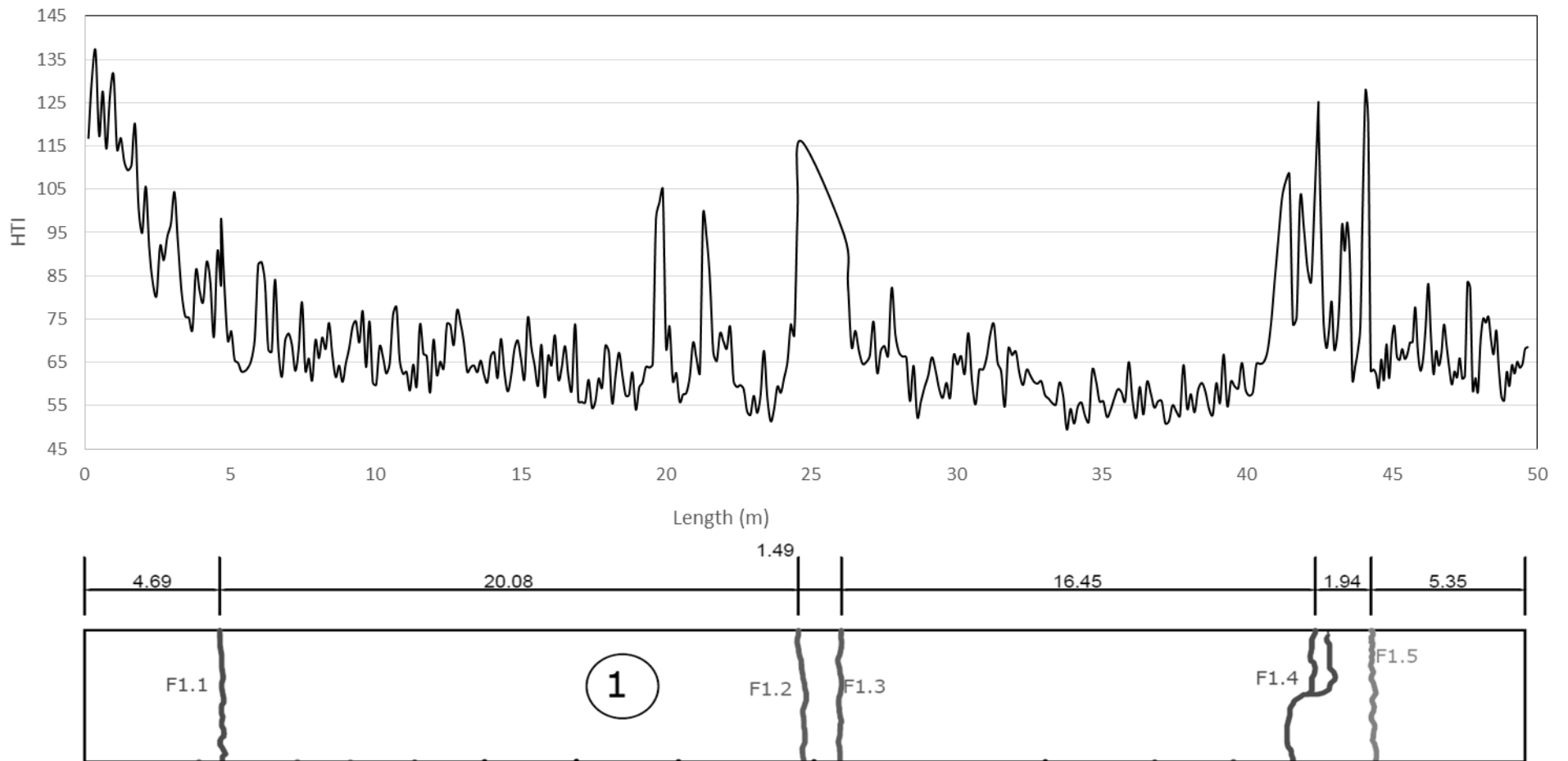


Figure 87. HTI trough Section 1

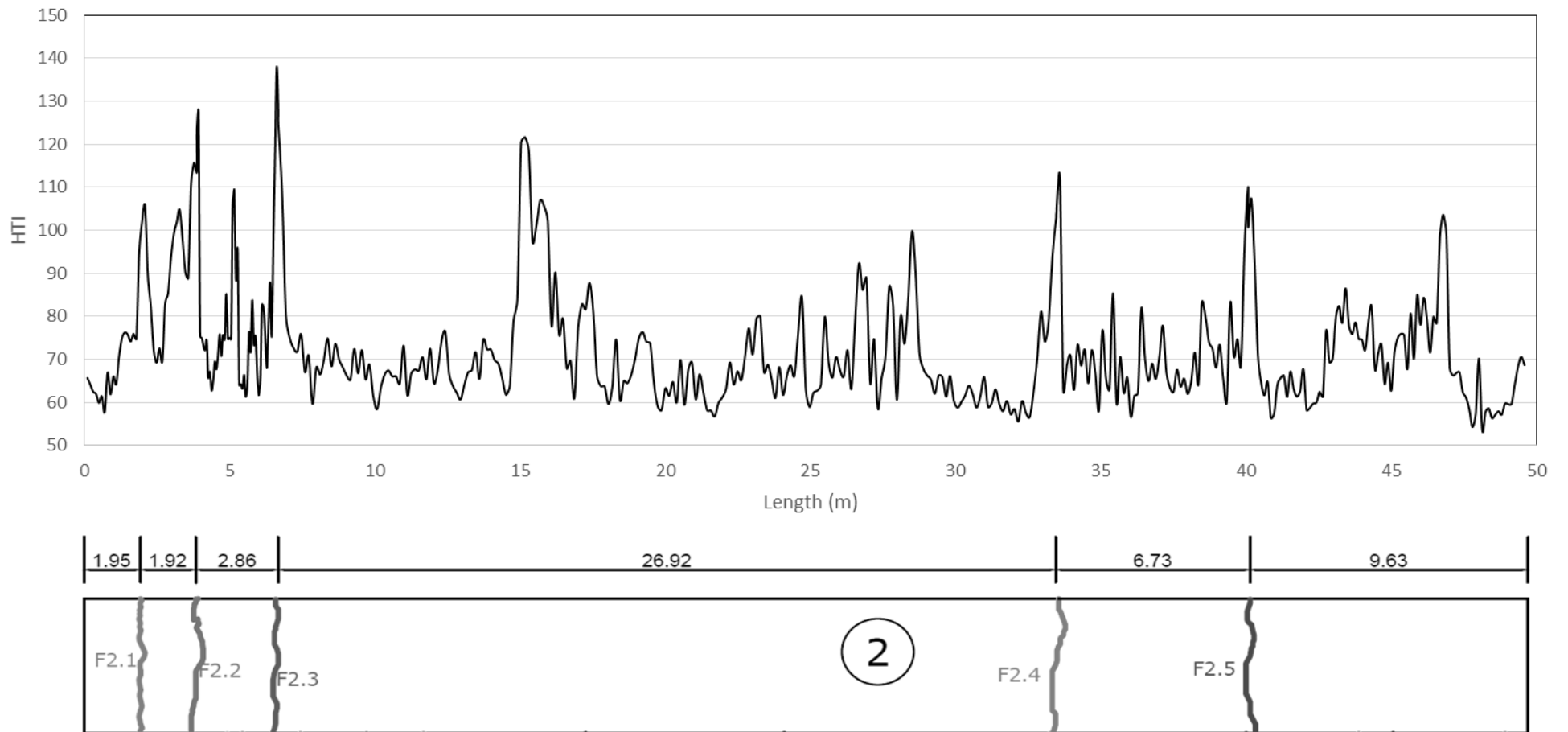


Figure 88. HTI trough Section 2

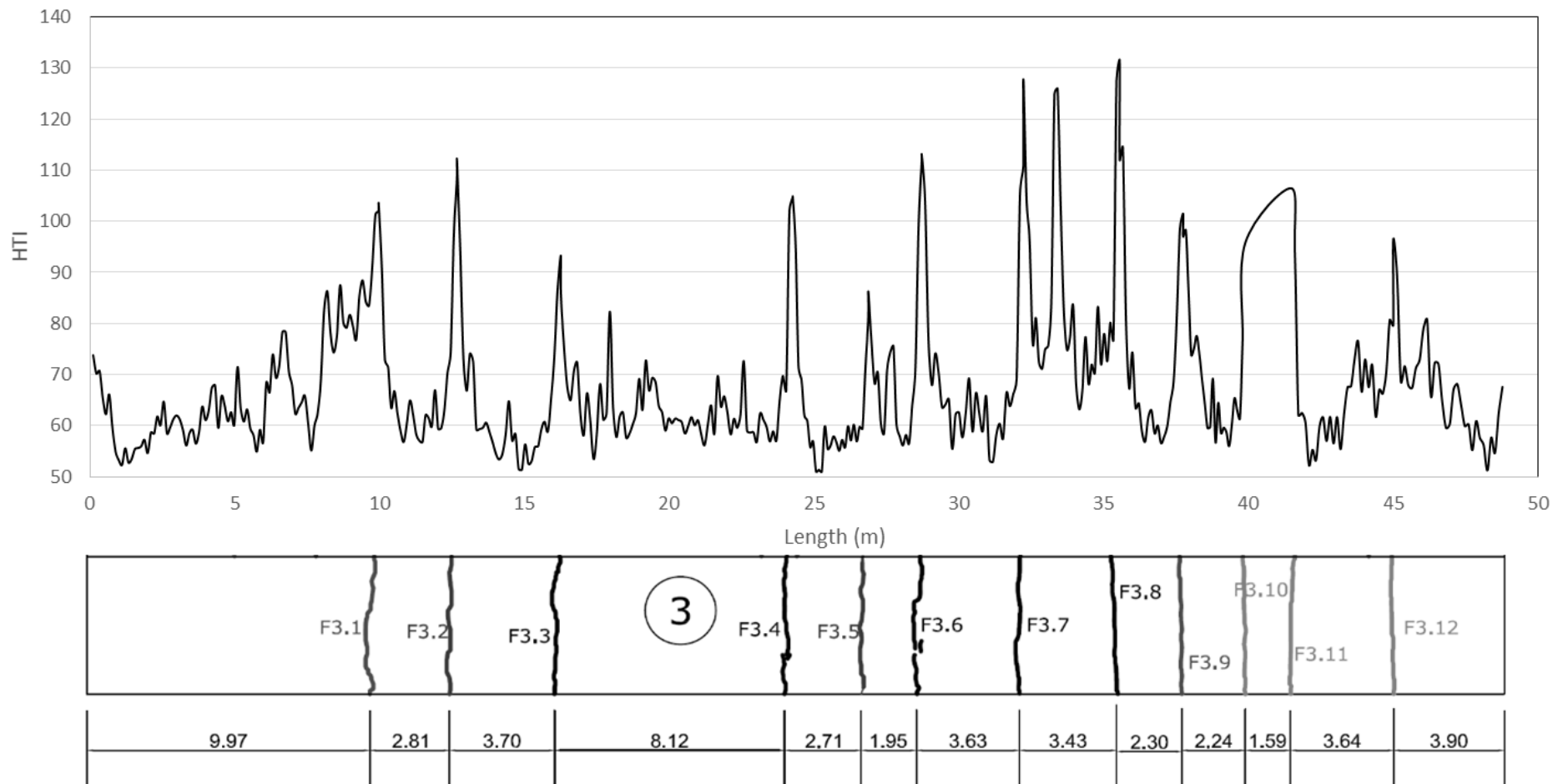


Figure 89. HTI trough Section 3

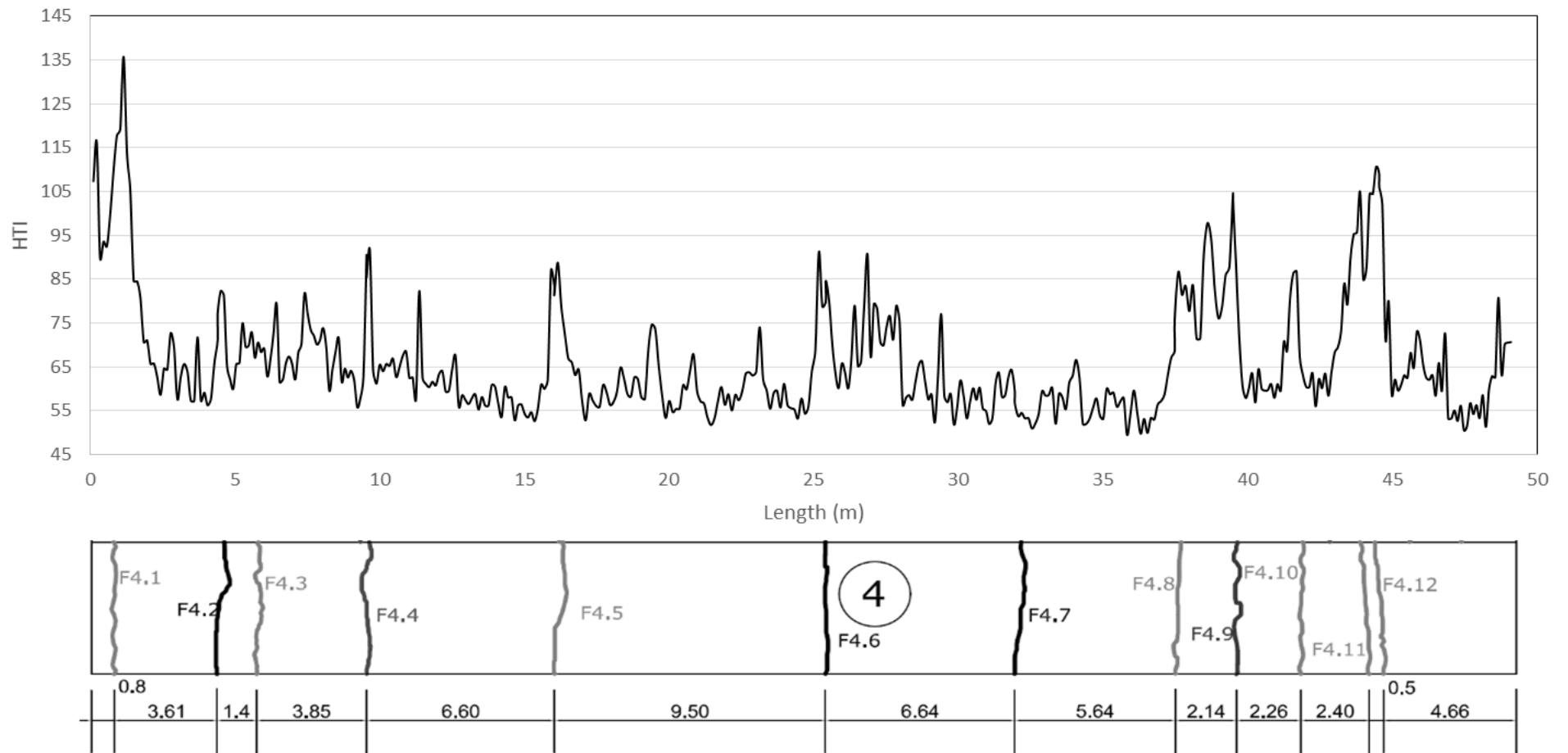


Figure 90. HTI trough Section



Figure 91. Distresses in the transition between interlock pavement and the short CRCP

Table 10 presents the results for the non-visible (IC) crack analysis. The distance from the section's edge (traffic direction) and the crack depth based on signal loss are displayed. Unlike the visible cracks, the majority of the non-visible cracks are partially developed, as anticipated since they do not yet show on the slab surface. However, some cracks presented a fully developed signal loss characterization. Those are intuitively expected to show up at the slab surface in the next crack surveys.

Table 10. Non-visible cracks

Section 1			Section 2			Section 3			Section 4		
Non-visible crack	Dist. (m)	Depth									
IC-1.1	6.08	P	IC-2.1	3.17	F	IC-3.1	6.64	P	IC-4.1	7.41	P
IC-1.2	7.74	P	IC-2.2	5.16	F	IC-3.2	8.19	F	IC-4.2	11.37	P
IC-1.3	8.4	P	IC-2.3	6.11	P	IC-3.3	8.64	P	IC-4.3	19.4	P
IC-1.4	9.79	P	IC-2.4	12.46	P	IC-3.4	19.43	P	IC-4.4	20.85	P
IC-1.5	10.72	P	IC-2.5	13.73	P	IC-3.5	27.85	P	IC-4.5	26.86	P
IC-1.6	16.89	P	IC-2.6	15.71	F	IC-3.6	33.63	F	IC-4.6	27.85	P
IC-1.7	19.89	F	IC-2.7	15.82	F	IC-3.7	34.17	P	IC-4.7	29.4	P
IC-1.8	21.4	F	IC-2.8	17.39	P	IC-3.8	35.24	P	IC-4.8	34.06	P
IC-1.9	27.02	P	IC-2.9	23.14	P	IC-3.9	38.97	P	IC-4.9	38.6	F
IC-1.10	41.34	F	IC-2.10	24.71	F	IC-3.10	44.43	P	IC-4.10	45.84	P
IC-1.11	45.08	P	IC-2.11	26.67	P	IC-3.11	46.81	P	IC-4.11	48.66	P
IC-1.12	46.25	P	IC-2.12	27.71	P						
IC-1.13	48.32	P	IC-2.13	28.49	F						
			IC-2.14	38.48	P						
			IC-2.15	43.2	F						
			IC-2.16	44.32	P						
			IC-2.17	46.12	P						
			IC-2.18	46.79	F						

For the partial cracks, the most predictable initiation pattern would be a bottom up (BU) crack due to the lack of surface development. However, several types of cracks were observed as can be seen in Figure 92. Only crack IC-3.3 presents a configuration that can be described as a BU crack below sensor 6. The majority of the partial cracks show the same characteristics of that of the visible cracks. This may be an indication that most non-visible cracks show a similar development pattern to that of the visible crack and will appear at the surface soon. It is assumed that for the short CRCP, most cracks begin at the reinforcement and develop up and down with time.

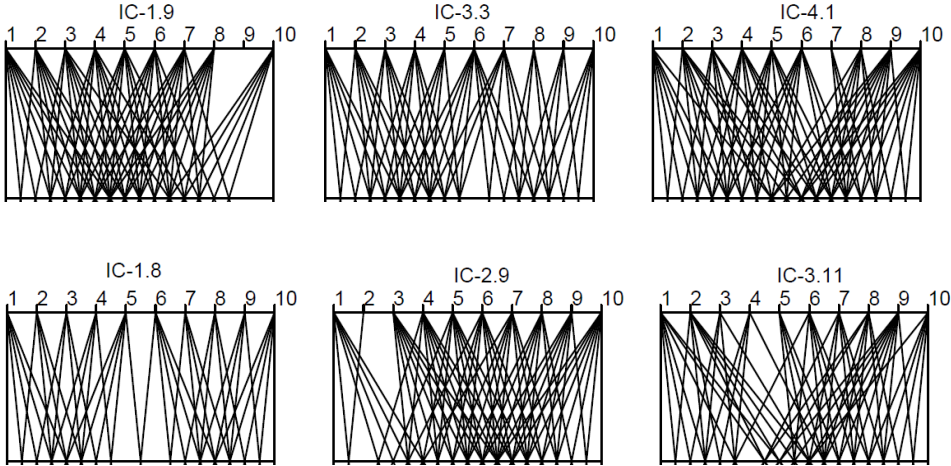


Figure 92. Signal loss due to high HTI in non-visible cracks

Figure 93 shows the new crack map with the addition of the non-visible cracks, as determined by the analysis techniques presented here. The new average crack spacing and pattern seems much more in line with traditional CRCP cracking.

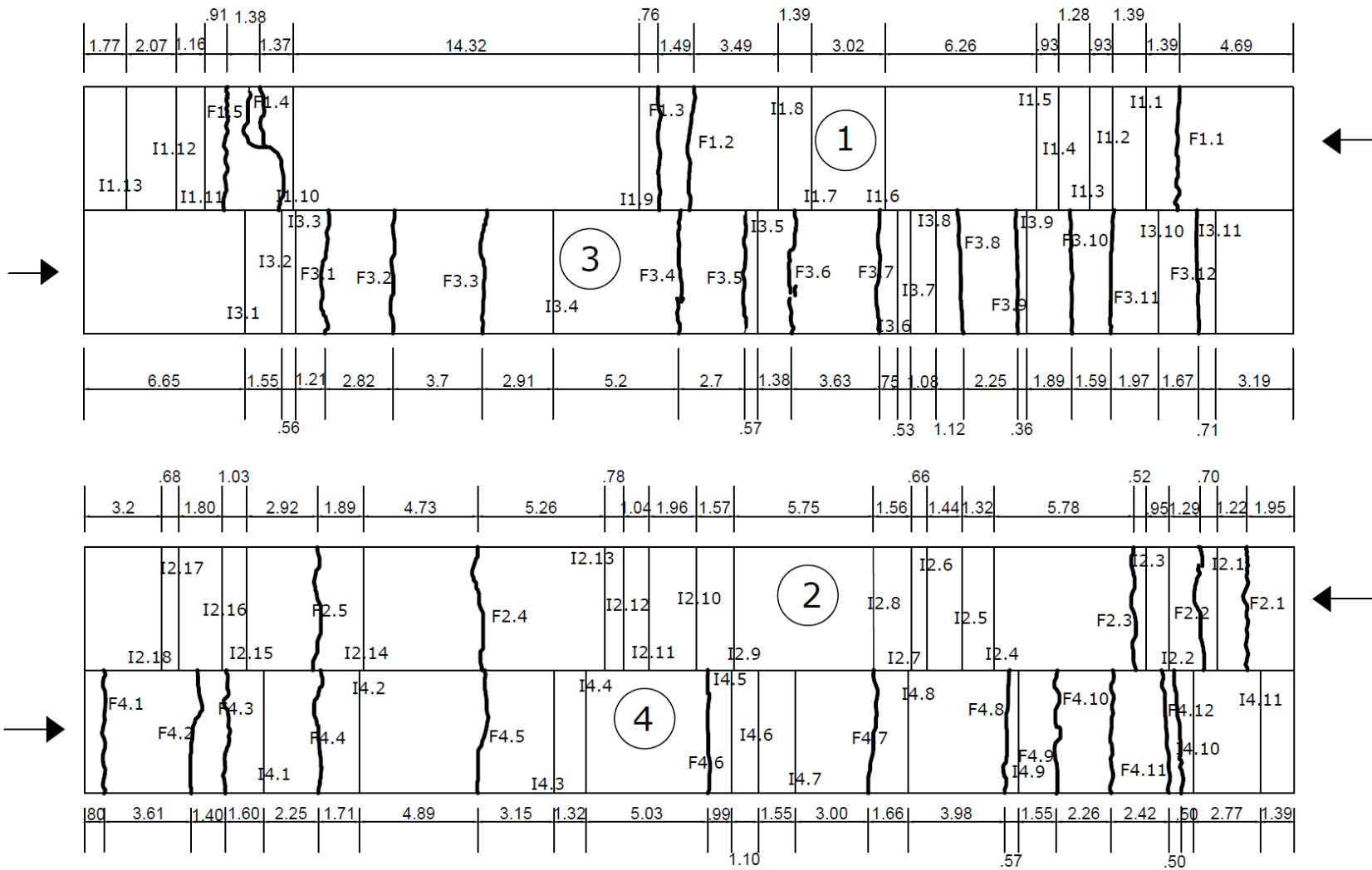


Figure 93. Crack map with non-visible cracks

6.4 CONCLUSIONS

Ultrasonic testing was performed on four CRCP sections in order to investigate transverse cracks. The analysis and interpretation of ultrasonic signals allows for the following conclusions and considerations:

- Most visible cracks presented a great level of damage (measured by means of HTI values). SAFT-Pan reconstructions showed attenuations around the slab mid-depth, proving the presence of distresses.
- The investigation of individual HTI values for each signal can be an indicator of the crack placement and stage of development. Cracks fully developed presented a signal loss (high HTI) indicative of the crack's shape and position.
- Peaks within the HTI values during the continuous panel survey allowed for the identification of all but one visible crack. The continuous survey also located the position of five cracks that would become visible in the slab surface a month after the survey, showing the technique's potential for detection of cracks not yet visible at the surface.
- Simulation of signal loss in the non-visible cracks showed development patterns similar to those found in visible cracks. It was expected that non-visible cracks would be bottom-up cracks, but only one crack presented this configuration. This may indicate that cracks initiate at the reinforcement (slab mid-depth).

CHAPTER 7 - SIMULATION

To verify the results outlined in the previous sections, a simulation program is being developed. This simulation aims to predict the outputs of MIRA, allowing for the creation of simulation reconstructions and velocity data. In the next sections the governing equations used for the simulation development are presented and later the equations are discretized by using elastodynamic finite integration technique.

7.1 GOVERNING EQUATIONS

Before discussing finite integration technique, the governing equations are presented. The equations of motion are

$$\rho \dot{v}_x = \frac{\partial \sigma_{xx}}{\partial x} + \frac{\partial \sigma_{xy}}{\partial y} + \frac{\partial \sigma_{xz}}{\partial z} + f_x \quad (21)$$

$$\rho \dot{v}_y = \frac{\partial \sigma_{xy}}{\partial x} + \frac{\partial \sigma_{yy}}{\partial y} + \frac{\partial \sigma_{zy}}{\partial z} + f_y \quad (22)$$

$$\rho \dot{v}_z = \frac{\partial \sigma_{xz}}{\partial x} + \frac{\partial \sigma_{yz}}{\partial y} + \frac{d\sigma}{dz} + f_z \quad (23)$$

where ρ is the density of the material under consideration; v_x , v_y and v_z are velocities; and f_x , f_y and f_z are body forces in x, y, and z directions, respectively. σ_{xx} , σ_{yy} , σ_{zz} , σ_{xy} , σ_{xz} and σ_{yz} are stress tensor components; note that $\sigma_{xy} = \sigma_{yx}$, $\sigma_{xz} = \sigma_{zx}$ and $\sigma_{yz} = \sigma_{zy}$. The dot on the velocity component represents the derivative with respect to time. As can be seen, the number of equations is three and the number of unknowns is nine. Therefore, six more equations are required. The other six equations are obtained from constitutive laws. Considering linear isotropic material and small deformations, Hooke's law results in the following constitutive equations:

$$\dot{\sigma}_{xx} = (\lambda + 2\mu) \left(\frac{\partial v_x}{\partial x} \right) + \lambda \left(\frac{\partial v_y}{\partial y} + \frac{\partial v_z}{\partial z} \right) \quad (24)$$

$$\dot{\sigma}_{yy} = (\lambda + 2\mu) \left(\frac{\partial v_y}{\partial y} \right) + \lambda \left(\frac{\partial v_x}{\partial x} + \frac{\partial v_z}{\partial z} \right) \quad (25)$$

$$\dot{\sigma}_{zz} = (\lambda + 2\mu) \left(\frac{\partial v_z}{\partial z} \right) + \lambda \left(\frac{\partial v_x}{\partial x} + \frac{\partial v_y}{\partial y} \right) \quad (26)$$

$$\dot{\sigma}_{xy} = \mu \left(\frac{\partial v_x}{\partial y} + \frac{\partial v_y}{\partial x} \right) \quad (27)$$

$$\dot{\sigma}_{xz} = \mu \left(\frac{\partial v_x}{\partial z} + \frac{\partial v_z}{\partial x} \right) \quad (28)$$

$$\dot{\sigma}_{yz} = \mu \left(\frac{\partial v_y}{\partial z} + \frac{\partial v_z}{\partial y} \right) \quad (29)$$

where λ and μ are material parameters which are called the Lamé constants.

7.2 FINITE INTEGRATION TECHNIQUE

Finite integration technique (FIT) was proposed by Weiland in 1977 to study electromagnetic waves (Weiland 1977). Fellingner et al. adapted Weiland's ideas to the governing equations of ultrasonic waves in solids, and developed a numerical procedure called the Elastodynamic Finite Integration Technique (EFIT) (Fellinger et al. 1995).

In addition to being accurate, EFIT is an appropriate tool for wave propagation problems in that it is able to handle strong heterogeneities while remaining computationally efficient. As a rule of thumb, the mesh size needs to be about one-tenth of the minimum wavelength of the emitted signal to avoid dispersion (Schubert et al. 1998).

For homogeneous media, EFIT is similar to finite difference time-domain (FDTD) methods if the latter also use the velocity-stress formalism on a staggered grid (Schubert et al. 1998), but EFIT can simulate strong heterogeneities better than FDTD. While finite element methods need huge computational time and memory to solve wave propagation problems, using EFIT can efficiently handle problems with hundreds of millions of nodes on a PC.

7.2.1 Discretized of Equations

The main idea of EFIT is to place the field component, which has to be calculated, at the center of an appropriate control volume, and to perform an integration of the corresponding equation over this cell. After discretizing the whole domain to finite volumes or cells, the governing equations are integrated over the cells, cubic cells in our problems. Figure 94 shows the arrangement of nine unknowns in finite integration technique; the velocity components are placed at the edge of the cell with the diagonal elements of the stress tensor on the corners and the off-diagonal elements on the faces of the cell, as shown in Figure 95.

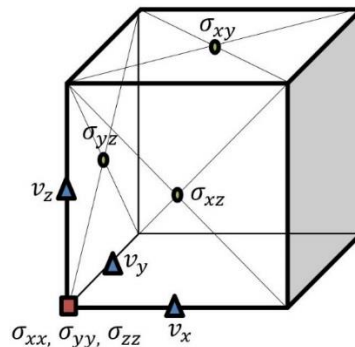


Figure 94. The cell for EFIT, in which velocity components are placed along the edges of the cell while the diagonal elements of the stress tensor are placed on the corners and the off-diagonal elements on the faces

In this method, one integrates the governing equations over the volume of the cells. Then the integrals in the right hand side of the equations are replaced by the integrals in the surface of the cells. Then all of the integrals are approximated using the midpoint rule. Applying this procedure to equations one yields:

$$\begin{aligned} \dot{v}_x^{(x_i, y_i, z_i)}(t) = \frac{1}{\rho^{(x_i, y_i, z_i)}} & \left(\frac{\sigma_{xx}^{(x_i + \frac{\Delta x}{2}, y_i, z_i)}(t) - \sigma_{xx}^{(x_i - \frac{\Delta x}{2}, y_i, z_i)}(t)}{\Delta x} \right. \\ & + \frac{\sigma_{xy}^{(x_i, y_i + \frac{\Delta y}{2}, z_i)}(t) - \sigma_{xy}^{(x_i, y_i - \frac{\Delta y}{2}, z_i)}(t)}{\Delta y} \\ & \left. + \frac{\sigma_{xz}^{(x_i, y_i, z_i + \frac{\Delta z}{2})}(t) - \sigma_{xz}^{(x_i, y_i, z_i - \frac{\Delta z}{2})}(t)}{\Delta z} \right) \end{aligned} \quad (30)$$

here x_i, y_i, z_i are the coordinates of the center of the cell associated to v_x ; $\Delta x, \Delta y, \Delta z$ are the size of velocity cell in the x, y, and z-directions; $\rho^{(x_i, y_i, z_i)}$ is the value of density at the center of velocity cell; $\dot{v}_x^{(x_i, y_i, z_i)}(t)$ is the value of acceleration at the center of velocity cell.

Applying central difference methods for time integration to Equation 30, velocity is determined:

$$v_x^{(x_i, y_i, z_i)} \left(t + \frac{\Delta t}{2} \right) = \dot{v}_x^{(x_i, y_i, z_i)}(t) \Delta t + v_x^{(x_i, y_i, z_i)} \left(t - \frac{\Delta t}{2} \right) \quad (31)$$

Applying finite integration technique to Equations 22 and 23, the following discretized forms are obtained:

$$\begin{aligned} \dot{v}_y^{(x_i, y_i, z_i)}(t) = \frac{1}{\rho^{(x_i, y_i, z_i)}} & \left(\frac{\sigma_{xy}^{(x_i + \frac{\Delta x}{2}, y_i, z_i)}(t) - \sigma_{xy}^{(x_i - \frac{\Delta x}{2}, y_i, z_i)}(t)}{\Delta x} + \frac{\sigma_{yy}^{(x_i, y_i + \frac{\Delta y}{2}, z_i)}(t) - \sigma_{yy}^{(x_i, y_i - \frac{\Delta y}{2}, z_i)}(t)}{\Delta y} \right. \\ & \left. + \frac{\sigma_{yz}^{(x_i, y_i, z_i + \frac{\Delta z}{2})}(t) - \sigma_{yz}^{(x_i, y_i, z_i - \frac{\Delta z}{2})}(t)}{\Delta z} \right) \end{aligned} \quad (32)$$

$$v_y^{(x_i, y_i, z_i)} \left(t + \frac{\Delta t}{2} \right) = \dot{v}_y^{(x_i, y_i, z_i)}(t) \Delta t + v_y^{(x_i, y_i, z_i)} \left(t - \frac{\Delta t}{2} \right) \quad (33)$$

$$\begin{aligned} \dot{v}_z^{(x_i, y_i, z_i)}(t) = \frac{1}{\rho^{(x_i, y_i, z_i)}} & \left(\frac{\sigma_{xz}^{(x_i + \frac{\Delta x}{2}, y_i, z_i)}(t) - \sigma_{xz}^{(x_i - \frac{\Delta x}{2}, y_i, z_i)}(t)}{\Delta x} + \frac{\sigma_{yz}^{(x_i, y_i + \frac{\Delta y}{2}, z_i)}(t) - \sigma_{yz}^{(x_i, y_i - \frac{\Delta y}{2}, z_i)}(t)}{\Delta y} \right. \\ & \left. + \frac{\sigma_{zz}^{(x_i, y_i, z_i + \frac{\Delta z}{2})}(t) - \sigma_{zz}^{(x_i, y_i, z_i - \frac{\Delta z}{2})}(t)}{\Delta z} \right) \end{aligned} \quad (34)$$

$$v_z^{(x_i, y_i, z_i)} \left(t + \frac{\Delta t}{2} \right) = \dot{v}_z^{(x_i, y_i, z_i)}(t) \Delta t + v_z^{(x_i, y_i, z_i)} \left(t - \frac{\Delta t}{2} \right) \quad (35)$$

The same procedure is applied to stress components and the following discretized equations are obtained:

$$\begin{aligned} \dot{\sigma}_{xx}^{(x_i, y_i, z_i)} \left(t + \frac{\Delta t}{2} \right) &= (\lambda^{(x_i, y_i, z_i)} + 2\mu^{(x_i, y_i, z_i)}) \left(\frac{v_x^{(x_i + \frac{\Delta x}{2}, y_i, z_i)} \left(t + \frac{\Delta t}{2} \right) - v_x^{(x_i - \frac{\Delta x}{2}, y_i, z_i)} \left(t + \frac{\Delta t}{2} \right)}{\Delta x} \right. \\ &\quad + \lambda^{(x_i, y_i, z_i)} \left[\frac{v_y^{(x_i, y_i + \frac{\Delta y}{2}, z_i)} \left(t + \frac{\Delta t}{2} \right) - v_y^{(x_i, y_i - \frac{\Delta y}{2}, z_i)} \left(t + \frac{\Delta t}{2} \right)}{\Delta y} \right. \\ &\quad \left. \left. + \frac{v_z^{(x_i, y_i, z_i + \frac{\Delta z}{2})} \left(t + \frac{\Delta t}{2} \right) - v_z^{(x_i, y_i, z_i - \frac{\Delta z}{2})} \left(t + \frac{\Delta t}{2} \right)}{\Delta z} \right] \right) \end{aligned} \quad (36)$$

$$\sigma_{xx}^{(x_i, y_i, z_i)} (t + \Delta t) = \dot{\sigma}_{xx}^{(x_i, y_i, z_i)} \left(t + \frac{\Delta t}{2} \right) \Delta t + \sigma_{xx}^{(x_i, y_i, z_i)} (t) \quad (37)$$

$$\begin{aligned} \dot{\sigma}_{yy}^{(x_i, y_i, z_i)} \left(t + \frac{\Delta t}{2} \right) &= (\lambda^{(x_i, y_i, z_i)} + 2\mu^{(x_i, y_i, z_i)}) \left(\frac{v_y^{(x_i, y_i + \frac{\Delta y}{2}, z_i)} \left(t + \frac{\Delta t}{2} \right) - v_y^{(x_i, y_i - \frac{\Delta y}{2}, z_i)} \left(t + \frac{\Delta t}{2} \right)}{\Delta y} \right. \\ &\quad + \lambda^{(x_i, y_i, z_i)} \left[\frac{v_x^{(x_i + \frac{\Delta x}{2}, y_i, z_i)} \left(t + \frac{\Delta t}{2} \right) - v_x^{(x_i - \frac{\Delta x}{2}, y_i, z_i)} \left(t + \frac{\Delta t}{2} \right)}{\Delta x} \right. \\ &\quad \left. \left. + \frac{v_z^{(x_i, y_i, z_i + \frac{\Delta z}{2})} \left(t + \frac{\Delta t}{2} \right) - v_z^{(x_i, y_i, z_i - \frac{\Delta z}{2})} \left(t + \frac{\Delta t}{2} \right)}{\Delta z} \right] \right) \end{aligned} \quad (38)$$

$$\sigma_{yy}^{(x_i, y_i, z_i)} (t + \Delta t) = \dot{\sigma}_{yy}^{(x_i, y_i, z_i)} \left(t + \frac{\Delta t}{2} \right) \Delta t + \sigma_{yy}^{(x_i, y_i, z_i)} (t) \quad (39)$$

$$\begin{aligned} \dot{\sigma}_{zz}^{(x_i, y_i, z_i)} \left(t + \frac{\Delta t}{2} \right) &= (\lambda^{(x_i, y_i, z_i)} + 2\mu^{(x_i, y_i, z_i)}) \left(\frac{v_z^{(x_i, y_i, z_i + \frac{\Delta z}{2})} \left(t + \frac{\Delta t}{2} \right) - v_z^{(x_i, y_i, z_i - \frac{\Delta z}{2})} \left(t + \frac{\Delta t}{2} \right)}{\Delta z} \right. \\ &\quad + \lambda^{(x_i, y_i, z_i)} \left[\frac{v_x^{(x_i + \frac{\Delta x}{2}, y_i, z_i)} \left(t + \frac{\Delta t}{2} \right) - v_x^{(x_i - \frac{\Delta x}{2}, y_i, z_i)} \left(t + \frac{\Delta t}{2} \right)}{\Delta x} \right. \\ &\quad \left. \left. + \frac{v_y^{(x_i, y_i + \frac{\Delta y}{2}, z_i)} \left(t + \frac{\Delta t}{2} \right) - v_y^{(x_i, y_i - \frac{\Delta y}{2}, z_i)} \left(t + \frac{\Delta t}{2} \right)}{\Delta y} \right] \right) \end{aligned} \quad (40)$$

$$\sigma_{zz}^{(x_i, y_i, z_i)} (t + \Delta t) = \dot{\sigma}_{zz}^{(x_i, y_i, z_i)} \left(t + \frac{\Delta t}{2} \right) \Delta t + \sigma_{zz}^{(x_i, y_i, z_i)} (t) \quad (41)$$

$$\begin{aligned} \dot{\sigma}_{xy}^{(x_i, y_i, z_i)} \left(t + \frac{\Delta t}{2} \right) &= \mu^{(x_i, y_i, z_i)} \left(\frac{v_x^{(x_i, y_i + \frac{\Delta y}{2}, z_i)} \left(t + \frac{\Delta t}{2} \right) - v_x^{(x_i, y_i - \frac{\Delta y}{2}, z_i)} \left(t + \frac{\Delta t}{2} \right)}{\Delta y} \right. \\ &\quad \left. + \frac{v_y^{(x_i + \frac{\Delta x}{2}, y_i, z_i)} \left(t + \frac{\Delta t}{2} \right) - v_y^{(x_i - \frac{\Delta x}{2}, y_i, z_i)} \left(t + \frac{\Delta t}{2} \right)}{\Delta x} \right) \end{aligned} \quad (42)$$

$$\sigma_{xy}^{(x_i, y_i, z_i)} (t + \Delta t) = \dot{\sigma}_{xy}^{(x_i, y_i, z_i)} \left(t + \frac{\Delta t}{2} \right) \Delta t + \sigma_{xy}^{(x_i, y_i, z_i)} (t) \quad (43)$$

$$\begin{aligned} \dot{\sigma}_{xz}^{(x_i, y_i, z_i)} \left(t + \frac{\Delta t}{2} \right) &= \mu^{(x_i, y_i, z_i)} \left(\frac{v_x^{(x_i, y_i, z_i + \frac{\Delta z}{2})} \left(t + \frac{\Delta t}{2} \right) - v_x^{(x_i, y_i, z_i - \frac{\Delta z}{2})} \left(t + \frac{\Delta t}{2} \right)}{\Delta z} \right. \\ &\quad \left. + \frac{v_z^{(x_i + \frac{\Delta x}{2}, y_i, z_i)} \left(t + \frac{\Delta t}{2} \right) - v_z^{(x_i - \frac{\Delta x}{2}, y_i, z_i)} \left(t + \frac{\Delta t}{2} \right)}{\Delta x} \right) \end{aligned} \quad (44)$$

$$\sigma_{xz}^{(x_i, y_i, z_i)} (t + \Delta t) = \dot{\sigma}_{xz}^{(x_i, y_i, z_i)} \left(t + \frac{\Delta t}{2} \right) \Delta t + \sigma_{xz}^{(x_i, y_i, z_i)} (t) \quad (45)$$

$$\dot{\sigma}_{yz}^{(x_i, y_i, z_i)} \left(t + \frac{\Delta t}{2} \right) = \mu^{(x_i, y_i, z_i)} \left(\frac{v_y^{(x_i, y_i, z_i + \frac{\Delta z}{2})} \left(t + \frac{\Delta t}{2} \right) - v_y^{(x_i, y_i, z_i - \frac{\Delta z}{2})} \left(t + \frac{\Delta t}{2} \right)}{\Delta z} + \frac{v_z^{(x_i, y_i + \frac{\Delta y}{2}, z_i)} \left(t + \frac{\Delta t}{2} \right) - v_z^{(x_i, y_i - \frac{\Delta y}{2}, z_i)} \left(t + \frac{\Delta t}{2} \right)}{\Delta y} \right) \quad (46)$$

$$\sigma_{yz}^{(x_i, y_i, z_i)} (t + \Delta t) = \dot{\sigma}_{yz}^{(x_i, y_i, z_i)} \left(t + \frac{\Delta t}{2} \right) \Delta t + \sigma_{yz}^{(x_i, y_i, z_i)} (t) \quad (47)$$

For heterogeneous media, a suitable discretization of the material parameters is essential. It is shown that the only consistent way to obtain stable results is to choose the material parameter grid to coincide with the σ_{ii} integration cells (Fellinger et al. 1995). As a consequence, the density and lame constants at grid points related to velocity and shear stresses must be obtained using averaging. The right-hand sides of Equations 30, 32, and 34 must be reconsidered respectively in terms of the expressions for density

$$\rho^{(x_i, y_i, z_i)} = \frac{1}{2} \left(\rho^{(x_i + \frac{\Delta x}{2}, y_i, z_i)} + \rho^{(x_i - \frac{\Delta x}{2}, y_i, z_i)} \right) \quad (48)$$

$$\rho^{(x_i, y_i, z_i)} = \frac{1}{2} \left(\rho^{(x_i, y_i + \frac{\Delta y}{2}, z_i)} + \rho^{(x_i, y_i - \frac{\Delta y}{2}, z_i)} \right) \quad (49)$$

$$\rho^{(x_i, y_i, z_i)} = \frac{1}{2} \left(\rho^{(x_i, y_i, z_i + \frac{\Delta z}{2})} + \rho^{(x_i, y_i, z_i - \frac{\Delta z}{2})} \right) \quad (50)$$

As the integration cells coincide with the material parameters grid, no averaging is needed for lame parameters in equations 42, 44 and 46. The shear modulus averaged for the equations mentioned, respectively are obtained from Equations 45, 46, and 47 accordingly

$$\frac{1}{\mu^{(x_i, y_i, z_i)}} = \frac{1}{4} \left(\frac{1}{\mu^{(x_i - \frac{\Delta x}{2}, y_i - \frac{\Delta y}{2}, z_i)}} + \frac{1}{\mu^{(x_i - \frac{\Delta x}{2}, y_i + \frac{\Delta y}{2}, z_i)}} + \frac{1}{\mu^{(x_i + \frac{\Delta x}{2}, y_i - \frac{\Delta y}{2}, z_i)}} + \frac{1}{\mu^{(x_i + \frac{\Delta x}{2}, y_i + \frac{\Delta y}{2}, z_i)}} \right) \quad (51)$$

$$\frac{1}{\mu^{(x_i, y_i, z_i)}} = \frac{1}{4} \left(\frac{1}{\mu^{(x_i - \frac{\Delta x}{2}, y_i, z_i - \frac{\Delta z}{2})}} + \frac{1}{\mu^{(x_i - \frac{\Delta x}{2}, y_i, z_i + \frac{\Delta z}{2})}} + \frac{1}{\mu^{(x_i + \frac{\Delta x}{2}, y_i, z_i - \frac{\Delta z}{2})}} + \frac{1}{\mu^{(x_i + \frac{\Delta x}{2}, y_i, z_i + \frac{\Delta z}{2})}} \right) \quad (52)$$

$$\frac{1}{\mu^{(x_i, y_i, z_i)}} = \frac{1}{4} \left(\frac{1}{\mu^{(x_i, y_i - \frac{\Delta y}{2}, z_i - \frac{\Delta z}{2})}} + \frac{1}{\mu^{(x_i, y_i + \frac{\Delta y}{2}, z_i - \frac{\Delta z}{2})}} + \frac{1}{\mu^{(x_i, y_i - \frac{\Delta y}{2}, z_i + \frac{\Delta z}{2})}} + \frac{1}{\mu^{(x_i, y_i + \frac{\Delta y}{2}, z_i + \frac{\Delta z}{2})}} \right) \quad (53)$$

In order for the three-dimensional EFIT algorithm to be numerically stable, the time step must satisfy

$$\Delta t \leq \frac{1}{c_{max} \sqrt{\frac{1}{\Delta x^2} + \frac{1}{\Delta y^2} + \frac{1}{\Delta z^2}}} \quad (54)$$

where c_{max} is the speed of longitudinal wave. In addition, to avoid numerical dispersion the following criterion must be met

$$\min(\Delta x, \Delta y, \Delta z) \leq \frac{1}{10} \lambda_{min} = \frac{1}{10} \frac{c_{min}}{f_{max}} \quad (55)$$

Where c_{min} the velocity of the shear is wave and f_{max} is the maximum frequency of the emitted signal.

7.3 DEVELOPED PROGRAM

We have developed a program based on finite integration technique. The program is capable of simulating wave propagation in two and three-dimensional elastic and viscoelastic heterogeneous medium. The program allows the user to simulate the propagation of waves in an elastic or viscoelastic media containing reinforcement, delaminated regions and vertical cracks. The user can also define free, fixed, or absorbing boundaries.

A special version of the program is devoted to the simulation of linear arrays. In this version of the program, a signal is sent by a sensor and is recorded by sensors located at the position of receiving transducers. After completing the simulation for one sensor, the program automatically restarts the simulation for the adjacent sending transducer. This process is repeated for all of sending sensors. Finally, all of the data recorded by the receiving transducers is written to a file for processing using SAFT.

In the following sections, some of the capabilities of the program are shown by presenting three examples. In all of the examples, propagation of MIRA signals in a two-dimensional media was simulated. Transmitting transducers of the device emits horizontal shear waves. It is assumed that the linear array device, which has ten rows of transducers, is located at the top boundary of the medium. Spacing between adjacent sensors is 0.040 m and the first transducer is located 0.40 m from the left top edge of the medium. Temporal and spatial grid size in all the examples are 0.2 μ s and 0.001 m, respectively. It is assumed that the transducers send and receive horizontal shear stresses. The center frequency of the emitted signals is 50 kHz.

7.3.1 Elastic medium with delamination

In this example, propagation of MIRA signals in an elastic medium containing a delaminated region is simulated. Density and shear velocity in the medium are assumed to be 2400 kg/m³ and 2300 m/s. The right and left boundaries of the medium are assumed to be absorbing, and the bottom boundary is free. Depth of the medium is 0.30 m. The delaminated region is located the depth 0.15 m. This region is assumed to be rectangular with 0.004 m thickness and 0.10 m width. Horizontal distance between the left end of the delaminated region and first sending transducers is 0.13 m. Acoustic impedance of this region is decreased by assuming that the velocity of shear wave in this region is 100 m/s. Propagation of shear waves in this medium when the second transducer is the sending transducer is shown in Figure 95.

The recorded signals are processed by using SAFT. The reconstructed images are shown in Figure 96. As can be seen, SAFT is placed the backwall and the delaminated region correctly.

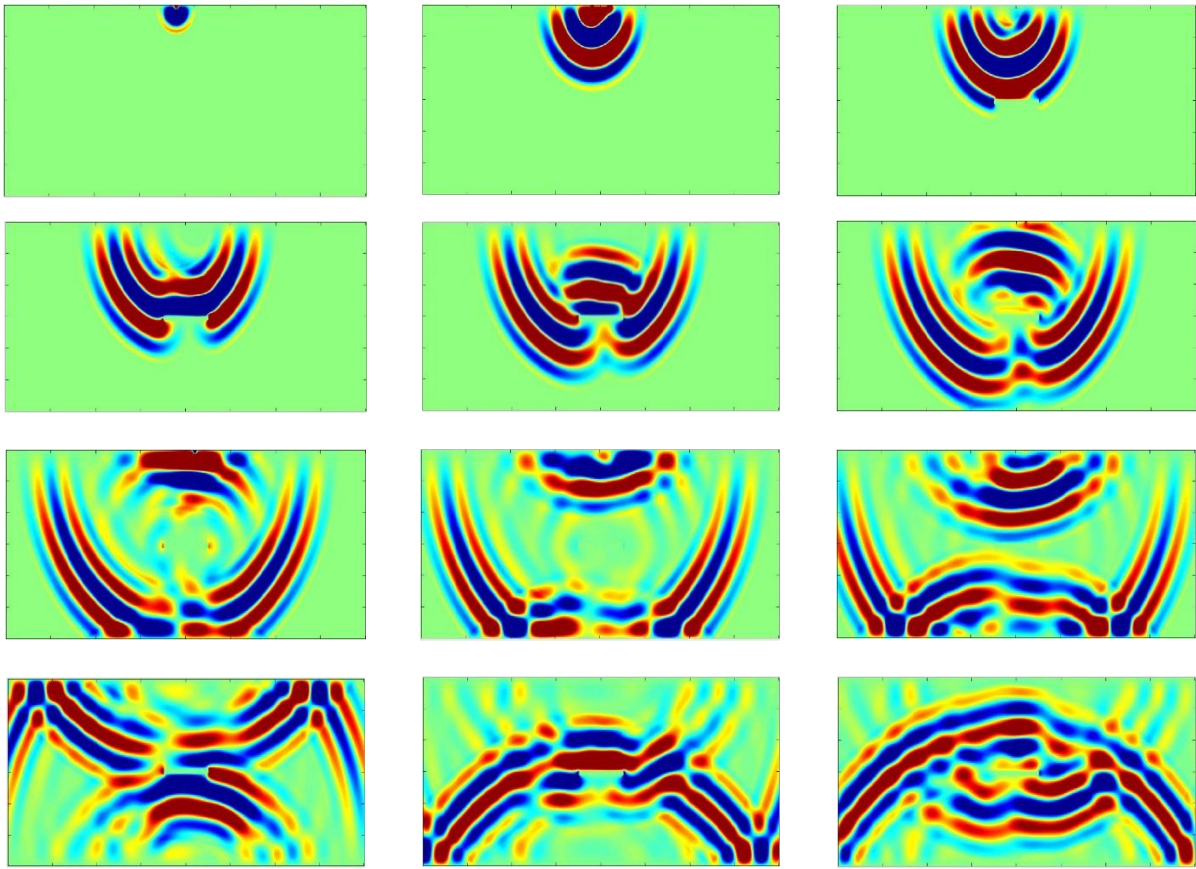


Figure 95. Wavefield Snapshots for an elastic medium with delamination.

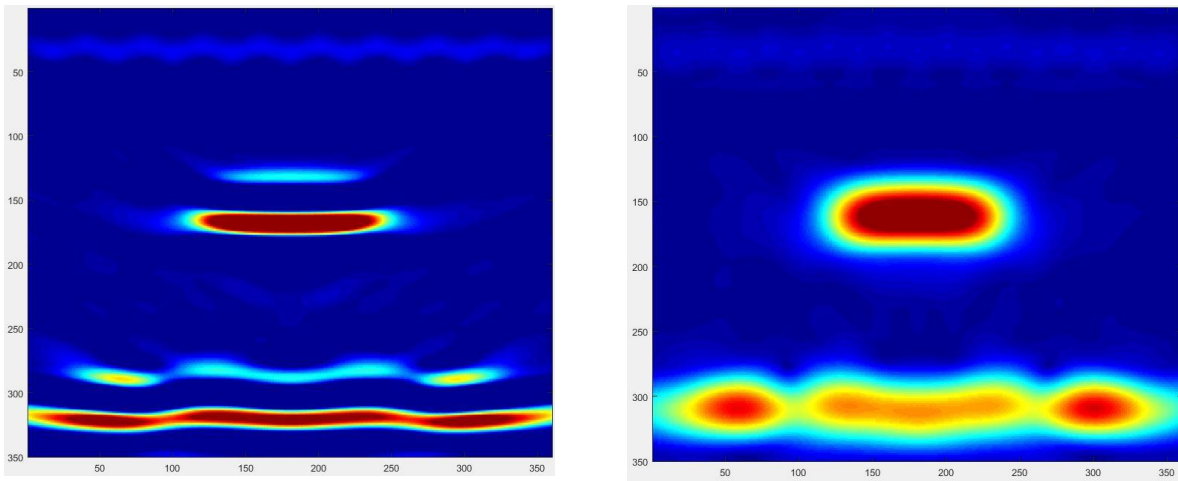


Figure 96. Instantaneous and full wave images for an elastic medium with delamination.

7.3.2 Viscoelastic medium with vertical cracks

In this example, the medium is assumed to be viscoelastic. The goal is to show the capability of the developed program in the simulation of the propagation of shear waves in such a medium with the presence of vertical cracks. The density of the medium and velocity of shear wave are assumed to be 2400 kg/m^3 and 2600 m/s , respectively. The depth of the medium is 0.20 m . Maxwell model presented in Kristek and Moczo (2003) is used to simulate viscosity. In the viscoelastic model only one anelastic coefficient is used. The value of this coefficient is 0.15 . The value of corresponding relaxation frequency is $60,000\pi \text{ rad/s}$. The cracks are started from the top surface of the medium. Here, two cracks are simulated where the first is located between transducers two and three and the second crack is between transducers 5 and 6. These cracks are simulated by rectangular regions with very low acoustic impedance. The density and shear velocity in the cracked region is assumed to be 50 kg/m^3 and 50 m/s . Although in reality, the crack mouth opening is very small, here we assume that it is 4 mm to avoid using a very fine mesh. Propagation of shear waves in this medium is shown in Figure 97. The reconstructed images obtained from the simulations are presented in Figure 98. As it is well known, SAFT is not capable of showing the surfaces of cracks. At best, it is only capable of locating the tip of cracks.

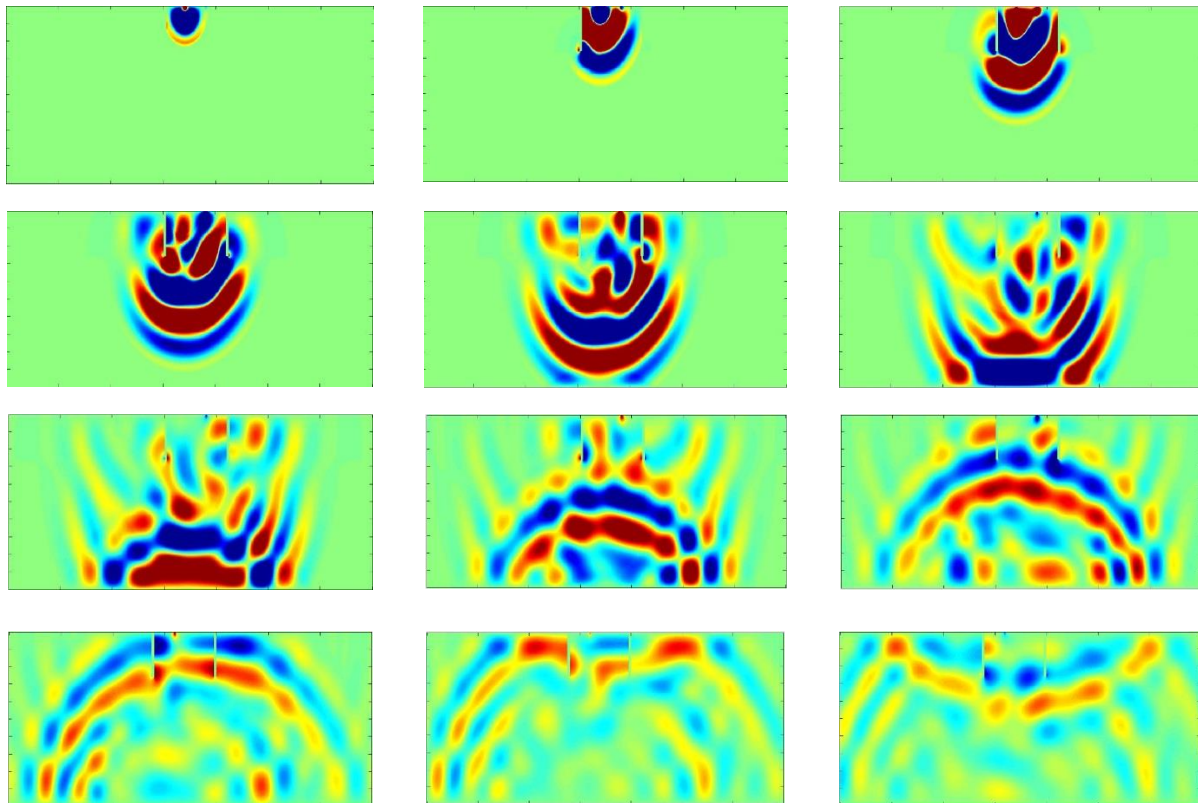


Figure 97. Wavefield Snapshots for a medium with vertical surface cracks.

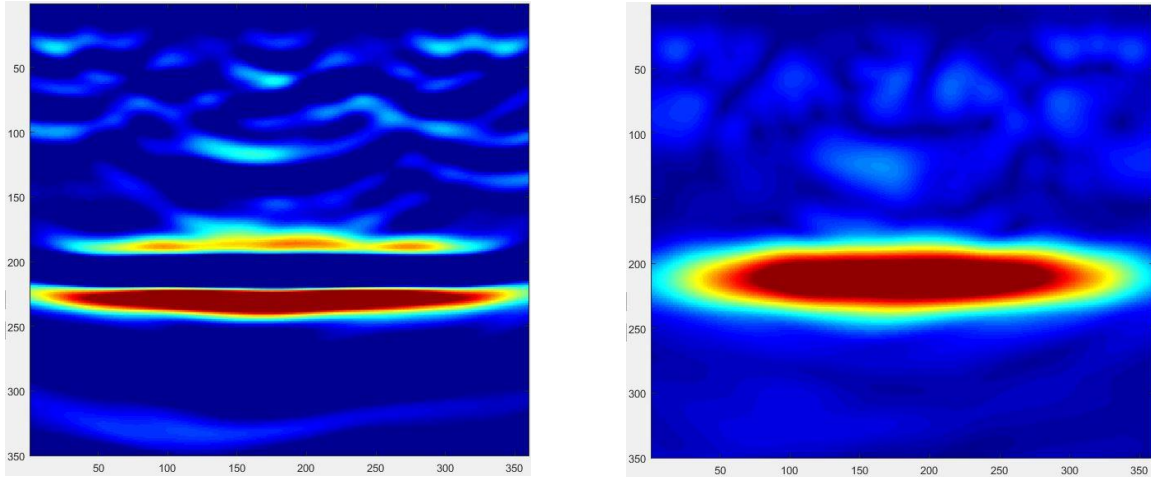


Figure 98. Instantaneous and full wave images for an elastic medium with two vertical cracks.

7.3.3 Viscoelastic medium containing steel rebar

In the last example, a reinforced concrete slab is considered. It is assumed that concrete is a viscoelastic medium. We account for viscosity to implicitly address attenuation of propagating waves in concrete due to its heterogeneity. Density and velocity of shear wave in concrete is assumed to be 2400 kg/m^3 and 2600 m/s , respectively. These values for the steel rebar are 7800 kg/m^3 and 3200 m/s , respectively. The viscoelastic model and the value of its parameters are the same as those presented in example two. Similar to the two previous examples, we first present some wavefield snapshots; these snapshots are shown in Figure 6. As can be seen, when waves encounter a material with different acoustic impedance such as a steel rebar, part of its energy passes through the new medium and part of that reflects back to the medium where the wave was transmitted. Reconstructed images of this problem is given in Figure 7. As it is seen from this figure, by processing the recorded signals by SAFT, one can locate the reinforcement successfully.

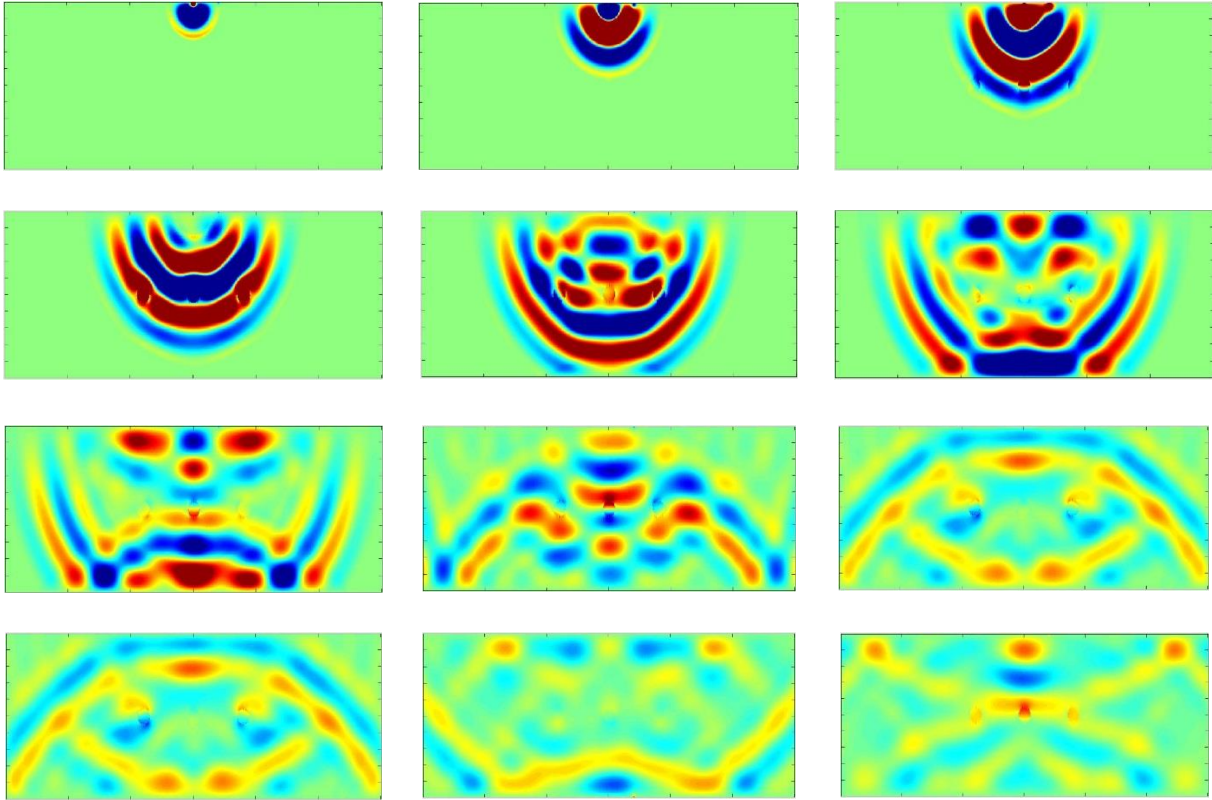


Figure 99. Wavefield Snapshots for a reinforced concrete.

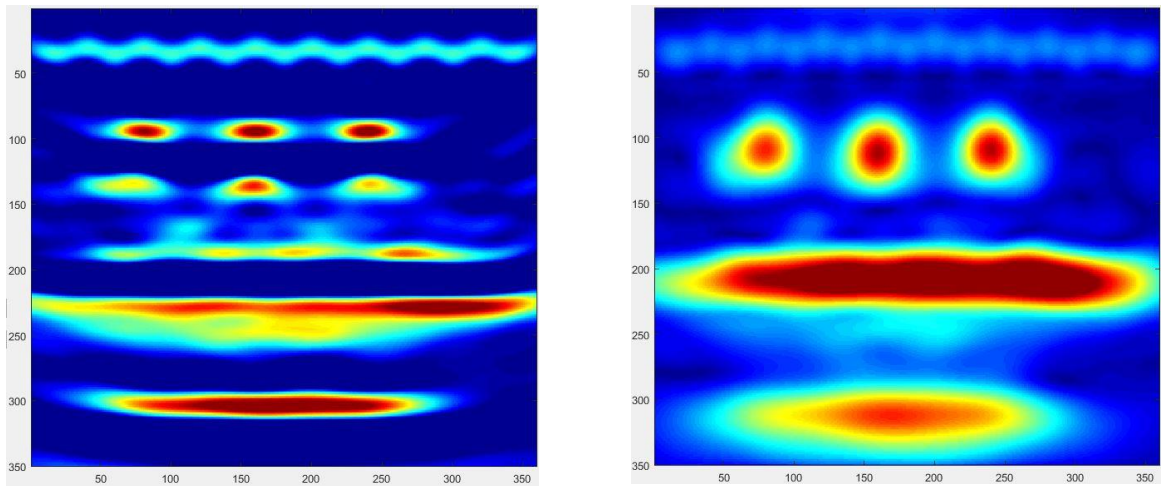


Figure 100. Instantaneous and full wave images for an elastic medium with three rebar.

Since three-dimensional simulations are unavoidable for many other problems, we are parallelizing the EFIT code to decrease the runtime. This part of the project is still in progress and is not completed. In the next sections we provide some preliminary results of parallelizations.

7.4 PARALLELIZATION WITH OPENMP AND GPU

Three different scenarios were used: tests with no parallelization, tests that were parallelized on the CPU using OpenMP directives, and tests that were parallelized on the GPU with OpenACC directives. Two different compilers were used to compare the results, GNU and Portland Group compilers. Depending on the compiler used, OpenMP directives were processed differently: with The Portland Group compiler, the number of cores that could be used to parallelize was limited to 4, while the GNU fortran compiler allowed for all 8 CPU cores to be used. This limitation exists in PGI version 16.5, but will be removed from the academic license we are using in version 16.7.

Sequential (non-parallelized) runs take a calculation done on a piece of independent data, and run it once on a piece of data, then move on and run it again on the next piece of data, and so on until the necessary number of computations are done. Runs parallelized with OpenMP take a certain number of these computations (4 or 8 in these cases) and run them at the same time, each on one CPU core. Runs parallelized with OpenACC take the data being worked on, transfer it to the GPU, then give each GPU core (1024 on the card tested (GeForce GTX 960 made by NVIDIA)) computations to run in parallel. The results are then transferred back to the CPU.

In the GNU fortran compiler, there are four different levels of optimization, defined by using the `-O*` flag at compilation time, with the star replaced by a number from 0 to 3. 0 introduces no optimization, while 3 introduces maximum optimization. These optimizations are of many different types. In The Portland Group compiler, there is only one commonly used optimization flag: `-fast`. For the PGI compiler, `-Minfo` tells the compiler to print what optimizations and parallelizations are being performed.

As mentioned earlier, another method for parallelizing a code in running that on GPU. The bottleneck of this method is transferring data between CPU and GPU. This process is very slow and must be managed efficiently. GPU memory management is only applied to the tests run on OpenACC, as the issue of transferring data arrays from the CPU to the GPU and back again only arises when using the GPU in order to parallelize computations. There are three possible ways to do this: letting the compiler handle transferring data, inserting openACC directives that define what data should be moved at what times (i.e. “manual” data movement), or using a newer technology called Managed Memory, which allows both the CPU and GPU to in a broad sense work from the same piece of memory.

7.4.1 Runtime Reduction with OpenMP and GPU

When accelerating, work starts with a piece of sequential code, say a loop that works on a different piece of data every time through so there is no run through that depends on a different run through (each cycle is independent).

The first option is to compile the code with optimization flags. This reduces the ability of the programmer to debug their software, but increases the speed using various techniques. The next step up in speed is parallelizing the process with the CPU and OpenMP. This will lead to speed ups of up to the number of CPU cores times better than the unaccelerated code.

The next and final step tried was GPU acceleration. This starts with the addition of directives in the code that tell the compiler what things can be parallelized on the GPU, for example our loop that we are working on. Just this step actually leads to dramatic slowdowns in speed, because the additional step of transferring data between the CPU and GPU is added, and handled by the compiler. This leads to the use of the extremely slow PCIe bus between the CPU and GPU during every computation cycle multiple times. The compiler attempts to be as safe as possible with the two (CPU and GPU) copies of the data, therefore updates both copies every time a parallelizable region starts or ends. By using openACC data directives, the times when data should be transferred back and forth can be specified by the programmer. This still leads to PCIe bus being used often, but much fewer times than if data management is decided by the compiler, since the programmer can make assumptions about what data can be left on the GPU between cycles. The last option is using a new technology called Managed Memory, which allows both the CPU and GPU to effectively use the same patch of memory. This is done by allocating a copy of the data on the GPU as pinned memory, which allows the GPU to access this copy without the help of the CPU, and the CPU can access the copy as well. This technology has the downside of being limited to the amount of available memory on the GPU, and has some use cases where it is slower than data management with directives.

7.4.2 Results

Here, we use two compilers to run a three-dimensional elastodynamic finite integration code. The medium is elastic and its sizes in x, y and z directions are 0.5 m, 0.5 m, and 0.15m respectively. Density of the medium is 2400 kg/m³ and velocity of normal and shear waves are 3500 m/s and 2300 m/s, respectively. All of the boundaries are assumed to be free. Sending and receiving sensors are located on the top boundary of the medium. Temporal and spatial grid sizes are 0.2 μ s and 0.001 m, respectively. Total time of simulation is 0.00025 s.

All test runs performed are shown in Table 1 with their characteristics. The fastest runtime was openACC accelerated with Unified Memory Management and the -fast flag, as expected, with a runtime of 10 minutes and 25 seconds. The slowest runtime experienced was with openACC parallelization with compiler managed memory movement with an optimization flag at 12 hours and 27 minutes. This was also an expected result, as the compiler is very safe with data movement between the CPU and GPU, and does a lot of these time-costly movements over the PCIe bus.

Unexpectedly, with openACC acceleration and manual data movement the optimization compiler flag made the runtime slower by 2 seconds compared to the unoptimized version. However, this result can be attributed to many causes (opening another program on the machine, waking the machine display to check run progress, etc.) and the difference between the two is tiny compared to the runtimes themselves.

Speedups were calculated for each compiler independently, with the base case being the unoptimized, non parallelized runtime for each compiler. OpenMP performed about as expected, reaching around an 8 times speedup over the base run, with some results even more sped up due to optimization flags. OpenACC performed very well, reaching speedups of over 28 times the base case. OpenMP on the PGI compiler did not perform as well as on the GNU compiler because the

PGI compiler restricts the OpenMP parallelization to a maximum of 4 cores compared to GNU's 8.

Table 11: Runtime for serial and parallel simulations

Compiler	Parallelization	Gpu Memory Management	Optimization Used	Runtime (s)	Runtime (hours)	xSpeedup over Unoptimized
gfortran	none	n/a	none	28223.443	7:50:23	1.0
gfortran	none	n/a	-O1	15877.676	4:30:15	1.8
gfortran	none	n/a	-O2	7034.6577	1:59:44	4.0
gfortran	none	n/a	-O3	6086.1064	1:43:36	4.6
gfortran	openmp	n/a	none	6175.9201	1:45:07	4.6
gfortran	openmp	n/a	-O1	3658.5739	1:02:16	7.7
gfortran	openmp	n/a	-O2	3372.3624	0:57:24	8.4
gfortran	openmp	n/a	-O3	3008.0411	0:51:12	9.4
pgi	openacc	Unified	-fast	611.61304	0:10:25	28.3
pgi	openacc	Unified	none	617.6004	0:10:31	28.0
pgi	openacc	manual	-fast	695.02623	0:11:50	24.9
pgi	openacc	manual	none	693.14201	0:11:48	25.0
pgi	openacc	no	-fast	42749.629	12:07:39	0.4
pgi	openacc	no	none	43919.854	12:27:34	0.4
pgi	openmp	n/a	-fast	2707.2734	0:46:05	6.4
pgi	openmp	n/a	none	5212.2985	1:28:43	3.3
pgi	none	n/a	-fast	4285.5634	1:12:57	4.0
pgi	none	n/a	none	17297.968	4:54:26	1.0

Figure 101 shows the effects of different GPU memory management techniques on runtimes, which is perhaps the most telling result gained: in GPU acceleration, by far the most important step to complete is dealing with memory transfers between the CPU and the GPU. These memory transfers can negate any speed gained through parallelization, even increasing the overall runtime dramatically as compared to the non-parallelized runtime (in this case a 10 times slowdown). As soon as some care is taken with the memory, either indicating to the compiler when to transfer the data or using Unified memory, the runtimes sped up by 25 to 28 times, a dramatic speedup. Figure 102 compares the two different compilers on their OpenMP runs. It shows that no matter if the run is optimized or no, PGI's compiler seems to create executable Fortran code that runs more quickly.

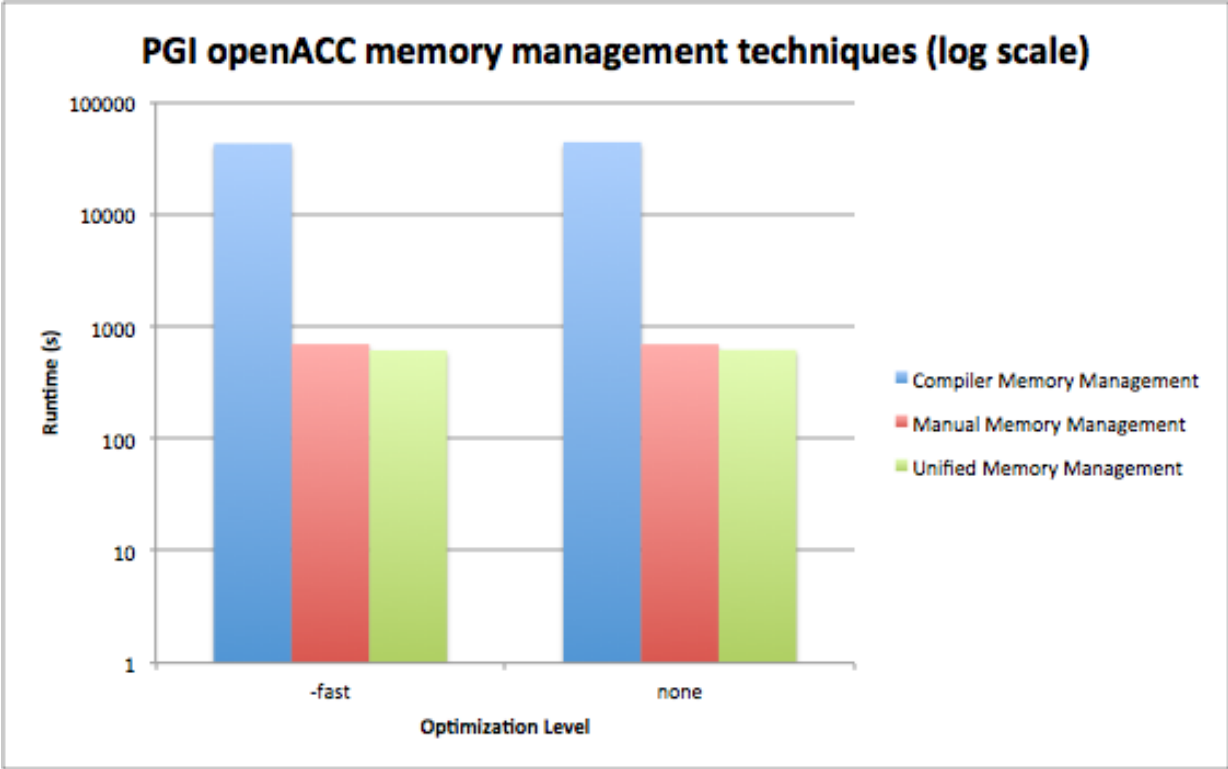


Figure 101. Effects of different GPU memory management techniques on runtimes.

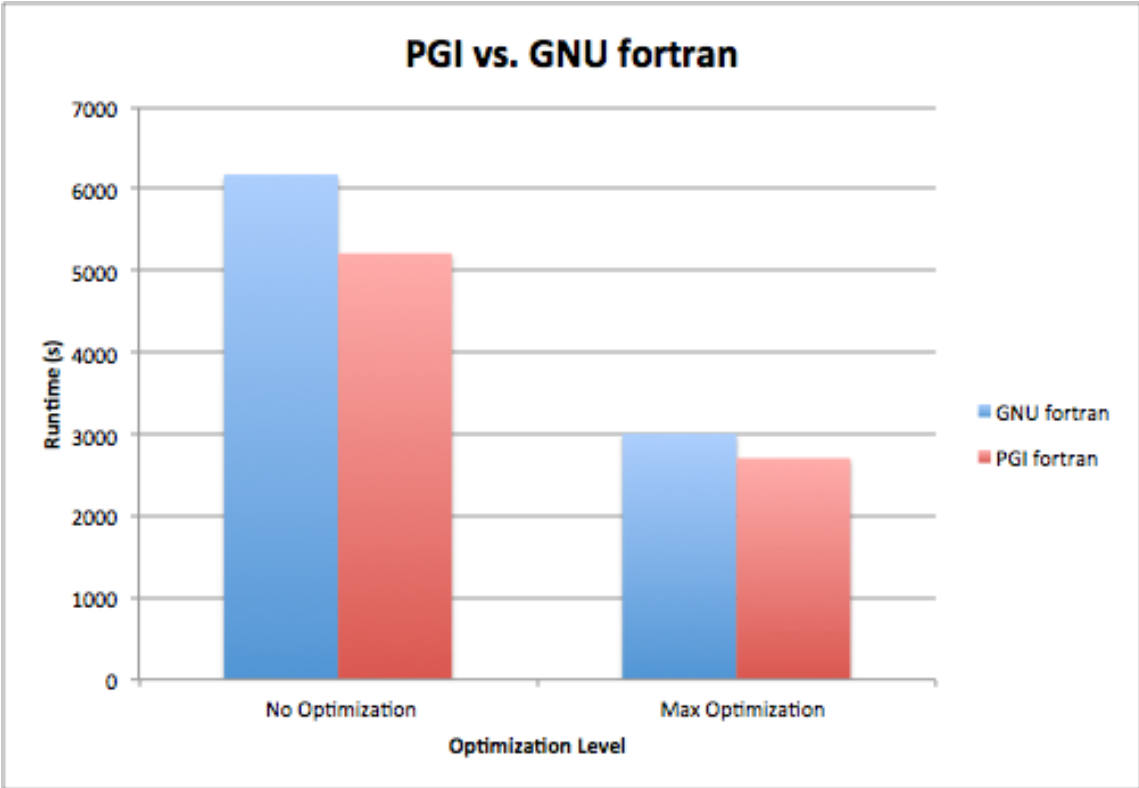


Figure 102. Comparison between PSI and GNU compilers on OpenMP runs.

Figure 103 shows the effect of OpenMP parallelization and compiler optimization on the GNU compiler. Optimization has a smaller, but still noticeable effect when OpenMP is used, but optimization is really effective when OpenMP is not used, bringing the runtimes nearly to the same level as unoptimized OpenMP code.

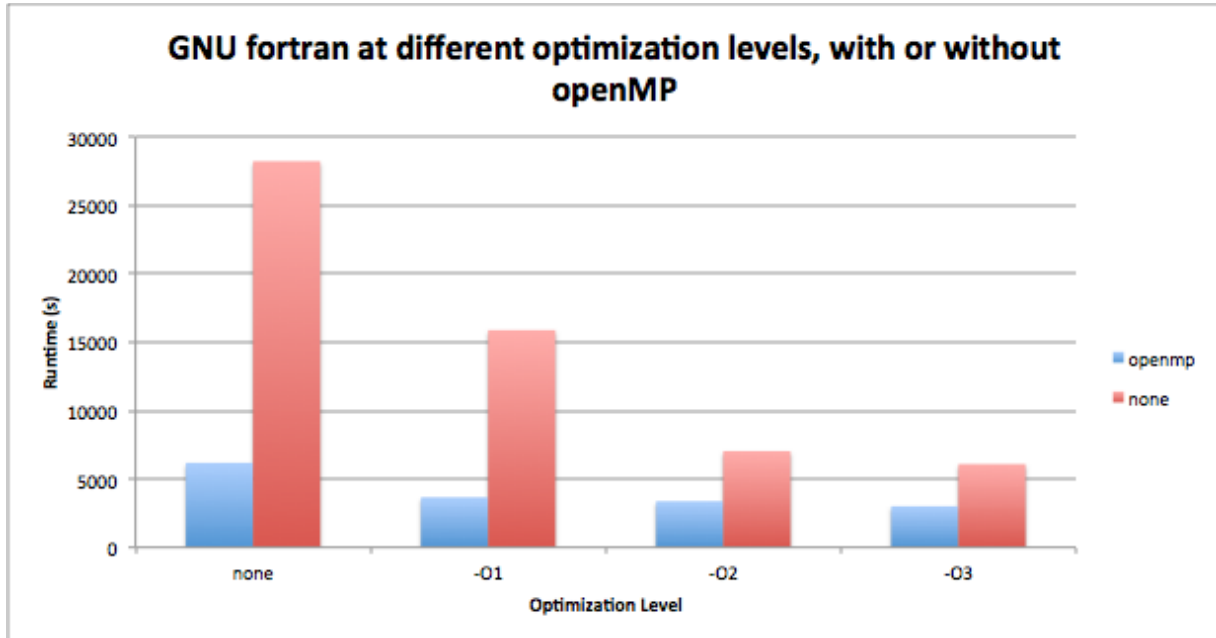


Figure 103. Effect of OpenMP parallelization and compiler optimization on the GNU compiler.

CHAPTER 8 - SUMMARY

This report discusses the investigation of several types of damage found in concrete specimens. Significant progress was made in improving nondestructive techniques for damage detection purposes. These applications include earthquake damage in concrete columns, freeze thaw and alkali-silica reaction damage in concrete pavements, and various stages of cracking in continuously reinforced concrete pavement sections. The most significant success was made in the progress of the detection of near-surface environmental damage. In addition, a simulation program is in development in order to verify and further explain the results found.

The panoramic reconstruction analysis and the development of a quantitative indicator of damage, HTI, were successful results of the investigation of environmental damage. The panoramic reconstructions exhibited common characteristics associated with backwall presence and regions of increased reflectivity which allowed for the diagnosis of the condition of the concrete in a visual manner. The HTI analysis revealed that the indicator was capable of detecting damage in an objective and consistent manner, regardless of mix design, climate conditions, and reinforcement presence. This standalone calculation allows for the in-situ diagnosis of concrete condition, without requiring historical data for a comparative analysis. The HTI analysis was successful in detecting both freeze thaw and ASR damage, as were the panoramic reconstructions. In spite of these successes, the detection of damage in concrete remains a challenging task. This is why progress has been made regarding the development of a simulation tool which can provide insight on the condition of concrete.

This report presented a variety of applications for damage detection in concrete specimens using an ultrasonic linear array device. However, a multitude of other damage types can be addressed using the same or similar analysis techniques to achieve broader implementation success. Moreover, the techniques developed and presented here could be advanced to determine the depth and/or extent of damage. Accurate knowledge of subsurface degradation could be beneficial for repair and rehabilitation efforts, and could lead to more educated decision making.

While the reconstruction and numerical indicator methods included in this research were successful in detecting the damage types considered, greater achievements could be attained via the fusion of other technologies with these techniques. For instance, it would be difficult, using only the methods presented here, to analyze a scenario in which a specimen contains reinforcement and also has significant subsurface damage and near surface delaminations. However, if the ultrasonic array technology was combined with magnetic methods, for example, both the reinforcement and the damage present in the structure could be successfully detected. Technological collaborations such as this would allow for greater applicability and enhance the capabilities of the nondestructive evaluation of concrete.

Additionally, automating the methods developed for this thesis could improve efficiency and reduce the analysis time required for condition determinations. Increased automatization would allow for real-time field implementation and diagnosis capabilities. Future work should continue to improve the productivity of the analysis techniques for future applications.

REFERENCES

- AASHTO, "AASHTO Guide for Design of Pavement Structures", American Association of State Highway & Transportation Officials, 1993.
- Abdallah, I. N., Williams, R. & Nazarian, S. "Application of Data Fusion Using Fuzzy Logic Method to Nondestructive Evaluation of Pavements." Transportation Research Board 88th Annual Meeting, 2009.
- Achenbach, J. D. 1973. *Wave propagation in elastic solids*, North-Holland Amsterdam.
- ACI Committee 318. (2011). Building Code Requirements for Reinforced Concrete and Commentary (ACI 318-11/ACI 318R-11). American Concrete Institute, Detroit, MI.
- ACPA, "Concrete Crack and Partial-Depth Spall Repair Manual." American Concrete Pavement Association, 2004.
- Aggelis, D. G., Shiotani, T., Momoki, S., & Hiram, A. (2009). Acoustic emission and ultrasound for damage characterization of concrete elements. *ACI Materials Journal*, 106(6).
- Al-Qadi, I.L., and Riad, S.M. (1996), Characterization of Portland Cement Concrete: Electromagnetic and Ultrasonic Measurement Techniques, Report submitted to the National Science Foundation, September.
- Al-Qadi, I. L., and S. Lahouar. "Measuring layer thicknesses with GPR—Theory to practice." *Construction and building materials* 19, no. 10 (2005a): 763-772.
- Al-Qadi, Imad L., and Samer Lahouar. "Measuring rebar cover depth in rigid pavements with ground-penetrating radar." *Transportation Research Record: Journal of the Transportation Research Board* 1907, no. 1 (2005b): 80-85.
- Al-Qadi, Imad L., Samer Lahouar, Kun Jiang, Kevin K. McGhee, and David Mokarem. "Accuracy of ground-penetrating radar for estimating rigid and flexible pavement layer thicknesses." *Transportation Research Record: Journal of the Transportation Research Board* 1940, no. 1 (2005c): 69-78.
- Al-Qadi, Imad L., Zhen Leng, S. Lahouar, and J. Baek. "In-place hot-mix asphalt density estimation using ground-penetrating radar." *Transportation Research Record: Journal of the Transportation Research Board* 2152, no. 1 (2010): 19-27.
- Arndt, R. W., Cui, J. and Huston, D. R. (2011). Monitoring Of Reinforced Concrete Corrosion and Deterioration by Periodic Multi-Sensor Non-Destructive Evaluation. AIP Conference Proceedings. 1371.
- ASTM Standard C666. (2015). Standard Test Method for Resistance of Concrete to Rapid Freezing and Thawing. *ASTM International*, West Conshohocken, PA, 10.1520/C0666_C0666M-15, www.astm.org.

ASTM C78 / C78M-15a. (2015). Standard Test Method for Flexural Strength of Concrete, ASTM International, West Conshohocken, PA.

ASTM D4788-03(2013), Standard Test Method for Detecting Delaminations in Bridge Decks Using Infrared Thermography, ASTM International, West Conshohocken, PA, 2013.

Azari, H., Nazarian, S., and Yuan, D. (2014). Assessing sensitivity of impact echo and ultrasonic surface waves methods for nondestructive evaluation of concrete structures. *Construction and Building Materials*, 71, 384-391.

Azevedo, Stephen G., Jeffrey E. Mast, Scott D. Nelson, E. T. Rosenbury, Holger E. Jones, Thomas E. McEwan, D. J. Mullenhoff et al. "HERMES: A high-speed radar imaging system for inspection of bridge decks." In *Nondestructive Evaluation Techniques for Aging Infrastructure and Manufacturing*, pp. 195-204. International Society for Optics and Photonics, 1996.

Barbone, P. E. & Gokhale, N. H. "Elastic modulus imaging: on the uniqueness and nonuniqueness of the elastography inverse problem in two dimensions." *Inverse Problems*, 20, 283, 2004.

Baladi, G. Y., T. Svasdisant, T. Van, N. Buch, and K. Chatti, "Cost-Effective Preventive Maintenance: Case Studies." *Transportation Research Record 1795*, Transportation Research Board, Washington, DC (2002) pp 17-26.

Bathe, K.J. (1996). *Finite element procedures*. Prentice Hall.

Bazant, Z.P., Steffens, A. (2000). Mathematical model for kinetics of alkali-silica reaction in concrete, *Cement and Concrete Research*, 30: 419-428.

Bazant, Z. P., Zi, G., Meyer, C. (2000a). Fracture mechanistic of ASR in concretes with waste glass particles of different sizes, *Journal of Engineering Mechanics*, 126, No. 3: 226-232.

Becker, J., Jacobs, L. J., and Qu, J. (2003) Characterization of cement-based materials using diffuse ultrasound. *Journal of Engineering Mechanics*, vol. 129, pp. 1478–1484.

Belli, K., Wadia-Fascetti, S. & Rappaport, C. 2008. Model based evaluation of bridge decks using ground penetrating radar. *Computer-Aided Civil and Infrastructure Engineering*, 23, 3-16.

Benedetto, A., Manacorda, G., Simi, A. and Tosti, F. (2012). Novel perspectives in bridges inspection using GPR. *Nondestructive Testing and Evaluation*, 27, 239-251.

Berra, M., Mangialardi, T., Paolini, A. E. (1999). Rapid evaluation of the threshold alkali level for alkali reactive siliceous aggregates in concrete, *Cement and Concrete Composites*, 21: 325–333.

Berra, M., Faggiani, C., Mangialardi, T., Paolini, A.E. (2010). Influence of stress restraint on the expansive behavior of concrete affected by alkali-silica reaction, *Cement and Concrete Research*, 40: 1403-1409.

- Bhardwaj, M. C., Neeson, I. & Stead, G. 2000. Introduction to contact-free ultrasonic characterization and analysis of consolidated materials. *NDT. net*, 5.
- Bishko, A., Samokrutov, A., and Shevaldykin, V. (2008). Ultrasonic echo-pulse tomography of concrete using shear waves low-frequency phased antenna arrays. In *Proceedings of the 17th World Conference on Nondestructive Testing*, vol. 25, no. 28.10.
- Bjegovic D, Mikulic D, Sekulic D. Non-destructive methods for monitoring of reinforcing steel in concrete. In: Forde MC, editor. *Proceedings of 9th int. conf. on structural faults and repair*. London: Engineering Technics Press; 2001. CDROM.
- Bomar, L.C., Horne, W.F., Brown, D. R., and Smart, J.L. (1988), *Determining Deteriorated Areas in Portland Cement Concrete Pavements Using Radar and Video Imaging*, NCHRP 304, Transportation Research Board, Washington, D.C.
- Borwick, J. (1990). *Microphones: technology and technique*, Focal Press Oxford.
- Boukari, Y., Bulteel, D., Rivard, P., & Abriak, N. E. (2015). Combining nonlinear acoustics and physico-chemical analysis of aggregates to improve alkali–silica reaction monitoring. *Cement and Concrete Research*, 67, 44-51.
- Bracci, J. M., Kunnath, S. K. and Reinhom, A. M. (1997). Seismic Performance and Retrofit Evaluation of Reinforced Concrete Structures, *Journal of Structural Engineering* 123(1), 3–10.
- Buckley, J. and Loertscher, H. (1999). Frequency considerations in air-coupled ultrasonic inspection. *Insight*, 41, 696-699.
- Bungey, J.H., Millard, S.G., and Shaw, M.R. (1994), “The Influence of Reinforcing Steel on Radar Surveys of Concrete Structures,” *Construction and Building Materials*, Vol. 8, No. 2, pp. 119-126.
- Candy, Bruce H. "Pulse induction time domain metal detector." U.S. Patent 5,576,624, issued November 19, 1996.
- Cao, Y. (2011). *Full Waveform Analysis of Ground Penetrating Radar Measurements*. University of Minnesota.
- Cao, Y., Guzina, B. B. and Labuz, J. F. (2008). *Pavement evaluation using ground penetrating radar*, Minnesota Department of Transportation, MN/RC 2008-10.
- Cao, Y., Labuz, J. and Guzina, B. (2011). *Evaluating a Pavement System Based on GPR Full-Waveform Simulation*. Transportation Research Board 90th Annual Meeting.
- Cardimona, S., Willeford, B., Webb, D., Hickman, S., Wenzlick, J., and Anderson, N. (2003). *Automated pavement analysis in Missouri using ground penetrating radar*. University of Missouri-Rolla, Department of Geology and Geophysics, No. RDT03-002, RI98-002.
- Carino, Nicholas J. "Nondestructive techniques to investigate corrosion status in concrete structures." *Journal of performance of constructed facilities* 13, no. 3 (1999): 96-106.

Carino, N. J. (2001). The impact-echo method: an overview. Proceedings of the 2001 Structures Congress and Exposition, May, 2001, 21-23.

Catapano, I., Crocco, L., Morabito, A. F. and Soldovieri, F. (2012). Tomographic imaging of holographic GPR data for non-invasive structural assessment: the Musmeci bridge investigation. *Nondestructive Testing and Evaluation*, 27, 229-237.

Celaya, Manuel, Parisa Shokouhi, and Soheil Nazarian. "Assessment of debonding in concrete slabs using seismic methods." *Transportation Research Record: Journal of the Transportation Research Board* 2016, no. 1 (2007): 65-75.

Chen, J., Jayapalan, A.R., Kim, J., Kurtis, K.E., Jacobs, L.J. (2010). Rapid evaluation of alkali-silica reactivity of aggregates using a nonlinear resonance spectroscopy technique, *Cement and Concrete Composites*, 40: 914-923.

Chen, H.L.R., Halabe, U.B, Sami, Z., and Bhandarkar, V. (1994), "Impulse Radar Reflection Waveforms of Simulated Reinforced Concrete Bridge Decks," *Materials Evaluation*, Vol. 52, No. 12, Dec., pp. 1382-1388.

Chen, D., and Scullion, T. (2008). "Detecting subsurface voids using ground-coupled penetrating radar." *ASTM Geotechnical Testing Journal*, 31(3), 217-224.

Cheng, C. C., and M. J. Sansalone. Effect on Impact-Echo Signals Caused by Steel Reinforcing Bars and Voids Around Bars. *ACI Materials Journal*, Vol. 90, No. 5, 1993, pp. 421-434.

Cho, Young S. "Non-destructive testing of high strength concrete using spectral analysis of surface waves." *NDT & E International* 36, no. 4 (2003): 229-235.

Choi, H. and Popovics, J. S. (2015). NDE application of ultrasonic tomography to a full-scale concrete structure. *Ultrasonics, Ferroelectrics, and Frequency Control*, *IEEE Transactions on*, 62(6), 1076-1085.

Clayton, Dwight A., Cyrus M. Smith, Christopher C. Ferraro, Jordan Nelson, Lev Khazanovich, Kyle Hoegh, Satish Chintakunta, and John Popovics. Evaluation of Ultrasonic Techniques on Concrete Structures. No. ORNL/TM-2013/430. Oak Ridge National Laboratory (ORNL), 2013.

Clayton, Dwight A., and Cyrus M. Smith. "Comparative testing of nondestructive examination techniques for concrete structures." In *SPIE Smart Structures and Materials+ Nondestructive Evaluation and Health Monitoring*, pp. 90631G-90631G. International Society for Optics and Photonics, 2014.

Clear, K. C. 1989. Measuring rate of corrosion of steel in field concrete structures. *Transportation research record*.

Clemeña, G. G. (1983), "Nondestructive Inspection of Overlaid Bridge Decks with Ground Penetrating Radar," *Transportation Research Record*, No. 899, Transportation Research Board, Washington, D.C.

Clemeña, G. G., Sprinkle, M., and Long, R. (1986), Use of Ground Penetrating Radar for Detecting Voids Underneath a Jointed Concrete Pavement, Final Report, Virginia Highway and Transportation Council, Charlottesville, VA..

Clemeña, G. G. (1991). Short-pulse radar methods.

Clemeña, G. G., Jackson, D. R. and Crawford, G. C. (1992). Inclusion of rebar corrosion rate measurements in condition surveys of concrete bridge decks. Transportation Research Record.

Colton, D. & Kress, R. 1998. Inverse acoustic and electromagnetic scattering theory, Springer.

Darter, M. I., Barenberg, E. J. & Salsilli, R. A. Calibrated Mechanistic Design Procedure To Prevent Transverse Cracking Of Jointed Plain Concrete Pavements. Fifth International Conference on Concrete Pavement Design and Rehabilitation, 1993.

Davidson, N.C., Hardy, M.S.A, Broughton, K.J., Forde, M.C., and Das, P.C. (1996), "Investigation of Bridge Scour Using Digital Impulse Radar," Proceedings of 3rd Conference on Nondestructive Evaluation of Civil Structures and Materials, M. P. Schuller, D. B. Woodham, and Atkinson-Noland & Associates, Inc., eds., September, pp. 69-79.

Davis, A. G., and B. H. Hertlein. "Nondestructive testing of concrete pavement slabs and floors with the transient dynamic response method." In Proc Int Conf Struct Faults Repair (Lond), vol. 2, pp. 429-433. 1987.

Davis, Allen G., Bernhard H. Hertlein, Malcolm K. Lim, and Kevin Michols. "Impact-echo and impulse response stress-wave methods: advantages and limitations for the evaluation of highway pavement concrete overlays." In Nondestructive Evaluation Techniques for Aging Infrastructure and Manufacturing, pp. 88-96. International Society for Optics and Photonics, 1996.

Davis, Allen G., James G. Evans, and Bernhardt H. Hertlein. "Nondestructive evaluation of concrete radioactive waste tanks." Journal of Performance of Constructed Facilities 11, no. 4 (1997): 161-167.

Davis, A. G. 2003. The nondestructive impulse response test in North America: 1985–2001. NDT & E International, 36, 185-193.

Davis, A. G., Lim, M. K. & Petersen, C. G. 2005. Rapid and economical evaluation of concrete tunnel linings with impulse response and impulse radar non-destructive methods. NDT & E International, 38, 181-186.

Deng, Yiming, and Xin Liu. "Electromagnetic imaging methods for nondestructive evaluation applications." Sensors 11, no. 12 (2011): 11774-11808.

Deroo, F., Kim, J. Qu, K. Sabra, G. Woodruff, W., and Jacobs, L.J. (2010). Detection of damage in concrete using diffuse ultrasound (L), Journal of Acoustical Society of America, 127, (6): 3315-3318.

- Diamanti, N., Redman, D., Giannopoulos, A., 2010. A study of GPR pavement crack responses using field data and numerical modelling. Proceedings of the 13th International Conference on Ground Penetrating Radar (GPR), 2010, Lecce, Italy.
- Diamanti, Nectaria, and David Redman. "Field observations and numerical models of GPR response from vertical pavement cracks." *Journal of Applied Geophysics* 81 (2012): 106-116.
- Donnelly, J. (2012). "Means and Methods of Evaluating Reinforced Concrete Structures," ACI Fall 2012 Convention, October 21-24; Toronto, ON.
- Dutoit, N. E., Brian, L. W. & Sang-Gook, K. I. M. 2005. Design considerations for MEMS-scale piezoelectric mechanical vibration energy harvesters. *Integrated Ferroelectrics*, 71, 121-160.
- Economou, N., Vafidis, A., Hamdan, H., Kritikakis, G., Andronikidis, N. and Dimitriadis, K. (2012). Time-varying deconvolution of GPR data in civil engineering. *Nondestructive Testing and Evaluation*, 27, 285-292.
- Edwards, L. & Mason, Q. 2011. Evaluation of Nondestructive Methods for Determining Pavement Thickness. DTIC Document.
- Evans, Robert, Matthew Frost, Martyn Stonecliffe-Jones, and Neil Dixon. "Assessment of in situ dielectric constant of pavement materials." *Transportation Research Record: Journal of the Transportation Research Board* 2037, no. 1 (2007): 128-135.
- Farnam, Y., Bentz, D., Sakulich, A., Flynn, D., & Weiss, J. (2014). Measuring freeze and thaw damage in mortars containing deicing salt using a low-temperature longitudinal guarded comparative calorimeter and acoustic emission. *Adv. Civ. Eng. Mater*, 3(1), 23.
- Fellinger, P. (1991). A Method for the Numerical Solution of Elastic Wave Propagation Problems in the Time Domain by Direct Discretization of the Elastodynamic Governing Equations. PhD Thesis, University of Kassel, Kassel, Germany.
- Fellinger, P., Marklein, R., Langenberg, K. J., & Klaholz, S. (1995). Numerical modeling of elastic wave propagation and scattering with EFIT—elastodynamic finite integration technique. *Wave motion*, 21(1), 47-66.
- Fernandes, Bertrand, Michael Titus, Douglas Karl Nims, Al Ghorbanpoor, and Vijay Kumar Devabhaktuni. "Practical assessment of magnetic methods for corrosion detection in an adjacent precast, prestressed concrete box-beam bridge." *Nondestructive Testing and Evaluation* 28, no. 2 (2013): 99-118.
- FHWA, "Transportation Statistics Annual Report." Federal Highway Administration, United States Department of Transportation. Washington, DC, 2013.
- Forest, R., and V. Utsi. "Non destructive crack depth measurements with ground penetrating radar." In *Ground Penetrating Radar, 2004. GPR 2004. Proceedings of the Tenth International Conference on*, pp. 799-802. IEEE, 2004.
- Freeseaman, K., Hoegh, K., Khazanovich, L. (2015). Characterization of Concrete at Various

Freeze-Thaw Damage Conditions Using SH-Waves. Proceedings of the 42nd Review of Progress in Quantitative Nondestructive Evaluation (QNDE), 26-31 July, Minneapolis, MN. <http://dx.doi.org/10.1063/1.4940463>.

Freeseaman, K., Khazanovich, L., Hoegh, K., Nojavan, A., Schultz, A. E., Chao, S. (2016). Nondestructive monitoring of subsurface damage progression in concrete columns damaged by earthquake loading. *Engineering Structures*, Volume 114, 1 May 2016, 148-157.

Ghee, A. B., Priestley, M. J. N., and Paulay, T. (1989). Seismic Shear Strength of Circular Reinforced Concrete Columns. *Structural Journal*, American Institute of Concrete. 86(1), 45-59.

Ghorbanpoor, A., Shi, S., Assessment of Corrosion of Steel in Concrete Structures by Magnetic based NDE Techniques, Techniques to Assess the Corrosion Activity of Steel Reinforced Concrete Structures, ASTM STP 1276, Neal S. Berke, Edward Escalante, Charles K. Nmai, and David Whiting, EDS. American Society for Testing and Materials, 1996.

Giaccio, G., Zerbino, R., Ponce, J.M., Batic, O.R. (2008). Mechanical behavior of concretes damaged by alkali-silica reaction. *Cement and Concrete Research*, 38: 993-1004.

Gibson, Alexander H. "Advances in nondestructive testing of concrete pavements." PhD diss., University of Illinois at Urbana-Champaign, 2005.

Godinho, L., Dias-da-Costa, D., Areias, P., Júlio, E., and Soares, D. (2013). Numerical study towards the use of a SH wave ultrasonic-based strategy for crack detection in concrete structures. *Engineering Structures*, 49, 782-791.

Graff, K. F. 1991. *Wave motion in elastic solids*, Dover publications.

Graveen, Cole. M.S.C.E., Purdue University. (2001). *Nondestructive Test Methods To Assess Pavement Quality For Use In A Performance-Related Specification*. Major Professor: W. Jason Weiss.

Graves, R.W. (1988). Simulating seismic wave propagation in 3D elastic media using staggered-grid finite differences. *Bull. Seismic Soc. Am.*, 86, 1091–1106.

Green JR, R. E. 2004. Non-contact ultrasonic techniques. *Ultrasonics*, 42, 9-16.

Griffiths, D. J. and Reed, C. (1999). *Introduction to electrodynamics*, prentice Hall New Jersey.

Grove, J., Jones, K., Ye, D. & Gudimettla, J. M. 2012. Nondestructive Tests of Thickness Measurements for Concrete Pavements. *Transportation Research Record: Journal of the Transportation Research Board*, 2268, 61-67.

Gucunski, N., S. Antoljak, and A. Maher. Seismic Methods in Post-Construction Condition Monitoring of Bridge Decks. In *Use of Geophysical Methods in Construction*, Geotechnical Special Publications, No. 108 (S. Nazarian and J. Diehl, eds.), GeoInstitute, ASCE, Reston, Va., 2000, pp. 35–51.

Gucunski, N., Consolazio, G.R., Maher, A. (2006) "Concrete bridge deck delamination detection by integrated ultrasonic methods," Intl. J. Material and Product Technology, Special Issue on NDT and Failure Preventive Technology, Vol. 26., No. ½, pp. 19-34.

Gucunski, N., Z. Wang, T. Fang, Y. Chen and C. Rascoe, "Automated Interpretation of Bridge Deck Impact Echo Data Using Three-Dimensional Visualization", Proc. of NDE / NDT for Highways and Bridges SMT, Oakland (2008), United States, pp. 33-41.

Gucunski, Nenad, Michelle Yan, Zhe Wang, Tong Fang, and Ali Maher. "Rapid bridge deck condition assessment using three-dimensional visualization of impact echo data." Journal of Infrastructure Systems 18, no. 1 (2011): 12-24.

Haardt, P. "NDT Methods for the inspection of highway structures." In International Symposium Non-Destructive Testing in Civil Engineering (NDT-CE). Berlin, Germany. 2003.

Halabe, Udaya B., and R. Kenneth. "Condition assessment of reinforced concrete structures using electromagnetic waves." ACI materials Journal 92, no. 5 (1993), 511-523.

Halabe, U. D., Chen, H.L., Allu, M.K., and Pei, L. (1996), "Laboratory Radar Evaluation of Concrete Decks and Pavements With and Without Asphalt Overlay," Structural Materials Technology: An NDT Conference, P. E. Hartbrower and P. J. Stolarski, eds., Feb., pp. 373-377.

Halabe, U. B., Vasudevan, A., Klinkhachorn, P. & Gangarao, H. V. S. 2007. Detection of subsurface defects in fiber reinforced polymer composite bridge decks using digital infrared thermography. Nondestructive Testing and Evaluation, 22, 155-175.

Harmelink, D., and T. Aschenbrener. Extent of Top-Down Cracking in Colorado. CDOT-DTD-R-2003-7. Colorado Department of Transportation, Denver, 2003.

Harris, Dwayne A. "Pavement thickness evaluation using ground penetrating radar." PhD diss., Purdue University, 2006.

Hazaree, C., Wang, K., Ceylan, H., and Gopalakrishnan, K. (2011). Capillary Transport in RCC: Water-to-Cement Ratio, Strength, and Freeze-Thaw Resistance. *J. Mater. Civ. Eng.*, 10.1061/(ASCE)MT.1943-5533.0000284, 1181-1191.

Hertlein, B. H., and A. G. Davis. "Locating concrete consolidation problems using the nondestructive impulse response test." In American Concrete Institute Fall Convention, Los Angeles. 1998.

Hevin, G., O. Abraham, H. A. Pedersen, and M. Campillo. "Characterization of surface cracks with Rayleigh waves: a numerical model." NDT & E International 31, no. 4 (1998): 289-297.

Hillemeier, B., "Location of Reinforcement by Induction-Thermography". The International Society of Optical Engineers - Thermosense VII. SPIE 520 (1984) pp. 197-206.

Hoegh, Kyle Edward. (2013). Ultrasonic linear array evaluation of concrete

pavements. Retrieved from the University of Minnesota Digital Conservancy, <http://purl.umn.edu/155823>.

Hoegh, K., Khazanovich, L., Maser, K. R. and Tran, N. (2012a). Evaluation of Ultrasonic Technique for Detecting Delamination in Asphalt Pavements. Transportation Research Board 91st Annual Meeting.

Hoegh, K., Worel, B., Yu, H. T., and Khazanovich, L. (2013). Detection of Subsurface Joint Deterioration. Transportation Research Record: Journal of the Transportation Research Board. Volume 2367. Issue 1: 3-12.

Hoegh, K. and Khazanovich, L. (2012b). Correlation Analysis of 2D Tomographic Images for Flaw Detection in Pavements. Journal of Testing and Evaluation. American Society for Testing and Materials 40(2): 247-255.

Hoegh, K. and Khazanovich, L. (2012). Concrete Pavement Joint Diagnostics Using Ultrasonic Tomography. Transportation Research Record: Journal of the Transportation Research Board. Volume 2305: 54–61.

Hoegh, K., Yu, H. T., and Khazanovich, L. (2011). Ultrasonic Tomography Technique for Evaluation of Concrete Pavements. Transportation Research Record: Journal of the Transportation Research Board. Volume 2232: 85–94.

Hoegh, K. and Khazanovich, L. (2015). Extended Synthetic Aperture Focusing Technique for Ultrasonic Imaging of Concrete. NDT & E International. doi:10.1016/j.ndteint.2015.05.001.

Hossain, M. Shabbir, and Mohamed K. Elfino. Field Demonstration of Magnetic Tomography Technology for Determination of Dowel Bar Position in Concrete Pavement. No. FHWA/VTRC 06-R40. 2006.

Huston, D. R., Pelczarski, N. V., Esser, B., and Maser, K. R. (2000) "Damage detection in roadways with ground penetrating radar." Proceedings of the Eighth International Conference on Ground Penetrating Radar, Gold Coast, Australia, 91-94.

Jackson, D. J. "Pavement Preventive Maintenance Guidelines." In Second International Symposium on Maintenance and Rehabilitation of Pavements and Technological Control. Segundo Simposio Sobre Manutencao e Rehabilitacao de Pavimentos e Controle Tecnologico, no. 01-128. 2001.

Jiang, Hong, and Xuancang Wang. "Signal Analysis and Processing for Detecting Void Phenomenon under Concrete Pavement by Using Ground Penetrating Radar." Journal of Highway and Transportation Research and Development 1 (2010): 006.

Joyce R. P. (1985). Rapid Nondestructive Delamination Detection. Final Report No. FHWA/RD-85/051. Federal Highway Administration, Washington, D. C.

Keefe, D. H., Ling, R. & Bulen, J. C. 1992. Method to measure acoustic impedance and reflection coefficient. The Journal of the Acoustical Society of America, 91, 470.

- Kellezi, L. 2000. Local transmitting boundaries for transient elastic analysis. *Soil dynamics and earthquake engineering*, 19, 533-547.
- Khazanovich, L., Velasquez, R. & Nesvijski, E. G. 2005. Evaluation of top-down cracks in asphalt pavements by using a self-calibrating ultrasonic technique. *Transportation Research Record: Journal of the Transportation Research Board*, 1940, 63-68.
- Khazanovich, L., Booshehrian, A., Dynamic Visco-Elastic Analysis of Falling Weight Deflectometer Deflections for Rigid and Flexible Pavements, To be published in *Transportation Research Record: Journal of the Transportation Research Board*, 2015.
- Kim, G., In, C. W., Kim, J. Y., Kurtis, K. E., and Jacobs, L. J. (2014). Air-coupled detection of nonlinear Rayleigh surface waves in concrete—Application to microcracking detection. *NDT & E International*, 67, 64-70.
- Koerner, R.M., Lord, A. Jr., Boweders, J., and Dougherty, W. (1982), "CW Microwave Location of Voids Beneath Paved Areas," *Journal of Geotechnical Engineering Division*, ASCE, Vol. 108, No. 1, pp. 133-144.
- Korhonen, C. (2002). New developments in cold-weather concreting. In *Proceedings, The 11th International Conference of Cold Regions Engineering*, pp. 531-537.
- Kristek, J., & Moczo, P. (2003). Seismic-wave propagation in viscoelastic media with material discontinuities: A 3D fourth-order staggered-grid finite-difference modeling. *Bulletin of the Seismological Society of America*, 93(5), 2273-2280.
- Krstulovic-Opara, N., Woods, R. D. & Al-Shayea, N. 1996. Nondestructive testing of concrete structures using the Rayleigh wave dispersion method. *ACI Materials Journal*, 93.
- Kuo, M. K., T. R. Lin, P. L. Liu, and T. T. Wu. "Locating the crack tip of a surface-breaking crack Part I. Line crack." *Ultrasonics* 36, no. 7 (1998): 803-811.
- Langenberg, Karl-Jörg, René Marklein, and Klaus Mayer. (2012). *Ultrasonic Nondestructive Testing of Materials: Theoretical Foundations*. CRC Press.
- Lee, H.K., Yim, H.J. & Lee, K.M. 2003. Velocity-strength relationship of concrete by impact echo method. *ACI Material Journal* 100(1): 49-54.
- Lenngren, Carl A., Joergen Bergstrom, and Benny M. Ersson. "Using ground-penetrating radar for assessing highway pavement thickness." In *International Symposium on Optical Science and Technology*, pp. 474-483. International Society for Optics and Photonics, 2000.
- Leong, P., Tighe, S., Rothenburg, L., and Hein, D. Finite Difference Modeling of Misaligned Dowel Bars and Their Effects on Joint Performance. Paper presented at the 85th Annual Meeting of the Transportation Research Board, Washington, D.C., January 22-26, 2006.
- Leong, P. Analysis of Effects of Dowel Bar Misalignment on the Performance of Concrete Pavement Joints. Thesis, University of Waterloo, Ontario, Canada, 2006.
- Leśnicki, K. J., Kim, J. Y., Kurtis, K. E., and Jacobs, L. J. (2011). Characterization of ASR

- damage in concrete using nonlinear impact resonance acoustic spectroscopy technique. *NDT & E International*, 44(8), 721-727.
- Leśnicki, K. J., Kim, J. Y., Kurtis, K. E., and Jacobs, L. J. (2013). Assessment of alkali–silica reaction damage through quantification of concrete nonlinearity. *Materials and structures*, 46(3), 497-509.
- Levander, A. (1988). Fourth-order finite-difference P-SV seismograms. *Geophysics*, 53, 1425–1436.
- Li, J., Zollinger, D. G. and Lytton, R. L. (2008). Detection of delamination in concrete pavements using ground-coupled ground-penetrating radar technique. *Transportation Research Record: Journal of the Transportation Research Board*, 2087, 68-77.
- Li, W., Pour-Ghaz, M., Castro, J., and Weiss, J. (2012). Water Absorption and Critical Degree of Saturation Relating to Freeze-Thaw Damage in Concrete Pavement Joints. *J. Mater. Civ. Eng.*, 10.1061/(ASCE)MT.1943-5533.0000383, 299-307.
- Liang, Ming-Te, and Po-Jen Su. "Detection of the corrosion damage of rebar in concrete using impact-echo method." *Cement and Concrete research* 31, no. 10 (2001): 1427-1436
- Liang, J. R. & Liao, W. H. 2009. Piezoelectric energy harvesting and dissipation on structural damping. *Journal of Intelligent Material Systems and Structures*, 20, 515-527.
- Lin, Yiching, and M. Sansolone. "Detecting flaws in concrete beams and columns using the impact-echo method." *ACI Materials Journal* 89, no. 4 (1992).
- Lingvall, F., Olofsson, T., and Stepinski, T. (2003). Synthetic aperture imaging using sources with finite aperture: Deconvolution of the spatial impulse response. *The Journal of the Acoustical Society of America* 114.1: 225-234. <http://dx.doi.org/10.1121/1.1575746>.
- Liu, Pei-Ling, Chong-Dao Tsai, and Tsung-Tsong Wu. "Imaging of surface-breaking concrete cracks using transient elastic waves." *NDT & E International* 29, no. 5 (1996): 323-331.
- Liu, J., Zollinger, D. G. & Lytton, R. L. 2008. Detection of Delamination in Concrete Pavements Using Ground-Coupled Ground-Penetrating Radar Technique. *Transportation Research Record: Journal of the Transportation Research Board*, 2087, 68-77.
- Loken, Marc C. Use of ground penetrating radar to evaluate Minnesota roads. Minnesota Department of Transportation, Research Services Section, 2007.
- Loulizi, Amara. "Development of ground penetrating radar signal modeling and implementation for transportation infrastructure assessment." PhD diss., Virginia Polytechnic Institute and State University, 2001.
- Luukkala, M. & Meriläinen, P. 1973. Metal plate testing using airborne ultrasound. *Ultrasonics*, 11, 218-221.
- Maierhofer, Ch, A. Brink, M. Röllig, and H. Wiggenhauser. "Transient thermography for

structural investigation of concrete and composites in the near surface region." *Infrared Physics & Technology* 43, no. 3 (2002): 271-278.

Maierhofer, C. 2003. Nondestructive evaluation of concrete infrastructure with ground penetrating radar. *Journal of Materials in Civil Engineering*, 15, 287-297.

Maierhofer, Ch, H. Wiggenhauser, A. Brink, and M. Röllig. "Quantitative numerical analysis of transient IR-experiments on buildings." *Infrared physics & technology* 46, no. 1 (2004): 173-180.

Maierhofer, Ch, A. Brink, M. Röllig, and H. Wiggenhauser. "Quantitative impulse-thermography as non-destructive testing method in civil engineering—Experimental results and numerical simulations." *Construction and Building Materials* 19, no. 10 (2005): 731-737.

Maierhofer, Ch, R. Arndt, M. Röllig, C. Rieck, A. Walther, H. Scheel, and B. Hillemeier. "Application of impulse-thermography for non-destructive assessment of concrete structures." *Cement and Concrete Composites* 28, no. 4 (2006): 393-401.

Marchetti, M., Ludwig, S., Dumoulin, J., Ibos, L. & Mazioud, A. Active infrared thermography for non-destructive control for detection of defects in asphalt pavements. 9th international conference on quantitative infrared thermography, 2008.

Maser, K. R. (1996). Condition assessment of transportation infrastructure using ground-penetrating radar. *Journal of infrastructure systems*, 2, 94-101.

Maser, K. R. (2000). Pavement characterization using ground penetrating radar: State of the art and current practice. *ASTM special technical publication*, 1375, 313-326.

Maser, K. R. (2008). Integration of Ground Penetrating Radar and Infrared Thermography for Bridge Deck Condition Evaluation. *Proceedings of the Symposium of NDE/NDT for Highways and Bridges, SMT, 2008*. Citeseer, 67-74.

Maser, K. R. and Roddis, W. M. K. (1990). Principles of thermography and radar for bridge deck assessment. *Journal of transportation engineering*, 116, 583-601.

Moheimani, S. O. R. 2003. A survey of recent innovations in vibration damping and control using shunted piezoelectric transducers. *Control Systems Technology, IEEE Transactions on*, 11, 482-494.

Moore, J.R., Echard, J.D., and Neill, C.G. (1980), "Radar Detection of Voids Under Concrete Highways," CH1493-6/80/0000-0131, Georgia Department of Transportation, IEEE International Radar Conference, Piscataway, NJ.

Morey, R. M. (1998). Ground penetrating radar for evaluating subsurface conditions for transportation facilities, *Transportation Research Board*.

Mozco, P., Kristek, J., and Galis, M. (2014). *The finite Difference Modeling of Earthquake Motions*. Cambridge University Press.

Mozco, P., Kristek, J., Galis, M., and Pazak, P. (2010). On accuracy of the finite-difference

and finite-element schemes with respect to P-wave to S-wave speed ratio. *Geophysical Journal International*, 493-510.

Moczó, P., Kristek, J., Vavryčuk, V., Archuleta, R.J., and Halada, L. (2002). 3D heterogeneous staggered-grid finite-difference modeling of seismic motion with volume harmonic and arithmetic averaging of elastic moduli and densities. *Bull. Seismic Soc. Am.*, 92, 3042–3066.

Multon, S., Cyr, M., Sellier, A., Diederich, P., Petit, L. (2010). Effects of aggregate size and alkali content on ASR expansion. *Cement and Concrete Research*, 40: 508 - 516.

Multon, S., Sellier, A., Cyr, M. (2009). Chemo–mechanical modeling for prediction of alkali silica reaction (ASR) expansion. *Cement and Concrete Research*, 39: 409 - 500.

Nazarian, Soheil, and Kenneth H. Stokoe. "In Situ Determination of Elastic Moduli of Pavement Systems by Spectral-analysis-of-surface-waves Method: Practical Aspects." (1985).

Nazarian, S., Yuan, D. and Tandon, V. (1999). "Structural field testing of flexible layers with seismic methods for quality control." *Transportation Research Record: Journal of the Transportation Research Board*, 1654, 1–27.

NCHRP. (2003). *Guide for Mechanistic-Empirical Design of New and Rehabilitated Pavement Structures*. Final Report, NCHRP Project 1-37A, National Cooperative Highway Research Program, Transportation Research Board, National Research Council, Washington, D.C.

Nesvijski, E. 1997. On the Problem of Application of the Conic and Exponential Wave Guiding Extensions for Ultrasonic Transducers for Materials Testing. *Journal: NASTA Technical Bulletin*, Philadelphia, PA, USA, 49-56.

Nojavan, A., Schultz, A. E., Chao, S-H., Haselton, C., Simasathien, S., Palacios, G., and Liu, X. (2014). Preliminary Results for NEESR Full-Scale RC Column Tests under Collapse-Consistent Loading Protocols. 10th U.S. National Conference on Earthquake Engineering, Anchorage, AK, July 21-25.

Nojavan, A., Schultz, A.E., Haselton, C., Simathathien, S., Liu, X., and Chao, S-H. (2015). A New Dataset for Full-Scale RC Columns under Collapse-Consistent Loading Protocols. *Earthquake Spectra*, EERI, 31(2): 1211-1231.

NRMCA. (2006). *Concrete in Practice: What, Why and How? CIP 39- Maturity Methods to Estimate Concrete Strength*. National Ready Mixed Concrete Association. Silver Spring MD.

Olek, J., M. D. Cohen, C. F. Scholer, and D. R. Mandrekar. (2003). Use of Modulus of Rupture, Fatigue Resistance and Maturity in Determining Opening to Traffic Time for Concrete Pavements. Publication FHWA/IN/JTRP-2000/25. Joint Transportation Research Program, Indiana Department of Transportation and Purdue University, West Lafayette, Indiana.

Olsen, K.B., Archuleta, R.J., Matarese, J.R. (1995). Magnitude 7.75 earthquake on the San

Andreas Fault: three-dimensional ground motion in Los Angeles, *Science*. 270, 1628–1632.

Öztürk, T., Kroggel, O., Grubl, P., Popovics, J.S.: Improved ultrasonic wave reflection technique to monitor the setting of cementbased materials. *NDT&E Int.* 39, 258–263 (2006)

Park, Y.-J., and Ang, A. H.-S. (1985). Mechanistic Seismic Damage Model for Reinforced Concrete. *Journal of Structural Engineering*, 111(4), pp. 722–739.

Park, C. B., Miller, R. D. & Xia, J. 1999. Multichannel analysis of surface waves (MASW). *Geophysics*, 64, 800-808.

Packard, R. G. 1984. Thickness design for concrete highway and street pavements.

Pederson C.M., Senkowski L.J. “Slab Stabilization of Portland Cement Concrete Pavements” *Transportation Research Record*, Issue 1083, 1986, p. 1-7.

Pitarka, A. (1999). 3D elastic finite-difference modeling of seismic motion using staggered grids with nonuniform spacing. *Bull. seism. Soc. Am.*, 89, 54–68.

Plati, C. and Loizos, A. (2012). Using ground-penetrating radar for assessing the structural needs of asphalt pavements. *Nondestructive Testing and Evaluation*, 27, 273-284.

Popovics, J. S., Oh, T. and Ham, S. (2012). Effective visualization of impact-echo data for bridge deck NDE. *AIP Conference Proceedings*. 1681.

Popovics, S. and Popovics, J. S. (1992). A critique of the ultrasonic pulse velocity method for testing concrete. *Nondestructive testing of concrete elements and structures*. ASCE, 94-103.

Popovics, J. S., W.-S. Song, M. Ghandehari, K. Subramaniam, J. Achenbach, and S. P. Shah. Application of Surface Wave Transmission Measurements for Crack Depth Determination in Concrete. *ACI Materials Journal*, Vol. 97, No. 2, 2000, pp. 127–135.

Popovics, J. S., Oh, T. & Ham, S. Effective visualization of impact-echo data for bridge deck NDE. *AIP Conference Proceedings*, 2012. 1681.

Popovics, John S., and Kolluru VL Subramaniam. "Review of Ultrasonic Wave Reflection Applied to Early-Age Concrete and Cementitious Materials." *Journal of Nondestructive Evaluation* (2014): 1-12.

Qu, J., Bazant, Z., Jacobs, L. J., and Guimaraes, M. (2015). Nonlinear ultrasonic diagnosis and prognosis of ASR damage in dry cask storage. Project. No. 12-3736. Nuclear Energy University Programs (NEUP). U. S. Department of Energy.

Rao, S., Hoegh, K., Yu, T. & Khazanovich, L. 2009. Evaluation of dowel alignment constructability in Portland cement concrete pavements. *Transportation Research Record: Journal of the Transportation Research Board*, 2098, 86-93.

Rapoport, J., Popovics, J.S., Subramaniam, K.V., Shah, S.P.: The use of ultrasound to monitor the stiffening process of Portland cement concrete with admixtures. *ACI Mater. J.* 97, 675–683 (2000)

- Rhazi, J., Dous, O., Ballivy, G., Laurens, S., and Balayssac, J. P. (2003). "Non destructive health evaluation of concrete bridge decks by GPR and half cell potential techniques." International Symposium on Non-Destructive Testing in Civil Engineering, CD-ROM, Berlin, Germany.
- Rivard, P., Ballivy, G., Gravel, C., & Saint-Pierre, F. (2010). Monitoring of an hydraulic structure affected by ASR: A case study. *Cement and concrete research*, 40(4), 676-680.
- Rohne, Ryan J., and Bernard I. Izevbekhai. (2009). Demonstration of Concrete Maturity Test Process on the TH-694/ TH-35E Interchange - Unweave the Weave. Rep. no. MN/RC 2009-26.
- Saarenketo, Timo, and Thomas Scullion. Ground penetrating radar applications on roads and highways. No. TX-95/1923-2F. 1994.
- Saarenketo, T. & Scullion, T. 2000. Road evaluation with ground penetrating radar. *Journal of applied geophysics*, 43, 119-138.
- Sadri, A. & Mirkhani, K. 2009. Wave Propagation Concrete NDT Techniques for Evaluation of Structures and Materials.
- Sagar, R. Vidya, and BK Raghu Prasad. "A review of recent developments in parametric based acoustic emission techniques applied to concrete structures." *Nondestructive Testing and Evaluation* 27, no. 1 (2012): 47-68.
- Sansalone, M., Carino, N. J. & Hsu, N. N. 1987. A finite element study of transient wave propagation in plates. *Journal of research of the National Bureau of Standards*, 92, 267-278.
- Sansalone, M., and N. J. Carino. Detecting Delaminations in Concrete Slabs With and Without Overlays Using the Impact-Echo Method. *ACI Materials Journal*, Vol. 86, No. 2, 1989, pp. 175–184.
- Sansalone, M. J. Detecting Delaminations in Concrete Bridge Decks With and Without Asphalt Overlays Using an Automated Impact-Echo Field System. *Proceedings of the British Institute of Non-Destructive Testing International Conference NDT in Civil Engineering*, Liverpool, United Kingdom, 1993, pp. 807–820.
- Sansalone, M. J., and W. B. Streett. *Impact-Echo: Nondestructive Evaluation of Concrete and Masonry*. Bullbrier Press, Ithaca, N.Y., 1997.
- Sansalone, Mary. "Impact-echo: the complete story." *ACI Structural Journal* 94, no. 6 (1997).
- Saxena, P, Hoegh, K., Khazanovich, L. "Laboratory and analytical modelling of misaligned dowel." *International Journal of Pavement Engineering* 13.3 (2012): 209-215.
- Schickert, M., Krause, M. and Müller, W. (2003). Ultrasonic imaging of concrete elements using reconstruction by synthetic aperture focusing technique. *Journal of Materials in Civil Engineering*, 15, 235-246. Permalink: [http://dx.doi.org/10.1061/\(ASCE\)0899-1561\(2003\)15:3\(235\)](http://dx.doi.org/10.1061/(ASCE)0899-1561(2003)15:3(235)).

- Schubert, F., Peiffer, A., Köhler, B., & Sanderson, T. (1998). The elastodynamic finite integration technique for waves in cylindrical geometries. *The Journal of the Acoustical Society of America*, 104(5), 2604-2614.
- Schubert, F. and Koehler, B. (2001). Three-dimensional time domain modeling of ultrasonic wave propagation in concrete in explicit consideration of aggregates and porosity. *Journal of computational acoustics*, 9, 1543-1560.
- Schubert, F. and Köhler, B. (2008). Ten lectures on impact-echo. *Journal of Nondestructive Evaluation*, 27, 5-21.
- Schubert, F., Lausch, R. and Wiggemhauser, H. (2003). Geometrical effects on impact-echo testing of finite concrete specimens. *Proceedings of International Symposium Non-Destructive Testing in Civil Engineering (NDT-CE)*, 16-19.
- Scott, M., Duke, J. C., Davidson, N., Washed, G. and Weyers, R. (2000). Automated characterization of bridge deck distress using pattern recognition analysis of ground penetrating radar data. *Materials evaluation*, 58, 1305-1309.
- Scott, M., Rezaizadeh, A., Delahaza, A., Santos, C. G., Moore, M., Graybeal, B. and Washer, G. (2003). A comparison of nondestructive evaluation methods for bridge deck assessment. *NDT & E International*, 36, 245-255.
- Scullion, T., Lau, C., and Chen, Y. (1994), Implementation of the Texas Ground Penetrating Radar System, Research Report 1233-1, Texas Transportation Institute.
- Scullion, T. and Saarenketo, T. (1995). Ground penetrating radar technique in monitoring defects in roads and highways.
- Seusy, F. E., W. C. Dass, and K. R. Maser. "Nondestructive Layer Thickness Determination Techniques for an Advanced Pavement System Analyzer." Air Force Civil Engineering Support Agency, Tyndall Air Force Base, FL (1992).
- Sheftick, D.E., and Bartoski, T.A. (1997), Study of Void Detection Methods and Slab Stabilization Procedures, Final Report, Research Project 86-102, Pennsylvania Department of Transportation, Bureau of Construction and Materials.
- Shevaldykin, V. G., Samokrutov, A. A., and Kozlov, V. N. (2002). Ultrasonic Low-Frequency Transducers with Dry Dot Contact and Their Applications for Evaluation of Concrete Structures. *IEEE Ultrason. Symp. Proc.*, Vol. 1-2, 2002, pp. 793-798.
- Smith, Stanley S., and T. Scullion. "Development of ground-penetrating radar equipment for detecting pavement condition for preventive maintenance." *NASA STI/Recon Technical Report N 95* (1993): 11904.
- Soize, Christian. "Maximum entropy approach for modeling random uncertainties in transient elastodynamics." *The Journal of the Acoustical Society of America* 109, no. 5 (2001): pp 1979-1996.
- Stang, H., Mobasher, B., & Shah, S. P. (1990). Quantitative damage characterization in

polypropylene fiber reinforced concrete. *Cement and Concrete Research*, 20(4), 540-558.

Steinway, W.J., Echard, J.D., and Luke, C.M. (1981), *Locating Voids Beneath Pavements Using Pulsed Electromagnetic Waves*, NCHRP Report 237, Transportation Research Board, Washington, DC.

Stokoe, K. H., Wright, S. G., Bay, J. A. & Roesset, J. M. 1994. Characterization of geotechnical sites by SASW method. Technical Report” Geophysical Characterization of Sites, 15-26.

Subramaniam, K.V., Mohsen, J.P., Shaw, C.K., Shah, S.P.: Ultrasonic technique for monitoring concrete strength gain at early age. *ACI Mater. J.* 99, 458–462 (2002).

Takeda, Toshikazu, Sozen, M. A. and Nielsen, N. Norby. (1970). Reinforced Concrete Response to Simulated Earthquakes. *Journal of Structural Engineering*, American Society of Civil Engineers, December 1970.

Tanesi, J., and Meininger, R. (2006). Freeze-Thaw Resistance of Concrete with Marginal Air Content. *FHWA-HRT-06-117*, Federal Highway Administration, Washington, DC, 83 pp.

Tompkins, D., Khazanovich, L, Darter, M, Fleischer. "Design and Construction of Sustainable Pavements." *Transportation Research Record: Journal of the Transportation Research Board* 2098.-1 (2009): 75-85.

Uddin, F., A. K. M., Kenichiro Numata, Jun Shimasaki, Mitsuhiro Shigeishi, and Masayasu Ohtsu. "Mechanisms of crack propagation due to corrosion of reinforcement in concrete by AE-SiGMA and BEM." *Construction and Building Materials* 18, no. 3 (2004): 181-188.

Vladišauskas, A., Raišutis, R., Šlitteris, R., Seniūnas, G. & Jankauskas, A. 2010. Investigation of the characteristics of the low frequency broadband contact transducers. *Ultragarsas (Ultrasound)*, 65, 41-44.

Vladišauskas, A., Mažeika, L., Sliteris, R., Raišutis, R. & Jankauskas, A. 2011. Pulse and frequency responses of broadband low frequency ultrasonic transducers. *Ultragarsas "Ultrasound"*, 66, 32-39.

Voigt, Th., Ch. U. Grosse, Z. Sun, S. P. Shah, and H. -W. Reinhardt. (2005). Comparison of Ultrasonic Wave Transmission and Reflection Measurements with P- and S-waves on Early Age Mortar and Concrete. *Materials and Structures* 38.8: 729-38.

Voigt, T., G. Ye, Z. Sun, S. Shah, And K. Vanbreugel. (2005). Early Age Microstructure of Portland Cement Mortar Investigated by Ultrasonic Shear Waves and Numerical Simulation. *Cement and Concrete Research* 35.5, 858-66.

Voigt, Thomas, Yilmaz Akkaya, and Surendra P. Shah. (2003). Determination of Early Age Mortar and Concrete Strength by Ultrasonic Wave Reflections. *Journal of Materials in Civil Engineering* 15.3.

Vosooghi, A. and Saiidi, M. (2013). Shake-Table Studies of Repaired Reinforced Concrete Bridge Columns Using Carbon Fiber-Reinforced Polymer Fabrics. *ACI Structural Journal*, V.

110, No. 11, Jan-Feb., pp. 105-114.

Wang, S., Llamazos, E., Baxter, L., & Fonseca, F. (2008). Durability of biomass fly ash concrete: freezing and thawing and rapid chloride permeability tests. *Fuel*, 87(3), 359-364.

Warhus, J.P., Mast, J.E., Johanson, E.M, and Nelson, S.D. (1994), "Advanced Ground Penetrating Radar," Proceedings of SPIE - The International Society for Optical Engineering, Nondestructive Advanced Microwave and Millimeter-Wave Detectors, S.S. Udpa and H.C. Han, eds., Vol. 2275, July 25-26, pp. 177-185.

Warhus, John P., Jeffrey E. Mast, and Scott D. Nelson. "Imaging radar for bridge deck inspection." In *Nondestructive Evaluation of Aging Infrastructure*, pp. 296-305. International Society for Optics and Photonics, 1995.

Weiland, T. (1977). A discretization method for the solution of Maxwell's equations for six-component fields. *Electronics and Communication (AEÜ)*, vol. 31, p. 116.

Willett, D. A., K. C. Mahboub, and B. Rister. Accuracy of Ground-Penetrating Radar for Pavement-Layer Thickness Analysis. *Journal of Transportation Engineering*, Vol. 132, No. 1, 2006, pp. 96–103.

Wu, T-T., J-S. Fang, and P-L. Liu. "Detection of the depth of a surface-breaking crack using transient elastic waves." *The Journal of the Acoustical Society of America* 97, no. 3 (1995): 1678-1686.

Yang, Z. (2004). Assessing cumulative damage in concrete and quantifying its influence on life cycle performance modeling (*Doctoral dissertation, Purdue University*).

Yang, Z., Weiss, W. J., & Olek, J. (2006). Water transport in concrete damaged by tensile loading and freeze–thaw cycling. *Journal of Materials in Civil Engineering*.

Yeih, W., and R. Huang. "Detection of the corrosion damage in reinforced concrete members by ultrasonic testing." *Cement and concrete research* 28, no. 7 (1998): 1071-1083.

Yoon, Dong-Jin, W. Jason Weiss, and Surendra P. Shah. "Assessing damage in corroded reinforced concrete using acoustic emission." *Journal of engineering mechanics* 126, no. 3 (2000): 273-283.

Yu, H. Thomas, and L. Khazanovich. Use of Magnetic Tomography Technology to Evaluate Dowel Placement. US Department of Transportation, Federal Highway Administration, 2005.

YU, H. T., TAYABJI, S. D. Need for Improved Specifications on Dowel Bar Placement Tolerance. Transportation Research Board 86th Annual Meeting, 2007.

Yuan D., and S. Nazarian. Feasibility of Detecting Flaws in Concrete Walls of Nuclear Power Plants. Center for Highway Materials Research, Pasadena, Calif., 2000.

Zhu, J. and Popovics, J. (2002). Non-contact detection of surface waves in concrete using an air-coupled sensor. *AIP Conference Proceedings*, 2002. 1261.

Zhu, J. and Popovics, J. S. (2007). Imaging concrete structures using air-coupled impact-echo. *Journal of engineering mechanics*, 133, 628-640.

Zhu, J., Popovics, J. S. and Schubert, F. (2004). Leaky Rayleigh and Scholte waves at the fluid–solid interface subjected to transient point loading. *The Journal of the Acoustical Society of America*, 116, 2101.

Zollinger, D. G., Senadheera, S. P. & TANG, T. 1994. Spalling of continuously reinforced concrete pavements. *Journal of transportation engineering*, 120, 394-411.

Appendix A - EFIT Program User Manual

The EFIT modeling program simulates shear wave propagation in a homogeneous elastic or viscoelastic medium, including reinforcement and delamination. EFIT is written in FORTRAN. However, visualization of the output results from FORTRAN are conducted using Java. The program is capable of simulating the propagation of horizontal shear waves.

A.1 PREPARING INPUT FILES FOR EFIT

For a simulation using EFIT, two input files need to be prepared. The first file, named InputFile, is a text file. This file is generated using a graphical user interface, EFIT_GUI, which will be introduced in the following section. The second file, named ExcData.csv, has information regarding the emitted signals.

A.1.1 GUI to generate InputFile.txt

As mentioned, a graphical user interface (GUI), shown in Figure A1, is used to define the geometry of the medium, material properties, grid size, location and size of transmitting and receiving transducers and the other required data (see Figures 1 and 2). Defining these variables and running GUI provides the InputFile.txt which will be read by the EFIT program as an input file. To have this graphical interface, the user needs to run the EFIT_GUI.exe file.

The screenshot displays the EFIT_GUI interface with the following fields and controls:

- Width of Medium:** 0.5
- Depth of Medium:** 0.3
- Medium Material's Density:** 2400.0
- Medium Material's Shear Velocity:** 2300
- Relaxation Frequency:** 188495
- Anelastic Coefficient:** 0.15
- Material Elasticity Type:** Elastic, Viscoelastic
- Delaminated:** Not Delaminated, Delaminated
- Delam Region's Density:** 1600.0
- Delam Region's Shear Vel.:** 1600.0
- Enter number of regions:** 0
- Enter Coords of Delaminated Regions:** (empty text area)
- Boundary Conditions:** Free, Fixed, Absorbing. Left: Free, Fixed, Absorbing. Right: Free, Fixed, Absorbing. Bottom: Free, Fixed, Absorbing.
- Frequency of Visualization:** 50
- Time Step:** 0.0000002
- Mesh Size:** 0.001
- Total time of simulation:** 0.0005
- Concrete Type:** Plain Concrete, Reinforced Concrete
- Density of Reinforcements:** 7800.0
- Shear Vel. of Reinforcements:** 3200.0
- Number of Reinforcements:** 0
- x-coordinate of first sens.:** 0.10
- Dist between adjacent sensors:** 0.04
- Total # of transducers:** 10
- Choose the sending transducers for visualization:** 1 2 3 4 5 6 7 8 9 10 11 12 13 14 15 (radio buttons 1-10 are selected)
- Buttons:** Generate File, Import File, Run EFIT, Visualize, Exit.
- Text on right:** Choose run options at left and select 'Generate File' OR Start a new project with an old file by selecting 'Import File'. C:\Users\laziz\ADI\Desktop choose project dir.

Figure A1. Graphical user interface to define the input data

If making a new input file, select a project directory for it to be placed. Directories called InputFiles and OutputFiles will be created in that project directory:

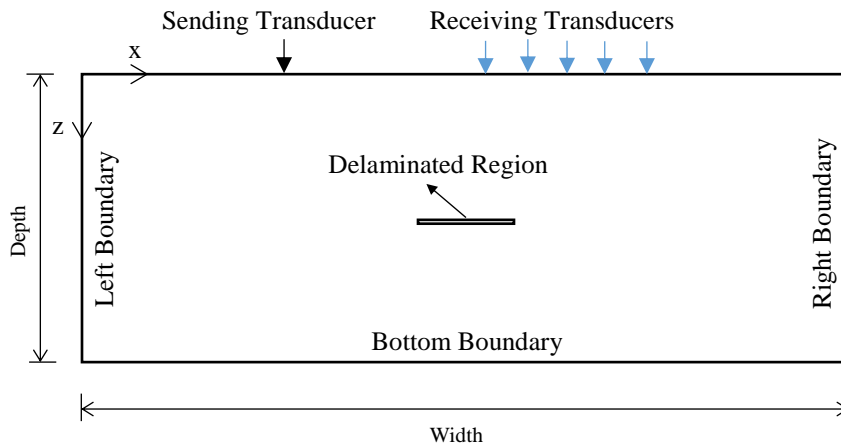
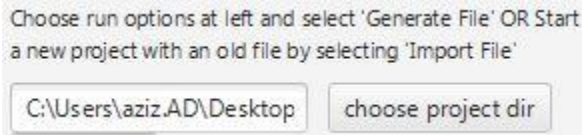
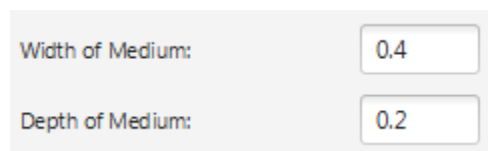
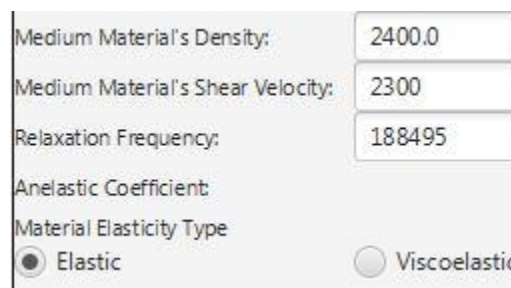


Figure A2. A typical problem simulated using the EFIT program

It should be noted that the SI units (m, s, Kg) are used in this manual. User can define the width and depth of the domain using the GUI.



The medium is defined in the xz -plane. The x -axis defines the top surface and the z -axis is always downward. The origin of the coordinate system is located on the top left corner of the domain, see Figure A2. The material of the medium can be elastic or viscoelastic. In the case of elastic material, the user only needs to define the density and shear velocity of the materials.



For viscoelastic materials, the user needs to define two more variables: relaxation frequency and anelastic coefficient. The relaxation frequency is always chosen to be the central angular frequency of emitted signal. For example, for a 30 KHz signal, this value is

$$\omega = 2\pi \times 30,000 \cong 188495 \text{ rad/s}$$

The variable anelastic coefficient specifies the attenuation; a larger value indicates bigger attenuation. The value of this parameter depends on the application. For concrete this number can be between 0.1 and 0.2; 0.15 can be chosen as default.

Width of Medium:	0.5
Depth of Medium:	0.3
Medium Material's Density:	2400.0
Medium Material's Shear Velocity:	2300
Relaxation Frequency:	188495
Anelastic Coefficient:	0.15
Material Elasticity Type	
<input type="radio"/> Elastic	<input checked="" type="radio"/> Viscoelastic

The user can also include or exclude a delamination in the simulation. A delamination is simulated by assigning a low velocity or even low density to the material within the delaminated region. For delaminated concrete, the user is required to define the geometry of the delaminated region. The delaminated region is assumed to have rectangular shape, so the user needs to enter x and z coordinates of the top left corner and the bottom right corner of the rectangle (see Figure 1). Material properties of the delaminated region, density and shear velocity, need to be assigned as well. Shear wave velocity is assumed to be very small for this region.

Delaminated			
<input type="radio"/> Not Delaminated		<input checked="" type="radio"/> Delaminated	
Delam Region's Density		1600.0	
Delam Region's Shear Vel.		1600.0	
Enter number of regions:		2	
Enter Coords of Delaminated Regions			
Top X	Top Z	Bottom X	Bottom Z
.1	.1	.3	.11
.2	.2	.3	.21

To perform a simulation, boundary conditions need to be defined. The top boundary of the medium is always considered to be free. As a result, the boundary conditions of the left, right and bottom boundaries need to be defined (see Figure A2). A boundary can be free, fixed, or absorbing. For an absorbing boundary, the boundary absorbs the incident wave and does not permit reflections. Absorbing boundaries are used when a large medium is replaced with a small one to save

computationally and to eliminate reflections. Absorbing boundaries are artificial and do not exist in the real world; they are also known as artificial boundaries.

Boundary Conditions	Free	Fixed	Absorbing
Left	<input type="radio"/>	<input type="radio"/>	<input checked="" type="radio"/>
Right	<input type="radio"/>	<input type="radio"/>	<input checked="" type="radio"/>
Bottom	<input checked="" type="radio"/>	<input type="radio"/>	<input type="radio"/>

Afterwards the size of time step and mesh size is defined. These values have to be defined carefully. Large values of spatial grid size cause numerical dispersion and large values of temporal grid size cause instability. On the other hand, too small values for these variables make computations inefficient. Spatial grid size is usually taken 1/10 of the minimum wavelength of the emitted signals. For MIRA’s signal, a candidate for time step size can be 0.0000002 s and 0.001 mm for mesh size.

Time Step

Mesh Size

Then the total time of simulation needs to be assigned. This value must be large enough to let the signals travel, hit the inclusions or free boundaries and to be received by output transducers. User can evaluate this number by dividing the distance that wave travels by the velocity of the wave.

Total time of simulation

The user has two options for outputting the results of simulation. One option is to output only the information of output transducers, this can be done by choosing “No” for Visualize. The other option is to output information of all grid points for visualization of results plus the information of output transducers. This can be done by choosing yes for Visualize.

Visualize: Yes No

Frequency of Visualization

When one writes information for all of the nodes to the files, if the size of the medium and the number of time steps is large, then the size of output files, fout files, can be huge. To avoid large files, the user can reduce the number of frames which will be visualized. This is done by choosing

a number for frequency of visualization. For instance, if this number is 50, then after each 50 time steps the data is written to files for visualization, and if the total number of steps is 1000, for example, the number of frames will be 20.

The user can include reinforcement. For a reinforced concrete, user need to provide the density of reinforcement and shear wave velocity in reinforcement. Geometry and location of reinforcements is defined by specifying their radius and x and z coordinated of their center

The screenshot shows a form titled "Concrete Type" with two radio buttons: "Plain Concrete" (unselected) and "Reinforced Concrete" (selected). Below this are input fields for "Density of Reinforcements" (7800.0), "Shear Vel. of Reinforcements" (3200.0), and "Number of Reinforcements" (2). A section titled "Enter X,Z coords and Radius of Reinforcements" contains three columns of input fields: "X", "Z", and "Radius". The "X" column has values ".1" and ".2". The "Z" column has values ".1" and ".2". The "Radius" column has values ".01" and ".01".

Next, the user defines the number of sending and receiving transducers in an ultrasonic linear array. These transducers are located on the top surface of the medium. Therefore, to define their locations, the x-coordinate of the first row of transducers, distance between adjacent rows of transducers and total number of rows of transducers must be specified

The screenshot shows a form with three input fields: "x-coordinate of first sens..." (0.10), "Dist between adjacent sensors" (0.04), and "Total # of transducers" (10).

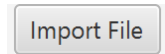
Select visualization options, including which transducers to visualize:

The screenshot shows a form titled "Choose the sending transducers for visualization" with a row of 15 radio buttons numbered 1 through 15. The radio button for transducer 4 is selected.

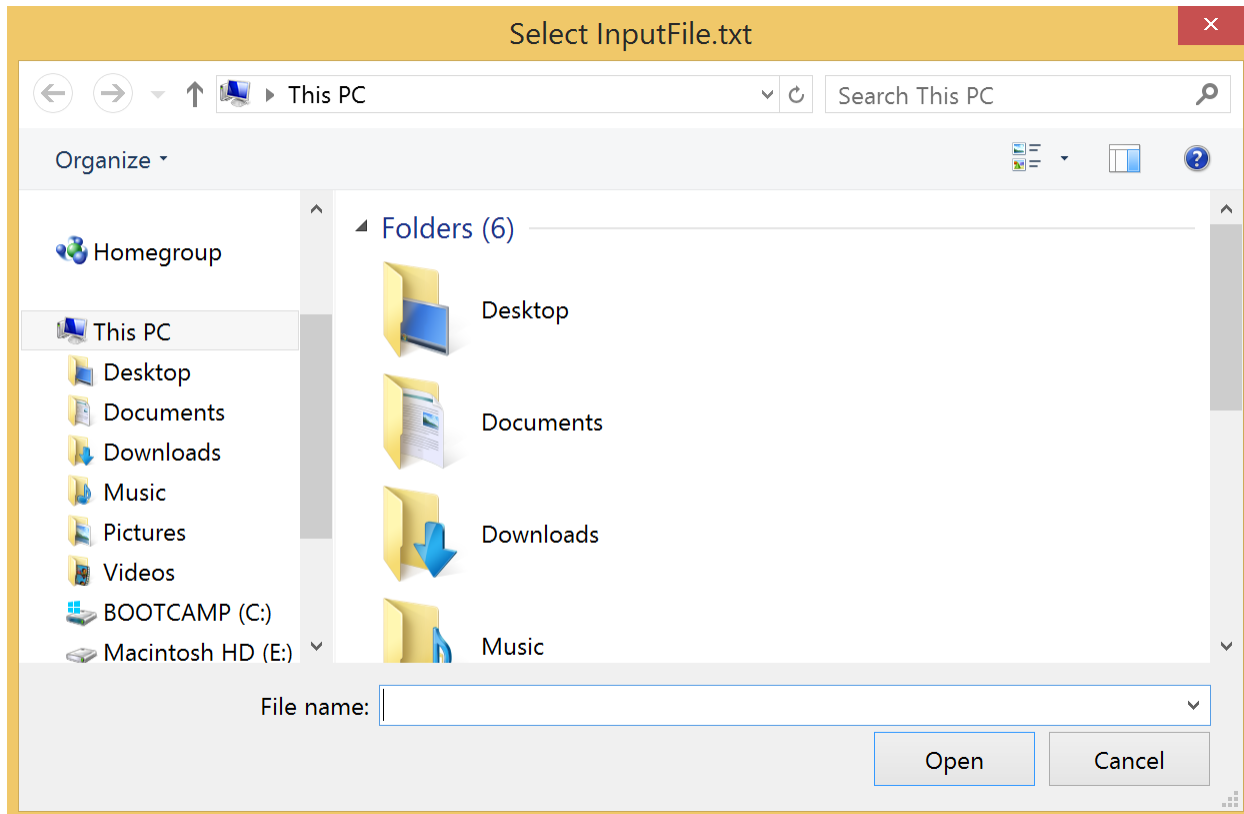
Hitting the Generate File button, program provides InputFile.txt, which then is read by UMN_EFIT program as input file.

The screenshot shows a single button labeled "Generate File".

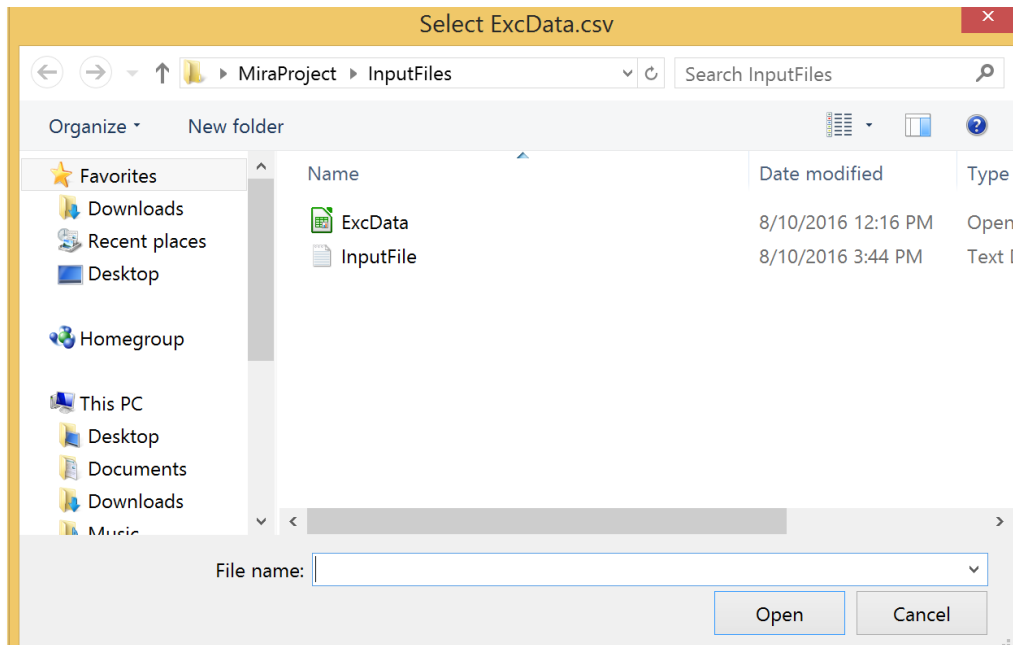
If user wants import an existing InputFile.txt, then s/he can do that by hitting the bottom “Import File”



Then user can select the input file you would like to use (named InputFile.txt)



After generating or importing the InputFile, select the ExcData.csv file you would like to use



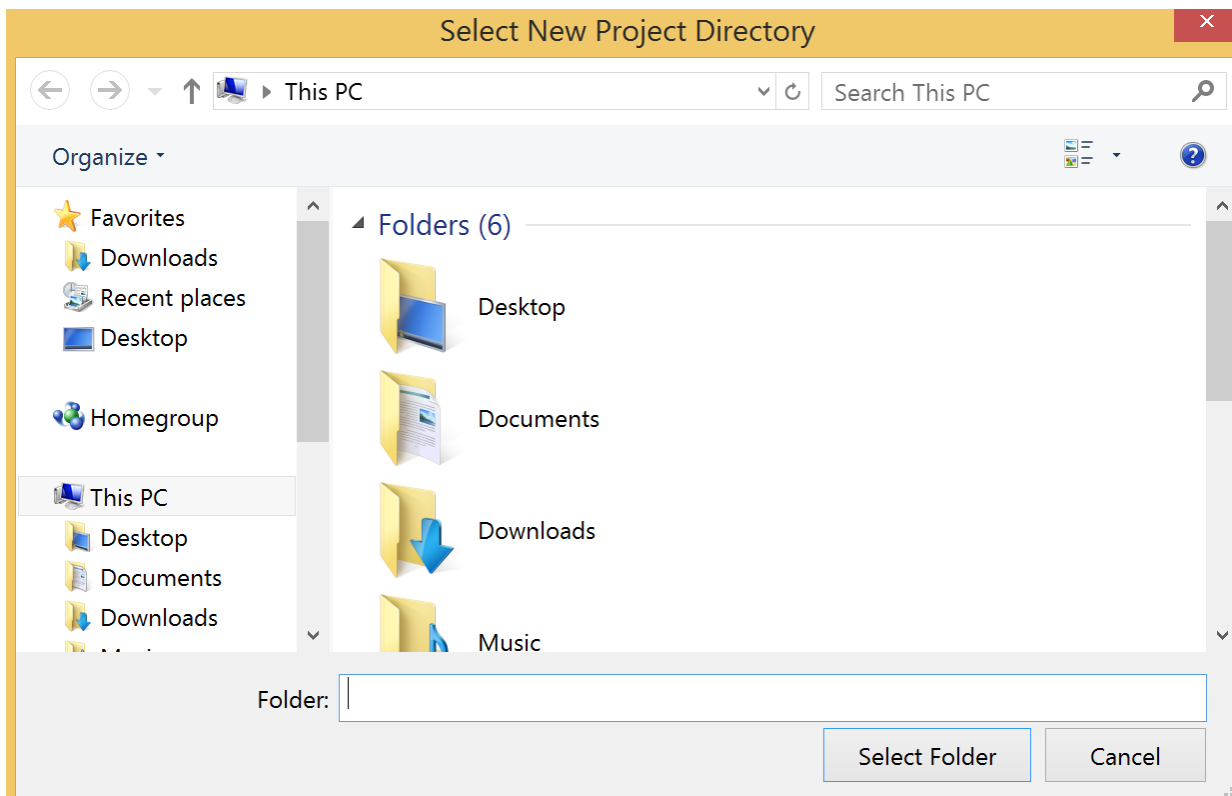
The data corresponding to transmitting signals are read from the comma-separated value file ExcData.csv. An example of this file is given in Table A1. The first column in this file represents the time values, and columns thereafter correspond to sensors and associated values of velocity signals. Note that the number of columns (i.e. the number of sensors) corresponds to the number of sending transducers. The first column represents the emitted signal by the first sending transducer and so on.

Table A1. Example of main EFIT input file “ExcData.csv”

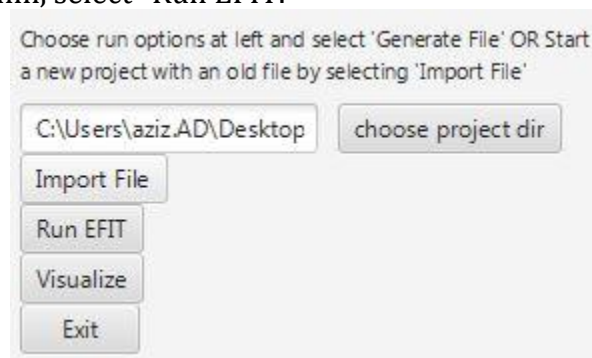
Line number	Excdata.csv
1	0,0,0
2	0.000001,8555.642519,8555.642519
3	0.000002,15191.02152,15191.02152
4	0.000003,18190.62893,18190.62893
5	0.000004,16230.28225,16230.28225
6	0.000005,8528.837081,8528.837081
7	0.000006,-5048.726835,-5048.726835
8	0.000007,-23946.5566,-23946.5566
9	0.000008,-46936.34047,-46936.34047
10	0.000009,-72198.39857,-72198.39857
11	0.00001,-97459.65382,-97459.65382
12	0.000011,-120177.8138,-120177.8138
13	0.000012,-137757.0588,-137757.0588
14	0.000013,-147777.6645,-147777.6645
15	0.000014,-148220.5339,-148220.5339
16	0.000015,-137667.6944,-137667.6944
17	0.000016,-115461.4449,-115461.4449
18	0.000017,-81807.88584,-81807.88584
19	0.000018,-37814.81078,-37814.81078
20	0.000019,14540.96642,14540.96642
21	0.00002,72516.20993,72516.20993
22	0.000021,132767.5716,132767.5716
23	0.000022,191570.2433,191570.2433
24	0.000023,245073.2667,245073.2667
25	0.000024,289572.6869,289572.6869
26	0.000025,321782.0474,321782.0474
27	0.000026,359079.6208,359079.6208
28	0.000027,339713.2757,339713.2757
29	0.000028,322946.8762,322946.8762
30	0.000029,289136.3875,289136.3875
31	0.00003,239729.0757,239729.0757
32	0.000031,177184.9571,177184.9571
33	0.000032,104825.5114,104825.5114
34	0.000033,26620.1806,26620.1806
35	0.000034,-53074.10073,-53074.10073
36	0.000035,-129801.5265,-129801.5265
37	0.000036,-199303.2302,-199303.2302
38	0.000037,-257798.7771,-257798.7771
39	0.000038,-302232.9194,-302232.9194
40	0.000039,-330469.8403,-330469.8403
41	0.00004,-341421.1048,-341421.1048
42	0.000041,-335098.5644,-335098.5644
43	0.000042,-312589.1371,-312589.1371
44	0.000043,-275954.2626,-275954.2626
45	0.000044,-228062.4658,-228062.4658
46	0.000045,-172368.4026,-172368.4026
47	0.000046,-112655.645,-112655.645

48	0.000047,-52762.98278,-52762.98278
49	0.000048,3685.008781,3685.008781
50	0.000049,53523.02348,53523.02348
51	0.00005,94247.77961,94247.77961
52	0.000051,124164.1148,124164.1148
53	0.000052,142464.6956,142464.6956
54	0.000053,149238.9599,149238.9599
55	0.000054,145412.5341,145412.5341
56	0.000055,132623.819,132623.819
57	0.000056,113049.2967,113049.2967
58	0.000057,89192.98657,89192.98657
59	0.000058,63658.07546,63658.07546
60	0.000059,38919.86644,38919.86644
61	0.00006,17118.75501,17118.75501
62	0.000061,-110.0049091,-110.0049091
63	0.000062,-11756.27029,-11756.27029
64	0.000063,-17495.59431,-17495.59431
65	0.000064,-17686.37379,-17686.37379
66	0.000065,-13304.86418,-13304.86418
67	0.000066,-5824.584834,-5824.584834
68	0.000067,0,0

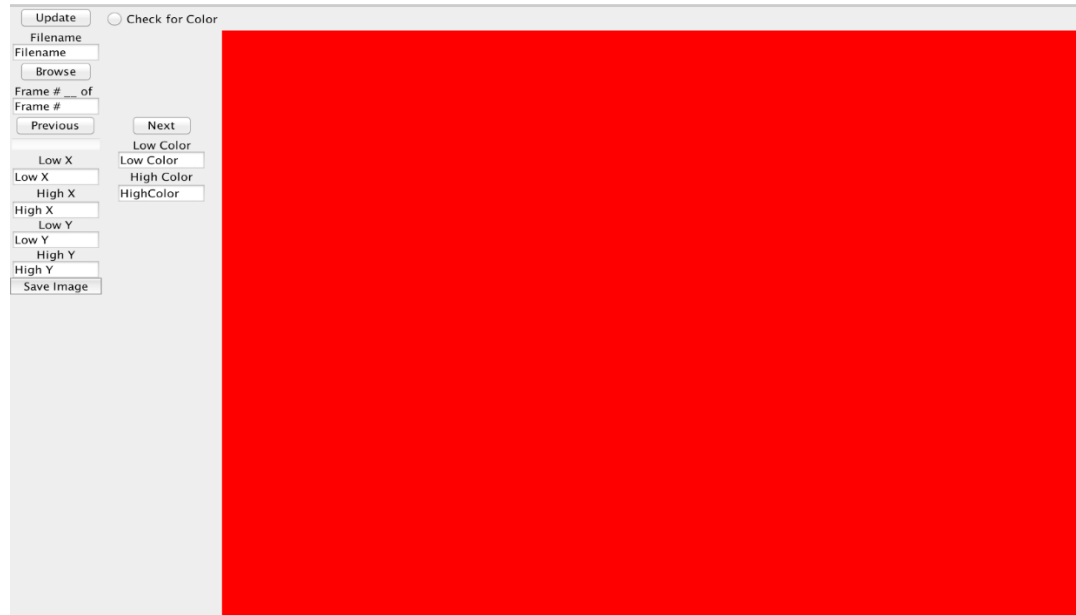
Afterwards, select a folder to be used as the project folder (InputFiles and OutputFiles folders will be generated inside of it)



To run the EFIT algorithm, select “Run EFIT.”



Output files will be placed in the “Output Files” directory. The window may tell you that the program is “not responding,” this is normal while the EFIT algorithm is running. EFIT algorithm information will be displayed in the console window that launched with the graphic interface, as long as new information is printing there the program is fine. To visualize the results, select “Visualize”, This will launch a new window.



Hit “Browse” to select a file for visualization (will be located in the “OutputFiles” directory) By using the “Previous” and “Next” buttons, different frames of the run can be seen. The slider can also be used for this. The area visualized can be changed by changing the values in “Low X”, “High X”, “Low Y”, “High Y” to the desired minimum and maximum x and y values and hitting “Update”. The lowest and highest values mapped to a color/grayscale value can be changed using “Low Color” and “High Color” to provide greater resolution in areas of interest by changing the values in the boxes then hitting “Update”. Color vs. Grayscale images can be changed by checking the “Check for Color” checkbox and hitting “Update” Hitting “Save Image” can generate a .png image file of the currently displayed frame. It will be saved in the project directory with a filename based on the current system time in milliseconds.